SOLID-STATE PROTON NUCLEAR MAGNETIC RESONANCE STUDIES OF HYDROGEN SITE OCCUPANCIES, ELECTRONIC STRUCTURE PROPERTIES, AND DIFFUSION BEHAVIOR IN TRANSITION METAL HYDRIDES

Thesis by

Robert Clark Bowman, Jr.

In Partial Fulfillment of the Requirements

for the Degree of

Doctor of Philosophy

California Institute of Technology
Pasadena, California

1983

(Submitted August 30, 1982)

ACKNOWLEDGEMENTS

Many individuals have assisted and supported me during my return to graduate school. However, three deserve special credit. First, it was the enthusiastic reception and sponsorship of the late Robert W. Vaughan that made Caltech a reality. I will always regard his untimely death in the May 1979 Chicago airline crash as a personal loss. However, if Sunney I. Chan had not volunteered to become my advisor even though my research plans and objectives were outside his own interests, my opportunity to come to Caltech would have effectively died with Dr. Vaughan. Although Sunney has not been able to teach me biochemistry, I have learned many things from him and I am most grateful. Won-Kyu Rhim generously made available his laboratory and spectrometer and also introduced me to the new techniques heavily used in my research. Won-Kyu has always given me sound advice and unfaltering support and I regard his friendship as important.

I owe a great debt to my management at MRC-Mound and in particular to Drs. William T. Cave, Richard E. Vallée, Warren H. Smith, and Layton J. Wittenberg. Not only did they provide me with the unique opportunity to come to Caltech at company expense and supplied the necessary financial support during my studies, but they allowed me time and freedom to complete my writing. I hope to merit their faith in me.

I have always enjoyed the comfort, support, and love of my family - Judy, Becky, and Missy. However, the changes associated with my return to graduate school added new challenges and stresses to our lives. It takes some adjustments when Dad postpones helping you with your homework when he has his homework to do first. Becky and Missy, I hope that my preoccupation has not deprived us of too many shared experiences. Throughout our marriage, Judy has encouraged me to obtain my goals even though she had to sacrifice many of her personal objectives. I appreciate her caring and devotion.

The research contained in the thesis has benefitted from the collaboration and support of many able scientists. There would have been no

NMR studies if the well-characterized and carefully prepared samples had not been provided by John R. Johnson, William L. Johnson, Arnulf J. Maeland, Wayne E. Tadlock, and Eugene L. Venturini. Bartlett D. Craft helped with some of the NMR measurements; Michael P. Guse assisted with some of the calculations; James F. Lynch performed the magnetic susceptibility measurements; and Donald B. Sullenger obtained and analyzed the x-ray diffraction data. Albert Attalla has worked closely with me for ten years and provided many special services during my stay at Caltech. I thank all of these gentlemen. The comments and discussions with George C. Abell and Gust Bambakidis are appreciated.

The very special friendship of Scott and Barbara Armstrong to myself and my family has been among the best results of going to California.

The entire manuscript, with several revisions and alterations, was competently and cheerfully prepared by Mrs. Betty J. Weidner. Betty is by far the best technical typist that I have ever worked with and a fine person as well.

The research has been supported by the Caltech President's Fund and Chemical Sciences Branch of the Office of Basic Energy Sciences, U. S. Department of Energy.

ABSTRACT

Solid-state NMR techniques have been used to measure the proton lineshapes, Knight shifts, and relaxation times in several transition metal hydrides. The objective of these studies is to obtain a better understanding of the roles of host metal structure and substitutional alloying on the hydrogen site occupancy, the electronic structure properties, and diffusion mechanisms.

An improved method for observing the rigid-lattice proton lineshapes and extracting the second moments has been developed. Comparisons of the experimental second moments for polycrystalline samples with the values calculated from Van Vleck formulas for nuclear dipolar interactions have indicated that only tetrahedral interstitial sites are occupied by the protons in TiH_x, ZrH_x, crystalline $TiCuH_{0.94}$, $Ti_2CuH_{1.9}$, and Zr_2PdH_x (with $x < 2$) while both tetrahedral and octahedral sites can be occupied in amorphous a-$TiCuH_{1.4}$, $Ti_2CuH_{2.6}$, and Zr_2PdH_x ($x > 2$).

The proton Knight shifts and low-temperature spin-lattice relaxation times have been related to the local densities of electron states at the Fermi levels $N(E_F)$ in $Ti_{1-y}V_yH_x$, $TiCr_{1.8}H_x$, $TiCr_{1.9}H_x$, $TiCuH_x$, Ti_2CuH_x, ZrH_x, and Zr_2PdH_x. The dominant conduction electron hyperfine interaction for protons is a transferred "core-polarization" of the paired hydrogen 1s electrons through spin exchange with the unpaired metal d electrons. The proton NMR parameters have confirmed that decreases in $N(E_F)$ through a Jahn-Teller type mechanism are associated with the temperature and composition dependent tetragonal distortions in $Ti_{1-y}V_yH_{1.95}$ and ZrH_x (where $1.75 \leqslant x \leqslant 2.0$). The proton NMR results are consistent with recent band theory calculations and photoemission spectra. Unusual $N(E_F)$ increases with hydrogen content, which are supported by independent magnetic susceptibility data, have been observed in $TiCr_{1.8}H_x$, $TiCr_{1.9}H_x$, and Ti_2CuH_x. The proton parameters suggest that significant differences in $N(E_F)$ for the crystalline and amorphous phases of $TiCuH_x$ and Zr_2PdH_x may reflect a smearing of energy levels in the disordered phases.

The proton rotating-frame relaxation times for $Ti_{1-y}Cu_yH_x$ indicate both crystal structure and hydrogen site occupancies greatly influence diffusion behavior. A significant enhancement in hydrogen mobility for amorphous a-$TiCuH_{1.4}$ has been confirmed; but, short range order is probably retained in the structure of a-$TiCuH_{1.4}$. Reductions in activation energies are observed when octahedral sites exist in the diffusion paths between tetrahedral sites.

TABLE OF CONTENTS

		Page
Acknowledgements		ii
Abstract		iv
Chapter 1:	Introduction and Some Properties of Transition Metal Hydrides	1
Chapter 2:	Concepts and Methods of Nuclear Magnetic Resonance as Applied to Metal Hydrides	18
Chapter 3:	A Simple Magic Echo Sequence for Second Moment Measurements	45
Chapter 4:	Proton NMR Lineshapes in ZrH_x	59
Chapter 5:	Proton NMR Studies of Electronic Structure in $Ti_{1-y}VyH_{1.95}$	74
Chapter 6:	Electronic Structure of Zirconium Hydride - A Proton NMR Study	85
Chapter 7:	Proton NMR and Magnetic Susceptibility Study of $TiCr_{1.8}H_x$	130
Chapter 8:	Proton NMR Studies of Hydrogen Diffusion and Electronic Structure in Crystalline and Amorphous Titanium - Copper Hydrides	148
Chapter 9:	Proton Site Occupancies and Electronic Properties in Crystalline and Amorphous Zr_2PdH_x	192
Chapter 10:	Summary and Conclusions	216
Propositions		221

CHAPTER 1

INTRODUCTION AND SOME PROPERTIES OF TRANSITION METAL HYDRIDES

I. INTRODUCTION

Many metals and intermetallic compounds can reversibly react with hydrogen gas to form a subclass of interstitial compounds known as the metal hydrides (1-4). The transition metals of groups III, IV, and V, rare earths, actinides, and Pd react exothermally with hydrogen to form rather stable binary hydrides with hydrogen-to-metal atom ratios between 0.5 and 3.5. These transition metal hydrides generally have the large electrical conductivities that are typical of metals, but the hydrides are usually harder and more brittle than the pure host metals. Furthermore, the interstitial metal hydrides are usually nonstoichiometric and often exist in several phases with significant structural changes for each metal to produce rather complex phase diagrams (1-4). These hydride alloys are quite distinct from the covalent transition metal complexes (5,6) that now form a major subfield of inorganic chemistry. The transition metals of groups VI, VII, VIII (with the notable exception of Pd), and the noble metals react endothermally with hydrogen and absorb very small quantities of hydrogen except under very high pressure (i.e., >kbars) or nonequilibrium conditions such as electrolytic charging or ion implanation.

Within the past decade, metal hydrides have received increasing attention as components in energy storage systems (7-10). Some of the possible applications include the mobile and stationary storage of hydrogen to be subsequently consumed as fuel in internal combustion engines or fuel cells, thermal storage using the often large exothermic heats of reaction, chemical heat pumps, hydrogen gas compressors, isotope separation, and the simultaneous purification and storage of hydrogen for the chemical process industries. The prime consideration in all these applications is a sufficiently rapid and reversible reaction between the host metal and gaseous hydrogen. Furthermore, a large hydrogen absorption capacity (i.e., H/M ratio $\geq$1.0) is usually required and the equilibrium dissociation pressure should vary between 0.1 atm and 10 atm over the temperature range of device operation. To increase

overall efficiencies the heat needed to decompose the hydrides should be obtainable from the ambient surroundings or low-grade waste heat (i.e., engine exhaust or cooling system fluids). These restrictions eliminate all the binary metal hydrides with the possible exception of MgH_2. Hence, the discovery of moderately unstable hydride phases for several classes of intermetallic compounds AB_n (where n may be nonintegral) has provided the major impetus for the energy storage applications. The desired reversible reaction between the intermetallic alloy and hydrogen is

$$AB_n + x\ H_2 \rightleftarrows AB_nH_{x/2} \qquad (1)$$

where metal A forms a stable binary hydride AH_x, but metal B either forms no hydride or else a very unstable one. If B were to form a stable BH_x phase, the ternary hydride $AB_nH_{x/2}$ is almost always too stable for any practical storage application. Representative intermetallics that are suitable are TiFe, $LaNi_5$, and $TiCr_2$. However, the behavior of literally hundreds of intermetallics and alloys with respect to hydrogen has been investigated in recent years as is readily apparent from the proceedings of several specialized conferences (11-15) on metal hydrides. In addition to the energy storage applications, metal hydrides are very important to the hydrogen-embrittlement problems of metals and fusion reactor technology. There are also indications that some transition metal hydrides may be useful heterogeneous catalysts (16).

Besides the various technological aspects, the interstitial transition metal hydrides are interesting materials for study by solid-state chemists and physicists (17). Fundamental physical properties such as electrical behavior, magnetism, and superconductivity behavior can be significantly altered by the absorption of hydrogen. Some hydride alloys are model systems for thermodynamics of phase transitions - particularly, in the case of order-disorder phenomena (18). Although the diffusion of heavy interstitials (i.e., carbon, oxygen, nitrogen,

etc.) in metals is normally very slow with diffusion coefficients $<10^{-20}$ cm^2/s at 300 K, the diffusivities of hydrogen atoms are in the range of $\sim 10^{-12}$ cm^2/s to $\sim 10^{-5}$ cm^2/s at 300 K for most metal hydrides (19,20). Furthermore, the combination of high mobility and the light masses of the hydrogen isotopes lead to the possibility of quantum mechanical contributions (21) to the diffusion mechanism. Among the more interesting problems associated with metal hydrides are the roles of host metal structure and substitutional alloying on the hydrogen site occupancy, the electronic properties reflecting the metal-hydrogen bond character, and the hydrogen diffusion mechanisms. The inherent complexities of most ternary metal hydrides and the often incomplete knowledge of structural parameters and other fundamental physical properties have generally limited efforts to understand these relationships. With the continuing intense interest in metal hydride behavior, systematic studies that can clarify the relative contributions of crystal structure and the presence of different metal atoms at a particular site for model metal hydride phases are highly desirable.

The objective of the present research has been to evaluate some fundamental properties of the binary hydrides TiH_x and ZrH_x and several related ternary hydrides containing other transition metals using the solid-state techniques of proton nuclear magnetic resonance spectroscopy. The emphasis of these NMR experiments has been to establish hydrogen interstitial site occupancies from improved measurements of the proton lineshapes and characterizing the electronic properties using proton Knight shifts and spin-lattice relaxation times. The NMR results have been correlated with various supplemental studies involving x-ray diffraction, neutron diffraction, inelastic neutron scattering, magnetic susceptibility measurements, and APW band-theory calculations. Critical comparisons of the hydrogen diffusion behavior in crystalline and amorphous hydrides have also been made for the Ti-Cu system.

Brief general descriptions of the crystal structures, electronic structure properties, and diffusion behavior in transition metal hydrides

are being presented in this chapter to establish the scope of the NMR studies. Although proton relaxation times have been extensively utilized to evaluate diffusion behavior in metal hydrides, the power and versatility of many recently developed solid-state NMR techniques for studying the structural features (i.e., hydrogen site occupancies) and the electronic properties of metal hydrides have not been generally exploited. A goal of the present work has been to determine the potential of several novel solid-state NMR techniques through their use on some model and representative metal hydrides. The benefits and limitations of these techniques need to be identified if they are to be incorporated in the future NMR studies of metal hydrides or other areas of materials research.

II. CRYSTAL STRUCTURE CONSIDERATIONS

The formation of a metal hydride is often (but not always) accompanied by a distortion or modification of the metal lattice although hydrogen absorption nearly always gives a substantial volume increase (22). Many binary hydrides MH_x (e.g., TiH_2, VH_2, PdH_x, and the rare earth dihydrides and some trihydrides) have the face-centered cubic (fcc) structure for the metal sublattice (1). Fig. 1 shows that the hydrogen atoms can occupy either the octahedral or tetrahedral interstitial sites of the fcc metal lattice. When only the octahedral sites are occupied, the limiting composition is MH with the NaCl structure as found in PdH_x. Occupancy of only tetrahedral sites gives MH_2 (i.e., TiH_2 or VH_2) with the fluorite (CaF_2) structure. There are also hydrides such as LaH_x ($2 \leqslant x \leqslant 3$) where both types of interstitial sites are simultaneously occupied. It is a general characteristic that metal hydrides are nonstoichiometric with variable numbers of the hydrogen sites being vacant. Furthermore, many metal lattices have far more available interstitial sites than absorbed hydrogen atoms. In these cases, the hydrogen atoms can often order on specific sites to form various superlattice structures, which has produced the complex phase diagrams found (23) in the group V transition metal hydrides with the

bcc structures.

Although x-ray diffraction can usually determine the metal sublattice for a hydride, it cannot locate the hydrogen atoms. Neutron diffraction studies of the corresponding deuterides can often determine the total crystal structure including the deuterium atom location. However, it has been established that VH_x and VD_x are not isomorphic (23) at some compositions and the deuteride structure from neutron diffraction does not always represent the hydride structure. Furthermore, the large volume expansions and brittleness of most metal hydrides usually preclude the production of single crystals. Hence, only powder diffraction patterns can be obtained for both the x-rays and neutrons which often limit the structure determinations for the ternary hydrides with more complex structures.

III. ELECTRONIC STRUCTURE

The electronic structure of transition metal hydrides has long been a subject of interest and controversy. Until the early 1970s, rather simple models based upon rigid bands were advocated to account for the observed electronic properties of the metallic hydrides. The "proton" model proposed that electrons migrate from the hydrogen atoms to the valence band of the metal resulting in a screened proton at the interstitial site. The dominant effect in this model is an upward shift in the position of the Fermi level E_F. The alternative "anion" model assumed that hydrogen acts as an electron acceptor with the net result that electrons shift from the vicinity of the metal atoms towards the hydrogen sites which causes E_F to shift downwards. Recently, band theory calculations have been reported for several transition metal hydrides (24-29). These one-electron type calculations contradict the above rigid-band ideas that had left the host metal band structure essentially unchanged. The APW-band calculations of Switendick (24,25) clearly showed that the 1s electrons of the hydrogens interact with specific metal s, p, and d bands to lower their energies and form a hybridized bonding band several electron volts below E_F. Fig. 2

presents a very schematic picture of the electronic structure changes in going from pure metal (MH_0) to a monohydride (MH_1) and finally to a dihydride (MH_2). The major effects of hydrogen absorption are: (1) formation of the hydrogen-metal peaks near the bottom of the d-bands; (2) a small upward shift in E_F as $MH_0 \rightarrow MH_1 \rightarrow MH_2$ since not enough metal levels are lowered (24) to accommodate all the electrons added with the hydrogen atoms; (3) some minor changes in the d-band itself; and (4) the formation of hydrogen bonding and antibonding combinations for MH_2. The nature of the hydrogen-metal and hydrogen-hydrogen interactions depend strongly upon crystal structure and the interatomic separations (24,25). Recent experimental studies on several metallic hydrides using photoemission spectroscopies (30-33) have semi-quantitatively verified most of the band calculation results including the presence of the new hydrogen-induced peak below E_F.

There remain some serious quantitative difficulties with both the theoretical and experimental evaluations of electronic structures for most metallic hydrides. Due to either computational constraints or approximation methods of the one-electron models (24,25), most of the published band calculations have limited accuracy in determining the absolute energy levels, although trends are usually correctly predicted (24-28). To make the computations more tractable, most calculations have been performed on stoichiometric binary hydrides with high cubic symmetry. Only very recently have some theoretical band structures become available for an intermetallic hydride such as $TiFeH_{1.0}$(34). The problems concerning nonstoichiometry and alloy hydrides have scarcely been addressed. Yet, the nonstoichiometric ternary hydrides exhibit much of the more interesting electronic, magnetic, and structural behavior (3,4,11-16). Although the photoemission spectroscopies are proving to be very useful for the study of the electronic properties of metallic hydrides, the few tenths of electron volt resolution (30-32) makes evaluation of the more subtle effects like hydrogen in multiple sites or lattice distortions difficult but sometimes possible (32).

Since these are surface techniques, high-vacuum (i.e., pressures $\leqslant 10^{-10}$ Torr) is required to avoid the formation of surface oxides (30-33). Hence, only the very stable metallic hydrides (e.g., TiH_x, ZrH_x, rare earth dihydrides) can be reliably studied without special precautions. Consequently, the more unstable intermetallic hydrides have not yet been systematically studied by photoemission spectroscopy. Conventional measurements of low-temperature specific heats, magnetic susceptibilities, and superconducting parameters, as well as Mössbauer and NMR spectroscopies, are also valuable by providing information on $n(E_F)$, the density of electronic states at the Fermi level. Although these later techniques cannot monitor the total changes in the band structures, the experiments can usually be performed on unstable hydrides of intermetallics or alloys and some of these techniques can provide insights on the local electronic structure at particular atomic sites.

IV. DIFFUSION

Although the kinetics for hydrogen absorption and desorption are often controlled by hydrogen dissociation reactions at the metal surface (35), the atomic diffusion through the bulk metal or hydride can be rate-controlling under suitable conditions. There have been many experimental studies of the diffusion parameters in the hydride phases of pure metals and intermetallics. Much of this data is summarized in the reviews of Völkl and Alefeld (19,20) and Cotts (36). Host crystal structure, hydrogen site occupancy, phase transitions (i.e., ordering phenomena), alloying, and isotope substitution can greatly influence diffusion behavior.

From a microscopic viewpoint the diffusion coefficient D can be represented by atomic jumps between equilibrium positions using the expression

$$D = f_T \frac{a^2}{6\tau_d} \qquad (2)$$

where a is the mean jump distance, τ_d is the mean time between the

atomic jumps, and f_T is the tracer correlation factor. Although f_T is structure sensitive and typically varies between 0.5 and 1.0, explicit calculation of f_T is generally quite difficult - especially for low symmetries or extensive disorder as found in many hydrides. Consequently, f_T is normally assumed to be unity unless highly accurate comparisons between D and τ_d are being made to estimate a. Fig. 3a illustrates the idealized diffusion process involving direct jumps between potential well minima separated by a. Here, E_a is the barrier activation energy corresponding to the Arrhenius relation

$$D = D_o \exp(-E_a/k_B T) \qquad (3)$$

where the preexponential factor contains the jump attempt frequency, k_B is the Boltzmann's constant, and T is the absolute temperature. However, there is extensive evidence (19,20,36-38) that hydrogen mobility in many metal hydrides is actually far more complex. Although quantum mechanical effects (21) may sometimes be important, the classical diffusion process becomes very complicated if several distinct interstitial sites are simultaneously occupied by hydrogen atoms or the jumppaths include one or more metastable intermediate sites. Fig. 3b shows a rather simple diffusion path with one intermediate high energy site. In this case the relationship between the experimentally observed activation energies and the depths of the potential wells is much less straightforward. In fact, the apparent hydrogen diffusion path in the nearly ideal case of fcc γ-phase TiH_x has been found (36-38) to be more involved than the naively expected simple hop to a neighboring vacant interstitial site. Understanding the hydrogen diffusion mechanisms in the intermetallic hydrides remains a formidable challenge.

V. PREVIEW OF PROTON NMR STUDIES

The present NMR studies address two of the most interesting and important features in the physical characterization of transition metal hydrides: (1) the identification of interstitial sites that are actually occupied by the hydrogen atoms, and (2) the local electronic structure properties at the hydrogen site. Although the proton NMR experiments do not usually provide unequivocally quantitative and comprehensive results that are independent of any supplemental information, the proton parameters do offer some unique insights that complement other methods. The results described in the following chapters will illustrate the capabilities of proton NMR spectroscopy for obtaining a better understanding of some representative metal hydrides. From a range of options, it was decided to concentrate upon some specific properties in several Ti and Zr based hydrides. The intent was to examine diverse problems in similar systems that could demonstrate the advantages of the proton NMR techniques in both straightforward as well as nontrivial situations while avoiding undue complications from unfavorable material properties. The chosen Ti and Zr based hydrides are particularly good candidates for the NMR experiments since they are not strongly paramagnetic nor produce ferromagnetic impurity phases upon hydriding as has been observed in the $LaNi_5$ or TiFe hydrides.

The hydrogen site occupancies have been determined from the rigid-lattice proton lineshapes. A new technique for obtaining reliable lineshapes is described and demonstrated on polycrystalline TiH_x. The proton lineshapes indicate exclusive tetrahedral site occupancies in the ZrH_x and crystalline $TiCuH_{1.0}$ phases while mixed tetrahedral and octahedral site occupancies are observed at some compositions in Ti_2CuH_x, Zr_2PdH_x, and amorphous $TiCuH_{1.4}$. These hydrogen arrangements are consistent with the available neutron scattering and diffraction results.

The proton Knight shifts and spin-lattice relaxation times have been measured in $Ti_{1-y}V_yH_{1.95}$, $TiCuH_x$, Ti_2CuH_x, $TiCr_2H_x$, ZrH_x, and Zr_2PdH_x. In every instance, the dominant proton hyperfine interaction appears to be

to the polarization of the paired s-electrons in the hydrogen bands by the unpaired metal d-electrons at the Fermi level. Although the NMR parameters cannot provide a total description of the local electronic structure at the proton site, some qualitative estimates of the relative s and d contributions have been made for the first time. The comparisons with the band structure calculations for cubic TiH_2 and ZrH_2 have supported the general validity of the present interpretations of the proton NMR results. However, more extensive band theory results are needed at different hydrogen stoichiometries and lower symmetries as well as for the various ternary hydrides to permit more detailed assessment of the electronic structures.

Because of the extensive application of proton NMR to diffusion studies in metal hydrides (36-38), this area has not been emphasized in the present study. However, the particularly interesting results with regards to the important roles of crystal structure and hydrogen site occupancy on the hydrogen diffusion behavior in the $Ti_{1-y}Cu_yH_x$ system are described.

REFERENCES

1. G. G. Libowitz, The Solid-State Chemistry of Binary Metal Hydrides (Benjamin, New York, 1965).
2. W. M. Mueller, J. P. Blackledge, and G. G. Libowitz (Eds.), Metal Hydrides (Academic, New York, 1968).
3. G. Alefeld and J. Völkl (Eds.), Hydrogen in Metals I: Basic Properties (Springer-Verlag, Berlin, 1978).
4. G. Alefeld and J. Völkl (Eds.), Hydrogen in Metals II: Application-Oriented Properties (Springer-Verlag, Berlin, 1978).
5. A. P. Ginsberg, Transition Metal Chem. 1, 112 (1965).
6. H. D. Kaesz and R. B. Saillant, Chem. Rev. 72, 231 (1972).
7. R. Wiswall, in Hydrogen in Metals II: Application-Oriented Properties, G. Alefeld and J. Völkl, Eds. (Springer-Verlag, Berlin, 1978) p. 201.
8. J. J. Reilly, Zeits. Physk. Chem. N. F. 117, 155 (1979).
9. J. J. Reilly and G. D. Sandrock, Sci. Amer. 242, 118 (1980).
10. R. L. Cohen and J. H. Wernick, Science 214, 1081 (1981).
11. R. Bau (Ed.), Transition Metal Hydrides - Advances in Chemistry Series 167 (American Chemical Society, Washington, DC, 1978).
12. I. R. Harris and J. P. G. Farr (Eds.), Hydrogen in Metals - Proc. U Birmingham Meeting (Elsevier, Lausanne, 1976).
13. A. F. Andresen and A. J. Maeland (Eds.), Hydrides for Energy Storage (Pergamon, Oxford, 1978).
14. G. G. Libowitz and G. D. Sandrock (Eds.), Metal Hydrides 1980 - Proc. Int. Symp. Properties and Application of Metal Hydrides, Colorado Springs (Elsevier, Lausanne, 1980).
15. G. Bambakidis (Ed.), Metal Hydrides (Plenum, New York, 1981).
16. H. Oesterreicher, Appl. Phys. 24, 169 (1981).
17. D. G. Westlake, C. B. Satterthwaite, and J. H. Weaver, Phys. Today 31, No. 11, 32 (1978).
18. V. A. Somenkov and S. S. Shil'stein, Prog. Mater. Sci. 24, 267 (1980).

19. J. Völkl and G. Alefeld, in Diffusion in Solids-Recent Developments, A. S. Nowick and J. J. Burton, Eds. (Academic, New York, 1975), p. 232.
20. J. Völkl and G. Alefeld, in Ref. 3, p. 322.
21. K. W. Kehr, in Ref. 3, p. 197.
22. H. Peisl, in Ref. 3, p. 53.
23. T. Schober and H. Wenzl, in Ref. 4, p. 11.
24. A. C. Switendick, in Ref. 3, p. 101.
25. A. C. Switendick, Z. Physk. Chem. N. F. 117, 89 (1979).
26. D. J. Peterman, B. N. Harmon, J. Marchiando, and J. H. Weaver, Phys. Rev. B 19, 4867 (1979).
27. M. Gupta and J. P. Burger, Phys. Rev. B 22, 6074 (1980).
28. M. Gupta and J. P. Burger, Phys. Rev. B 24, 7099 (1981).
29. A. Fujimori and N. Tsuda, Solid State Comm. 41, 491 (1982).
30. J. H. Weaver and D. T. Peterson, Z. Physk. Chem. N.F. 117, 57 (1979).
31. B. W. Veal, D. J. Lam, and D. G. Westlake, Phys. Rev. B 19, 2586 (1979).
32. J. H. Weaver, D. J. Peterman, D. T. Peterson, and A. Franciosi, Phys. Rev. B 23, 1692 (1981); D. J. Peterman, J. H. Weaver and D. T. Peterson, Phys. Rev. B 23, 3903 (1981).
33. K. Tanaka, N. Hamasaka, M. Yasuda and Y. Fukai, Solid State Comm. 30, 173 (1979).
34. M. Gupta, J. Phys. F: Met. Phys. 12, L57 (1982).
35. L. Schlapbach, A. Seiler, F. Stucki, and H. C. Siegmann, J. Less-Common Met. 73, 145 (1980); P. D. Goodell, G. D. Sandrock and E. L. Huston, J. Less-Common Met. 73, 135 (1980).
36. R. M. Cotts, Ber. Bunsenges. Physik Chem. 76, 760 (1972); R. M. Cotts, in Ref. 3, p. 227.
37. R. C. Bowman, Jr., in Ref. 15, p. 109.
38. R. G. Barnes, in Nuclear and Electron Resonance Spectroscopies Applied to Materials Science, E. N. Kaufmann and G. Shenoy, Eds.

(Elsevier-North Holland, Amsterdam, 1981), p. 19.

FIGURE CAPTIONS

Fig. 1. Unit cell for the fcc metal hydride structure.

Fig. 2. Schematic diagrams of the density of states for a metal (MH_0), a monohydride (MH_1), and a dihydride (MH_2). In part a, the partially occupied metal d bands are shown to be superimposed on the parabolic sp bands. The hybridized H-M bonding band *for the monohydride (b) splits into two bands for the dihydride* (c) because of the H-H interaction.

Fig. 3. Schematic representation of potential wells for diffusion process: a) simple activated hopping between neighboring wells separated by distance a; b) jumps involving an intermediate metastable site.

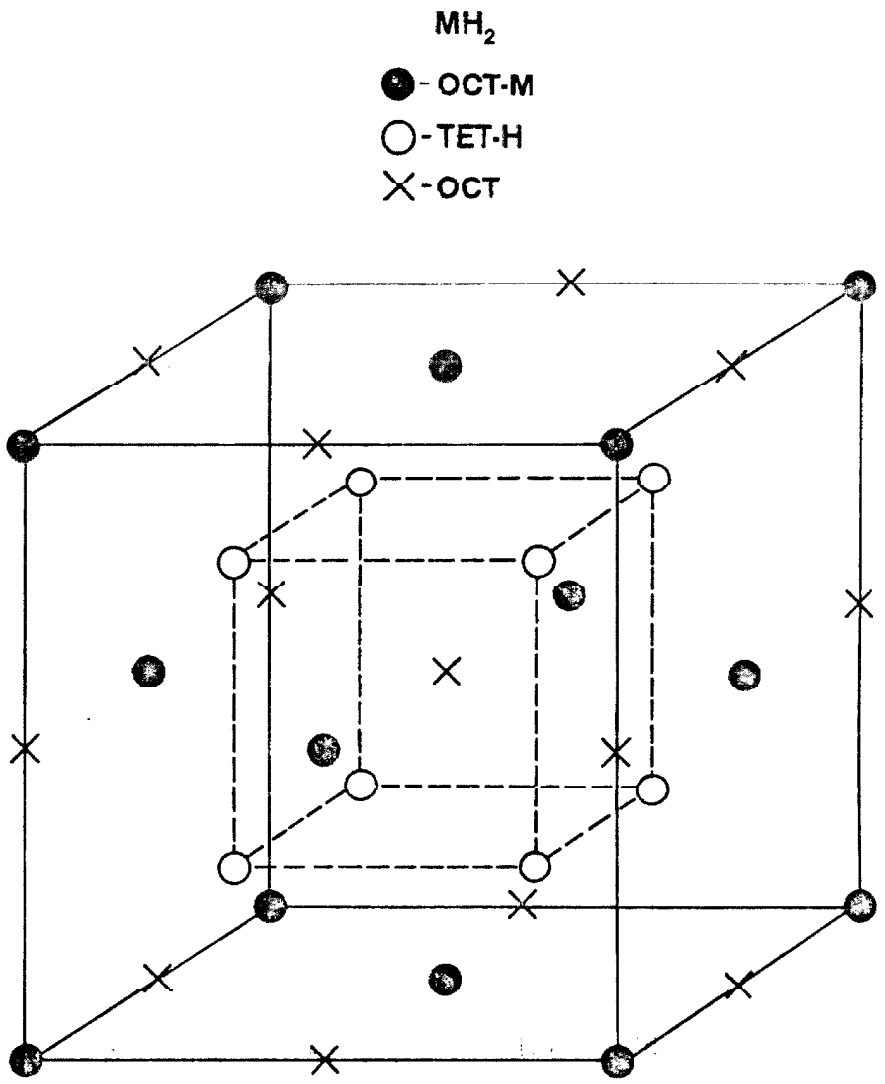

FIGURE 1

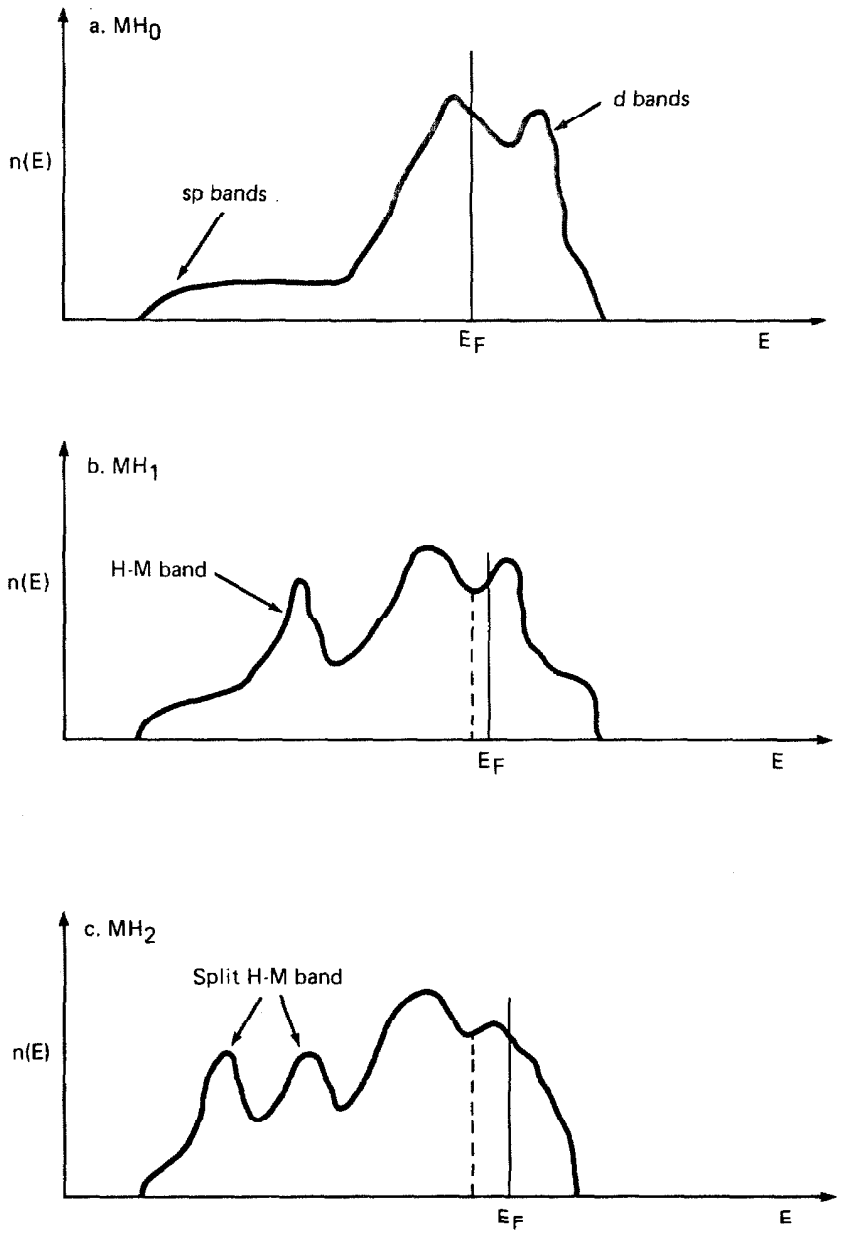
a. MH_0
n(E)
sp bands
d bands
E_F
E
b. MH_1
n(E)
H-M band
E_F
E
c. MH_2
Split H-M band
n(E)
E_F
E

FIGURE 2

a. Simple Activated Hopping Process

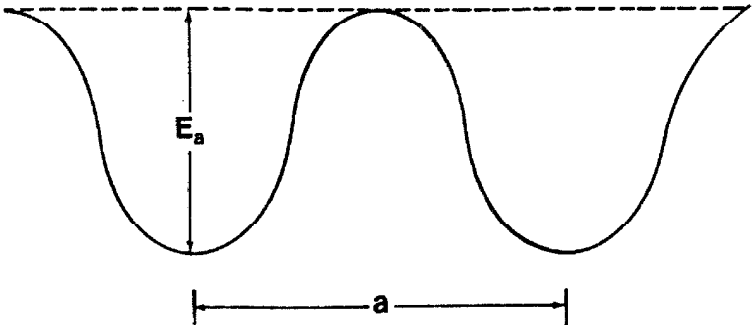

b. Jumps Involving Intermediate Site

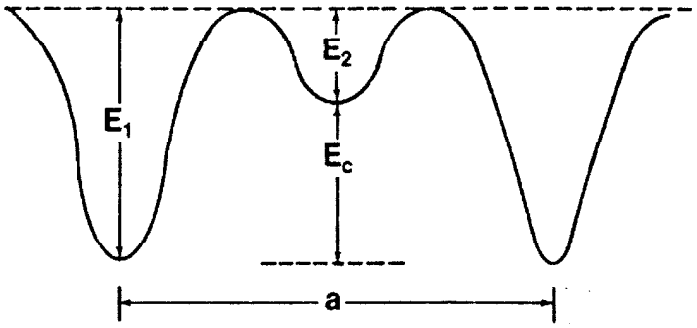

FIGURE 3

CHAPTER 2

CONCEPTS AND METHODS OF NUCLEAR MAGNETIC RESONANCE AS APPLIED TO METAL HYDRIDES

I. GENERAL BACKGROUND

The phenomenon of nuclear magnetic resonance (NMR) occurs when nuclei with non-zero spin angular momentum (which is denoted by the quantum number I) are placed in an external magnetic field (H_o) and are subjected to electromagnetic radiation at a radiofrequency (rf) that satisfies the Larmor equation

$$\omega_o = 2\pi\nu_o = \gamma_I H_o. \qquad (1)$$

Here, ν_o is the resonance frequency in MHz and γ_I is the nuclear gyromagnetic ratio for a nucleus with $I \geqslant 1/2$. The spin properties for protons and the metallic nuclei corresponding to the transition metal hydrides that are being investigated in this work are summarized in Table 1. The interaction experienced by all nuclear spins with nonzero I is the magnetic dipole-dipole interaction. Furthermore, nuclei with $I \geqslant 1$ possess a nuclear electric quadrupole moment Q that interacts with electric field gradients when the symmetry at the nucleus is lower than cubic. Since I = 1/2 for protons, which is the only resonant spin system being measured in the present study, quadrupolar effects do not occur in proton NMR and will not be considered further. Comprehensive descriptions of both dipolar and quadrupolar interactions for nuclear spin systems can be found in the books by Abragam (1) and Slichter (2).

The NMR signal can be observed by two methods:

1. In CW-NMR, low-power continuous rf radiation is applied. A spectrum is obtained as the magnetic field or rf frequency is slowly varied and the absorption of energy by the sample is recorded.
2. In pulse-NMR, short bursts of high-power (i.e., >100 watts) rf radiation are applied at a frequency equal (or very near) to ν_o in eqn. (1) and the response to this pulse is recorded. The response following the rf pulse is called the free induction decay (FID) where the loss in signal amplitude is usually expressed by the time constant T_2^*.

The CW-spectrum and FID are mathematically related to each other through a Fourier transformation. A typical linewidth for a proton spectrum in a metal hydride at low temperature (to establish static dipolar fields) is about 50 kHz and corresponds to a T_2^* of about 10 μs. Pulse-NMR is currently the preferred method to characterize nuclear spin behavior in solids. This is partly due to the higher effective sensitivity of the pulse techniques since an entire spectrum (i.e., the FID signal) can be rapidly obtained after a single rf pulse; whereas, a much slower sweep through resonance is normally required in the CW method. Furthermore, the pulse techniques directly measure (3) the nuclear relaxation times and offer much greater flexibility in obtaining lineshapes and frequency shifts using a variety of recently developed solid-state procedures (4, 5).

At thermodynamic equilibrium the nuclear spin system can be represented (6) by a magnetization vector precessing parallel to the applied field H_o, which usually defines the z-axis of the coordinate system for the magnetization vector (3). When an rf-pulse satisfying eqn. (1) is applied perpendicular to H_o, the magnetization is rotated away from its equilibrium direction by the angle θ according to the relation

$$\theta = \gamma_I H_1 t_p \qquad (2)$$

where H_1 is the effective magnetic field in gauss of the rf radiation and t_p is the width of the rf pulse in seconds. The two most important θ values are 90°, which gives the maximum FID amplitude, and 180°, which inverts the magnetization. The nuclear spins will interact among themselves to establish an internal equilibrium and a corresponding spin temperature (7) and with various external degrees of freedom (collectively known as the "lattice") to ultimately return the spin system to its initial thermodynamic equilibrium. The time constants for these processes are known as the nuclear relaxation times and are the parameters that can be directly related (1-3) to the dynamical properties

within an NMR sample. Since I = 1/2 for protons, their spin interactions occur only through modulation of the magnetic dipole moments.

The application of NMR spectroscopy to metals has been described by various authors (8-12) and to the metal hydrides by Cotts (13). The Hamiltonian for a nuclear spin without a quadrupole moment (e.g., protons) can be written

$$H_{Spin} = H_Z + H_D + H_K + H_C + H_{RF}(t) \qquad (3)$$

where H_Z is the Zeeman interaction responsible for the resonance of eqn. (1), H_D is the nuclear dipolar interaction term, H_K represents the hyperfine interaction with the conduction electrons, which was initially demonstrated by Knight (14), H_C is the chemical shift term which is usually (but, not always) much smaller than H_K, and $H_{RF}(t)$ is the explicitly time-dependent Hamiltonian for the rf fields generated during an NMR experiment. When compared to an ionic or molecular solid, the primary characteristics for NMR in a metal are the Knight shift in the resonance frequency and the conduction electron contributions to the spin-lattice relaxation time T_1. In the absence of nuclear electric quadrupole interactions and large internal fields due to sample ferromagnetism or strong paramagnetism, the nuclear dipolar fields are the primary contributions to the resonance linewidth. The form of dipolar Hamiltonian for the interaction between spin i and spin j is

$$H_D(ij) = \frac{\hbar^2 \gamma_i \gamma_j}{r_{ij}^3} \left[\underset{\sim}{I}_i \cdot \underset{\sim}{I}_j - \frac{3(\underset{\sim}{I}_i \cdot \underset{\sim}{r}_{ij})(\underset{\sim}{I}_j \cdot \underset{\sim}{r}_{ij})}{r_{ij}^2} \right] \qquad (4)$$

where $\underset{\sim}{I}_i$ and $\underset{\sim}{I}_j$ are spin operators and $\underset{\sim}{r}_{ij}$ is the vector distance between the spins i and j. When the spins remain at fixed positions (i.e., in the "rigid-lattice" limit), the above dipole-dipole interaction determines the NMR linewidth and shape. If the spins can change positions such as by random atomic motion during translational diffusion, the dipolar fields are averaged toward zero and the NMR spectrum becomes

narrower. At sufficiently rapid diffusion rates, the time-dependent dipolar fields will dominate the spin-lattice relaxation time of the spin system.

A fundamental difficulty in observing NMR in metals is the skin effect which prevents the penetration of an rf field into an electrical conductor. To avoid the loss in signal intensity as well as other complications involving lineshape distortions and phase shifts, metallic samples are usually in the form of powders, wires, or thin foils with at least one dimension less than about 100 μm. Since most transition metal hydrides are quite brittle, it is usually no problem to prepare powders that are suitable for NMR experiments. Although the formation of a thin surface-oxide film normally provides an adequate electrical insulation between the particles, care should be exercised to prevent excessive oxidation (i.e., by grinding in inert atmosphere gloveboxes) or the introduction of ferromagnetic contaminants such as free iron. The internal demagnetization fields due to the bulk magnetic susceptibility can produce inhomogeneous magnetization (15) in powdered samples. This effect can lead to anomalous NMR linewidths (i.e., larger than predicted for the dipolar interactions) in highly paramagnetic hydrides (16) as well as affect the measurements of frequency shifts (17) and some relaxation times (18). However, the hydrides chosen for the present study do not have large magnetic susceptibilities nor contain significant levels of highly paramagnetic (i.e., Mn or rare earth elements) or ferromagnetic (i.e., free Fe or Ni) impurities. Hence, the various inhomogeneous contributions that arise from the magnetization effects (15-18) in powdered samples are minimal for these hydrides.

II. SECOND MOMENTS IN DIPOLAR LINESHAPES

If the inhomogeneous contributions from both magnetic impurities and the sample demagnetization effects (15) are negligible, the proton lineshapes in solids are exclusively determined by the nuclear dipolar interactions of eqn. (4) (i.e., the homonuclear interactions among the protons as well as possible heteronuclear interactions with other nuclei).

hence, in the rigid-lattice limit it is often possible to determine the hydrogen locations from the proton lineshapes providing the structure of the heavier atoms is known from x-ray diffraction or another technique. In fact, the hydrogen occupancies of interstitial sites have been obtained in numerous transition metal hydrides (13,19,20) from analyses of the proton NMR lineshapes. However, the development of improved techniques (13,21) for measuring rigid-lattice lineshapes and the preparation of many new ternary hydrides should stimulate more extensive NMR studies that can supplement the x-ray and neutron diffraction techniques. Several examples of the measurements and analyses of rigid-lattice lineshapes for binary and ternary metallic hydrides are presented in the following chapters.

The shape of an FID in the rigid-lattice limit that is due only to dipolar interactions is given by the general expression (22)

$$G(t) = Tr\{\exp(-iH_{Do}t)I_x\exp(iH_{Do}t)I_x\}/Tr\{I_x^2\} \qquad (5)$$

where Tr{A} denotes the trace of operator A, I_x is the total spin operator along the x-axis of the rotating frame (1,2), and H_{Do} is the secular part of the dipolar Hamiltonian H_D and commutes the Zeeman Hamiltonian H_Z. Although an exact solution for G(t) from eqn. (5) is extremely difficult, a power expansion of G(t) in terms of its time derivatives (22) gives

$$G(t) = G(o) + \sum_{n=1}^{\infty} \frac{1}{n!}\left(\frac{d^nG}{dt^n}\bigg|_{t=0}\right) t^n \qquad (6)$$

$$= G(o) + \sum_{n=1}^{\infty} \frac{1}{(-i)^n n!} M_n t^n \qquad (7)$$

where the moments M_n are defined as

$$M_n = (-i)^n \left.\frac{d^n G}{dt^n}\right|_{t=o} . \tag{8}$$

Since G(t) is a symmetric function, the odd moments must vanish. A general procedure to evaluate the M_{2n} that was originally described by Van Vleck (23) gives a formal solution for M_{2n} in the following form (22)

$$M_{2n} = \frac{(-1)^n}{Tr(I_x^2)} Tr \{[H_{Do},[H_{Do},\ldots,[H_{Do},I_x]\ldots]^2\} \tag{9}$$

where [A,B] denotes the commutator for operators A and B. The calculation of M_4 is usually difficult and determination of the higher M_{2n} values are prohibitively complicated; however, a comparison between calculated and experimental M_2 values is usually adequate to establish the rigid-lattice arrangements of the nuclei in most practical situations. For example, consider a two spin system where I is the resonant species and S is the non-resonant species. The secular dipolar H_{Do} in this case is

$$\begin{aligned} H_{Do} &= H_{Do}^{II} + H_{Do}^{IS} \\ &= \sum_{i<j} \frac{\hbar^2 \gamma_I^2 (1-3\cos^2\theta_{ij})}{2 r_{ij}^3} (3 I_{iz} I_{jz} - \underset{\sim}{I}_i \cdot \underset{\sim}{I}_j) \\ &\quad + \sum_{j<k} \frac{\hbar^2 \gamma_I \gamma_S}{r_{ik}^3} (1-3\cos^2\theta_{ik})(I_{iz} S_{kz}) \end{aligned} \tag{10}$$

where the subscript i refers to the lattice position of spin I; subscript j is the position of another spin I; subscript k is the lattice position of a spin S; and θ_{ij} and θ_{ik} are the polar angles of the inter-

nuclear distances $\underset{\sim}{r}_{ij}$ and $\underset{\sim}{r}_{ik}$, respectively, relative to the Z-axis that is parallel to H_o. For a powder sample where spins I and S each occupy only one type of lattice site, substitution of eqn. (10) into the expression for M_2

$$M_2 = -Tr\{[H_{Do}, I_x]^2\}/Tr(I_x^2) \qquad (11)$$

gives after some algebra and evaluation of traces the result

$$M_2 = \frac{3}{5}\hbar^2\gamma_I^2\, I(I+1) \sum_j r_{ij}^{-6} + \frac{4}{15}\hbar^2\gamma_S^2\, S(S+1) \sum_k r_{ik}^{-6} \qquad (12)$$

in units of Gauss^2 where the sum $\sum_j r_{ij}^{-6}$ extends over all other sites occupied by I spins from a typical I site labeled by the subscript i and $\sum_k r_{ik}^{-6}$ extends over all spin S sites from the same I site. Using the spin parameters from Table 1, it is easy to calculate the dipolar M_2 for proton lineshapes in a metal hydride once the lattice summations have been evaluated for a model arrangement of nuclei in a given lattice structure. Generalizations of the above formula can account (19,20) for the relative isotopic abundances of spins, contributions from spin I occupying inequivalent lattice sites, and the simultaneous presence of two or more spin S nuclei.

III. RELAXATION TIMES

A. General Properties

There are three relaxation times that are of primary interest in the study of transition metal hydrides:

1. T_1 is the spin-lattice relaxation time in the applied magnetic field H_o and corresponds to the return to thermodynamic equilibrium after a perturbation by the rf irradiation.
2. $T_{1\rho}$ is the spin-lattice relaxation time along the rotating H_1 field of an rf pulse when the nuclear magnetization is "locked" parallel to the H_1 field.

3. T_2 is the spin-spin relaxation time that corresponds to the loss of phase coherency without requiring the transfer of the excitation energy from the spins. The time constant for the FID is T_2^* and usually contains homogeneous (i.e., lifetime of the spin states and the I-I dipolar couplings) as well as many potential inhomogeneous (i.e., spatially variant) contributions.

The procedures for measuring these relaxation times are well established and the experimental details are described in the book by Farrar and Becker (3). Cotts (13) has provided a thorough discussion of the application of nuclear relaxation times to characterize the metal hydrides.

The nuclear relaxation times often have several contributions from different physical processes (1-3). For example, the proton T_1 in most metal hydrides can be separated into three distinct terms

$$T_1^{-1} = T_{1e}^{-1} + T_{1d}^{-1} + T_{1p}^{-1} \qquad (13)$$

where T_{1e} represents the relaxation processes (9,10) from interactions with the unpaired conduction electrons at the Fermi level; T_{1d} is the modulation of the proton dipolar interactions because of atomic diffusion (1,2,13); and T_{1p} describes interactions with paramagnetic atoms (i.e., localized magnetic moments). This last term in eqn. (13) is often negligible if the metal hydrides are not strongly paramagnetic (16) or contain large concentrations of the magnetic impurities. A similar separation of the proton $T_{1\rho}$ relaxation time is also possible; however, the diffusion contributions are nearly always dominant (13) for this parameter. The homogeneous contributions to T_2 can often be determined by various spin-echo pulse sequences (3); however, any interaction which affects the phase of a precessing spin will contribute to the T_2 relaxation,

even in a spin echo experiment that had removed the static inhomogeneties in H_o (3). Zamir and Cotts (18) were the first to recognize these complications for T_2 relaxation behavior in metal hydrides.

B. Diffusion Contributions

The general relationships between the nuclear relaxation times and the diffusion induced modulation of the nuclear dipole-dipole interactions are well understood (1-3, 13). To illustrate these relationships consider a solid containing a single type of magnetic nuclei with I = 1/2 and these nuclei experience random jumps during diffusion. Since only the magnetic dipolar interactions among identical nuclei need be considered, the nuclear relaxation rates (i.e., the inverse of the relaxation time) are given by (13)

$$\frac{1}{T_{1d}} = \frac{3}{2} C_I[J^{(1)}(\omega_o) + J^{(2)}(2\omega_o)] \tag{14}$$

$$\frac{1}{T_{1\rho}} = \frac{3}{8} C_I[J^{(0)}(2\omega_1) + 10J^{(1)}(\omega_o) + J^{(2)}(2\omega_o)] \tag{15}$$

$$\frac{1}{T_2} = \frac{3}{8} C_I[J^{(0)}(0) + 10J^{(1)}(\omega_o) + J^{(2)}(2\omega_o)] \tag{16}$$

where $C_I = \gamma_I^4 \hbar^2 I(I+1)$, $\omega_o = \gamma_I H_0$, $\omega_1 = \gamma_I H_1$, and

$$J^{(q)}(\omega) = \int_{-\infty}^{\infty} G^{(q)}(t) e^{-i\omega t}\, dt, \tag{17}$$

which relates the relaxation rates to the correlation function $G^{(q)}(t)$ for the time-dependent modulation of the nuclear dipolar interactions. These expressions are valid when $\gamma_I M_2^{1/2} \tau_c << 1$ where τ_c is the

correlation time for the diffusion process. For mobile nuclei $\tau_c = \tau_d/2$ where τ_d is the average time between the atomic jumps and is inversely proportional to the diffusion constant D. The simplest assumption for $G^{(q)}(t)$ was first suggested by Bloembergen, Purcell and Pound (24) who proposed that dipolar field correlations decay as $\exp(-t/\tau_c)$. This model (widely known as the BPP model) gives

$$J^{(q)}(\omega) = G^{(q)}(0) \frac{2\tau_c}{1+\omega^2\tau_c^2} \qquad (18)$$

which when substituted into eqns. (14-16) can determine the τ_c values from the experimental relaxation times. The BPP model has been widely used (1-3) to analyze atomic motion in fluids and many classes of solids including many metal hydrides (13). Fig. 1 shows the typical dependences (13) of T_{1d}, $T_{1\rho}$, and T_2 upon τ_c in terms of the BPP model.

The maxima for T_{1d}^{-1} and $T_{1\rho}^{-1}$ occur when $\omega_o\tau_c \approx 1$ and $2\omega_1\tau_c \approx 1$, respectively, while T_2^{-1} increases smoothly up to the value for rigid-lattice dipolar interactions. Diffusion is the dominant nuclear relaxation process in the regions of these maxima. Since $\omega_o \geq 500\ \omega_1$ in nearly all NMR studies, the T_{1d}^{-1} and $T_{1\rho}^{-1}$ maxima occur at very different τ_c values and permit the evaluation of τ_c over wide ranges. In particular, $T_{1\rho}$ measurements can usually yield reliable parameters for diffusion behavior when $10^{-8}\ s \leq \tau_c \leq 10^{-3}\ s$ while T_{1d} measurements cover the range $10^{-10}\ s \leq \tau_c \leq 10^{-6}\ s$. Although the absolute τ_c values from the BPP model can be in error by as much as 50%, their relative temperature behavior is usually much more reliable and gives diffusion activation energies that agree within about 10% with other techniques (13).

More accurate models for $G^{(q)}(t)$ have been developed (13) that attempt to account for the orientation dependent jumps between the specific lattice sites in solids. However, the complexities of the resulting numerical analyses have limited their application to the few high symmetry cubic structures. Furthermore, these lattice specific models usually exhibit the same qualitative behavior as the simpler BPP model (13,25). The most serious shortcoming of all the current models for diffusion relaxation times is their inability (25,26) to represent the more complex diffusion processes involving alternative diffusion pathways and/or multiple site occupancies. With the exception of some preliminary work by Fedders (26), all the diffusion models that have been applied to metal hydrides have only considered the simple atomic hopping processes. However, there is increasing experimental evidence (27-30) that more involved jump pathways are contributing to hydrogen diffusion in those hydrides where more than one type of interstitial site can be occupied. This problem will be addressed in a later chapter when $T_{1\rho}$ data for crystalline and amorphous Ti-Cu hydrides are presented and discussed.

C. Interactions with Conduction Electrons

The nuclear spin systems in metals are affected by the electron structure of the metal through the hyperfine fields produced at the site of the nucleus. The time dependence of the transverse components of the hyperfine fields from the unpaired electrons that are within $\sim k_B T$ of Fermi energy E_F provides an efficient mechanism (10) for the spin lattice relaxation time [i.e., T_{1e}^{-1} given in eqn. (13)] in metals. In transition metals and alloys, which include the metal hydrides, the electrons at E_F will, in principle, occupy both s and d orbitals; however, the densities of d-electron states are usually much larger than the densities of the s-electron states since E_F lies in the rather narrow d-band formed by overlaps of the

transition metal orbitals. Although detailed models for the hyperfine interactions have been formulated (9-11), the general expressions are rarely applied to transition metals where unique identifications of the several contributions are normally not possible. Instead, a partitioned model, which neglects effects of electron-electron correlation and the mixing of the s and d bands, has been extensively used (9-11) to analyze the T_{1e} data for transition metals and transition metal alloys. In this model the relaxation rate obeys

$$\frac{1}{T_e} = 4\pi\hbar\gamma_I^2 k_B T\{[H_{hf}(s)N_s(E_F)]^2 + [H_{hf}(d)N_d(E_F)]^2 q + [H_{hf}(o)N_d(E_F)]^2 p\} \tag{19}$$

where T is the absolute temperature; k_B is the Boltzmann's constant; $N_s(E_F)$ and $N_d(E_F)$ are the s-band and d-band density of states at the Fermi level, respectively; and p and q are reduction factors resulting from d electron orbital degeneracy at E_F. The quantities $H_{hf}(s)$, $H_{hf}(d)$, and $H_{hf}(o)$ are the hyperfine fields at the resonant nuclei caused by the following three mechanisms: Fermi contact interaction with the unpaired s electrons at E_F, core polarization of the spin-paired s orbitals at energies below E_F by the unpaired d electrons at E_F; and the effect of orbital motion of d-electrons. Although the contact term gives the most effective spin-lattice relaxation for a single unpaired electron, the large $N_d(E_F)$ in most transition metal systems usually insures that core-polarization and/or the orbital term will dominate T_{1e}. As long as E_F does not fall on a sharp peak in the density of states, the quantities enclosed by the brackets {} in eqn. (19) are essentially independent of temperature and T_{1e} will obey

$$T_{1e}T = C_e \tag{20}$$

where C_e is a constant. However, if E_F lies on a sharp peak in the density of states, $N_d(E_F)$ can change rapidly with temperature and the product $T_{1e}T$ will not be constant. Because eqn. (19) requires several parameters that cannot be easily or independently evaluated, T_{1e} data will not directly establish the quantitative character of the local electronic structure around the nucleus. However, analyses of T_{1e} parameters in conjunction Knight shifts and magnetic susceptibilities have often provided significant insights on many transition metal systems (8-13).

The conduction electrons in transition metal hydrides will produce hyperfine fields at the proton sites as well as the metal sites. Although Korn and Zamir (31) were apparently the first to explicitly identify T_{1e} contributions to the proton T_1 values in γ-phase TiH_x, the conduction electron interaction is an important T_1 relaxation process for protons at both low and high temperatures where the diffusion rates are either too slow or too fast to make significant contributions to T_1. Most recent proton NMR studies of metal hydrides have included at least cursory estimates of the T_{1e} terms, and there is growing interest in analyzing these parameters in order to gain a better understanding of the electronic structure at the hydrogen sites.

IV. KNIGHT SHIFTS AND KORRINGA RELATIONS

The average component of the hyperfine field parallel to H_o causes a shift in the Larmor frequency for nuclei in metals as was first observed by Knight (14). For a constant applied field H_o, the shift σ_K is given by

$$\sigma_K = (\nu_m - \nu_{Ref})/\nu_{Ref} \qquad (21)$$

where ν_m is the resonance frequency for the metal and ν_{Ref} is the resonance frequency of a suitable reference material, which is usually a

diamagnetic salt of the metal ion. A nucleus can also experience other frequency shifts such as various paramagnetic or diamagnetic contributions from valence and core electrons (i.e., chemical shifts) and the demagnetizing fields induced by several classical magnetism effects (32) arising from nonspherical sample shapes and the use of powders to avoid the skin-depth problems. Because these last contributions give shifts of 10^{-5}-10^{-4} for most nuclei in the nonferromagnetic metals, they are usually neglected for the Knight shifts in the transition metal nuclei where $\sigma_K \approx 10^{-3}$-10^{-2}. However, the hyperfine fields are small for protons (11) to give $\sigma_K(H) \cong 10^{-5}$-$10^{-4}$ and the chemical shift and demagnetization effects must be more carefully treated during the evaluation (15,32) of the proton Knight shifts as will be discussed later in this section. The σ_K are positive when $\nu_m > \nu_{Ref}$, and negative when $\nu_m < \nu_{Ref}$. This is the common sign convention (11) for Knight shifts in metals, but an opposite sign convention is used for the chemical shifts.

The partitioned models (9-11) are also widely used to analyze Knight shifts in the transition metal systems. In this approach σ_K is separated into three components

$$\sigma_K = \frac{1}{N_A \mu_B} [H_{hf}(s)\chi_s + H_{hf}(d)\chi_d + H'_{hf}(o)\chi_o] \qquad (22)$$

where N_A is Avogadro's number and μ_B is the Bohr magneton. The magnetic susceptibility terms correspond to the Pauli interaction with unpaired s-electrons (χ_s), the Pauli interaction with unpaired d-electrons (χ_d), and the Van Vleck paramagnetic orbital interactions with the d-electrons (χ_o). Although the hyperfine fields $H_{hf}(s)$ and $H_{hf}(d)$ are the same as for the T_{1e}^{-1} expression in eqn. (19), the orbital hyperfine field for the Knight shift $H'_{hf}(o)$ is an average (9) over all contributing states of the d band and does not depend on just the electronic states at E_F as was the case for the orbital hyperfine field $H_{hf}(o)$ in eqn. (19). In the free-electron approximation (1,2,9-11) the contact and core-polarization susceptibilities are given by

$$\chi_s = 2\mu_B^2 N_s(E_F) \tag{23}$$

$$\chi_d = 2\mu_B^2 N_d(E_F). \tag{24}$$

However, χ_o arises from second-order electron-nuclear hyperfine interactions (10,11) where both the occupied and unoccupied states over the entire d band contribute to produce the paramagnetic moment at the nucleus. Hence, the orbital term in σ_K does not directly depend upon $N_d(E_F)$ and, furthermore, is usually temperature-independent unless there are a large number of strongly mixed states within k_BT of E_F. From these considerations, the Knight shift in eqn. (22) can be written as

$$\sigma_K = 2\mu_B[H_{hf}(s)N_s(E_F) + H_{hf}(d)N_d(E_F)] + (\frac{1}{N_A\mu_B})H'_{hf}(o)\chi_o. \tag{25}$$

Although the contact hyperfine field $H_{hf}(s)$ is always positive and the orbital hyperfine fields $H_{hf}(o)$ and $H'_{hf}(o)$ are also nearly always positive (9-11,33), the core-polarization field $H_{hf}(d)$ is negative (11,33) for the transition metals. Hence, significant cancellations can occur in σ_K to give positive, negative, or even zero shifts depending on the relative magnitudes of the three terms in eqn. (25). Since only the squares of the hyperfine fields influence T_{1e}^{-1} as shown in eqn. (19), the three contributions are always additive for the spin-lattice relaxation rate.

Using the free-electron model, Korringa (34) derived

$$\sigma_K^2 T_{1e} T = C_K \tag{26}$$

where $C_K = \hbar\gamma_e^2/(4\pi k_B\gamma_I^2)$ when the Fermi contact terms dominates both the Knight shift and spin-lattice relaxation time. A very similar expression

$$\sigma_K^2 T_{1e} T = C_K/q \tag{27}$$

is valid when the core-polarization term dominates both σ_K and T_{1e} where the reduction factor q from eqn. (19) is directly proportional (9) to the fractional character of the t_{2g} d-orbitals at the Fermi surface. However, a Korringa-type relation does not hold for the orbital contributions to σ_K and T_{1e}. Although the orbital contribution to T_{1e} in eqn. (19) depends on the density of states at E_F, the orbital Knight shift depends on an average density of states throughout the entire d band. Nevertheless, the Korringa relations have been very useful (9-11) in deducing the relative contributions of the hyperfine interactions and band structures for numerous transition metals and alloys. If there are comparable contact and core-polarization contributions, C_K/q can be much less than one and even approach zero if $\sigma_K \cong 0$ because of a fortuitous cancellation of two possibly large positive and negative Knight shift terms.

Because the intrinsic hyperfine field from the hydrogen 1s orbital is small (11), the transferred hyperfine interactions from the d-orbitals of the transition metals should be the major contributors to the proton Knight shifts and T_{1e} in the transition metal hydrides. In fact, this view has been adopted in several recent analyses (35-39) of the proton NMR parameters for binary and ternary hydrides. The current evidence appears to favor the dominance of a "transferred" core-polarization from the metal d-orbitals to the filled hydrogen 1s orbitals lying below E_F which are associated with the formation of the metal-hydrogen chemical bond (40).

Since the proton Knights are small (i.e., typical $|\sigma_K|$ values are 10^{-4} or smaller), the chemical shift contribution and choice for a reference frequency in eqn. (21) are much more important for the proton σ_K than for the Knight shifts of most metal nuclei. In some previous studies (41-43) of the proton Knight shifts for metal hydrides, the frequency of the bare proton nucleus was chosen as the reference. This particular choice may have been biased by historic use of the proton model to rationalize (13) the NMR results in metal hydrides. However,

photoemission spectroscopy (44,45) and x-ray emission spectra (46,47) provide direct experimental evidence for electron transfer from the metal atom to the hydrogen atom in several metal hydrides. The band theory calculations (40,48,49) also indicated an increased electron density about hydrogen atoms in several metal hydrides. Hence, it is more appropriate to reference the σ_K to the frequency for the hydride ion(H^-) rather than the bare proton(H^+). The chemical shift for the H^-ion is 27 ppm upfield from the H^+ reference according to Mason (50). From a study of the proton shifts in the alkaline hydrides CaH_2, SrH_2, and BaH_2 by Nicol and Vaughan (51), an average upward shift of 23 $\pm$ 2 ppm relative to bare protons is indicated for the hydride ion. A similar chemical shift is also expected for the protons in the transition metals although it is impossible to uniquely determine the absolute value. Consequently, all proton shifts obtained during the present studies are referenced to tetramethylsilane (TMS) which is about 30 ppm upfield from the bare proton frequency. The choice of TMS as the reference may give an absolute uncertainty of $\pm$5-10 ppm in the σ_K values, but TMS should give a better representation of the chemical shift effects than the alternative reference of the bare proton frequency.

The combination of small Knight shifts and the broad linewidths for rigid-lattice dipolar interactions involving protons gives probable errors of 25-50% or more when the proton σ_K values for the metal hydrides (35,37,52) are derived from conventional cw spectra that have been measured at low temperatures. Although more accurate σ_K measurements can be obtained when the proton spectra are extensively narrowed by rapid hydrogen diffusion (41,42), only limited temperature ranges may be experimentally accessible before various sample dissociation or decomposition effects severely interfere with the σ_K measurements. Some of the recently developed multiple pulse techniques that are designed to average dipolar fields to zero (4,5) have provided more accurate proton σ_K parameters in a few metal hydrides (39,43,51,53). However, the multiple pulse techniques are highly susceptible to pulse errors, probe

detuning, and rf field inhomogeneities (which can be substantial in the electrically conducting hydrides) and also cannot remove the often large heteronuclear dipolar linewidth contributions associated with many metal nuclei such as ^{51}V, ^{63}Cu, or ^{65}Cu. Although these techniques, in principle, permit resolution of the individual Knights on inequivalent sites (i.e., leading to assessments of variations in local electronic structures with a single phase), the expected small differences in the proton shifts as well as overlaps due to the anisotropic terms in lineshapes (4,5) for the polycrystalline samples and the residual heteronuclear broadening will probably always prevent observations of these resolved spectra without the addition of magic-angle sample spinning procedures (39,43).

Since the objective of the present studies was to obtain "average" proton Knight shifts for direct comparisons with proton T_{1e} parameters and for use in Korringa-type analyses, the line-narrowing multiple pulse techniques (4,5) have not been employed. Instead, another multiple pulse technique recently developed by Burum, et al. (54) that can measure the "average" shift of a dipolar broadened NMR line to within ± 1 ppm has been exclusively used during the present evaluations of the Ti and Zr based binary and ternary metal hydrides. This technique is a variation of the well-known (1,2,55) "zero-crossing" experiments of solid-state NMR where a spin temperature is established during a long rf pulse at a frequency ω and the initial amplitude of the transverse magnetization M_x is observed. For the sudden application of the rf pulse, this initial amplitude obeys (55)

$$\frac{M_x}{M_o} = \frac{h\, H_1}{h^2+H_L^2+H_1^2} \tag{28}$$

where M_o is the equilibrium magnetization, H_L is the local dipolar field defined by

$$H_L^2 = Tr[H_{Do}^2]/[\gamma_I^2 \, Tr(I_Z^2)] \tag{29}$$

with $H_L^2 = M_2/3$, and the off resonance term h is given by

$$h = N^{-1} \sum_j [H_o(1 + \sigma_{zzj}) - \omega/\gamma_I] \tag{30}$$

for a total shift σ_{zzj} (i.e., the combination of Knight, chemical, and possibly other terms) of the j^{th} spin in a total of N spins. For a polycrystalline sample with an average shift of $<\sigma_{zz}>_i$ in the i^{th} particle and the application of a sufficiently large H_1 field to satisfy the condition

$$H_L^2 + H_1^2 >> (H_o <\sigma_{zz}>_i)^2, \tag{31}$$

the zero crossing of M_x/M_o in eqn. (28) will occur at the frequency

$$\omega = \gamma_I N^{-1} \sum_{i,j} H_o(1 + \sigma_{zzij}) \tag{32}$$

which corresponds to the exact center (or average) of all the individual shifts within the polycrystalline sample. By applying a train of closely spaced short rf pulses and sampling the steady-state magnetization between the pulses, Burum, et al. (54) have developed an analogous zero-crossing technique for measuring the average frequency shift which has several orders of magnitude greater effective sensitivity than the corresponding cw technique (55). The multiple pulse zero-crossing technique is also easy to use under varying experimental conditions such as during large temperature changes and will work equally well in the presence of heteronuclear dipolar interactions or other inhomogeneous broadening contributions to the NMR lineshapes. The most significant limitation of the multiple pulse zero-crossing technique is an inability to

separate the individual shifts for inequivalent nuclei that can occur in the more complex crystal structures. However, the accurate measurements of the average proton Knight shifts with this technique have provided many useful insights on the electron structures of several metal hydrides as will be demonstrated in several subsequent chapters.

V. INSTRUMENTATION

Two transient NMR spectrometers were used to perform all of the measurements that constituted this study of the transition metal hydrides.

The proton lineshapes, Knight shifts, and T_1 values at 56.4 MHz were obtained using the previously described (56) wide-band spectrometer illustrated in Fig. 2. The original spectrometer has been modified by the additions of a computer controlled programmable pulse generator (57), a 400 watt final rf amplifier, a Biomation Model 1010 transient recorder, and a magnetic field lock system. Rf irradiation at frequencies near 56.4 MHz is applied to samples contained in 5 mm o.d. tubes using a single coil for both the rf transmitter and receiver systems. Four different phases of rf are available with relative shifts of 0°, 90°, 180°, and 270°, which correspond to irradiation along the x, y, -x, and -y coordinate axes of the rotating frame of magnetization (3). Pulse timing and phase channel selection is determined through the use of rf switches, or "gates," which are controlled by a pulse sequence generator (57) programmed by the PDP 11/10 computer but operating independently. The receiver "dead" time (i.e., the time following the end of an rf pulse during which the receiver is saturated and accurate data are not detectable) for this spectrometer is about 3 μsec. The typical time required to produce a 90° pulse was 1.5 μsec.

A commercial Bruker BKR-SXP spectrometer system was used for the measurements of all the $T_{1\rho}$ data and the T_1 data at 34.5 MHz. A single coil, which would accept 8 mm o.d. sample tubes, was used by both the rf transmitter and receiver systems. The deadtime of this spectrometer is

about 10 μsec and the 90° pulse length was about 1.0 μsec. A Biomation Model 8100 transient recorder and a Nicolet Model 1074 signal averager were used for the data collection system.

REFERENCES

1. A. Abragam, The Principles of Nuclear Magnetism (Clarendon, Oxford, 1961).
2. C. P. Slichter, Principles of Magnetic Resonance, 2nd Edition (Springer-Verlag, Berlin, 1978).
3. T. C. Farrar and E. D. Becker, Pulse and Fourier Transform NMR-Introduction to Theory and Methods (Academic, New York, 1971).
4. U. Haeberlen, High Resolution NMR in Solids - Selective Averaging (Academic, New York, 1976).
5. M. Mehring, High Resolution NMR Spectroscopy in Solids (Springer-Verlag, Berlin, 1976).
6. Reference 2, Chapter 2.
7. M. Goldman, Spin Temperature and Nuclear Magnetic Resonance in Solids (Clarendon, Oxford, 1970).
8. L. E. Drain, Metallurgical Rev. 119, 195 (1967).
9. A. Narath, in Hyperfine Interactions, A. J. Freeman and R. B. Frankel, Eds. (Academic, New York, 1967), p. 287.
10. J. Winter, Magnetic Resonance in Metals (Clarendon, Oxford, 1971).
11. G. C. Carter, L. H. Bennett, and D. J. Kahan, Metallic Shifts in NMR (Pergamon, Oxford, 1977).
12. L. H. Bennett, in Nuclear and Electron Resonance Spectroscopies Applied to Materials Science, E. N. Kaufmann and G. K. Shenoy, Eds. (Elsevier, Amsterdam, 1981) p. 3.
13. R. M. Cotts, Ber. Bunsenges. Physik. Chem. 76, 760 (1972); R. M. Cotts, in Hydrogen in Metals II: Basic Properties, G. Alefeld and J. Völkl, Eds. (Springer-Verlag, Berlin, 1978) p. 227.
14. W. D. Knight, Phys. Rev. 76, 1259 (1949).
15. L. E. Drain, Proc. Phys. Soc. 80, 1380 (1962).

16. J. Grunzweig-Genossar, M. Kuznietz, and B. Meerovici, Phys. Rev. B1, 1958 (1970).
17. D. S. Schreiber and L. D. Graham, J. Chem. Phys. 43, 2573 (1965).
18. D. Zamir and R. M. Cotts, Phys. Rev. 134, A666 (1964); D. Zamir and R. M. Cotts, Proc. XIII Colloque Ampere (North Holland, Amsterdam, 1964), p. 276.
19. R. G. Barnes, W. C. Harper, S. O. Nelson, D. K. Thome, and D. R. Torgeson, J. Less-Common Met. 49, 483 (1976).
20. D. L. Anderson, R. G. Barnes, D. T. Peterson, and D. R. Torgeson, Phys. Rev. B21, 2625 (1980).
21. W.-K. Rhim, A. Pines, and J. S. Waugh, Phys. Rev. B3, 684 (1971).
22. Reference 1, Chapter 4.
23. J. H. Van Vleck, Phys. Rev. 74, 1168 (1948).
24. N. Bloembergen, E. M. Purcell, and R. V. Pound, Phys. Rev. 73, 679 (1948).
25. C. A. Sholl, J. Phys. C: Solid State Phys. 14, 447 (1981).
26. P. A. Fedders, Phys. Rev. B18, 1055 (1978).
27. Y. Fukai and S. Kazama, Acta Met. 25, 59 (1977).
28. R. F. Karlicek, Jr., and I. J. Lowe, J. Less-Common Met. 73, 219 (1980).
29. R. C. Bowman, Jr., B. D. Craft, A. Attalla, M. H. Mendelsohn, and D. M. Gruen, J. Less-Common Met. 73, 227 (1980).
30. R. C. Bowman, Jr., and A. J. Maeland, Phys. Rev. B24, 2328 (1981).
31. C. Korn and D. Zamir, J. Phys. Chem. Sol. 31, 489 (1970).
32. Reference 11, Sec. 5.5.
33. L. H. Bennett, R. E. Watson, and G. C. Carter, in Electron Density of States, L. H. Bennett, Ed., (NBS Special Publication 323, Washington, DC, 1971), p. 601.
34. J. Korringa, Physica 16, 601 (1950).
35. C. Korn, Phys. Rev. B17, 1707 (1978).
36. M. Peretz, D. Zamir, and Z. Hadari, Phys. Rev. B18, 2059 (1978).

37. B. Nowak, O. J. Zogal, and M. Minier, J. Phys. C: Solid State Phys. 12, 4591 (1979).

38. R. C. Bowman, Jr., and W.-K. Rhim, Phys. Rev. B24, 2232 (1981).

39. R. Göring, R. Lukas, and K. Bohmhammel, J. Phys. C: Solid State Phys. 14, 5675 (1981).

40. A. C. Switendick, Z. Physk. Chem. N. F. 117, 89 (1979).

41. P. Brill and J. Voitländer, Ber. Bunsen. Physk. Chem. 77, 1097 (1973).

42. S. Kazama and Y. Fukai, J. Less-Common Met. 53, 25 (1977).

43. R. E. Taylor, T. Taki, and B. C. Gerstein, Phys. Rev. B23, 5729 (1981).

44. B. W. Veal, D. J. Lam, and D. G. Westlake, Phys. Rev. B19, 2856 (1979).

45. J. H. Weaver, D. J. Peterman, D. T. Peterson, and A. Franciosi, Phys. Rev. B23, 1692 (1981).

46. K. Tanada, N. Hamaska, M. Yasuda, and Y. Fukai, Solid State Comm. 30, 173 (1979).

47. V. V. Nemoshkalenko, M. M. Kindrat, V. P. Krivitskii, B. P. Mamko, and A. I. Kharlamov, Inorg. Mater. (USSR) 17, 699 (1981).

48. M. Gupta and A. J. Freeman, Phys. Rev. B17, 3029 (1978).

49. A. Fujimori and N. Tsuda, Solid State Comm. 41, 491 (1982).

50. J. Mason, J. Chem. Soc. Dalton, 1422 (1975).

51. A. T. Nicol and R. W. Vaughan, J. Chem. Phys. 69, 5211 (1978).

52. B. Stalinski, C. K. Coogan, and H. S. Gutowsky, J. Chem. Phys. 34, 1191 (1961).

53. K. F. Lau, R. W. Vaughan, and C. B. Satterthwaite, Phys. Rev. B15, 2449 (1977).

54. D. P. Burum, D. D. Elleman, and W.-K. Rhim, J. Chem. Phys. 68, 1164 (1978).

55. Reference 7, Chapter 2.

56. R. W. Vaughan, D. D. Elleman, L. M. Stacey, W.-K. Rhim, and J. W. Lee, Rev. Sci. Instrum. 43, 1356 (1972).

57. J. Dart, D. P. Burum, and W.-K. Rhim, Rev. Sci. Instrum. 51, 224 (1980).

Table 1. Some Spin Properties of Selected Nuclei

Nucleus	I	Natural Abundance (%)	γ_I (rad/Gauss)	Quadrupole Moment (barns)
H	1/2	99.984	26751.0	----
^{47}Ti	5/2	7.28	-1507.9	+0.29
^{49}Ti	7/2	5.51	-1508.3	+0.24
^{51}V	7/2	99.76	7032.6	-0.05
^{53}Cr	3/2	9.55	-1512.0	0.03
^{63}Cu	3/2	69.09	7090.4	-0.211
^{65}Cu	3/2	30.91	7595.8	-0.195
^{91}Zr	5/2	11.23	2487.2	?
^{105}Pd	5/2	22.23	1225.2	+0.8

FIGURE CAPTIONS

Fig. 1. Relaxation rates, in arbitrary units, as a function of $\omega_0\tau_d$ for T_1^{-1}, $T_{1\rho}^{-1}$, and T_2^{-1} as calculated with the BPP model for the correlation function $G^{(q)}(t)$ and with $\omega_0 = 500\ \omega_1$ [after Cotts (13)].

Fig. 2. Schematic diagram of the wide-band pulse NMR spectrometer operating at 56.4 MHz.

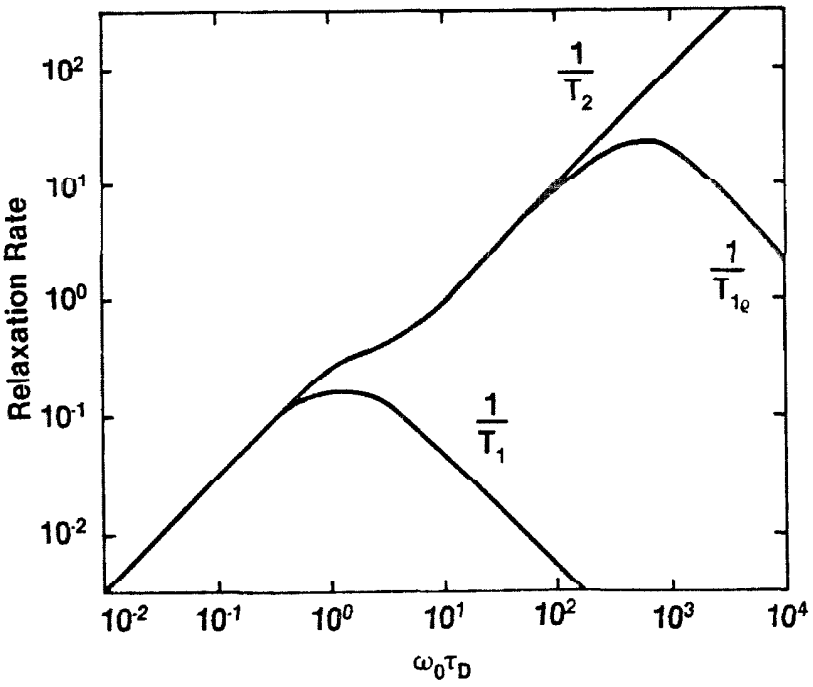
Relaxation Rate
10^2
10^1
10^0
10^{-1}
10^{-2}
$\frac{1}{T_2}$
$\frac{1}{T_{1\varrho}}$
$\frac{1}{T_1}$
10^{-2} 10^{-1} 10^0 10^1 10^2 10^3 10^4
$\omega_0\tau_D$

FIGURE 1

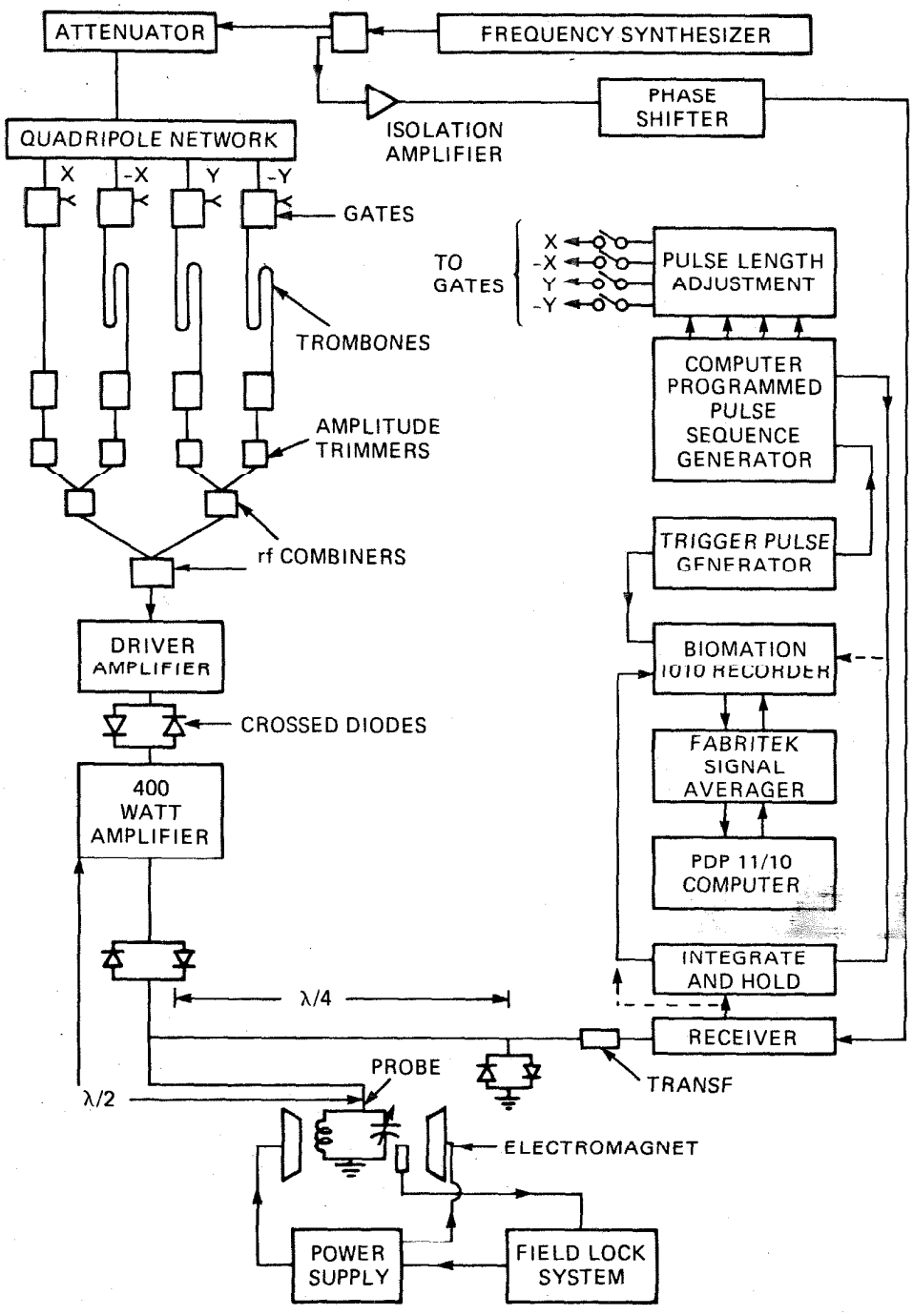
ATTENUATOR
FREQUENCY SYNTHESIZER
PHASE SHIFTER
ISOLATION AMPLIFIER
QUADRIPOLE NETWORK
X
-X
Y
-Y
GATES
TO GATES
X
-X
Y
-Y
PULSE LENGTH ADJUSTMENT
TROMBONES
COMPUTER PROGRAMMED PULSE SEQUENCE GENERATOR
AMPLITUDE TRIMMERS
rf COMBINERS
TRIGGER PULSE GENERATOR
DRIVER AMPLIFIER
BIOMATION 1010 RECORDER
CROSSED DIODES
FABRITEK SIGNAL AVERAGER
400 WATT AMPLIFIER
PDP 11/10 COMPUTER
INTEGRATE AND HOLD
λ/4
RECEIVER
PROBE
TRANSF
λ/2
ELECTROMAGNET
POWER SUPPLY
FIELD LOCK SYSTEM

FIGURE 2

CHAPTER 3

A SIMPLE MAGIC ECHO SEQUENCE FOR SECOND MOMENT MEASUREMENTS

[This chapter is essentially an article with the same title by R. C. Bowman, Jr. and W.-K. Rhim in Journal of Magnetic Resonance, August 1982 Issue (in press).]

ABSTRACT

A relatively simple pulse sequence that generates magic echoes for dipolar solids in the rigid-lattice limit is presented. The proton lineshapes from the magic echoes obtained using polycrystalline $TiH_{1.98}$ yield second moments in excellent agreement with calculations based upon the Van Vleck expressions.

The dipolar lineshapes of nuclear magnetic resonance spectra have been widely used to either determine or clarify the structures of numerous solids. Although a general solution to the NMR lineshape is an extremely difficult problem, detailed analyses are possible using the magnetic moments as defined by the expression(1)

$$M_n = (-i)^n \frac{d^n G(t)}{dt^n G(0)} \Bigg|_{t=0} \qquad [1]$$

where G(t) is the free induction decay following an rf pulse at the resonance frequency. In practice, structure determinations from NMR lineshapes usually consist of comparing the experimental second moment M_2 with calculated dipolar values using the well-known Van Vleck expressions(2). The dipolar M_2 values are calculated for alternative arrangements of the magnetic nuclei to obtain the best agreement consistent with other parameters such as x-ray lattice constants, etc. Unfortunately, the initial portion of G(t), which makes the most important contribution to M_2, is always hidden by the recovery of the probe and receiver circuits from the rf pulse overload. Hence, an accurate determination of M_2 from G(t) becomes more difficult as M_2 increases unless great instrumental effort is made to reduce the recovery times. Although conventional CW NMR techniques can be used to measure M_2 while avoiding receiver blocking, compromises in operating conditions are often required to obtain adequate signal-to-noise factors with minimal modulation and saturation contributions to the CW lineshapes. Powles and Strange(3) have developed a simple two-pulse solid echo technique that partially overcomes the recovery time

difficulties by generating a well-defined echo. Although the solid echo has been commonly used for M_2 determinations, it is generally inferior to the 'magic' dipolar echo devised by Rhim et al(4). The major advantages of the magic echo sequence are the formation of a well-defined echo maximum with minimal lineshape distortion(4) well beyond the instrumental recovery time and the much greater efficiency(4) of echo recovery. However, rather complex multiple-pulse sequences were originally utilized (4) to produce the magic echoes, which may have discouraged any extensive M_2 determinations from the magic echoes although accurate M_2 values were obtained(5) for single crystal CaF_2. The present paper describes a simplified version of the magic echo sequence that yields remarkably accurate M_2 values for polycrystalline $TiH_{1.98}$ which provides a rather severe test due to a high density of protons with strong homonuclear dipolar interactions. This technique should provide reliable M_2 determinations whenever dipolar lineshapes are in the rigid-lattice limit (1,2).

Since the spin dynamics associated with magic echo phenomena have been previously described in great detail(4,6), only a brief sketch of the theoretical foundations will be given. Consider a dipolar solid where the secular Hamiltonian $H_d(Z)$ determines(1) the NMR lineshape and moments M_n. When a long rf pulse is applied at the exact resonance frequency along the Y-axis of the rotating frame for a duration $2t_d$, the dipolar interactions during this interval can be represented(6) by the effective Hamiltonian $(-1/2)\ H_d(Y)$ where contributions from various non-

idealities are assumed to be small(4). Hence, spin system will be evolving "backwards" during this Y-pulse as though there has been a reversal in time as has been thoroughly discussed by Rhim et al(4). If this pulse is immediately followed by a 90°-phase shifted $\pi/2$-pulse, the magnetization vector will lie in the X, Y-plane of the rotating reference frame rather than the initial equilibrium direction along the Z-axis. This orientation permits observation of the formation and decay of the magic echo signal from which the magnetic moments can be extracted. The magic echo maximum occurs at the time t_d after the end of the Y-pulse. It has been demonstrated(7) that continuous rf irradiation can be replaced by a string of identical, small angle pulses without modifying the physics as long as the average applied rf field H_1 is much larger than the local dipolar field H_L and the condition

$$\omega_1/\Omega << 1 \qquad [2]$$

is satisfied. Here, $\omega_1 = \theta\Omega/2\pi$ is the average precession frequency in the rotating frame due to the rf pulses applied with repetition frequency $\Omega/2\pi$ and θ is the pulse angle. Hence, the pulse sequence

$$(\theta_{-Y} - \tau)^N - X \qquad [3]$$

with N short pulses of angle θ along the -Y direction of the rotating frame separated by times τ much shorter than the spin-spin relaxation time T_2 and X representing a $\pi/2$-pulse along the X-direction will produce a magic echo completely analogous to the more complex pulse sequences previously described(4). The major advantage of using a string of closely spaced short pulses rather than a long continuous pulse is the

ability to accurately align the magnetization along the receiver phase for maximum signal amplitude at any convenient t_d value by simply adjusting the common width of each pulse in the string. However, with a long continuous pulse only a few, specific $2t_d$ lengths will give a maximum amplitude for a given receiver phase, which can make the tuning procedures rather tedious and complicated, and the echo maxima will occur at a different t_d if the phase is changed. Although the simplified sequence given by eq. [3] is not as efficient as the original version(4) for the long term recovery of the magic echo, with $N \leqslant 10$ it has been found to generate well-resolved echo maxima as well as reliable M_2 values for proton lineshapes in various metal hydrides where the M_2 values are usually quite large (i.e., $M_2 > 10$ gauss^2).

In order to assess the reproducibility and reliability of M_2 values derived from magic echoes generated by several variant pulse sequences based upon eq. [3], a series of experiments have been performed on a sample of polycrystalline $TiH_{1.98}$, which is isomorphic with the traditional NMR standard CaF_2 except M_2 for TiH_2 is about 3.5 times larger (8). Pulse sequences with N=8 and N=10 were utilized and the θ_{-y} lengths were extensively varied while retaining a constant separation of 3 μsec between the beginning of each θ pulse. The echo signals were detected with the receiver phase experimentally set along either the Y or X directions of the rotating reference frame. The widths of θ_{-y} pulses were carefully adjusted to produce maximum amplitudes for the magic echoes. Whenever an extrema in echo intensity was obtained, the

M_2 values were evaluated from gaussian plots of the signal decays for about 10-12 μsec after the experimentally defined peak of the magic echo, which corresponds to G(0) in the free induction decay. The nominal proton frequency was 56.4 MHz where exact resonance conditions were established by the multiple-phase zero-crossing technique(9). The sample was maintained at 18.0 ± 1.0°C throughout the measurements.

The apparatus consisted of a home-built wide-band transient spectrometer(10) that had been modified by the addition of a programmable pulse generator(11), an external magnetic field lock system, and a Biomation Model 1010 transient recorder to permit data collection at a 10 MHz sampling rate. The spectrometer produces a $\pi/2$-pulse in about 1.5 μsec and has a total recovery time of about 3 μsec from the end of the rf pulse. Each measurement had 64 scans stored in the memory of a Fabritek Model 1072 signal averager. For half of these scans the magic echo sequence had been preceded by an initial π-pulse and the resulting inverted signals were digitally subtracted from the echoes produced using only the sequence of eq. [3]. This procedure was very effective in reducing systematic noise as well as probe ringing and the weak background signals.

Several magic echoes for protons in $TiH_{1.98}$ that have been created using the pulse sequence of eq. [3] with N=10 are presented in Fig. 1. Positive or negative echoes have been formed along either the X or Y axes of the rotating reference frame by varying the θ_{-y} angles. Thus, this simple pulse sequence permits great flexibility for the observation of the magic echoes and gives relatively versatile signal detection configurations. For example, the extrema in echo amplitudes can be obtained by either varying θ_{-y} for a constant detector phase setting or alternating the phase setting at a constant θ_{-y} value. As can be readily seen in Fig. 1, the primary advantage of the magic echo technique is the formation of easily identified echo peaks well outside of the instrumental recovery time, which allows accurate determination of the echo maximum to establish the initial point in the lineshape decay G(t). In contrast, the peak for the solid echo sequence(3) typically occurs just beyond the experimental recovery time because the spacing between the two pulses must be kept as short as possible to minimize lineshape distortions(12). Hence, it is often difficult to clearly define the maximum point in the solid echo which can seriously affect the accuracy of the corresponding M_2 value.

Table 1 summarizes the experimental proton M_2 values for the polycrystalline $TiH_{1.98}$ sample using the magic echo sequence with N=8 and 10 at several θ_{-y} values. Although a wide range of pulse lengths are included and a significant variation in maximum echo amplitudes are observed, the moments exhibit excellent consistency. In fact, the average of all the measurements in Table 1 is $M_2 = 24.6$ gauss^2 with a standard deviation of

0.5 gauss^2. The theoretical dipolar M_2 for protons in $TiH_{1.98}$, including the very small contributions from the ^{47}Ti and ^{49}Ti nuclei, is calculated to be 24.7 gauss^2 using the Van Vleck formulas(2) with the measured cubic lattice parameter $a = 4.448 \times 10^{-8}$ cm and assuming the protons randomly occupy 99% of the tetrahedral interstitial sites of the TiH_2 crystal structure. Although this remarkable agreement between the experimental and calculated proton M_2 values may be somewhat fortuitous considering the experimental uncertainty, the reliability of the simplified magic echo sequence to determine accurate M_2 values has been clearly demonstrated. Successful M_2 measurements that have been performed on several other metal hydrides including ZrH_x, $TiCr_2H_x$, and $TiCuH_x$ will be published elsewhere. The results in Table 1 are also in good agreement with M_2 values previously measured in TiH_x by broadline NMR techniques(8). Because the proton dipolar M_2 is very large for TiH_2, determination of reliable experimental M_2 values was found to be much more difficult with either solid echoes or free induction decays.

The systematic decrease in the magic echo amplitudes with large N and reduction in θ_{-y} length probably reflects some limitations in the simplified version relative to the original(4) magic echo sequence. However, the M_2 values from the simple sequence of eq. [3] appear not to be seriously affected by these limitations. If a relatively unattenuated magic echo at long t_d is desired, the rather complex multiple-pulse sequence of Rhim, et al(4) should be employed. Nevertheless, for an accurate determination of M_2 in most practical situations the sequence represented by eq. [3] should

be quite satisfactory and experimentally very convenient while avoiding potentially expensive instrumental modifications to generate and transmit the long trains of phase-alternated pulses of the original magic echo sequence. Finally, the simple magic echo sequence has been found to provide a readily observable signal that monitors the magnetization of samples whose short G(t) decays are mostly lost in the spectrometer recovery time. This capability has proven to be very useful in measuring spin-lattice relaxation times.

Acknowledgements: The support and advice of Dr. S. I. Chan is greatly appreciated. We thank W. E. Tadlock for preparing the $TiH_{1.98}$ sample. This work was supported by Division of Chemical Sciences of U. S. Department of Energy, the Caltech's President's Fund, and the National Aeronautics and Space Administration under Grant No. NAS 7-100.

REFERENCES

1. A. Abragam, Principles of Nuclear Magnetism (Clarendon Press, London, 1961).

2. J. H. Van Vleck, Phys. Rev. 74, 1168 (1948).

3. J. G. Powles and J. H. Strange, Proc. Phys. Soc. 82, 6 (1963).

4. W.-K. Rhim, A. Pines, and J. S. Waugh, Phys. Rev. Lett. 25, 218 (1970); W.-K. Rhim, A. Pines, and J. S. Waugh, Phys. Rev. B 3, 684 (1971); A. Pines, W.-K. Rhim, J. S. Waugh, J. Magn. Res. 6, 457 (1972).

5. D. Fenzke, W. Rinck, and H. Schneider, Phys. Stat. Sol. (a)26, 437 (1974).

6. W.-K. Rhim and H. Kessemeier, Phys. Rev. B 3, 3655 (1971).

7. W.-K. Rhim, D. P. Burum, and D. D. Elleman, Phys. Rev. Lett. 37, 1764 (1976).

8. K. Nakamura, J. Magn. Res. 14, 31 (1974).

9. D. P. Burum, D. D. Elleman, and W.-K. Rhim, J. Chem. Phys. 68, 1164 (1978).

10. R. W. Vaughan, D. D. Elleman, L. M. Stacey, W.-K. Rhim, and J. W. Lee, Rev. Sci. Instrum. 43, 1356 (1972).

11. J. Dart, D. P. Burum, and W.-K. Rhim, Rev. Sci. Instrum. 51, 244 (1980).

12. P. Mansfield, Phys. Rev. 137A, 961 (1965).

Table 1. Proton second moments (M_2) for polycrystalline $TiH_{1.98}$ obtained from magic echoes generated by the pulse sequence $(\theta_{-y} - \tau)^N - 90_x$

N	Nominal θ_{-y} Length	Detector Phase Direction	Maximum Echo Amplitude[a]	M_2 ($gauss^2$)
8	90°	Y	0.925	24.0
8	79°	X	0.912	24.4
8	68°	Y	-0.893	24.6
10	81°	X	-0.825	24.9
10	72°	Y	0.812	25.2
10	63°	X	0.788	24.7
10	54°	Y	-0.775	25.2
10	45°	X	-0.744	24.9
10	36°	Y	0.650	23.9

[a]Relative to amplitude of free induction decay signal immediately after receiver deadtime. Negative values correspond to inverted echoes as shown in parts C and E of Fig. 1.

FIGURE CAPTION

Figure 1. Representative magic echoes for polycrystalline $TiH_{1.98}$ at 18°C obtained using the pulse sequence described in the text with N=10. Parts B and D were generated under identical pulse parameters except the detector phase was shifted by 90°. Each trace is 51.2 μsec long.

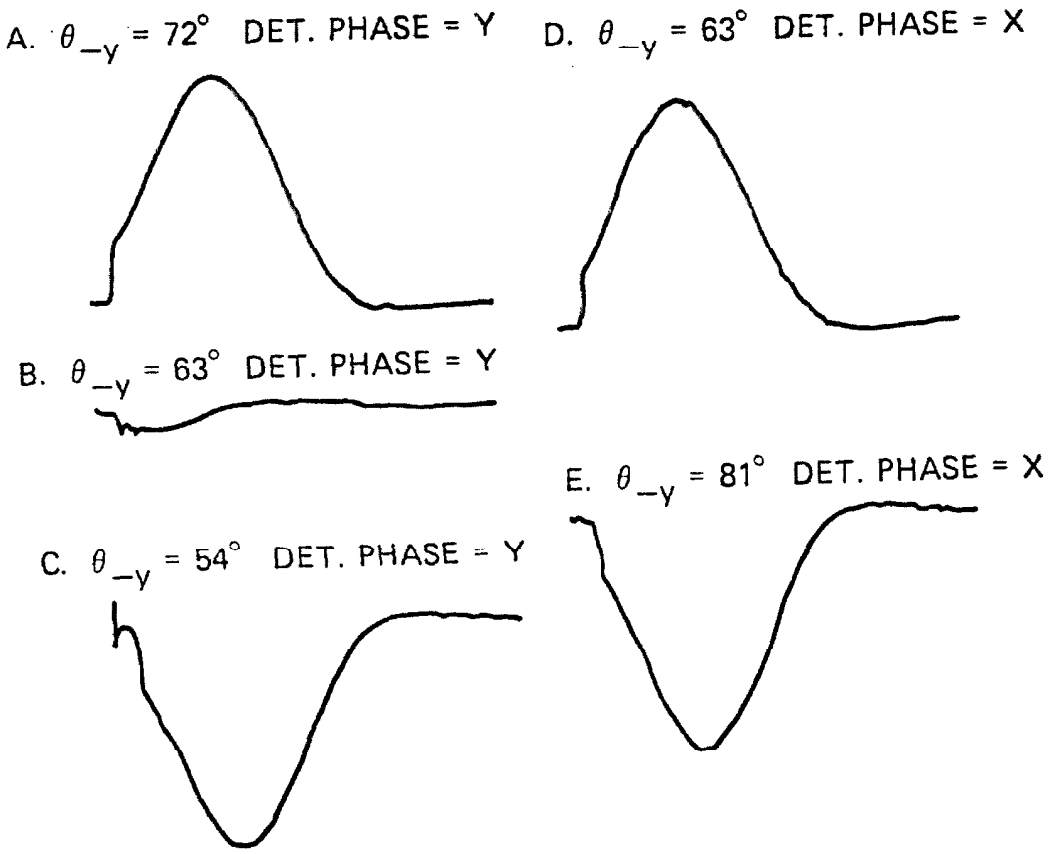
A. θ_{-y} = 72° DET. PHASE = Y
D. θ_{-y} = 63° DET. PHASE = X
B. θ_{-y} = 63° DET. PHASE = Y
E. θ_{-y} = 81° DET. PHASE = X
C. θ_{-y} = 54° DET. PHASE = Y

FIGURE 1

CHAPTER 4

PROTON NMR LINESHAPES IN ZrH_x

[This chapter is essentially an article with the same title by R. C. Bowman, Jr., E. L. Venturini, and W.-K. Rhim in Physical Review B, September 1, 1982 Issue (in press).]

ABSTRACT

The second moments (M_{2D}) were obtained from magic echo measurements of the proton lineshapes for high purity polycrystalline ZrH_x. Contrary to previous reports of anomalously large M_{2D} values in ZrH_x, the present results are in excellent agreement with the calculated dipolar moments which assume random occupancy of protons on only tetrahedral interstitial sites.

I. INTRODUCTION

Nuclear magnetic resonance (NMR) has proven to be a very valuable technique to evaluate the hydrogen site occupancies, electronic properties, and diffusion behavior in numerous metal-hydrogen systems(1,2). Since protons are spin 1/2 nuclei without a nuclear quadrupole moment, the lineshapes of the proton spectra are usually dominated by the well-understood(1,2) nuclear dipolar interactions as long as strong local magnetic moments such as those occurring in ferromagnetic materials are absent. In particular, the second moments (M_{2D}) of proton lineshapes measured in the rigid-lattice limit (i.e., when the various diffusion motions become sufficiently slow) have often been directly related(3-6) to the arrangement of the H-atoms in a host metal lattice. The hydrogen locations are identified by comparing the experimental M_{2D} for a powder metal hydride sample with a theoretical value calculated using the dipolar expressions(1,2) for a model arrangement of H-atoms that considers stoichiometry and the host metal lattice structure. This comparison is most straightforward when the proton-metal dipolar term is small due to either small gyromagnetic moments or low isotopic abundance of magnetic metal nuclei (e.g., Ti, Cr, Y, Zr. Pd, etc.).

The proton M_{2D} have generally yielded hydrogen arrangements(3-6) that were in excellent agreement with independent elastic and inelastic neutron scattering measurements. However, two previous broadline (CW) (NMR) studies(7,8) of the proton spectra in δ-phase (fcc) and ε-phase

(fct) ZrH_x gave experimental M_{2D} values that greatly exceeded the calculated dipolar values. These results are summarized in Table 1. Since ZrH_x does not exhibit any other unusual electrical or magnetic properties(9,10) (in fact, ZrH_x can be considered a prototype transition metal hydride), these anomalously large experimental M_{2D} values are completely unexpected considering the very good agreement between the measured and calculated M_{2D} values(3,8,11) for isostructural and isoelectronic γ-phase TiH_x. Nakamura(8) has reported that the experimental M_{2D} values were sample dependent for ZrH_x, but not for TiH_x, and he concluded that impurities probably contributed to the line broadening in the ZrH_x phases. Because no subsequent investigation has apparently attempted to clarify the anomalous proton linewidths for ZrH_x, the magic echo pulse sequence(11) has been utilized to determine the proton M_{2D} values for four samples of ZrH_x prepared from high-purity Zr metal. In contrast to the previous studies(7,8), the present experimental M_{2D} values are in good-to-excellent agreement with the dipolar values calculated assuming random occupancy in only the tetrahedral sites.

II. EXPERIMENTAL DETAILS

The ZrH_x samples were prepared by the direct reaction between zone-refined Zr metal as 254 μm-thick foils(12) and hydrogen gas that had been purified by diffusion through a Pd-Ag tube. To minimize oxygen on the surfaces, narrow strips of the Zr foil were sandblasted, which was followed by a 3 to 5 min. ultrasonic cleaning in acetone. Each sample of about a dozen cleaned strips was weighed and placed into a molyb-

denum boat prior to insertion in a quartz reaction tube. The loaded reactor was quickly evacuated and flushed several times with purified hydrogen prior to heating to 600°C under dynamic vacuum of about 10^{-4} Pa. The desired quantity of hydrogen was stored in a calibrated stainless steel cylinder. After isolating the reactor from vacuum, the hydrogen gas was admitted. After 20 min. at 600°C, the temperature was adjusted to between 450°C and 650°C to give an approximate equilibrium pressure of 500 Pa. After remaining at this temperature overnight, the reactor was cooled at a rate of 20°/hr until the pressure fell below 10 Pa when final cooling occurred during an air quench. The hydrided ZrH_x foils were removed from the reactor, weighed, and quickly sealed in evacuated glass tubes. The ZrH_x compositions are x = 1.60, 1.80, 1.90, and 2.00 where the volumetric analyses of absorbed hydrogen and weight gains agree within $x = \pm 0.01$.

The glass tubes containing the ZrH_x foils were passed into a glovebox that circulated a purified argon atmosphere. Each tube was opened and the brittle ZrH_x foils removed. The foils were ground in an agate mortar and pestle to produce a powder that passes a 200-mesh sieve (i.e., corresponding to a 74 μm particle size). Weighed amounts of each ZrH_x powder were loaded into 5 mm o.d. NMR sample tubes, which were evacuated and torch sealed.

Powder x-ray diffraction measurements confirmed that each ZrH_x sample

was single phase with the following lattice constants: δ-$ZrH_{1.60}$(a_o = 4.7775(8)Å), ε-$ZrH_{1.80}$(a_o = 4.954(6)Å and c_o = 4.50(2)Å), ε-$ZrH_{1.90}$(a_o = 4.986(22)Å) and c_o = 4.461(37)Å), and ε-$ZrH_{2.00}$ (a_o = 4.971(5)Å) and c_o = 4.426(6)Å).

The proton lineshapes for the ZrH_x samples were obtained using the simplified magic echo pulse sequence described elsewhere(11). The proton resonance frequency (ν_H) was 56.4 MHz and the transient NMR spectrometer and measurement procedures have been discussed(11). Since well-resolved echo maxima were obtained for the ZrH_x samples, the zero-time point(2,11) for the proton lineshapes was easily established. Gaussian plots of the initial portion of this decay of the magic echo signal were used to determine the M_{2D} parameters. The magic echo sequence has been found(11) to yield very reliable M_{2D} values in γ-$TiH_{1.98}$ as well as several other metal-hydrogen systems.

III. RESULTS AND DISCUSSION

The proton M_{2D} parameters for the high-purity ZrH_x (x = 1.60, 1.80, 1.90, 2.00) polycrystalline samples are summarized in Table 2. The experimental values have been derived from analyses of the magic echo lineshapes. The calculated values are obtained using the expression(1, 5)

$$M_{2D} = M_2(H\text{-}H) + M_2(H\text{-}Zr) \qquad (1)$$

where

$$M_2(H\text{-}H) = \frac{3}{5}\hbar^2\gamma_H^2\, I(I+1)f_I \sum_i r_i^{-6} \qquad (2)$$

$$M_2(H\text{-}Zr) = \frac{4}{15}\hbar^2\gamma_S^2\, S(S+1)f_S \sum_k r_k^{-6}. \qquad (3)$$

Here, γ_H and γ_S are the gyromagnetic moments of protons and ^{91}Zr, respectively; I and S are the spin quantum numbers; f_I is the isotopic abundance of ^{91}Zr; $\hbar$ is Planck's constant divided by 2π; $\sum_i r_i^{-6}$ is the H-H lattice sum for occupancy on only tetrahedral sites; and $\sum_k r_k^{-6}$ is the H-Zr lattice sum centered on a proton site. These lattice sums were computed by direct summations over a radius of about 40Å for both the fcc and fct lattices. The experimental lattice constants for the ZrH_x samples were used. For the fcc structure, the present summations converged to the values of Gutowsky and McGarvey(13). Although the $M_2(H\text{-}Zr)$ term has been included in the calculated M_{2D} values shown in Table 2, it is very small (i.e., $\sim 0.1\ G^2$); hence, $M_{2D} \cong M_2(H\text{-}H)$ within the accuracy of both the experiments and the calculations.

In contrast to the anomalously large M_{2D} parameters measured by Hon(7) and Nakamura(8) and shown in Table 1, the ratios of experimental M_{2D} to the theoretical dipolar values given in Table 2 are found to lie between 0.95 and 1.00. Hence, the proton lineshapes for δ and ε phase ZrH_x are accurately represented by only rigid-lattice dipolar interactions - providing the ZrH_x samples are sufficiently pure. Although

the source of the earlier anomalous M_{2D} values(7,8) cannot be definitely established, the rather large Fe content in these samples, as shown in Table 1, appears to be the obvious choice. This view is further supported by the field dependent magnetic susceptibilities for ZrH_x as reported by Ducastelle, et al(9) (about 40 ppm Fe) and Nemchenko and Charnetskii(10) (<160 ppm Fe). Since the Fe content was only 20 ppm in the starting Zr metal and none should have been inadvertently introduced in preparing the ZrH_x powder samples, the present proton lineshapes measurements gave only the expected dipolar values for M_{2D} that are completely analogous to the behavior for γ-TiH_x(3,8,11) as well as many other metal-hydrogen systems(4-6).

The experimental M_{2D} values in Table 2 are actually systematically slightly smaller than the calculated dipolar values. A small loss in hydrogen content from the initial synthesis compositions can easily account for this difference. However, the experimental and calculated M_{2D} values are generally within their combined uncertainty of about $\pm$5%. If there was disordering of protons from the tetrahedral sites to octahedral sites, which has been reported for the fcc hydrides LaH_x(4) and YH_x(6), the experimental M_{2D} would be larger than the values calculated assuming only occupancy on tetrahedral sites(4,6). Hence, the present proton M_{2D} experiments imply only tetrahedral site occupancy in both δ and ε ZrH_x. This conclusion is consistent with elastic and inelastic neutron scattering studies(14,15) on ZrD_x and ZrH_x.

The M_{2D} comparisons have only been made at 291 K in Table 2 since the low-temperature lattice constants are unavailable. However, the experimental M_{2D} values become larger as the temperature decreases. This is consistent with smaller lattice constants at the lower temperatures.

Finally, Soviet workers(16-18) have reported experimental evidence that both δ and ε phase ZrH_x undergo phase transitions below 230 K. Naskidashvili(19) has proposed that hydrogen ordering to form either δ-$ZrH_{1.50}$ (3-transitions) or ε-$ZrH_{1.75}$ (1-transition) superlattices in the tetrahedral sites causes these transitions. Table 3 summarizes the predicted proton dipolar M_{2D} parameters for δ-$ZrH_{1.50}$ and ε-$ZrH_{1.75}$ for random hydrogen occupancy of the tetrahedral sites as well as the four superlattices of Naskidashvili(19). It would be very difficult to make any definite statements concerning models II and III for δ-$ZrH_{1.50}$ and model IV for ε-$ZrH_{1.75}$ since the differences with random occupancy are quite small. However, model I for δ-$ZrH_{1.50}$ predicts a rather large decrease in M_{2D}, whereas the experimental values for δ-$ZrH_{1.60}$ in Table 2 are seen to increase slightly between 291 K and 89 K. Hence, the proton M_{2D} parameters in Table 2 do not provide any support to Naskidashvili's mechanism. Furthermore, no superlattices were found by neutron diffraction measurements(14) when $ZrD_{1.82}$ was cooled to liquid nitrogen temperature. Thus, no structural technique has yet verified that hydrogen atoms can order in δ- or ε-ZrH_x to form superlattices on tetrahedral sites(19).

IV. CONCLUSIONS

The experimental M_{2D} parameters for the proton lineshapes of both δ(fcc) and ε(fct) phase ZrH_x are accurately given by only rigid-lattice dipolar interactions contrary to earlier measurements(7,8) on lower purity ZrH_x samples. The protons occupy only tetrahedral interstitial sites and probably do not form ordered superlattices at low temperatures.

V. ACKNOWLEDGEMENTS

The assistance of A. Attalla in preparing the NMR samples and D. B. Sullenger in making the x-ray diffraction measurements is greatly appreciated. This work was supported by Office of Basic Energy Sciences, Division of Chemical Sciences, U. S. Department of Energy, the Caltech's President's Fund, and the National Aeronautics and Space Administration under Grant No. NAS7-100. Sandia National Laboratori are supported by the U. S. Department of Energy under Contract No. DE-AC04-76-DP00789. This is Caltech Contribution #6631.

REFERENCES

1. R. M. Cotts, Ber. Bunsenges. Physk. Chem. 76, 760 (1972).

2. R. M. Cotts, in Hydrogen in Metals I - Basic Properties, edited by G. Alefeld and J. Völkl (Springer-Verlag, Berlin, 1978) p. 227.

3. B. Stalinski, C. K. Coogan and H. S. Gutowsky, J. Chem. Phys. 34, 1191 (1961).

4. D. S. Schreiber and R. M. Cotts, Phys. Rev. 131, 1118 (1963).

5. R. C. Bowman, Jr., A. Attalla and A. J. Maeland, Solid State Commun. 27, 501 (1978).

6. D. L. Anderson, R. G. Barnes, D. T. Peterson and D. R. Torgeson, Phys. Rev. B 21, 2625 (1980).

7. J. F. Hon, J. Chem. Phys. 36, 759 (1962).

8. K. Nakamura, J. Magn. Reson. 14, 31 (1974).

9. F. Ducastelle, R. Caudron and P. Costa, J. Physique 31, 57 (1970).

10. V. F. Nemchenko and V. G. Charnetskii, Inorg. Mater. 10, 392 (1974).

11. R. C. Bowman, Jr. and W.-K. Rhim, submitted to J. Magn. Reson.

12. MAR7-grade (i.e.,stated purity of 99.99%) from Materials Research Corporation, Orangeburg, New York, 10962. Independent emission spectroscopy analysis has verified vendor claim of 20 ppm Fe and the absence of any detectable amount of other magnetic element (i.e., Ni, Co, etc.).

13. H. S. Gutowsky and B. R. McGarvey, J. Chem. Phys. 20, 1472 (1952).

14. V. F. Petrunin, V. P. Glazkov, V. I. Savin, V. A. Somenko, V. F. Fedotov, S. SH. Shil'shteyn and S. V. Marchenko, Phys. Met. Metall. 46, 181 (1979).

15. V. F. Petrunin, S. K. Dolukhanyan, M. G. Zemlyanov, S. V. Marchenko and P. P. Parshin, Sov. Phys. Solid State 23, 1126 (1981).

16. L. S. Topchyan, I. A. Naskidashvili, R. A. Andrievskii and V. I. Savin, Sov. Phys. Solid State 15, 1461 (1974).

17. I. A. Naskidashvili, Yu. G. Sharimanov, N. Vilcu, D. Demco and V. Simplaceanu, Sov. Phys. Solid State 19, 2026 (1977).

18. I. N. Bydlinskaya, I. A. Naskidashvili, V. A. Melik-Shakhnazarov and V. I. Savin, Sov. Phys. Solid State 22, 517 (1980).

19. I. A. Naskidashvili, Sov. Phys. Solid State 18, 874 (1976).

Table 1. Summary of previously published proton M_{2D} parameters for δ-phase (fcc) and ε-phase (fct) ZrH_x.

Sample Composition	ν_H (MHz)	T (K)	Experimental M_{2D} (G^2)	Calculated M_{2D} (G^2)	Ratio ($\frac{\text{experimental}}{\text{calculated}}$)	Fe content[b] (wt %)	Reference
δ-$ZrH_{1.54}$	?	300	29[a]	12.3	2.4	~0.2	Hon (1962)
ε-$ZrH_{1.99}$	?	300	32[a]	16.9	1.9	~0.2	Hon (1962)
δ-$ZrH_{1.60}$	16	300(?)	18.1 ± 0.4	13.1	1.38	0.09	Nakamura (1974)
ε-$ZrH_{1.88}$	16	300(?)	20.3 ± 0.4	15.8	1.29	0.09	Nakamura (1974)
ε-$ZrH_{1.98}$	16	300(?)	17.3 ± 0.4	16.6	1.04	0.09	Nakamura (1974)
ε-$ZrH_{1.98}$	8	300(?)	17.1 ± 0.4	16.6	1.03	0.09	Nakamura (1974)

(a) From rigid lattice linewidth assuming Gaussian lineshape.

(b) In starting Zr metal as reported in reference.

Table 2. Proton M_{2D} parameters for high purity (i.e., 0.002 wt % Fe) ZrH_x from magic echo lineshapes at ν_H = 56.4 MHz.

Sample Composition	T (K)	Experimental M_{2D} (G^2)	Calculated Dipolar M_{2D} (G^2)	Ratio ($\frac{\text{experimental}}{\text{calculated}}$)
δ-$ZrH_{1.60}$	291	12.4[a]	13.1	0.946
	187	12.5	---	---
	89	12.6	---	---
ε-$ZrH_{1.80}$	291	14.6	14.72	0.995
	187	15.1	---	---
	89	14.9	---	---
ε-$ZrH_{1.90}$	291	15.3	15.6	0.981
ε-$ZrH_{2.00}$	291	16.7	16.9	0.988
	187	16.8	---	---
	89	16.9	---	---

(a) The experimental error is ± 0.4 G^2.

Table 3. Theoretical M_{2D} parameters for rigid lattice dipolar interactions in ZrH_x. Only tetrahedral sites are occupied by protons and M_2(H-Zr) term is included.

Composition	Nature of tetrahedral site occupancy	M_{2D} (G^2)	Model
δ-$ZrH_{1.50}$ (a)	Random	12.29	-
	Ordered (Fig. 1 of Ref. 19)	11.23	I
	Ordered (Fig. 2 of Ref. 19)	11.91	II
	Ordered (Fig. 3 of Ref. 19)	12.36	III
ϵ-$ZrH_{1.75}$ (b)	Random	14.49	-
	Ordered (Fig. 4 of Ref. 19)	14.24	IV

(a) a_o = 4.7745 Å

(b) a_o = 4.9338 Å c_o = 4.5027 Å

CHAPTER 5

PROTON NMR STUDIES OF ELECTRONIC STRUCTURE IN $Ti_{1-y}V_yH_{1.95}$

[This chapter is essentially an article by R. C. Bowman, Jr. and W.-K. Rhim entitled "Proton NMR Studies of Electronic Structures in $Ti_{1-y}V_yH_x$," Physical Review B 24, 2232-5 (1981).]

The nonstoichiometric γ-phase of TiH_x, which exists for hydrogen-to-metal ratios of $1.5 \leq x \leq 2.0$, is often regarded as a prototype transition metal hydride and has been the subject of numerous experimental and theoretical studies. When x approaches 2, fcc γ-TiH_x experiences a tetragonal (fct) distortion below about 310 K. Ducastelle, et al.(1) originally suggested this fcc → fct transition arises from a Jahn-Teller type effect which reduces the density of electron states at the Fermi energy (E_F). Support for this mechanism is provided by recent APW band theory calculations(2,3) which place E_F for fcc TiH_2 on doubly degenerate metal d-bands to yield a partially occupied very sharp peak in the density of states $N(E_F)$. The fct distortion removes this degeneracy to produce a large decrease in $N(E_F)$. No Jahn-Teller effect can occur if the degenerate states are either empty or filled.

The magnetic susceptibility and x-ray diffraction measurements of $Ti_{1-y}V_yH_x$ (where $0 \leq y \leq 0.5$ and $1.6 \leq x \leq 1.92$) by Nagel, et al.(4) indicate that substitution of V (with one more electron than Ti) significantly alters the fcc - fct transition behavior. Any combination of hydrogen substoichiometry and V substitution which places E_F in the sharp d-bank peak should give the Jahn-Teller distortion. Although this interpretation is consistent with the results of Nagel, et al(4), there have not been any subsequent experiments to deduce the temperature dependence of $N(E_F)$ in $Ti_{1-y}V_yH_x$.

In this chapter we present NMR measurements of proton shifts and spin-lattice relaxation times (T_1) for $TiH_{1.95}$, $Ti_{0.85}V_{0.15}H_{1.96}$, and $Ti_{0.5}V_{0.5}H_{1.94}$ in the temperature region (i.e., between 80 K and 360 K) where $TiH_{1.95}$ undergoes the tetragonal distortion associated(1,2) with a reduction in $N(E_F)$. Our observations agree with the $Ti_{1-y}V_yH_x$ phase diagram proposed by Nagel, et al.(4) and also confirm Switendick's predictions(2) that V substitution can eliminate the Jahn-Teller effect. Although previous NMR studies have indicated that $N(E_F)$ in γ-TiH_x(5,6) and isomorphic ternary $Ti_{1-y}Nb_yH_x$(7) consist almost entirely of d-electrons, the specific nature of the hyperfine interactions between protons

and conduction electrons has not been definitely established. Korn(6) suggested a transferred orbital interaction with the Ti d-electrons dominating the proton hyperfine couplings in γ-TiH_x; whereas, Nowak, et al. (7) invoked a "core-polarization" interaction with the completely occupied(2,3) H s-states lying below E_F. The similar temperature and composition dependences of proton shifts and T_1 for the three $Ti_{1-y}V_yH_{1.95}$ samples strongly favor the core-polarization mechanism used by Nowak, et al.(7).

The hydrides were prepared by the direct reaction of high purity hydrogen gas with Ti metal or the $Ti_{1-y}V_y$ alloy at temperatures between 500°C - 600°C before slowly cooling to room temperature. Zone-refined Ti and V metals with purities of 99.99% were obtained from Materials Research Corporation and the $Ti_{1-y}V_y$ alloys prepared by multiple arc melting under purified argon. The hydride stoichiometries were determined to within $\pm$1% by volumetric analyses of the hydrogen evolved during thermal decomposition. Powder x-ray diffraction verified that the samples contained only the γ-phase. The powdered hydrides were sealed in evacuated 5 mm o.d. NMR sample tubes.

The NMR experiments were performed at a proton resonance frequency of 56.4 MHz on a wide-band transient spectrometer. The standard inversion-recovery technique gave T_1 values with an accuracy of $\pm$5%. The recently developed multiple-pulse zero-crossing technique(8) yielded proton frequency shifts with a precision of $\pm$1-2 ppm over the temperature range 100 K to 360 K. A spherical sample of tetramethylsilane (TMS) served as an external reference. In contrast, the previous cw NMR measurements of proton shifts in TiH_x(5,6) and $Ti_{1-y}Nb_yH_{1.94}$(7) had uncertainties of at least $\pm$20-30 ppm because of limitations imposed by the broad proton linewidths. The much greater precision of the zero-crossing data now permits more detailed comparisons of the temperature behavior of the proton shift and T_1 parameters.

Although hydrogen diffusion is often a major proton T_1 relaxation mechanism in metal hydrides(9), the observations during this study that

rigid-lattice dipolar interactions completely determine the proton linewidths for the three $Ti_{1-y}V_yH_{1.95}$ samples below 350 K as well as the previous results for TiH_x(6) and $Ti_{1-y}Nb_yH_{1.94}$(7) should ensure the dominance of the electron-nuclear hyperfine interactions for the present conditions. Following the conventional(9,10) assumptions to neglect electron-electron coupling and inter-band mixing effects, the conduction electron T_1 relaxation in transition metals can be separated into three major terms

$$\frac{1}{T_1T} = \alpha_s N_s(E_F)^2 + \alpha_d N_d(E_F)^2 + \alpha_o N_d(E_F)^2 \qquad (1)$$

where α_s, α_d, and α_o are the electron-proton hyperfine coupling constants for the Fermi contact interaction, the "core" polarization arising from an s - d exchange interaction, and the d-electron orbital angular momentum, respectively; $N_s(E_F)$ and $N_d(E_F)$ are the densities of s and d electrons, respectively, at E_F. If any of the terms in eq. (1) is dominant, the density of electron states at E_F is directly proportional to $(T_1T)^{-\frac{1}{2}}$. Fig. 1 gives the temperature dependence of $(T_1T)^{-\frac{1}{2}}$ for the three $Ti_{1-y}V_yH_{1.95}$ samples. The significant decrease in $(T_1T)^{-\frac{1}{2}}$ for $TiH_{1.95}$ below 300 K agrees with Korn's previous results(6) for $TiH_{1.99}$ and the lowering the density of state via the Jahn-Teller effect. As anticipated from the experiments of Nagel, et al.(4) and the arguments of Switendick(2) that $Ti_{1-y}V_yH_2$ would not experience the Jahn-Teller distortion when $y \gtrsim 0.1$, $(T_1T)^{-\frac{1}{2}}$ for both $Ti_{0.85}V_{0.15}H_{1.96}$ and $Ti_{0.5}V_{0.5}H_{1.94}$ are independent of temperature within experimental accuracy.

Fig. 2 summarizes the temperature dependencies of the proton Knight shifts (σ_K) for the three $Ti_{1-y}V_yH_{1.95}$ samples obtained after correcting the experimental shifts relative to TMS for the demagnetization effects (9,11) arising from rather large paramagnetic bulk susceptibilities(4). Although the reductions in the proton shifts varied between 10-15% for the three samples, the relative differences and temperature-dependent

behavior were not significantly modified by this correction. Under the same conditions considered previously for T_1, σ_K can also be separated into three contributions(9,10)

$$\sigma_K = \beta_s N_s(E_F) + \beta_d N_d(E_F) + \beta_0 \chi_0 \qquad (2)$$

where β_s, β_d, and β_0 are analogous electron-proton coupling coefficients and χ_0 is the orbital (also called Van Vleck) paramagnetic susceptibility. Since χ_0 represents the mixing of the unoccupied states above E_F into "all" the occupied states below E_F, it is not directly related to $N_s(E_F)$ or $N_d(E_F)$. Because β_s always gives(10) a positive contribution to σ_K (i.e., higher resonance frequency than diamagnetic reference at constant applied magnetic field) whereas β_d and β_0 usually give(10) negative and positive shifts, respectively; partial cancellation occurs unless one of the terms in eq. (2) is dominant.

Examination and comparison of the proton σ_K and $(T_1T)^{-½}$ parameters in Figs. 1 and 2 lead to several interesting conclusions on the electron structure changes in γ-TiH_2 during the Jahn-Teller distortion and upon the partial substitution with V. The negative shifts observed for all the $Ti_{1-y}V_yH_{1.95}$ samples seem to preclude any significant s-electron contact interactions in general agreement with the previous NMR studies of TiH_x(5,6) and $Ti_{1-y}Nb_yH_x$(7). This interpretation is further supported by the theoretical work of Gupta(3) who has found negligible $N_s(E_F)$ at both the Ti and H sites of TiH_2. Hence, the first terms in eqs. (1) and (2) can be neglected during further analysis of the NMR parameters. Although the orbital term χ_0 nearly always gives(10) a temperature independent contribution to Knight shifts, the orbital contribution to $(T_1T)^{-½}$ is directly proportional to $N_d(E_F)$ and will usually exhibit a large variation with temperature whenever E_F occurs in or near a peak in the density of states. Hence, significant differences in the temperature dependence and effects of substituting V should exist between σ_K and $(T_1T)^{-½}$ if the orbital contributions are large for protons in

$Ti_{1-y}V_yH_{1.95}$. However, when core polarization is the major interaction, eqs. (1) and (2) predict very similar behavior since both parameters are now proportional to $N_d(E_F)$. A comparison of the σ_K and $(T_1T)^{-1/2}$ behavior in Figs. 1 and 2 clearly indicates the similarities for each sample. Furthermore, during the Jahn-Teller distortion of $TiH_{1.95}$ below 300 K, where the reduction in $N_d(E_F)$ is the primary consequence, the percentage decreases in σ_K and $(T_1T)^{-1/2}$ are nearly identical. If the orbital contributions were mainly responsible for σ_K and $(T_1T)^{-1/2}$, these close correlations would not occur. Hence, the present proton NMR parameters for $Ti_{1-y}V_yH_{1.95}$ are completely consistent with the core polarization interactions while the transferred orbital mechanism suggested by Korn(6) does not seem justified when $x \approx 2$. It is possible that changes in the relative positions of the "s" and "d" bands as well as a general lowering of E_F with decreasing x could increase α_0 and β_0 to the point where the orbital terms become important contributors in χ-TiH_x. However, if decreasing x raises the hydrogen antibonding s-band (2,3) sufficiently near to E_F, the direct contact interaction previously ignored by Korn(6) could also become an important contributor to the proton parameters. A resolution of this point would require an extensive evaluation of the NMR parameters for both stoichiometry and temperature behavior as well as more detailed calculations of the band structure in substoichiometric TiH_x.

From the above assertions that proton σ_K and $(T_1T)^{-1/2}$ directly represent $N_d(E_F)$ in $Ti_{1-y}V_yH_{1.95}$, the data in Figs. 1 and 2 indicate $N_d(E_F)$ remains essentially constant for $Ti_{0.85}V_{0.15}H_{1.96}$ and $Ti_{0.5}V_{0.5}H_{1.94}$ while $N_d(E_F)$ for $TiH_{1.95}$ at 100 K has decreased by about 25% from its temperature independent value above 310 K. This difference independently verifies the previous contentions(2-4) that V-substitution can eliminate the Jahn-Teller effect to produce a temperature independent $N_d(E_F)$ when $y \geq 0.15$. The proton parameters also suggest $N_d(E_F)$ for $Ti_{0.85}V_{0.15}H_{1.96}$ and $Ti_{0.5}V_{0.5}H_{1.94}$ increases by 16% and 21%, respectively, relative to $N_d(E_F)$ in cubic $TiH_{1.95}$. However, Nowak, et al.(7)

found Nb substitution to substantially decrease $N_d(E_F)$ in $Ti_{1-y}Nb_yH_{1.94}$ (e.g., $N_d(E_F)$ is reduced by about 40% for y = 0.5). If the only roles of V and Nb are to add electrons to a rigid TiH_2 band structure, $N_d(E_F)$ should have the same y-dependence. Hence, V and Nb must produce some different modification to the band structure above the E_F level of TiH_2. The most apparent physical difference is a decrease in the fcc lattice parameter with V substitution(4) and an increase for Nb(12). Although recent APW calculations(13) of transition metal dihydrides show the antibonding s-band to be quite sensitive to the lattice parameter, the total widths of the d-bands in the region of E_F did not significantly change with volume. Since the s-bands are completely occupied in both ternary hydrides, there must be some relative shifts in the d-band positions to account for the different $N_d(E_F)$ values. However, a detailed assessment must await future experiments and calculations that can better describe changes in the band structure and hyperfine interactions with varying lattice constants.

We thank W. E. Tadlock for preparing the hydrides and Dr. A. Attalla for assistance with the samples. The support and advice of Dr. S. I. Chan is greatly appreciated. This work was supported by Division of Basic Energy Sciences of DOE, Caltech's President's Fund, and the National Aeronautics and Space Administration under Grant No. NAS 7-100.

REFERENCES

1. F. Ducastelle, R. Caudron and P. Costa, J. Phys. (Paris) 31, 57 (1970).
2. A. C. Switendick, J. Less-Common Metals 49, 283 (1976).
3. M. Gupta, Solid State Comm. 29, 47 (1979).
4. H. Nagel and H. Goretzki, J. Phys. Chem. Solids 36, 431 (1975); H. Nagel and R. S. Perkins, Z. Metallkde 66, 362 (1975).
5. B. Stalinski, C. K. Coogan and H. S. Gutowsky, J. Chem. Phys. 34, 1191 (1961).
6. C. Korn, Phys. Rev. B 17, 1707 (1978).
7. B. Nowak, N. Pislewski and W. Leszczynski, Phys. Stat. Sol. (a) 37, 669 (1976); B. Stalinski and B. Nowak, Bull. Acad. Polon. Sci., Ser. Sci. Chim. 25, 65 (1977); B. Nowak, O. J. Zogal and M. Minier, J. Phys. C: Solid State Phys. 12, 4591 (1979).
8. D. P. Burum, D. D. Elleman and W.-K. Rhim, J. Chem. Phys. 68, 1164 (1978).
9. R. M. Cotts in Hydrogen In Metals I. Basic Properties, edited by G. Alefeld and J. Völkl (Springer-Verlag, Berlin, 1978), p. 227.
10. A. Narath in Hyperfine Interactions, edited by A. J. Freeman and R. B. Frankel (Academic Press, New York, 1967) p. 287.
11. K. F. Lau, R. W. Vaughan and C. B. Satterthwaite, Phys. Rev. B 15, 2449 (1977).
12. B. Stalinski and B. Nowak, Bull. Acad. Polon. Sci., Ser. Sci. Chim. 25, 451 (1977).
13. A. C. Switendick, Zeits. Physk. Chem. N.F. 117, 89 (1979).

FIGURE CAPTIONS

Fig. 1. Temperature dependence of proton $(T_1T)^{-\frac{1}{2}}$ for $Ti_{1-y}V_yH_{1.95}$. The break near 300 K for the $TiH_{1.95}$ sample corresponds to the fcc → fct transition induced by the Jahn-Teller effect.

Fig. 2. Knight shifts of the protons in $Ti_{1-y}V_yH_{1.95}$ as a function of temperature. The results are reported relative to tetramethylsilane and have been corrected for the temperature-dependent susceptibilities of $Ti_{1-y}V_yH_{1.95}$. Typical error bars are included on a few data points.

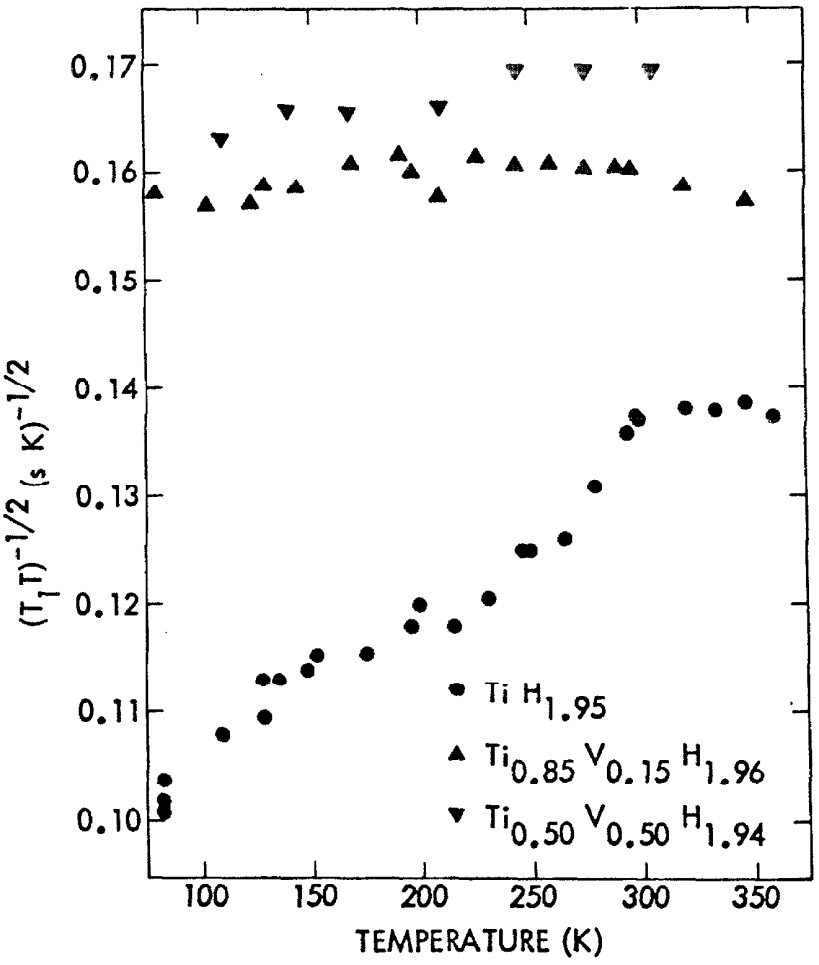
0.17
0.16
0.15
0.14
0.13
0.12
0.11
0.10
$(T_1T)^{-1/2}$ (s K)$^{-1/2}$
100
150
200
250
300
350
TEMPERATURE (K)
Ti $H_{1.95}$
$Ti_{0.85}V_{0.15}H_{1.96}$
$Ti_{0.50}V_{0.50}H_{1.94}$

FIGURE 1

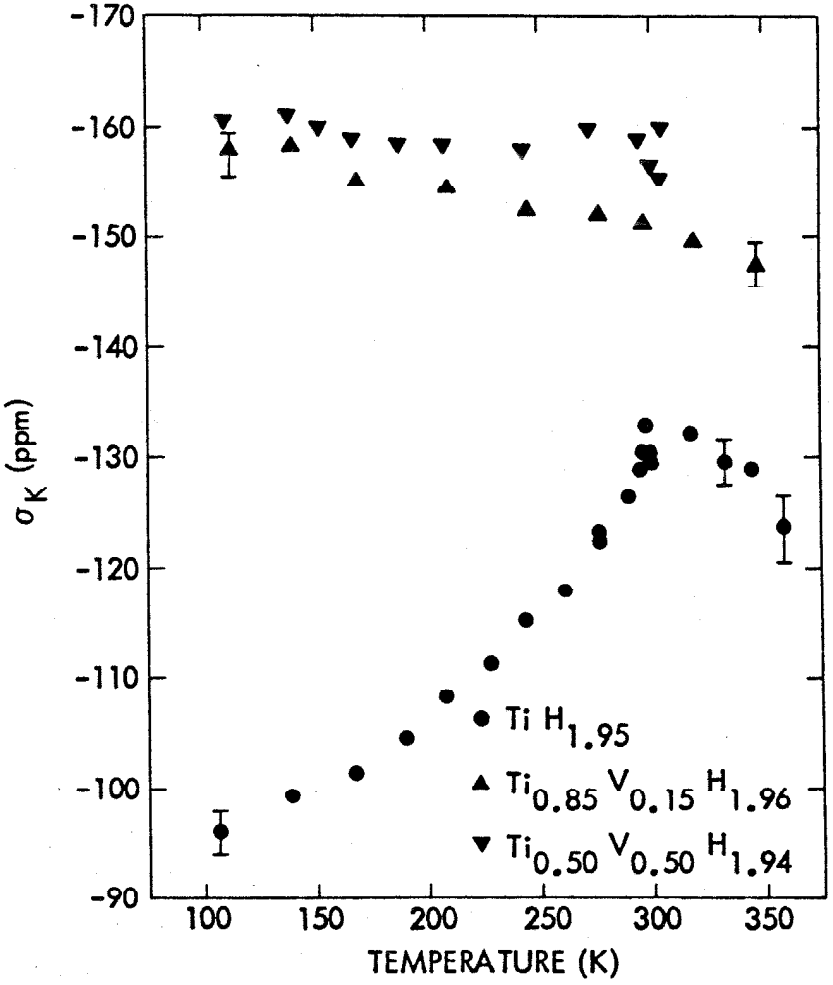
-170
-160
-150
-140
-130
-120
-110
-100
-90
σ_K (ppm)
100
150
200
250
300
350
TEMPERATURE (K)
Ti $H_{1.95}$
$Ti_{0.85}V_{0.15}H_{1.96}$
$Ti_{0.50}V_{0.50}H_{1.94}$

FIGURE 2

CHAPTER 6

ELECTRONIC STRUCTURE OF ZIRCONIUM HYDRIDE: A PROTON NMR STUDY

[This chapter is essentially an article with the same title by R. C. Bowman, Jr., E. L. Venturini, B. D. Craft, A. Attalla, and D. B. Sullenger that is submitted to Physical Review B.]

ABSTRACT

The proton spin-lattice relaxation times (T_1) and Knight shifts (σ_K) have been measured as a function of temperature in fcc (δ-phase) and fct (ε-phase) ZrH_x for hydrogen concentrations $1.5 \leqslant x \leqslant 2.0$. Interactions with the conduction electrons were found to be the only important T_1 relaxation processes below 320 K for the high-purity ZrH_x samples, and no anomalous temperature effects were observed between 320 K and 100 K. The dominant hyperfine interaction for the protons was the transferred core-polarization term from the Zr d band. Both $(T_{1e}T)^{-\frac{1}{2}}$ and σ_K indicate that the density of electronic states $N(E_F)$ at the Fermi level is very dependent upon hydrogen content with a maximum occurring near $ZrH_{1.83}$. This behavior is ascribed to modifications in $N(E_F)$ through the fcc-fct distortion associated with a Jahn-Teller effect in the d bands. The proton NMR results are consistent with a recent band theory calculation of fcc ZrH_2 and photoemission spectroscopy studies of ZrH_x when the changes in d-bands caused by the Jahn-Teller tetragonal distortion are included. The fcc-fct distortions and electronic structures of the ZrH_x phases are compared with the corresponding properties of the TiH_x system.

I. INTRODUCTION

The electronic properties of the non-stoichiometric dihydrides formed by the group IVb metals Ti, Zr, Hf and some of their alloys have been the subjects of numerous theoretical (1-9) and experimental (10-26) studies. Understanding the formation and characteristics of the metal-hydrogen bonds in transition metal hydrides has been a major motivating factor in most of this work. Much attention has also focused on the roles of temperature, hydrogen stoichiometry, and alloying on the cubic (fcc)-to-tetragonal (fct) distortions near the stoichiometric dihydride limit. The fcc-fct phase transitions have been associated (1,3, 4,7,11,15-17,20,22,25,26) with a splitting of the energy bands at the Fermi level (E_F) that is analogous to the Jahn-Teller distortions (27) for the orbitally degenerate electronic energy levels in molecular systems. According to the Jahn-Teller model, the fcc-fct distortion is accompanied (4,11,25,26) by a decrease in $N(E_F)$, the density of electronic states at the Fermi level.

As described in the recent reviews by Switendick (28,29), band theory calculations of the electronic structures in various metal-hydrogen systems have clearly demonstrated the inadequacies of the historic "protonic" and the alternative "anionic" models that had been formulated using rigid band concepts to describe metal hydride electronic properties. According to the band theory calculations for metal hydrides, interstitial hydrogen atoms interact strongly with metal bands of suitable symmetry (28,29) to form new hydrogen-metal bonding states (1-9) composed of the hybridized s-d levels and lying several electron volts below E_F of the host metal as well as other less significant changes in the d bands near E_F. Photoelectron spectroscopy measurements in IVb metal hydrides (18,22) have detected the presence of the hydrogen bonding peaks in the valence band levels that lie ~5-7 eV below E_F in semi-quantitative agreement with the theoretical (1-9) band structures. A general feature of the calculated band structures for the fcc dihydrides TiH_2 (2,3,7,9) and ZrH_2 (8) (the HfH_2 electronic structure has not

yet been calculated) is E_F being very near (or on) the exact center of an extremely sharp peak in the density of states. It is the decrease in $N(E_F)$ with an accompanying small movement of E_F to a lower energy as the degeneracy is reduced for the lower symmetry that is the suggested (1,3, 4,7) driving force for the fcc-fct distortion. In fact, reductions in $N(E_F)$ with an increase in the fct distortions are consistent with low-temperature specific heats (11), photoelectron spectra (22,), and results from nuclear magnetic resonance (NMR) spectroscopy (14-17, 20,21,25,26). Experimental studies (14,25,30-32) of the nominal dihydrides $Ti_{1-y}M_yH_x$ where M = V, Nb, or Ta (i.e., group Vb metals with one more valence electron than Ti) and $1.9 \lesssim x \lesssim 2.0$ have indicated the fcc-fct phase transition is eliminated when $y \geqslant 0.15$. With a cautious assumption (1, 8) of rigid-band behavior for the d bands near E_F, these observations imply that the extra electrons from the group Vb metals fill additional states to move the Fermi level above the sharp peak and thus stabilize the fcc phase since a Jahn-Teller splitting of the completely filled peak states cannot lower the energy. The changes in fcc-fct distortion behavior induced by varying the hydrogen concentration are more difficult to interpret (1,22,30,31) since band structure also changes with the hydrogen content and a rigid band description should not be rigorously valid. However, the fcc phases are stable when the hydrogen contents are sufficiently reduced to apparently shift E_F below the sharp peak (1). No Jahn-Teller effect can occur if the degenerate states are either empty or filled.

Although the non-self-consistent band theory calculations (1-4, 7-9) for stoichiometric TiH_2 and ZrH_2 have provided a sound theoretical framework for the Jahn-Teller distortion mechanism, the absolute accuracies of the calculated energy levels and density of states are quite sensitive to initial atomic configurations, input values of the muffin-tin parameters, and the numerical procedures used during the actual computations. Hence, there are several quantitative differences among the calculated TiH_2 band structures (1-5,7,9) and with the experimental photoelectron energy dis-

tribution curves obtained by Weaver, et al (22). While these differences do not lessen confidence in the fundamental validity of the Jahn-Teller model for the fcc-fct distortions, detailed theoretical assessments of temperature and composition dependences have not yet been possible. Furthermore, the band calculations have not yet been extended to the substoichiometric hydrides and only limited results (1,4) are available for fct TiH_2.

The experimental situation is somewhat better, but there are still some serious limitations. For example, the room temperature photoelectron spectra (22) of ZrH_x with x = 1.63, 1.77, 1.86, and 1.94 do show changes in the band structure near E_F and about 7 eV below E_F that correlate with the fcc-fct distortion. However, the approximately 0.5 eV spectral resolution prevents more detailed observations of any smaller changes and the temperature behavior has not been studied using this technique. The composition behavior of the electronic specific heats (11) of TiH_x and ZrH_x indicate $N(E_F)$ is reduced by the fcc-fct distortions, but only a few samples were measured and these results pertain to temperatures below 10 K. Magnetic susceptibilities (χ) have been measured in TiH_x (11,30), $Ti_{1-y}M_yH_x$ (30-32), for M = V, Nb, Ta, and ZrH_x (11, 13) and have been related to the fcc-fct distortions and the temperature and composition dependences of $N(E_F)$. However, χ for transition metals usually has large orbital (i.e., Van Vleck) contributions in addition to the Pauli terms that are directly proportional to $N(E_F)$. Hence, Switendick (28) has cautioned against assuming the χ changes only reflect variations in $N(E_F)$. NMR measurements of the Knight shifts (σ_K) and conduction electron contributions to the spin-lattice relaxation times (T_1) usually monitor $N(E_F)$ through hyperfine interactions (33-36) at the nucleus. In fact, recent studies (14,15,25,26) of the proton σ_K and T_1 values in TiH_x, $Ti_{1-y}V_yH_x$, and $Ti_{1-y}Nb_yH_x$ have given temperature and composition behavior that is in excellent agreement with the $N(E_F)$ variations expected (1,4,7) for the TiH_x band structure and the Jahn-Teller distortions. Only limited proton NMR data (12,16,20) address the similar

electronic properties for δ-phase (fcc) and ε-phase (fct) ZrH_x.

In the present study the temperature and composition dependences of the proton Knight shifts and spin-lattice relaxation times have been measured in high-purity polycrystalline ZrH_x for $1.5 \leqslant x \leqslant 2.0$. The purposes of this work are to provide some comprehensive conclusions on the electronic structures of δ and ε phase ZrH_x and to compare these results with recent theoretical predictions (1,2,7-9) and the similar proton NMR parameters (15,25) for the electronic structure of TiH_x. Analyses of the proton σ_K and T_1 data for the ZrH_x samples show the dominance of the transferred core-polarization hyperfine interaction (17,25,26) with the Zr d electrons at E_F and yield a composition dependent maximum in $N(E_F)$ near $x = 1.83$. These observations support the Jahn-Teller mechanism for the tetragonal distortion and are also consistent with recent APW band-theory calculations (8) for fcc ZrH_2 and the photoemission (18, 22) and soft x-ray emission (19) spectra for ZrH_x as well as an electron spin resonance study (24) of Er impurities in ZrH_x.

II. A BRIEF REVIEW OF SOME ZrH_x PROPERTIES

The phase diagram and physical properties of the zirconium-hydrogen system have been extensively studied (37). The several ZrH_x phases (37) are typical metallic solids with no unusual electrical properties (38) and normal paramagnetic behavior (11,13) for a transition metal alloy if ferromagnetic impurities (11,13) are avoided. For $x \geqslant 1.50$ and temperatures below 700K, the cubic (fcc) δ-phase and tetragonal (fct) ε-phase are the only known stable ZrH_x phases. A presumably metastable (39-41) γ-phase monohydride with a tetragonal crystal structure (42) coexists with the δ-phase for $x \lesssim 1.5$-1.6. Soviet workers (43-45) have reported some low-temperature (i.e., $T < 200$ K) phase transitions for ZrH_x with $1.65 \leqslant x \leqslant 1.85$, but there have been no confirmations for these transitions by other groups (24,46,47). The structures of the γ, δ, and ε phases have been established by x-ray and neutron diffraction (37,42,48, 49) where the hydrogen atoms only occupy tetrahedral interstitial sites

for each phase (42,46). However, the phase boundaries for the δ and ε phases have not been completely resolved (11,24,37,39,49) and contradictory behavior has been observed (39-42,46) for the γ-phase. Using the results taken from several sources (including present x-ray diffraction measurements on high purity ZrH_x samples), the single phase region for cubic δ-ZrH_x is $1.55(5) \leqslant x \leqslant 1.65(2)$ from above 300 K to much lower temperatures (i.e., $\lesssim$200 K) while the single phase region for tetragonal ε-ZrH_x is $1.74(2) \leqslant x \leqslant 2.0$ over a similar temperature range. A mixed δ and ε phase region exists for $1.65(2) \leqslant x \leqslant 1.74(2)$ while γ-phase $ZrH_{1.0}$ as well as the hcp Zr-metal α-phase are found (37,39-42) when $x \leqslant 1.55(5)$.

The ZrH_x phases are thermodynamically quite stable with very low dissociation pressures (37) at temperatures below 500 K. Because massive ZrH_x can be handled in air at room temperature without an apparent loss in stoichiometry, ZrH_x has often been assumed (37) rather unreactive to oxygen or water vapor. However, clean surfaces of zirconium metal and hydride have been observed (18) to rapidly form ZrO_2 films from the residual oxygen in a vacuum at the low 10^{-9} Torr range. The oxide film serves as a passivating layer which inhibits further reaction at ambient temperature. In massive samples only a relatively small quantity of Zr will be converted to the oxide and no significant reduction in hydrogen content is usually detected. However, fine powders of ZrH_x should be prepared and handled only in vacuum or inert atmosphere environments to avoid excessive oxidation.

Gupta and Burger (8) have, apparently, performed the most complete non-self-consistent one-electron band calculation of the electronic structure for fcc $ZrH_{2.0}$. Fig. 1 reproduces their theoretical total density of states where several features should be noted. First, the hydrogen-metal bonding states are split with peaks ~6 and ~7 eV below E_F. This reflects bonding/antibonding effect (28,29) between the two hydrogen atoms. The Fermi level falls exactly at the center of a very sharp peak in N(E) which rises out of a nearly flat plateau (actually, a slightly

decreasing density is found in the region below the peak). Finally, the metal-hydrogen peak is nearly completely separated from the higher d bands. The experimental photoelectron energy distribution curves (22) for fcc δ-$ZrH_{1.63}$ and fct ε-$ZrH_{1.94}$ are in excellent qualitative agreement with Fig. 1 although the experimental peaks in the presumed metal-hydrogen bonding region are only partially resolved and differ by about 1 eV from the calculated peak positions (8). However, both E_F and the detailed shape of the N(E) curve will change as the hydrogen concentration is decreased (i.e., in fcc δ-phase) and as the lattice is distorted in the fct ε-phase (i.e., the Jahn-Teller splitting of the sharp peak at E_F in Fig. 1). Hence, quantitative agreement with Fig. 1 should not be expected, but all of the major predicted properties (8) have been observed by Weaver, et al (22).

Since Ti and Zr have the same valency, the electronic properties and structures of the fcc and fct ZrH_x phases are very similar to those for the TiH_x system (1-4,7,9). However, the several minor differences in the photoelectron emission spectra (22) indicate the N(E) curves are clearly not identical for TiH_x and ZrH_x. Furthermore, Gupta's calculations (7,8) and several experimental studies (11,12,15,16,20,21) show that $N(E_F)$ values for ZrH_x are significantly smaller than the corresponding $N(E_F)$ values obtained for TiH_x samples with similar compositions. This may be at least partially attributed to the larger unit cell volumes (11) for the ZrH_x phases relative to corresponding TiH_x samples. There should be smaller metal-hydrogen overlap and metal-metal overlaps for the more diffuse 4d orbitals of Zr atoms compared to the corresponding overlaps for the 3d orbitals of the Ti atoms. Finally, the magnitudes of the fcc-fct distortions arising from the Jahn-Teller effect in the electronic energy bands are much greater for the ZrH_x system. The highest temperature for the existence of tetragonal $TiH_{2.0}$ is about 310 K with the fcc-fct transition temperature occurring at lower temperatures as the stoichiometry is decreased (11,15,30,31,48). However, tetragonal ε-ZrH_x is the stable room-temperature phase for $x \geq 1.74$ and $ZrH_{1.92}$ remains

tetragonal up to temperatures above 750 K according to Yakel (48). Nevertheless, any differences in fcc-fct behavior are more a matter of degree since the same basic mechanism is believed (22) responsible in all the group IV metal hydrides.

III. EXPERIMENTAL DETAILS

The ZrH_x samples were prepared by direct reaction between zone-refined Zr metal foils (50) and hydrogen gas that had been purified by diffusion through a Pd-Ag tube. The synthesis procedures have been previously described (47) and compositions between 1.50 and 2.00 were obtained where the volumetric analyses of absorbed hydrogen and weight gains usually agreed within $x = \pm 0.01$. The few discrepancies were resolved using volumetric analyses of hydrogen evolution during thermal desorption from portions of the samples. The ZrH_x foils were ground under a purified argon atmosphere to produce powders (47) that were subsequently sealed in evacuated glass tubes for the NMR experiments.

X-ray diffraction measurements using standard Debye-Scherrer photographic techniques to record the powder patterns were performed at room temperature on every ZrH_x sample. A small amount of γ-phase ZrH was detected in $ZrH_{1.50}$ while only the strongest γ-phase line was found (as a very weak line) in $ZrH_{1.55}$. The powder pattern for $ZrH_{1.70}$ gave approximately equal amounts of the δ and ε phases. All of the other ZrH_x samples were single phase within the detection limits of the x-ray diffraction method. Fig. 2 gives the room temperature lattice parameters for the ZrH_x samples with $x \geq 1.50$ and the corresponding phase boundaries. The lattice parameters in Fig. 2 are generally in very good agreement with values for ZrH_x from several previous measurements by others (11,22,39,49).

Wide-band transient spectrometers were used for all the NMR experiments. The proton spin-lattice relaxation times (T_1) were obtained by the standard inversion-recovery method at a resonance frequency of 34.5 MHz. Within experimental uncertainties the magnetization recoveries were exponential and yielded T_1 values with an average precision of $\pm 3\%$ over

the temperature range 100 K to 300 K. The proton Knight shifts were measured in four ZrH_x samples with the multiple-phase zero-crossing method of Burum, et al (51) on a spectrometer where the magnetic field was locked by an external probe system and the nominal proton resonance frequency was 56.4 MHz. The σ_K values are relative to an external reference of tetramethylsilane (TMS) contained in a spherical bulb and have an experimental precision of ± 2 ppm over the temperature range 170 K to 310 K. No corrections to the σ_K values for the demagnetization effects (35) due to sample susceptibility have been made since the X values for high-purity ZrH_x should be sufficiently small (11,13) to make relatively minor contributions of about 5 ppm to the total proton shifts.

IV. RESULTS

Figures 3 and 4 show the temperature dependent behavior of the proton T_1 values for several ZrH_x samples. There is no indication for any anomalous breaks from the smooth T_1 increases as the temperature is lowered below 200 K for any of the high-purity ZrH_x samples. This contrasts with the low temperature anomalies in proton T_1 that were reported by Naskidashvili, et al (44) for $ZrH_{1.65}$ and $ZrH_{1.75}$ which they associated with possible phase transitions implied by other techniques (43,45). However, from neutron diffraction studies, Petrunin, et al (46) saw no changes in the phase composition of $ZrD_{1.82}$ when it was cooled to liquid nitrogen temperature. Furthermore, no evidence for these low-temperature phase transitions was found from electron spin resonance studies (24) of Er ions in ZrH_x or low temperature proton lineshape measurements (47) on high purity ZrH_x samples. Petrunin, et al (46) have suggested that the low temperatures anomalies (43-45) may actually involve transitions of an impurity phase. Since no anomalies are found for the T_1 data in Figures 3 and 4 for high purity ZrH_x samples, there is again no confirmation for the low temperature phase transitions in ZrH_x as proposed by Naskidashvili, et al (43-45). Hence their existence remains unsubstantiated and must be regarded as highly speculative and will not be

considered further.

In general, the total relaxation rate T_1^{-1} in a metallic solid can be separated into three potential contributions

$$\frac{1}{T_1} = \frac{1}{T_{1e}} + \frac{1}{T_{1d}} + \frac{1}{T_{1p}} \qquad (1)$$

where T_{1e} represents relaxation due to hyperfine interactions (33-36) with the conduction electrons, T_{1d} is the well-known (36) diffusion contribution, and T_{1p} is the relaxation term for localized paramagnetic centers. The rigid-lattice dipolar lineshapes for proton NMR spectra (47) of polycrystalline ZrH_x at room temperature as well as previous proton T_1 measurements (16,20,21) imply that T_{1d} is not a significant contribution to the proton spin-lattice relaxation process until the temperature exceeds at least 400 K. Hence, the diffusion contributions to all the T_1 data in Figures 3 and 4 will be completely negligible. The temperature independent T_{1p} term can also be neglected since the concentration of any paramagnetic impurities is very low in these high-purity ZrH_x samples. Thus, the experimental T_1 values of Figures 3 and 4 only correspond to the conduction electron relaxation time T_{1e}. The anomalously short proton T_1 data of Khodosov and Shepilov (12) for ZrH_x, which are nearly a factor of 10 shorter than the T_1 values in Figures 3 and 4, probably contain large T_{1p} contributions although this cannot be directly established since the purities of their samples are unknown. It should be noted that Khodosov and Shepilov (12) also gave proton T_1 values for TiH_x samples that are much shorter than the spin-lattice relaxation times obtained for TiH_x by other research groups (15,21,25,26). Hence, the proton T_1 data of Khodosov and Shepilov (12) for ZrH_x and TiH_x are probably not reliable indicators of the conduction electron contributions to spin-lattice relaxation times.

The temperature dependence of the proton Knight shifts σ_K were measured for $ZrH_{1.60}$, $ZrH_{1.80}$, $ZrH_{1.90}$, and $ZrH_{2.00}$. These results are summarized in Fig. 5 where the σ_K values are negative (i.e., the shifts are upfield for a constant frequency) relative to the resonance frequency for the external standard of TMS. In some previous studies (52-54) of the proton Knight shifts for metal hydrides, the frequency of the bare proton nucleus (i.e., H^+) has been chosen as the reference. This choice may have been biased by use of the rigid-band proton model (28) to describe NMR results (36) in the hydrides. However, photoemission (18,22) and soft x-ray emission (19) spectroscopies as well as the band theory calculations clearly indicate an increased electron density about the hydrogen interstitials in ZrH_x. Hence, it is probably more appropriate to reference the proton Knight shift to the frequency for the hydride anion (i.e., H^-) rather than H^+. According to Mason (55) the chemical shift for free H^- is 27 ppm upfield from the H^+ reference. The measurements of Nicol and Vaughan (56) on proton shifts in the alkaline hydrides CaH_2, SrH_2, and BaH_2 imply an average upfield chemical shift of 23 ± 2 ppm for the hydride ion relative to H^+. A similar chemical shift is also expected for hydrogen interstitials in the transition metals, but it is impossible to uniquely define an absolute value. Consequently, the proton σ_K values are referenced to TMS which is about 30 ppm upfield from the bare proton frequency. The use of TMS as the reference may give an absolute uncertainty in σ_K of $\pm$5-10 ppm, but at least a consistent estimate of the chemical shift term has been included.

V. DISCUSSION

A. Hyperfine Interactions of Protons in ZrH_x

The nuclear spin systems in metals are affected by the electronic structure of the metal through the hyperfine fields produced by the conduction electrons at the sites of the nuclei. In transition metals and alloys, including the metal hydrides, the conduction electrons will primarily occupy the s and d orbitals of the constituent atoms. However, the

densities of d-electron states in the region of the Fermi level are usually much larger than the densities of the s-electron states since E_F lies in the rather narrow d band formed by the transition metal orbitals while the s band extends over a wide energy distribution. Although detailed models (33-35) have been formulated for the hyperfine interactions in the simple metals, the general expressions are rarely applied to transition metal systems since unique identification of the various hyperfine interactions is usually impossible. Instead, some simpler models that neglect effects from electron-electron correlation, mixing of the s and d bands, and various higher-order contributions have been extensively used (33-36) to analyze Knight shifts and T_{1e} parameters for transition metals and transition metal alloys. Within the free electron approximation and assuming only s and d orbitals contribute to the hyperfine interactions, the Knight shift and T_{1e} value can each be separated into three components

$$\sigma_K = 2\mu_B[H_{hf}(s)N_s(E_F) + H_{hf}(d)N_d(E_F)] + (\frac{1}{N_A\mu_B})H'_{hf}(o)X_o \qquad (2)$$

$$\frac{1}{T_{1e}T} = 4\pi\hbar\gamma_I^2 k_B\{[H_{hf}(s)N_s(E_F)]^2 + [H_{hf}(d)N_d(E_F)]^2 q + [H_{hf}(o)N_d(E_F)]^2 p\}. \qquad (3)$$

Here, μ_B is the Bohr magneton; N_A is Avogrodo's number; $\hbar$ is Planck's constant; γ_I is the gyromagnetic ratio for nuclei with quantum number I; k_B is the Boltzmann's constant; $N_s(E_F)$ and $N_d(E_F)$ are the s band and d band density of states at the Fermi level, respectively; X_o is the Van Vleck term of the magnetic susceptibility caused by paramagnetic orbital interactions (33) with the d-electrons; and p and q are the reduction factors resulting from d electron orbital degeneracy at E_F as described by Narath (33). The hyperfine fields at the nuclei are produced as follows: $H_{hf}(s)$ is due to the Fermi contact interaction with unpaired s electrons at E_F, $H_{hf}(d)$ is the "core" polarization of

spin-paired s orbitals at energies below E_F by the unpaired d electrons at E_F; and $H_{hf}(o)$ and $H'_{hf}(o)$ are the fields generated by the orbital motion of the d electrons. Although $H_{hf}(o)$ represents only d electrons at E_F, $H'_{hf}(o)$ is an average (33) over all contributing states in the d band lying above and below E_F. Since theoretical estimates of the orbital fields are very difficult (34), the approximation $H_{hf}(o) \approx H'_{hf}(o)$ is often used to analyze experimental data. Although the contact field $H_{hf}(s)$ is usually much larger (35) than the core polarization or orbital hyperfine fields, the large $N_d(E_F)$ in most transition metal systems usually insures that core polarization and/or orbital terms will dominate T_{1e} and σ_K. Although $H_{hf}(s)$ is always positive (33-35), $H_{hf}(d)$ is negative (33) for the transition metals. Hence, significant cancellations can occur in σ_K to give positive, negative, or even zero shifts depending upon the relative magnitudes of the three terms in eqn. (2). Since only the squares of the hyperfine fields influence $(T_{1e}T)^{-1}$, the three terms in eqn. (3) are always additive.

Because several independent parameters contribute to the σ_K and $(T_{1e}T)^{-1}$ values for transition metal systems, quantitative assessments of the individual hyperfine fields and density of states are usually very difficult without supplemental experimental and theoretical results. Nevertheless, many significant insights on the electron structures of transition metals have been obtained from the σ_K and $(T_{1e}T)^{-1}$ data (33-35) without explicitly evaluating all of the parameters in eqns. (2) and (3). If one of the terms dominates eqn. (3), $(T_{1e}T)^{-\frac{1}{2}}$ is directly proportional to the density of states at E_F. When either the Fermi contact or core polarization hyperfine interaction is dominant, both σ_K and $(T_{1e}T)^{-\frac{1}{2}}$ will directly correspond to $N_s(E_F)$ or $N_d(E_F)$, respectively, and the NMR parameters will exhibit very similar behavior when temperature or alloy composition is varied. Because the orbital terms $H'_{hf}(o)$ and X_o for σ_K in eqn. (2) depend upon averages over the entire d band (34-35), the orbital term is not proportional to $N_d(E_F)$ and usually gives a temperature independent contribution to σ_K. However, the orbital contribution to $(T_{1e}T)^{-\frac{1}{2}}$ is

directly proportional to $N_d(E_F)$ and will usually exhibit a large variation with temperature whenever E_F occurs in or near a peak in the density of states. Hence, significant differences in temperature behavior for σ_K and $(T_{1e}T)^{-\frac{1}{2}}$ are expected whenever orbital contributions are large and E_F falls near a peak in the density of states. The orbital contributions are generally large for the transition metal nuclei (33-35) and give positive contributions to σ_K as were observed (10) for Ti nuclei in TiH_x with $1.7 \leqslant x \leqslant 2.0$.

Because the hyperfine field from the hydrogen 1s orbital is intrinsically small, transferred hyperfine interactions from the metal d states are assumed (15-17,25,26) to be the major contributors to the proton Knight shifts and T_{1e} relaxation times. In fact, the transition metal d states appear to dominate the hyperfine interactions for any non-transition element nucleus (57-60) that is contained in a transition metal host. In his analysis of the electronic structure of TiH_x, Korn (15) proposed a transferred orbital hyperfine interaction for protons. His major justification was that the proton shifts of Stalinski, et al (61) did not show the same stoichiometry dependence as Korn's proton $(T_{1e}T)^{-\frac{1}{2}}$ data. This difference is consistent with the behavior expected (33) for orbital hyperfine interactions. However, the proton Knight shifts of Stalinski, et al (61) were obtained by CW-NMR techniques and are very imprecise since the shifts are much smaller than the dipolar linewidths. More reliable proton σ_K values for TiH_x were recently obtained by multiple-pulse techniques (26) and gave excellent agreement with both the composition and temperature dependencies of the proton $(T_{1e}T)^{-\frac{1}{2}}$ values (15,26). Similar agreement between σ_K and $(T_{1e}T)^{-\frac{1}{2}}$ behavior has been obtained (25) for protons in $Ti_{1-y}V_yH_{1.95}$. Hence, the original experimental basis for Korn's proposed orbital hyperfine interactions at the proton sites has been invalidated by subsequent (and more accurate) proton σ_K measurements (25,26). Furthermore, there is experimental and theoretical evidence (57-60) that orbital contributions are usually negligible for non-transition nuclei in transition metal hosts.

The recent NMR data for TiH_x and related alloy hydrides (17,25,26) favor the dominance of a "transferred" core-polarization hyperfine interaction from the metal d-orbitals to the filled hydrogen 1s orbitals lying below E_F. This interpretation is consistent with the band-theory calculations (1-4,7,9) which have indicated the formation of the s-d hybridized metal-hydrogen bonding band. The negative proton σ_K values (17,25,26,61) are easily associated with core-polarization interactions (33-35,57-60). In contrast the orbital hyperfine interaction usually gives positive Knight shifts and tenuous arguments were required to rationalize (15) the negative proton σ_K values in TiH_x. Since the valence bands of Ti and Zr are isoelectronic and the proton σ_K in ZrH_x are also negative as shown in Fig. 5, any orbital contributions to the proton hyperfine interactions will be neglected during the remaining discussion. Hence, the experimental proton σ_K and $(T_{1e}T)^{-\frac{1}{2}}$ parameters for ZrH_x are assumed proportional to the density of electron states at E_F through the Fermi contact and core-polarization terms as shown in eqns. (2) and (3).

A useful relationship that was originally derived by Korringa (62) for the contact hyperfine interaction can be generalized in the form

$$q_{exp} = C_K/\sigma_K^2 \; T_{1e}T \qquad (4)$$

where $C_K = \hbar\gamma_e^2/(4\pi k_B\gamma_I^2)$ and γ_e is the electron gyromagnetic ratio. When the Fermi contact terms dominate both σ_K and T_{1e}, $q_{exp} = 1.0$ if the electron-electron interactions (33) are excluded. For the core-polarization terms, $q_{exp} = q$, the reduction factor for T_{1e} relaxation by d electrons. In cubic lattices, q obeys (33)

$$q = \frac{1}{3} f^2(t_{2g}) + \frac{1}{2}[1 - f(t_{2g})]^2 \qquad (5)$$

where $f(t_{2g})$ is the fractional character of the t_{2g} d-orbitals at the Fermi surface. The minimum value for q is 0.20 when $f(t_{2g}) = 3/5$ and there is an equal population of all five d-orbitals at the Fermi level.

The maxima for q are 0.50 and 0.33 when $f(t_{2g})$ equals zero or one, respectively. However, $q_{exp} > 0.5$ are possible if both contact and core-polarization interactions contribute to σ_K because of the fortuitous cancellations of positive and negative shift contributions. In non-cubic lattices q will not be given by eqn. (5), but the ~10% tetragonal distortion in ε-ZrH_x should not lead to large deviations and $0.2 \lesssim q \lesssim 0.5$ should remain approximately valid for the core-polarization interaction.

The shift in the Fermi level and the widening of the electron distribution function about this level with increasing temperature can make σ_K and T_{1e} temperature dependent if E_F happens to lie in a region where the density of states is very dependent upon energy. This temperature dependence will be given by the expressions (15,26,63)

$$\sigma_K(T) = \sigma_K(0)\left\{1 + \frac{1}{6}\pi^2 k_B^2 T^2 \left[\frac{1}{N(E)}\frac{d^2N(E)}{dE^2} - \left(\frac{1}{N(E)}\frac{dN(E)}{dE}\right)2\right]_{E=E_F}\right\} \quad (6)$$

$$\frac{1}{T_{1e}(T)T} = \frac{1}{T_{1e}(0)T}\left[1 + \frac{1}{3}\pi^2 k_B^2 T^2 \left(\frac{1}{N(E)}\frac{d^2N(E)}{dE^2}\right)\right]_{E=E_F} . \quad (7)$$

Since $\sigma_K(T)$ depends on the difference between the first and second derivatives of N(E), $\sigma_K(T)$ will not necessarily exhibit the same temperature behavior as $[T_{1e}(T)T]^{-1}$. In fact, $\sigma_K(T)$ could have an opposite dependence or be temperature independent when $[T_{1e}(T)T]^{-1}$ varies with temperature. According to eqns. (6) and (7), the major factor determining σ_K and $(T_{1e}T)^{-1}$ temperature dependent behavior is the relative position of E_F to a peak. However, a second mechanism can also produce temperature dependent σ_K and $(T_{1e}T)^{-\frac{1}{2}}$ values. If $N(E_F)$ itself is strongly temperature dependent due to a change in some external parameter (e.g., an increasing tetragonal distortion from the Jahn-Teller effect), σ_K and $T_{1e}T$ will directly follow the change in $N(E_F)$ and changes associated with eqns. (6) and (7) probably make only secondary contributions. The reduction in

$N_d(E_F)$ for TiH_2 below 310 K is presumably responsible (25,26) for the temperature behavior of the proton σ_K and $(T_{1e}T)^{-1/2}$ parameters in TiH_x when $x \gtrsim 1.8$. In the next section it will be shown that a different situation apparently causes σ_K and $(T_{1e}T)^{-1/2}$ to be temperature dependent in ε-ZrH_x (i.e., the processes corresponding to eqns. (6) and (7) are responsible).

B. Relation of Proton NMR Parameters to fct Distortion and Electronic Structure in ZrH_x

Figures 6 and 7 show the temperature dependent behavior of the proton $(T_{1e}T)^{-1/2}$ values for the T_1 data presented in Figures 3 and 4, respectively. From the discussion of the previous section, $(T_{1e}T)^{-1/2}$ is presumed directly proportional to the local density of electron states at the Fermi level as sampled at the proton site. The proton Knight shifts are also proportional to $N(E_F)$. The negative σ_K values in Fig. 5 indicate the dominance of the transferred core-polarization hyperfine interactions over the Fermi contact contribution as has been previously concluded for protons in the Ti-based dihydrides (17,25,26). This implies $N_d(E_F) >> N_s(E_F)$ in all these hydrides which is completely consistent with the band theory calculations for TiH_2 (1-4,7,9) and ZrH_2 (8). Hence, $(T_{1e}T)^{-1/2}$ should also mainly represent $N_d(E_F)$ through the core-polarization interactions. However, some contributions from the contact term are expected for both σ_K and $(T_{1e}T)^{-1/2}$ since $N_s(E_F)$ is predicted (8) to be finite (although small) in fcc ZrH_2 and $H_{hf}(s)$ should be larger (35) than $|H_{hf}(d)|$.

The composition dependence of the proton σ_K and $(T_{1e}T)^{-1/2}$ parameters in ZrH_x is summarized in Fig. 8 for various temperatures. The major feature for $(T_{1e}T)^{-1/2}$ is an increase above $x = 1.75$ (i.e., in the ε-phase) to reach a maximum near $x = 1.83$ before decreasing smoothly with composition to $x = 2.00$. $(T_{1e}T)^{-1/2}$ exhibits the largest temperature effects for $1.80 \leq x \leq 1.85$ (i.e., at the peak). Similar behavior is also noted for the proton σ_K; however, neither the composition nor temperature dependence of σ_K is quite as large as seen for $(T_{1e}T)^{-1/2}$.

Korn (16) has reported preliminary measurements of the room temperature variation of proton $(T_{1e}T)^{-\frac{1}{2}}$ as a function of hydrogen concentration for ZrH_x with $1.54 \leq x \leq 2.00$. His $(T_{1e}T)^{-\frac{1}{2}}$ data also showed a large peak near $x = 1.82$ in excellent agreement with Fig. 8. However, Korn's $(T_{1e}T)^{-\frac{1}{2}}$ values are consistently 10-15% larger than the present results and Korn found $(T_{1e}T)^{-\frac{1}{2}}$ to increase by about 10% in the composition range $1.54 \leq x < 1.64$ (i.e., in the mixed $\gamma+\delta$ and pure δ-phase regions) while Fig. 8 indicates $(T_{1e}T)^{-\frac{1}{2}}$ at room temperature is essentially independent of composition for $1.50 \leq x \leq 1.65$, which is in better accord with the ZrH_x phase diagrams (37,39-42). Finally, Korn reports a $(T_{1e}T)^{-\frac{1}{2}}$ minimum in the $\delta+\varepsilon$ mixed phase near $x = 1.72$ that is not apparent in Fig. 8. Since Korn's paper (16) is brief, there is not enough information to resolve these discrepancies with the present data in Fig. 8 although his systematically larger $(T_{1e}T)^{-\frac{1}{2}}$ values may represent paramagnetic T_{1p} contributions to the spin-lattice relaxation times. Nevertheless, a well-defined $(T_{1e}T)^{-\frac{1}{2}}$ peak in the fct ε-phase region seems to be an unmistakable property of ZrH_x since it was so clearly present in both studies. This feature should be associated with changes in $N(E_F)$ as the hydrogen concentration is varied.

In order to obtain a better understanding of the proton hyperfine interactions and the character of electron states at E_F, the generalized Korringa relation of eqn. (4) was applied on the samples $ZrH_{1.60}$, $ZrH_{1.80}$, $ZrH_{1.90}$, and $ZrH_{2.00}$. The resulting parameters q_{exp} at 300 K and 170 K are summarized in Table I. Because the proton σ_K shifts for ZrH_x are small, their absolute values have rather large uncertainties due to choice of a zero shift reference (i.e., the TMS frequency) and the neglect of possible susceptibility corrections (25,26,35). Hence, the q_{exp} values in Table I have limited accuracy and should not be regarded as definitive in deducing the relative proportions of s and d electron character at E_F. However, more qualitative interpretations of q_{exp} should be fairly reliable. For example, there is probably an appreciable mixture of Fermi contact and core-polarization contributions for $ZrH_{1.60}$

since $q_{exp} > 1.0$. While the negative σ_K implies $N_d(E_F) > N_s(E_F)$ for $ZrH_{1.60}$, a more quantitative estimate of $N_s(E_F)$ and $N_d(E_F)$ is not possible since the relevant hyperfine fields $H_{hf}(s)$ and $H_{hf}(d)$ are unknown. The q_{exp} values for the three ε-phase samples with $x \geqslant 1.80$ are within the range expected (33) for the core-polarization reduction factor (i.e., $0.2 \leqslant q \leqslant 0.5$ for a cubic lattice). However, the tetragonal distortion (i.e., $c/a \approx 0.9$) in ε-ZrH_x may influence the allowed range since the orbital degeneracy of the d functions will change as the symmetry is reduced by the distortion. Furthermore, some residual contact contribution from s states at E_F could also be present, but this term must be much less than for the δ-phase since $q_{exp} < 0.5$ for the ε-phase samples. Hence, $N_d(E_F)$ is probably much larger than $N_s(E_F)$ for fct ε-ZrH_x, and E_F has moved further up into the d bands as the hydrogen concentration is increased. This trend is consistent with the general predictions (28,29) of the theoretical band structure calculations.

Table I also includes mean slopes of the temperature behavior of the proton σ_K and $(T_{1e}T)^{-1}$ parameters for several ZrH_x samples. Although positive or near zero slopes are observed when $x < 1.8$ or $x > 1.9$, the proton parameters for the samples with $1.80 \leqslant x \leqslant 1.85$ have strongly negative temperature dependence as shown in Figures 5-8 and Table I. Assuming the temperature dependence corresponds to the thermal broadening effects of the electron distribution functions, eqns. (6) and (7) can approximately relate the slopes of σ_K and $(T_{1e}T)^{-1}$ in Table I to the derivatives at E_F for the density of states with respect to electron energy. Since both σ_K and $(T_{1e}T)^{-1}$ have negative temperature slopes near $x = 1.83$, E_F must fall on a local maximum in the density of states at this composition. On the other hand, nearly flat (or, at least, more slowly changing functions with convex curvatures) density of states are indicated for the δ-phase and $x > 1.90$. This description of the ZrH_x density of states is not very consistent with the calculated (8) one shown in Fig. 1 for fcc ZrH_2 if a quasi-rigid band model is used to shift E_F to lower energies as the ZrH_x stoichiometry is decreased. However,

ε-phase ZrH_x is fct and the Jahn-Teller mechanism (1,4) predicts the energy levels responsible for the $N(E_F)$ peak in fcc ZrH_2 to split during the tetragonal distortion.

Schematic pictures of the density of states of the d-bands in the region near E_F for fcc δ-ZrH_x and fct ε-ZrH_x are given in Fig. 9. The calculated curves by Gupta and Burger (8) serve as the basis for N(E) in the fcc structure while the composition dependence of the proton $(T_{1e}T)^{-\frac{1}{2}}$ data and the presumably symmetric band splitting from the Jahn-Teller effect leads to the proposed density of states shape for the tetragonal structure. A quasi-rigid band model, which recognizes that some electrons associated with the hydrogen atoms will go into the metal-hydrogen bonding states (1,28,29) lying several electron volts below E_F, has been used to locate the Fermi levels at several ZrH_x compositions. The magnitude of the splitting between the two peaks for ε-ZrH_x will probably be sensitive to the c/a ratio as well as some secondary perturbations with changes in hydrogen concentrations since the rigid band cannot be rigorously valid (7,8). However, the c/a ratio only changes from 0.91 to 0.89 over the composition range $1.75 \leqslant x \leqslant 2.00$ which is small compared to the 10% distortion that characterizes the ε-phase. Hence, the increase of the Jahn-Teller splitting in ε-ZrH_x with increasing x should not be a large effect, but it could contribute (along with the electrons supplied by the hydrogen atoms) to accelerate the rise of E_F through the low energy peak in N(E) towards a presumably rather flat valley at x = 2.00.

Although a quantitative determination of the energy difference $\Delta E(\frac{c}{a})$ between the two maxima in N(E) is beyond the capabilities of the present analysis, it is probably one electron volt or smaller. This value was estimated from the photoelectron spectra of Weaver, et al (22) for $ZrH_{1.94}$ in which they observed a rather sharp peak in the d-band spectrum about 0.5 eV below their cutoff at E_F. Furthermore, the photoelectron spectra (22) for ε-ZrH_x are also consistent with E_F moving through a N(E) peak. Because the instrumental resolution of the photoelectron spectra is about 0.4 eV, Weaver, et al (22) cannot detect an $N(E_F)$ peak until E_F lies more

than about 0.4 eV above the peak. Hence, the sharp peak in Fermi-level emission spectra for $ZrH_{1.94}$ indicates E_F is a few tenths of an electron volt above a peak in N(E),which is in qualitative agreement with the Fermi level for $ZrH_{1.94}$ predicted in Fig. 9b. For $ZrH_{1.75}$, Weaver, et al (22) saw no indication of a peak in the Fermi-level emission of the photoelectron spectra while a small rise was observed for $ZrH_{1.88}$ as though E_F was near (or, just past) the middle of a peak which is being obscured by the instrumental resolution. These spectra suggest the N(E) shape in Fig. 9b is at least qualitatively correct for ε-ZrH_x although the peak maximum and width cannot be reliably specified.

Further evidence in favor of the N(E) distribution in Fig. 9b is provided by the electronic specific heat measurements of Ducastelle, et al (11) and by the electron spin resonance studies (24) of 0.1% Er substituted in ZrH_x. According to Ducastelle, et al (11) the $N(E_F)$ values for $ZrH_{1.55}$, $ZrH_{1.85}$, and $ZrH_{1.96}$ are 0.36, 0.76, and 0.46, respectively, in units of states/eV per metal atom. Hence, $N(E_F)$ is larger for the ε-ZrH_x samples than δ-$ZrH_{1.55}$ and the largest $N(E_F)$ occurs for ε-$ZrH_{1.85}$. This behavior is exactly as indicated in Fig. 9. Analyses (24) of the temperature dependent increase in the linewidths of the Er ESR spectra for several ZrH_x samples also imply that $N(E_F)$ was substantially larger for the fct ε-phase compositions with a maximum near x = 1.85 to 1.90. Thus, the N(E) peak in Fig. 9b is again consistent with another independent experimental technique that monitors $N(E_F)$ behavior.

C. Comparison of Electronic Structures in TiH_x and ZrH_x

Although the TiH_x and ZrH_x systems have similar phase diagrams, crystal structures, and electronic properties, a number of qualitative and quantitative differences have been noted in section II and in the literature (5,8,11,15,16,21,22,48). For example, Table II compares the theoretical (8) partial density of states (n_ℓ) at E_F for fcc TiH_2 and ZrH_2. The angular momentum representation of n_ℓ in Table II is relative to the local metal or hydrogen sites where the electron band structure is formed

mainly from the hydrogen 1s orbitals and the metal nd and (n+1) s orbitals. Thus, the n_p and n_f terms should not be considered to represent occupied p or f orbitals as an intra-atomic effect, but n_p and n_f at a given metal or hydrogen site primarily come from overlaps with the tails of the d orbitals from neighboring metal atoms (8). Hence, the hyperfine interactions at the proton sites are due to local s states and the transferred core-polarization interactions with the d states on neighboring metal atoms as was presumed in Section V A. The dominant n_d value at the metal site and all the n_ℓ values for the hydrogen sites are significantly larger for fcc TiH_2 to make the total $N(E_F)$ larger as well. This prediction is consistent with the various experimental results such as electronic specific heats (11) and magnetic susceptibilities (11,13,30,31) that are affected by $N(E_F)$. However, most of these experiments correspond to the fct phases for TiH_x and ZrH_x where $N(E_F)$ has already been decreased by the Jahn-Teller distortion, but the trend agrees with $N(E_F)$ values in Table II. The s electron contributions at E_F are small at both the metal and hydrogen sites in TiH_2 and ZrH_2. However, n_s gives a significantly larger contribution at the hydrogen sites than at the metal sites, but $n_s(H)$ is still less than 2% of the total partial $n_\ell(H)$ in fcc TiH_2 and ZrH_2. The relative $n_s(H)$ portion will probably be increased by the tetragonal distortion since the contributions from the metal d orbitals will be greatly reduced with only minor changes expected for the s band.

The proton $(T_{1e}T)^{-1/2}$ parameters of Göring, et al (26) for TiH_x and the present values for ZrH_x are compared in Fig. 10. If the proton hyperfine fields are assumed to be approximately equivalent for these systems, the proton $(T_{1e}T)^{-1/2}$ parameters in Fig. 10 imply the effective $N(E_F)$ values at the proton sites in ZrH_x are about 40% or less of the density of states at E_F in TiH_x. Taking the n_ℓ values with $\ell \geq 1$ for the hydrogen sites from Table II, the ratio of the $N(E_F)$ in the fcc dihydrides is 0.49. The good agreement is consistent with the expected dominance of the $N_d(E_F)$ term in both hydrides and again indicates the n_s terms are not

major contributors to the proton hyperfine interactions (25,26). However, the n_s term can give a larger relative contribution in the fct TiH_x and ZrH_x phases since $N_d(E_F)$ is substantially decreased by the Jahn-Teller effect. The much larger tetragonal distortion in ZrH_x [i.e., a minimum c/a ratio of about 0.89 compared to a c/a ratio of about 0.945 in TiH_2 according to Yakel (48)] should yield a greater relative $N_d(E_F)$ difference between TiH_x and ZrH_x when $x \approx 2.00$, which is consistent with the $(T_{1e}T)^{-½}$ data in Fig. 10.

The Korringa parameters for the ZrH_x samples in Table I suggest a larger s-electron contact contribution than was apparent in similar analyses for $TiH_{0.99}$ and $TiH_{1.99}$ by Göring, et al (22). However, the actual difference cannot be reliably estimated considering the difficulty in accurately defining the absolute σ_K values in both studies, but a systematically larger n_s level for ZrH_x would not be unreasonable since the $N_d(E_F)$ value is also smaller in ZrH_x. Although Göring, et al (26) concluded that the tetragonal distortion reduced the relative population of t_{2d} d states at E_F, a similar evaluation for ε-ZrH_x is more difficult since the n_s and the various non-rigid band structure effects (1,8) cannot be readily identified for these samples and interpretation of the Korringa parameter q becomes much less straightforward. A partial density of states analysis in fcc TiH_2 by Fujimori and Tsuda (9) indicated the peak at E_F is due to the t_{2g} states. Assuming a similar situation in ZrH_2, the split peaks in Fig. 9b should also be primarily t_{2g} d bands sitting on top of smoothly varying e_g states. Hence, the largest t_{2g} contribution should be at the peak (i.e., near $ZrH_{1.83}$) and the smallest portion of t_{2g} states at $ZrH_{2.00}$. Unfortunately, the present q_{exp} values in Table I do not permit a clear assessment of the fraction of t_{2g} states for any of the ε-ZrH_x samples.

Some significant differences in the temperature behavior of the proton $(T_{1e}T)^{-½}$ values for TiH_x and ZrH_x are also indicated in Fig. 10. When $x \gtrsim 1.95$, $(T_{1e}T)^{-½}$ values for ZrH_x decrease with x and are nearly independent of temperature; whereas, the $(T_{1e}T)^{-½}$ values for TiH_x

increase with x at 287 K and decrease with x at 122 K to produce an effective $N_d(E_F)$ reduction of nearly 25% for $TiH_{1.99}$ between these temperatures. This difference reflects the more rapid decrease (48) in the c/a ratio with decreasing temperature for the TiH_x system since the critical temperature is near 310 K while there will be only very minor variations in the ZrH_x c/a ratio,which has already become nearly temperature independent (37,48) at these temperatures and compositions. Since the $N_d(E_F)$ decrease is predicted (1,4,7) to be proportional to the c/a ratio through the Jahn-Teller effect, the $N_d(E_F)$ in TiH_x will change rapidly (25,26) below 310 K but will be nearly constant for ε-ZrH_x when $x \geqslant 1.95$. $(T_{1e}T)^{-\frac{1}{2}}$ in TiH_x system has only a positive temperature dependence, but a negative temperature dependence is observed for ZrH_x samples with $1.77 \leqslant x \leqslant 1.85$, which was related in the last section to E_F moving through a local maximum in the density of states with changes in hydrogen content. Although the $(T_{1e}T)^{-\frac{1}{2}}$ data in Fig. 10 suggests a peak in $N(E_F)$ may occur near $x \approx 1.75$ in TiH_x, it is clearly not of the same character as has been suggested for the N(E) peak in the ZrH_x system. The Jahn-Teller distortion will definitely reduce $N(E_F)$ in TiH_x by a broadening of the sharp peak (7,9) at E_F, but the resulting splittings of the energy levels for the observed (48) 5% (or less) tetragonal distortion in TiH_x apparently cannot generate the resolved peaks proposed in Fig. 9b for ε-ZrH_x (where the tetragonal distortion exceeds 9% when $x \geqslant 1.75$). Hence, a continual $N(E_F)$ decrease is observed (25,26) in TiH_x as the temperature is lowered and the tetragonal distortion presumably becomes larger. Whether this mechanism is also valid for TiH_x with $1.6 \leqslant x \leqslant 1.8$ will require further proton σ_K and T_1 measurements on additional samples as well as possible low-temperature x-ray diffraction measurements of the lattice parameters. However, the widely split N(E) peaks in Fig. 9b are quite consistent with the behavior of the proton $(T_{1e}T)^{-\frac{1}{2}}$ and σ_K in Fig. 8 as well as the other available experimental results (11,16,22,24) for ZrH_x. Band theory calculations of the electronic structure of tetragonal (i.e., $c/a \approx 0.90$) $ZrH_{2.0}$ should provide a more

quantitative verification of the split band model represented in Fig. 9b. Extensions of the existing calculations (1-9) to nonstoichiometric fcc and fct TiH_x and ZrH_x systems would be extremely helpful.

VI. CONCLUSIONS

Measurements of the proton spin-lattice relaxation times and Knight shifts in ZrH_x have indicated the dominance of a transferred core-polarization hyperfine interaction from the Zr d-band to the s-band at the hydrogen sites, which is completely analogous to the hyperfine interactions for protons in TiH_x (25,26) and related ternary hydrides (17,25). The ZrH_x band structure in the d-band region is significantly modified by the Jahn-Teller fct distortion when the hydrogen content exceeds $x = 1.75$. The predicted sharp peak at the Fermi level in fcc $ZrH_{2.0}$ is split into a resolved doublet in ε-ZrH_x with reduced densities of electron states as shown in Fig. 9. The composition and temperature dependences of the proton parameters $(T_{1e}T)^{-\frac{1}{2}}$ and σ_K indicate E_F will lie at different positions of the lower energy peak as the hydrogen content in ε-ZrH_x is varied. Photoelectron spectra (22) and other experimental results (11,24) are consistent with this model.

ACKNOWLEDGEMENTS

The support and advice of Dr. S. I. Chan is greatly appreciated. We thank Dr. W.-K. Rhim for providing the NMR spectrometer used to measure the Knight shifts. We also thank Dr. P. Richards for his helpful comments and suggestions. This work was supported by the Caltech President's Fund and Office of Basic Energy Sciences, Division of Chemical Sciences, U. S. Department of Energy. Mound is operated by Monsanto Research Corporation for the U. S. Department of Energy under Contract No. DE-AC04-76-DP00053. Sandia National Laboratories are supported by the U. S. Department of Energy under Contract No. DE-AC04-76-DP00789. This is Caltech Contribution #6685.

1. A. C. Switendick, J. Less-Common Met. 49, 283 (1976).
2. A. C. Switendick, in Transition Metal Hydrides-Advances in Chemistry Series 167, R. Bau, Ed. (American Chem. Soc., Washington, DC, 1978) p. 264.
3. N. I. Kulikov, V. N. Borzunov, and A. D. Zvonkov, phys. stat. sol. (b) 86, 83 (1978).
4. N. I. Kulikov and V. N. Borzunov, Inorg. Mater. (USSR) 14, 1292 (1978).
5. V. I. Savin, R. A. Andrievskii, V. I. Potorocha, and V. Ya. Markin, Inorg. Mater. (USSR) 14, 1254 (1978).
6. M. I. Darby, M. N. Read, and K. N. R. Taylor, phys. stat. sol. (b) 102, 413 (1980).
7. M. Gupta, Solid State Commun. 29, 47 (1979).
8. M. Gupta and J. P. Burger, Phys. Rev. B 24, 7099 (1981).
9. A. Fujimori and N. Tsuda, Solid State Commun. 41, 491 (1982).
10. R. C. Frisch and R. A. Forman, J. Chem. Phys. 48, 5187 (1968).
11. F. Ducastelle, R. Caudron, and P. Costa, J. de Physique 31, 57 (1970).
12. E. F. Khodosov and N. A. Shepilov, phys. stat. sol. (6) 49, K83 (1972); E. F. Khodosov and N. A. Shepilov, Sovt. Phys.-Solid State 14, 807 (1972).
13. V. F. Nemchenko and V. G. Charnetskii, Inorg. Mater. (USSR) 10, 392 (1974).
14. B. Nowak, N. Pišlewski, and W. Leszczyński, phys. stat. sol. (a) 37, 669 (1976).
15. C. Korn, Phys. Rev. B 17, 1707 (1978).
16. C. Korn, in Hydrides for Energy Storage, A. F. Andresen and A. J. Maeland, Eds. (Pergamon, Oxford, 1978) p. 119.
17. B. Nowak, O. J. Żogal, and M. Minier, J. Phys. C: Solid State Phys. 12, 4591 (1979).
18. B. W. Veal, D. J. Lam, and D. G. Westlake, Phys. Rev. B 19, 2856 (1979).

19. K. Tanada, N. Hamasaka, M. Yasuda, and Y. Fukai, Solid State Commun. 30, 173 (1979).

20. K. R. Doolan, P. P. Narang, and J. M. Pope, J. Phys. F: Metal Phys. 10, 2073 (1980).

21. J. M. Pope, P. P. Narang, and K. R. Doolan, J. Phys. Chem. Solids 42, 519 (1981).

22. J. H. Weaver, D. J. Peterman, D. T. Peterson, and A. Franciosi, Phys. Rev. B 23, 1692 (1981).

23. V. V. Nemoshkalendo, M. M. Kindrat, V. P. Krivitskii, B. P. Mamko, and A. I. Kharlamov, Inorg. Mater. (USSR) 17, 699 (1981).

24. E. L. Venturini, Bull. Am. Phys. Soc. 26, 337 (1981); *and to be* published.

25. R. C. Bowman, Jr., and W.-K. Rhim, Phys. Rev. B 24, 2232 (1981).

26. R. Göring, R. Lukas, and K. Bohmhammel, J. Phys. C: Solid State Phys. 14, 5675 (1981).

27. H. A. Jahn and E. Teller, Proc. Roy. Soc. (London) A161, 220 (1937).

28. A. C. Switendick, in Hydrogen in Metals I: Basic Properties, G. Alefeld and J. Völkl, Eds. (Springer-Verlag, Berlin, 1978) p. 101.

29. A. C. Switendick, Zeit. Physk. Chem. N. F. 117, 89 (1979).

30. H. Nagel and H. Goretzki, J. Phys. Chem. Solids 36, 431 (1975).

31. H. Nagel and R. S. Perkins, Z. Metallkde. 66, 362 (1975).

32. B. Stalinski and B. Nowak, Bull. Acad. Polon. Sci., Ser. Sci. Chim. 25, 65 (1977).

33. A. Narath, in Hyperfine Interactions, A. J. Freeman and R. B. Frankel, Eds. (Academic, New York, 1967) p. 287.

34. J. Winter, Magnetic Resonance in Metals (Clarendon, Oxford, 1971).

35. G. C. Carter, L. H. Bennett, and D. J. Kahan, Metallic Shifts in NMR (Pergamon, Oxford, 1977).

36. R. M. Cotts, in Hydrogen in Metals I: Basic Properties, G. Alefeld and J. Völkl, Eds. (Springer-Verlag, Berlin, 1978) p. 227.

37. R. L. Beck and W. M. Mueller, in Metal Hydrides, W. M. Mueller, J. P. Blackledge, and G. G. Libowitz, Eds. (Academic, New York 1968) p. 241.

38. P. W. Bickel and T. G. Berlincourt, Phys. Rev. B 2, 4807 (1970).

39. K.G. Barraclough and C. J. Beevers, J. Nucl. Mater. 34, 125 (1970).

40. S. Mishra, K. S. Sivaramakrishnan, and M. K. Asundi, J. Nucl. Mater. 45, 235 (1972/73).

41. K. G. Barraclough and C. J. Beevers, J. Less-Common Met. 35, 177 (1974).

42. S. S. Sidhu, N. S. Satya Murthy, F. P. Campos, and D. D. Zauberis, in Nonstoichiometric Compounds-Adv. Chem. Series 39, R. Ward, Ed. (Am. Chem. Soc., Washington, DC, 1963) p. 87.

43. L. S. Topchyan, I. A. Naskidashvili, R. A. Andrievskii, and V. I. Savin, Sov. Phys. Solid State 15, 1461 (1974).

44. I. A. Naskidashvili and Yu. G. Sharimanov, N. Vilcu, D. Demco, and V. Simplaceanu, Sov. Phys. Solid State 19, 2026 (1977).

45. I. N. Bydlinskaya, I. A. Naskidashvili, V. A. Melik-Shakhnazarov, and V. I. Savin, Sov. Phys. Solid State 22, 517 (1980).

46. V. F. Petrunin, V. P. Glazkov, V. I. Savin, V. A. Somenko, V. K. Fedotov, S. Sh. Shil'shteyn, and S. V. Marchenko, Phys. Met. Metall. 46, 181 (1979).

47. R. C. Bowman, Jr., E. L. Venturini, and W.-K. Rhim, submitted to Phys. Rev. B.

48. H. L. Yakel, Jr., Acta Cryst. 11, 46 (1958).

49. W. L. Korst, X-ray Studies of δ and ε Zriconium Hydrides, USAEC Report NAA-SR-6880, Atomic International, March 30, 1962 (unpublished).

50. MARZ-grade (i.e., stated purity of 99.99%) from Materials Research Corporation, Orangeburg, New York, 10962. Independent emission spectroscopy analysis at Mound has verified vendor claim of 20 ppm Fe and the absence of any detectable amount of other magnetic elements (e.g., Ni, Co, Mn, etc.).

51. D. P. Burum, D. D. Elleman, and W.-K. Rhim, J. Chem. Phys. 68, 1164 (1978).

52. P. Brill and J. Voitländer, Ber. Bunsen. Physk. Chem. 77, 1097 (1973).

53. S. Kazama and Y. Fukai, J. Less-Common Met. 53, 25 (1977).

54. R. E. Taylor, T. Taki, and B. C. Gerstein, Phys. Rev. B 23, 5729 (1981).

55. J. Mason, J. Chem. Soc. Dalton, 1422 (1975).

56. A. T. Nicol and R. W. Vaughan, J. Chem. Phys. 69, 5211 (1978).

57. K. Terakura and J. Kanamori, J. Phys. Soc. Japan 34, 1520 (1973).

58. N. Yokoyama, Y. Yamada, S. Kohzuki, and K. Asayama, J. Phys. Soc. Japan. 37, 73 (1974).

59. A. V. Skripov and A. P. Stepanov, Sov. Phys. Solid State 23, 560 (1981).

60. J. Kanamori, H. K. Yoshida, and K. Terakura, Hyperfine Interactions 9, 363 (1981).

61. B. Stalinski, C. K. Coogan, and H. S. Gutowsky, J. Chem. Phys. 34, 1191 (1961).

62. J. Korringa, Physica 16, 601 (1950).

63. Y. Yafet and V. Jaccarino, Phys. Rev. 133, A1630 (1964).

TABLE I. Korringa Parameters and slopes for temperature dependences of σ_K and $(T_{1e}T)^{-1}$ for ZrH_x Samples

Sample	$\frac{c}{a}$ Ratio	q_{exp} 300 K	q_{exp} 170 K	Slope σ_K ppm/deg	Slope $(T_{1e}T)^{-\frac{1}{2}}$ 10^{-4} s^{-1} K^{-1} /deg
δ-$ZrH_{1.60}$	1.000	1.73	1.47	~0	+0.022
ε-$ZrH_{1.75}$	0.913	---	---	---	+0.017
ε-$ZrH_{1.80}$	0.908	0.46	0.38	-0.053	-0.029
ε-$ZrH_{1.85}$	0.902	---	---	---	-0.047
ε-$ZrH_{1.90}$	0.895	0.43	0.35	-0.031	+0.010
ε-$ZrH_{1.95}$	0.893	---	---	---	+0.008
ε-$ZrH_{2.00}$	0.890	0.37	0.37	~0	+0.003

TABLE II. The partial-wave analysis n_ℓ of the density of electron states inside the muffin-tin metal and hydrogen spheres at the Fermi energy from APW calculations of Gupta and Burger (Ref. 8). $N_\uparrow(E_F)$ is the total density of states at E_F for one spin direction.

Sample	Site	n_s	n_p	n_d	n_f	$N_\uparrow(E_F)$
TiH_2	Ti	0.0015	0.0590	18.741	0.035	23.519
	1xH	0.015	0.8755	0.0535	0.0015	
ZrH_2	Zr	0.004	0.073	10.805	0.035	16.460
	1xH	0.008	0.432	0.021	0.001	

FIGURE CAPTIONS

FIG. 1. The total density of states (DOS) of fcc ZrH_2 as calculated by Gupta and Burger. DOS given by full line curve and left-hand-side scale with units of states of both spin per rydberg unit cell. The number of valence electrons given by dashed line and right-hand-side scale.

FIG. 2. Room temperature lattice parameters for high purity ZrH_x where phase boundaries are based upon several literature sources (i.e., Refs. 24, 39-42, 49).

FIG. 3. Temperature dependence of proton spin-lattice relaxation times for some ZrH_x samples. The curves through data points are merely visual aids.

FIG. 4. Temperature dependence of proton spin-lattice relaxation times for more ZrH_x samples. The curves are merely visual aids.

FIG. 5. Proton Knight shifts for polycrystalline ZrH_x measured using the multiple pulse zero-crossing technique of Ref. 51 at a resonance frequency of 56.4 MHz and referenced to an external standard of TMS.

FIG. 6. Temperature dependence of proton $(T_{1e}T)^{-½}$ for the ZrH_x samples given in Fig. 3. The straight lines are linear least square fits to the data.

FIG. 7. Temperature dependence of proton $(T_{1e}T)^{-½}$ for the ZrH_x samples given in Fig. 4. The straight lines are linear least square fits to the data.

FIG. 8. Composition dependence of proton $(T_{1e}T)^{-½}$ and σ_K parameters for various temperatures.

FIG. 9. Schematic densities of states of d bands for fcc (Part A) and fct (Part B) ZrH_x. Solid vertical lines are locations of E_F from proton $(T_{1e}T)^{-½}$ parameters while dashed vertical line in Part A is predicted (Ref. 8) E_F position for fcc ZrH_2. $\Delta E(c/a)$ is energy difference between N(E) maxima.

FIG. 10. Composition dependence of proton $(T_{1e}T)^{-\frac{1}{2}}$ for TiH_x (after Goring, et al, in Ref. 26) and ZrH_x (present study).

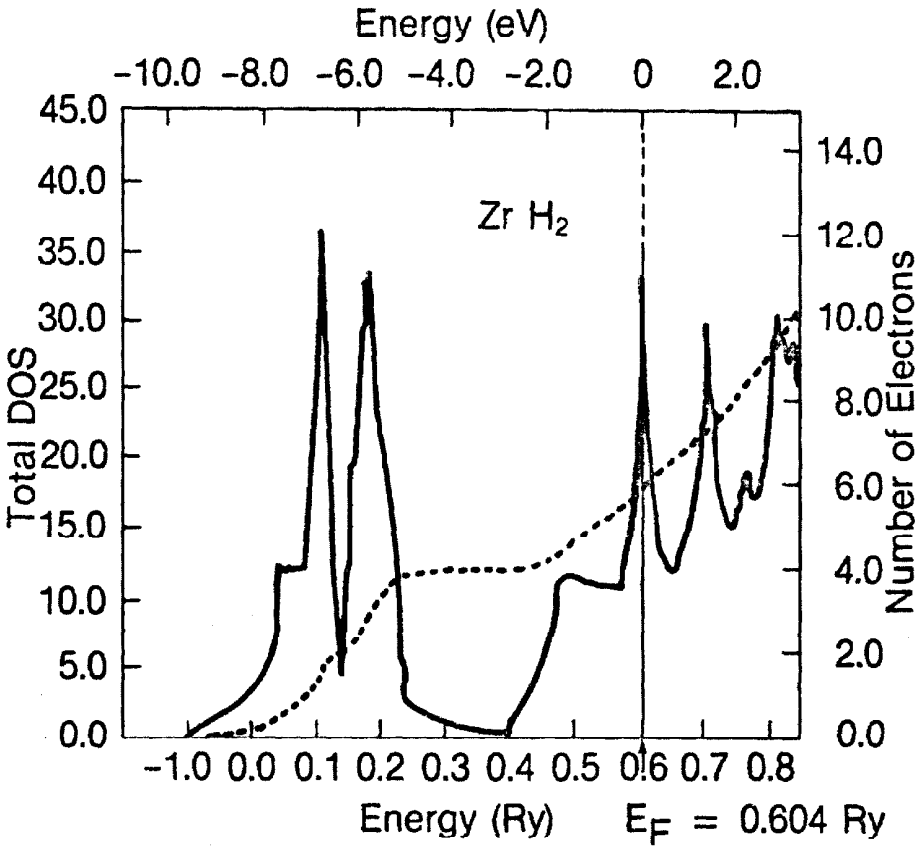
Energy (eV)
-10.0 -8.0 -6.0 -4.0 -2.0 0 2.0
45.0
40.0
35.0
30.0
25.0
20.0
15.0
10.0
5.0
0.0
Total DOS
Zr H2
14.0
12.0
10.0
8.0
6.0
4.0
2.0
0.0
Number of Electrons
-1.0 0.0 0.1 0.2 0.3 0.4 0.5 0.6 0.7 0.8
Energy (Ry)
EF = 0.604 Ry

FIGURE 1

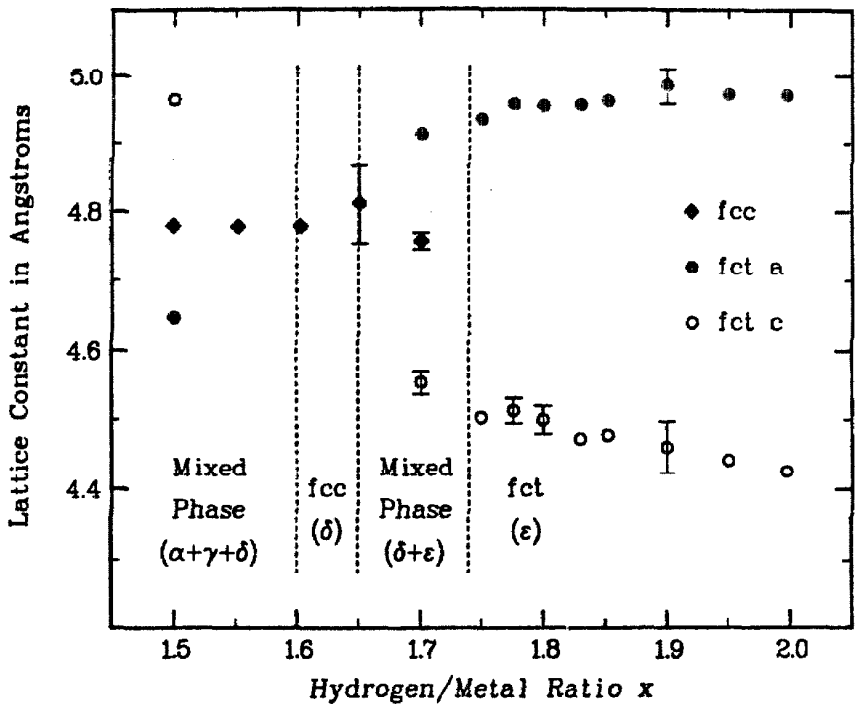
Lattice Constant in Angstroms
5.0
4.8
4.6
4.4
1.5
1.6
1.7
1.8
1.9
2.0
Hydrogen/Metal Ratio x
Mixed Phase (α+γ+δ)
fcc (δ)
Mixed Phase (δ+ε)
fct (ε)
fcc
fct a
fct c

FIGURE 2

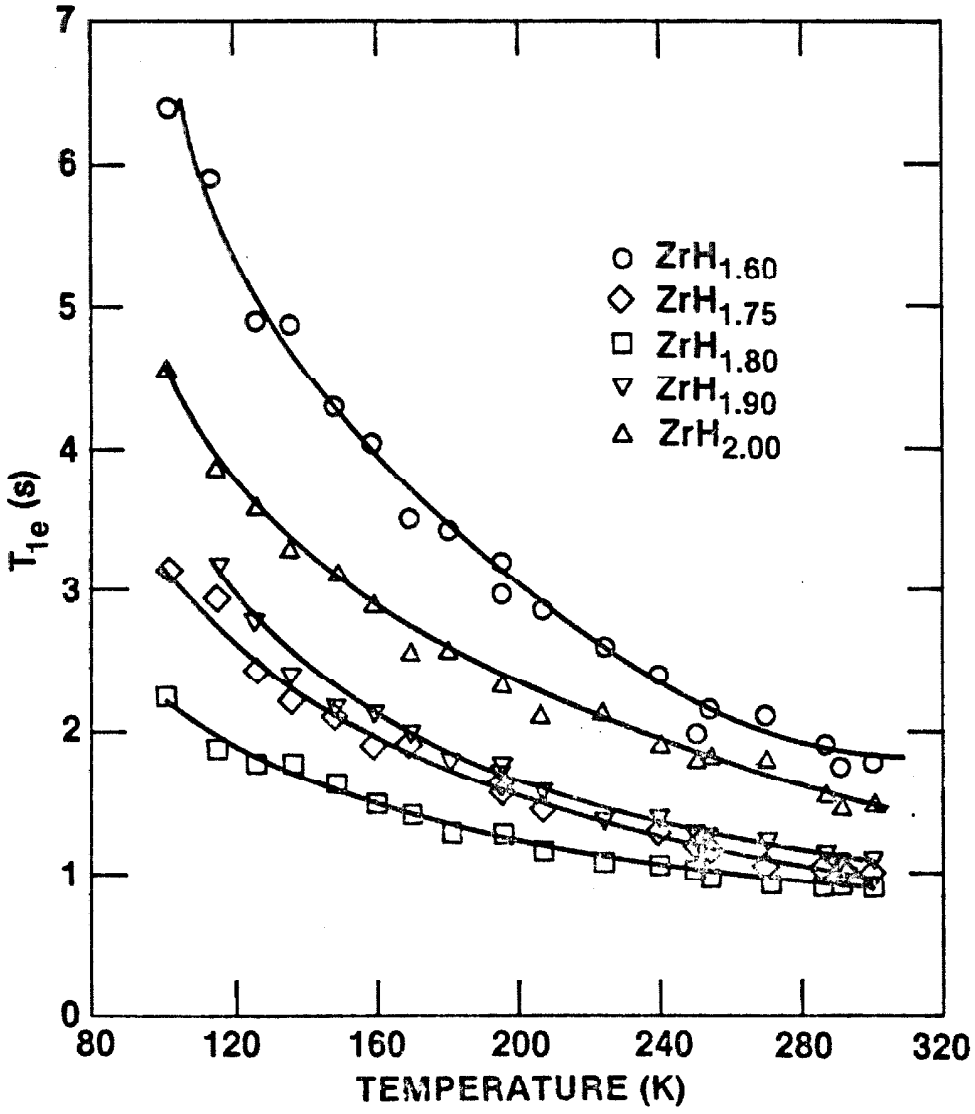
7
6
5
4
3
2
1
0
T_{1e} (s)
80
120
160
200
240
280
320
TEMPERATURE (K)
$ZrH_{1.60}$
$ZrH_{1.75}$
$ZrH_{1.80}$
$ZrH_{1.90}$
$ZrH_{2.00}$

FIGURE 3

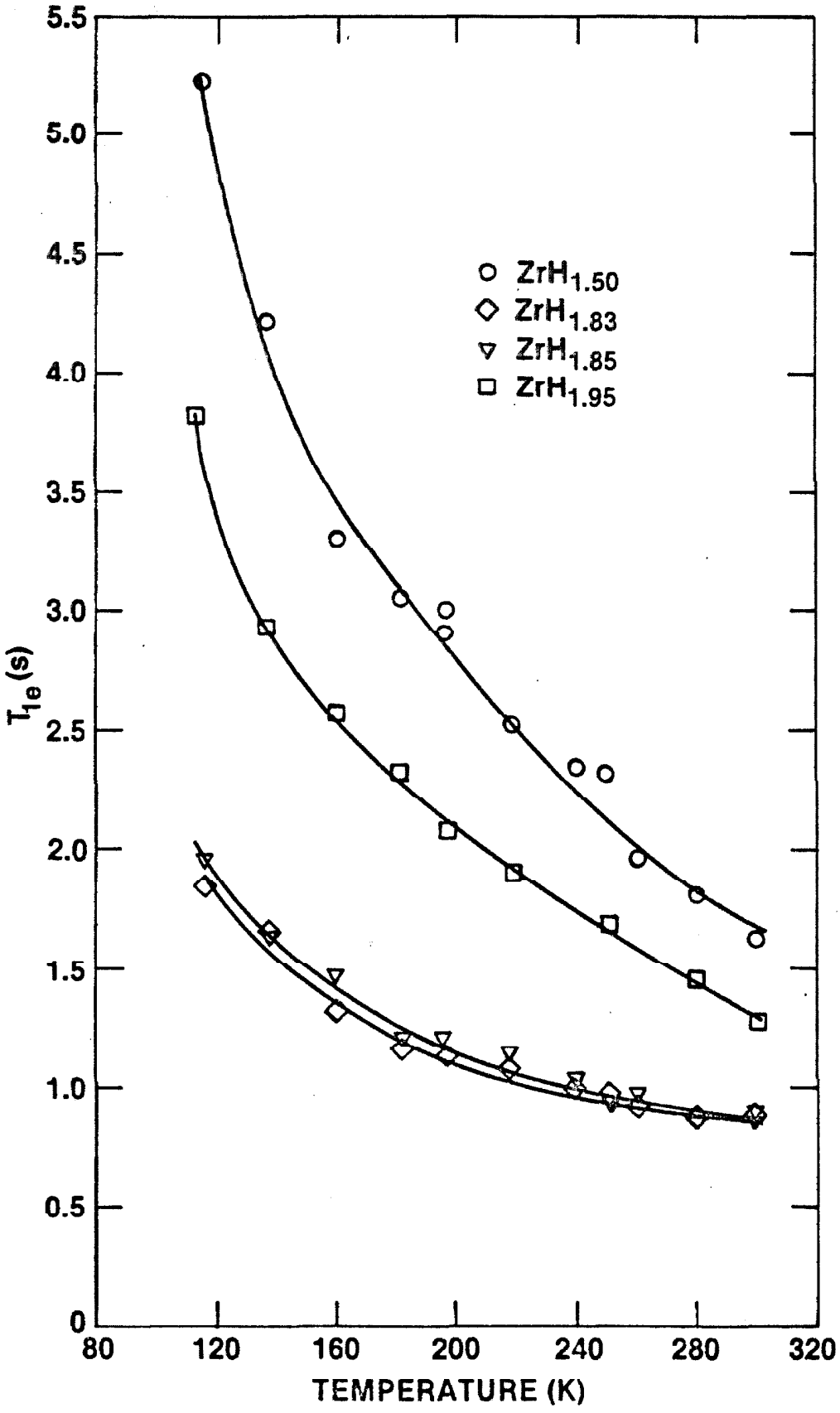
5.5
5.0
4.5
4.0
3.5
3.0
2.5
2.0
1.5
1.0
0.5
0
T_{1e} (s)
80
120
160
200
240
280
320
TEMPERATURE (K)
$ZrH_{1.50}$
$ZrH_{1.83}$
$ZrH_{1.85}$
$ZrH_{1.95}$

FIGURE 4

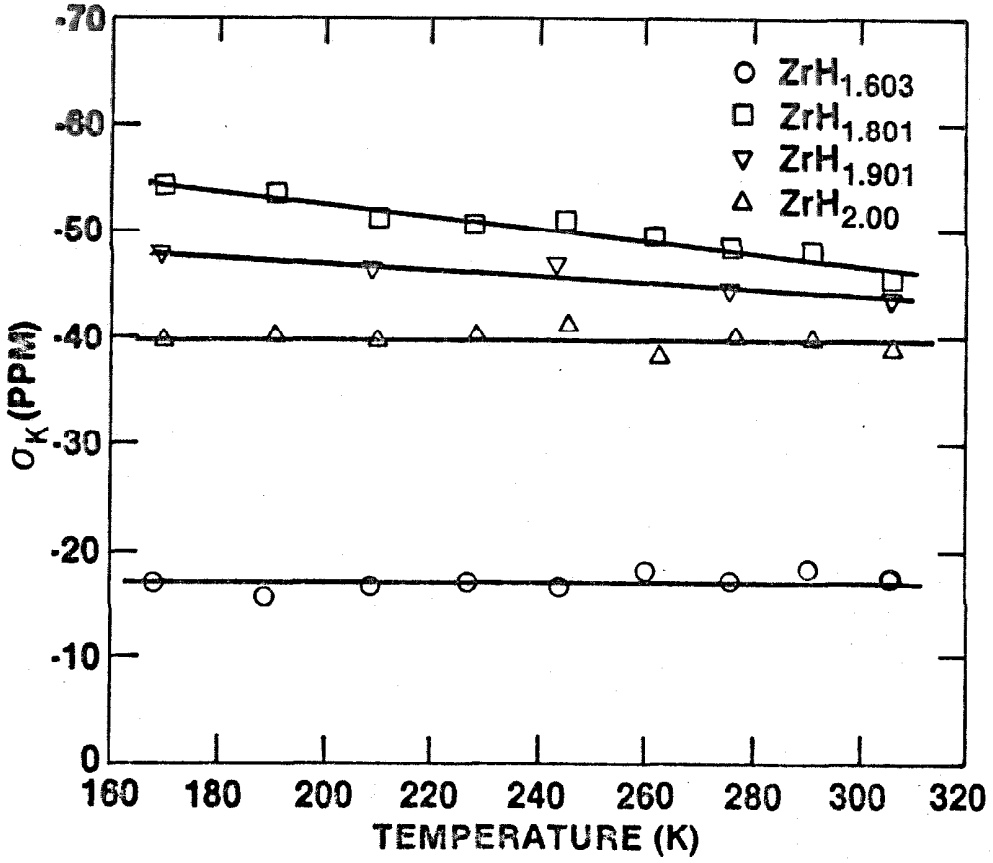
-70
-60
-50
-40
-30
-20
-10
0
σ_K(PPM)
160
180
200
220
240
260
280
300
320
TEMPERATURE (K)
$ZrH_{1.603}$
$ZrH_{1.801}$
$ZrH_{1.901}$
$ZrH_{2.00}$

FIGURE 5

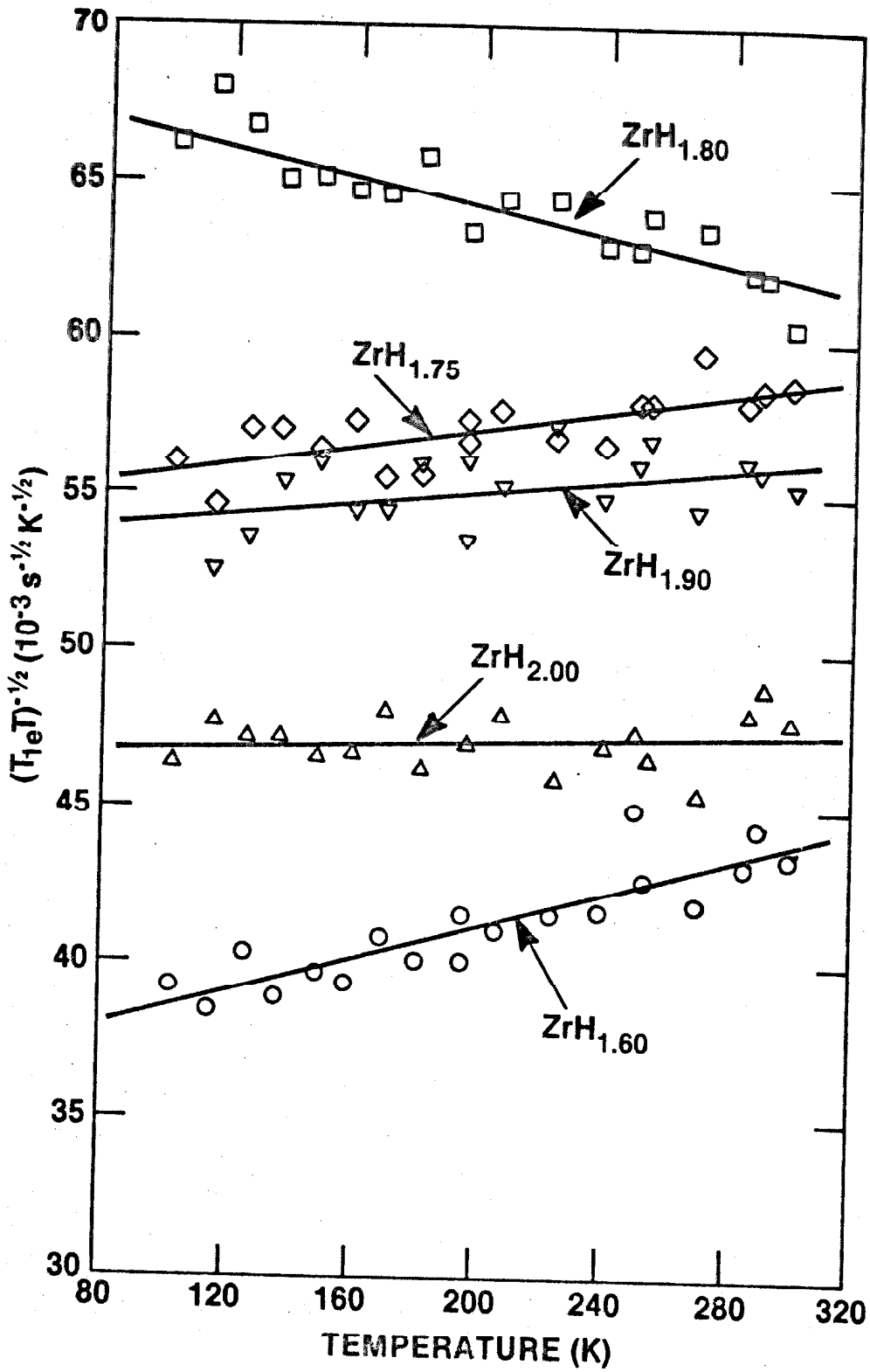
70
65
60
55
50
45
40
35
30
80
120
160
200
240
280
320
TEMPERATURE (K)
$(T_{1e}T)^{-1/2}$ (10^{-3} $s^{-1/2}$ $K^{-1/2}$)
$ZrH_{1.80}$
$ZrH_{1.75}$
$ZrH_{1.90}$
$ZrH_{2.00}$
$ZrH_{1.60}$

FIGURE 6

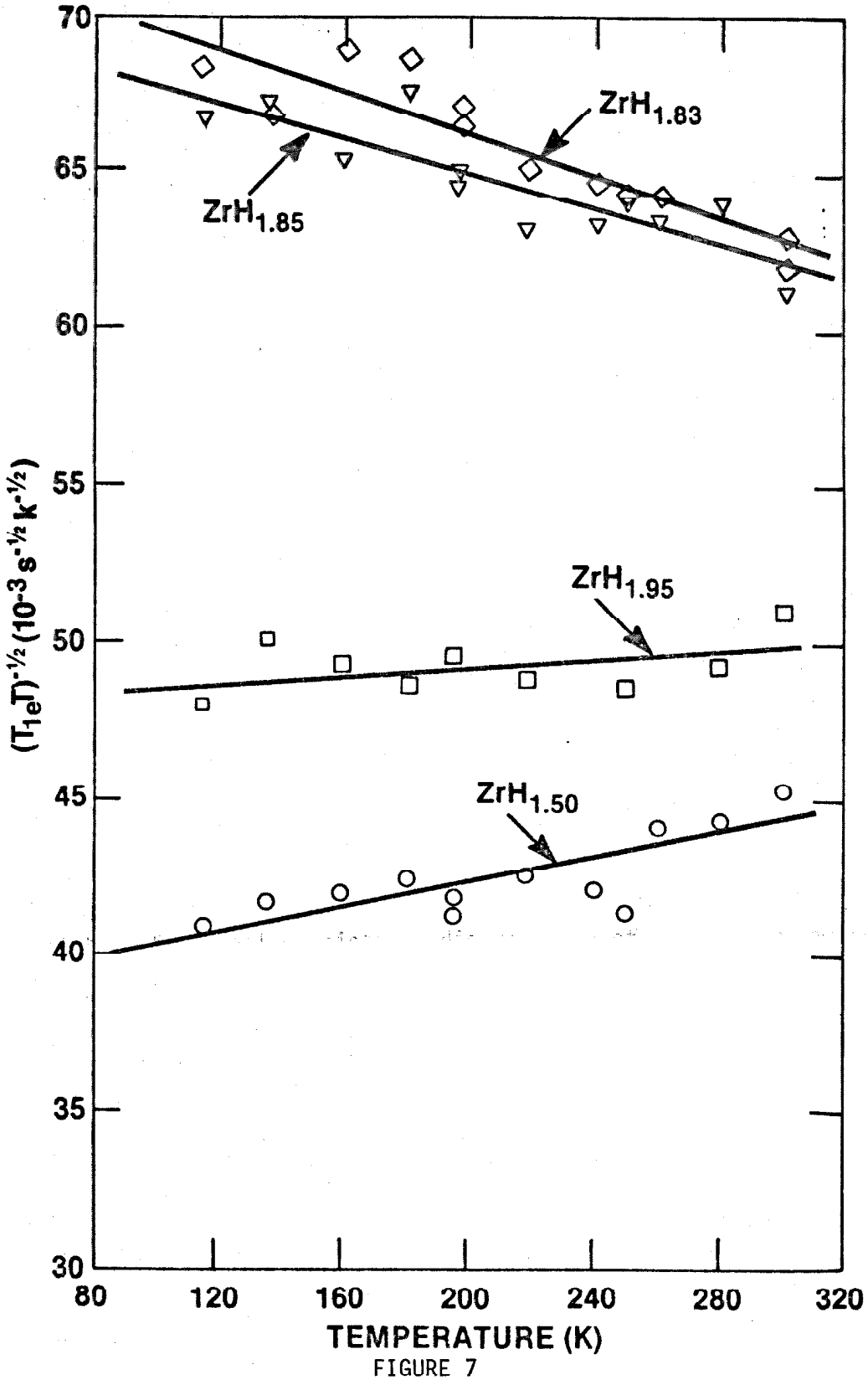
70
65
60
55
50
45
40
35
30
80
120
160
200
240
280
320
$(T_{1e}T)^{-1/2}$ $(10^{-3}\ s^{-1/2}\ K^{-1/2})$
TEMPERATURE (K)
$ZrH_{1.83}$
$ZrH_{1.85}$
$ZrH_{1.95}$
$ZrH_{1.50}$

FIGURE 7

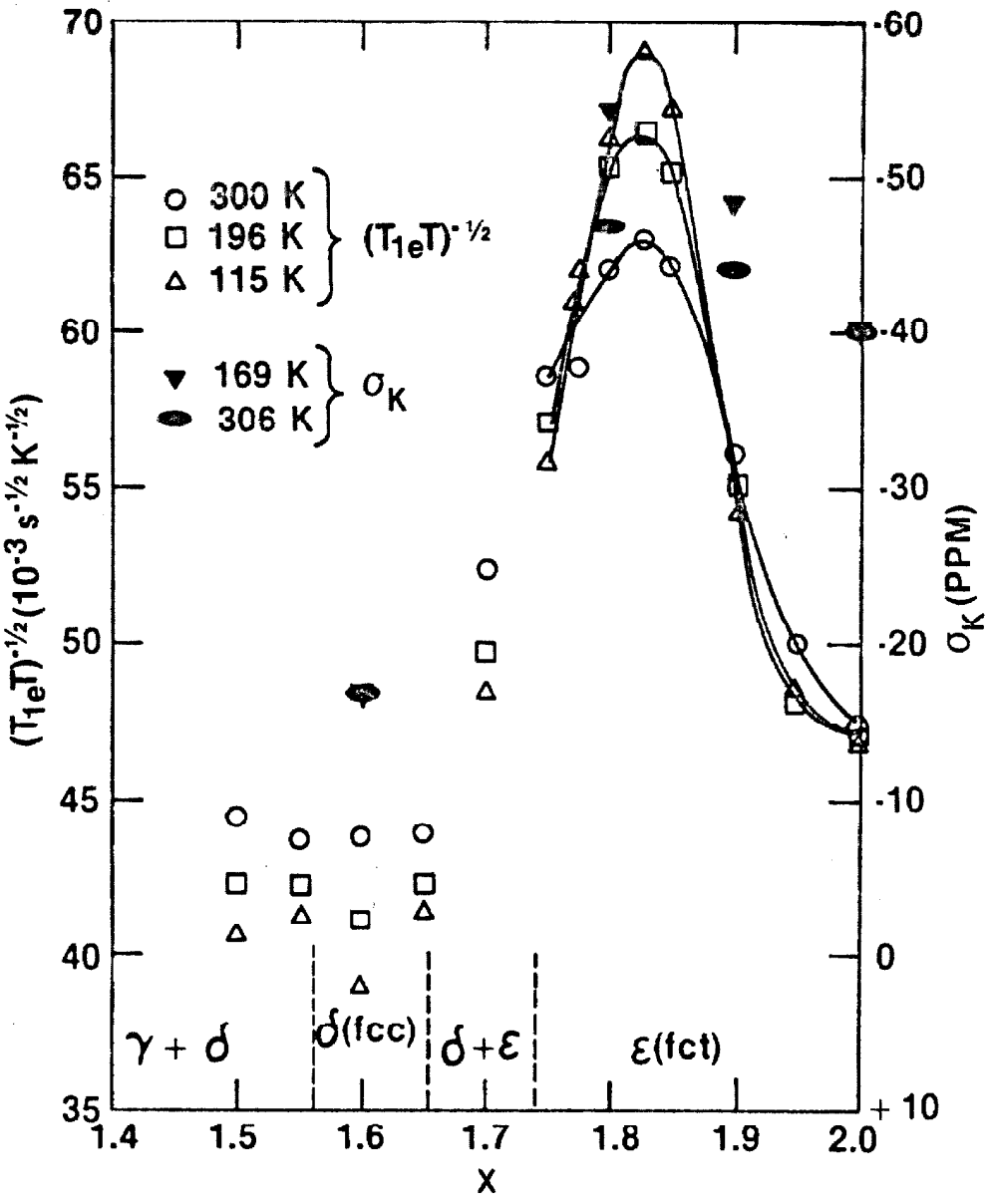
70
65
60
55
50
45
40
35
1.4
1.5
1.6
1.7
1.8
1.9
2.0
X
-60
-50
-40
-30
-20
-10
0
+10
$(T_{1e}T)^{-1/2}(10^{-3}\ s^{-1/2}\ K^{-1/2})$
σ_K(PPM)
300 K
196 K
115 K
$(T_{1e}T)^{-1/2}$
169 K
306 K
σ_K
γ + δ
δ(fcc)
δ+ε
ε(fct)

FIGURE 8

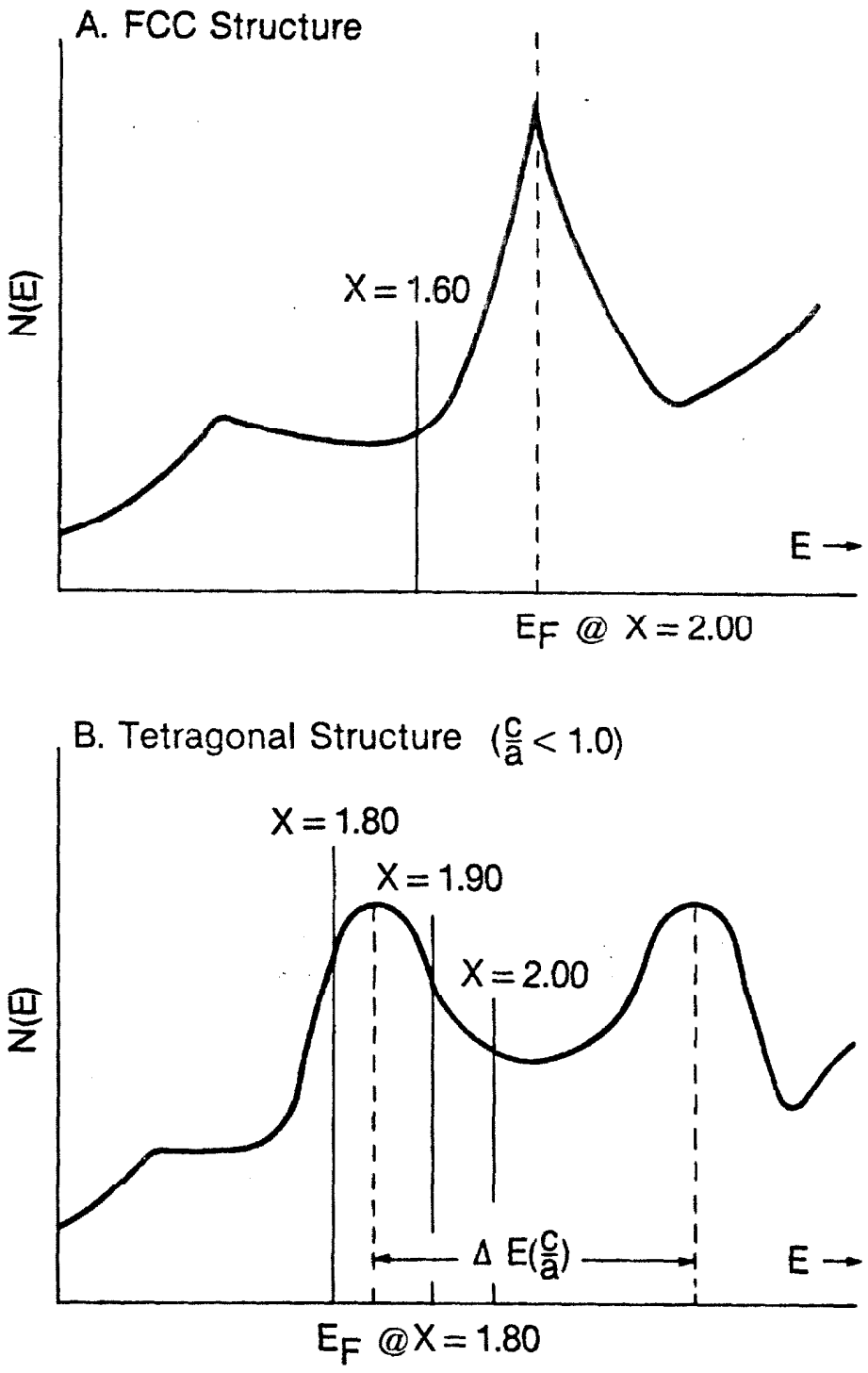
A. FCC Structure
N(E)
X = 1.60
E →
E_F @ X = 2.00
B. Tetragonal Structure ($\frac{c}{a} < 1.0$)
X = 1.80
X = 1.90
X = 2.00
N(E)
Δ E($\frac{c}{a}$)
E →
E_F @X = 1.80

FIGURE 9

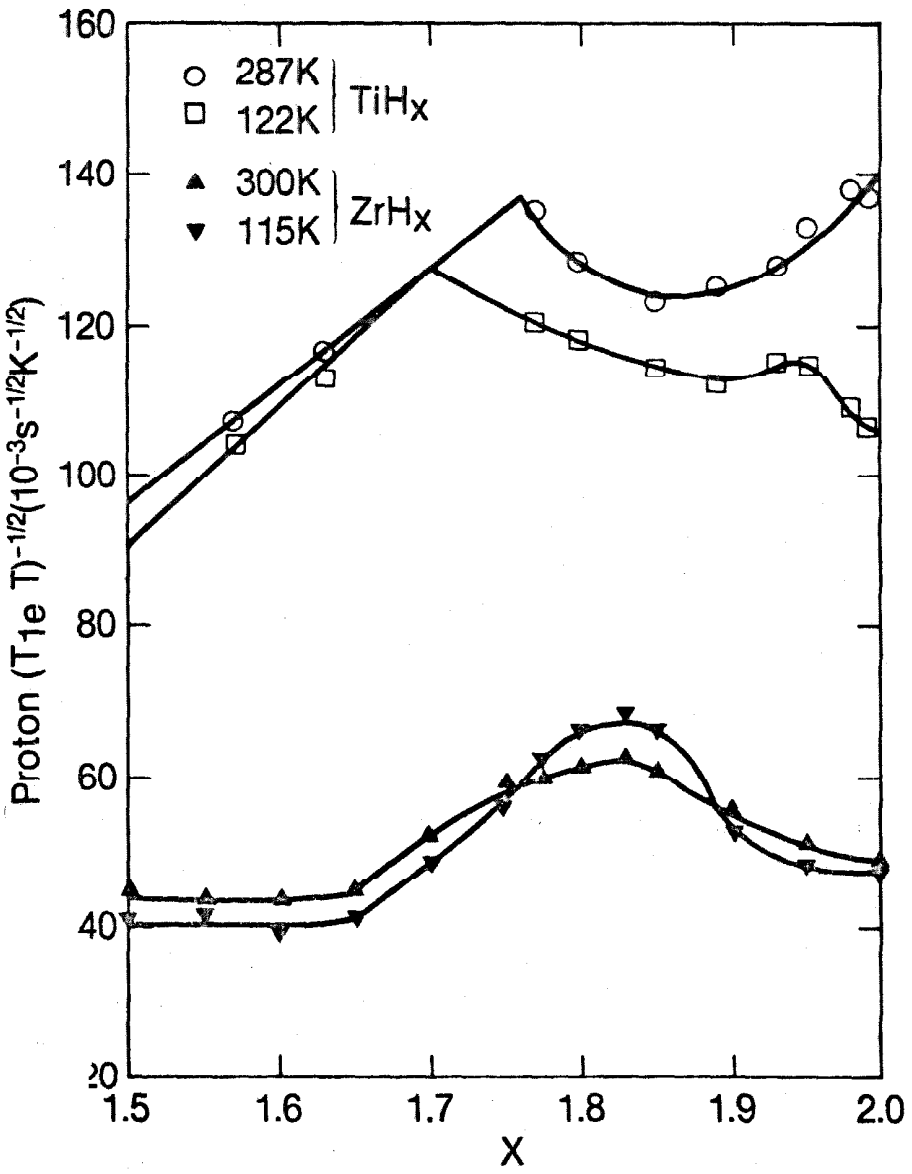
160
140
120
100
80
60
40
20
1.5
1.6
1.7
1.8
1.9
2.0
X
Proton $(T_{1e}\ T)^{-1/2}(10^{-3}s^{-1/2}K^{-1/2})$
287K
122K
TiHx
300K
115K
ZrHx

FIGURE 10

CHAPTER 7

PROTON NMR AND MAGNETIC SUSCEPTIBILITY STUDY OF $TiCr_{1.8}H_x$

[This chapter is a slightly expanded version of an article with the same title by R. C. Bowman, Jr., J. F. Lynch, and J. R. Johnson, that is submitted to Materials Letters.]

ABSTRACT

The electronic properties of the hexagonal (C-14) and cubic (C-15) allotropes of the nominal $TiCr_2$-hydrogen system have been examined via magnetic susceptibility and proton NMR measurements. Both methods indicate an unusual increase in $N(E_F)$, the electron density of states at the Fermi level, with increasing H/M for both allotropes; the trend extends into the α'-hydride phase. Although negative proton Knight shifts indicate the $N(E_F)$ increase is primarily due to d-electron states, a high concentration of s-electron states at E_F is also present. The results suggest a possible basis for thermodynamic anomalies reported for the solution of hydrogen in $TiCr_{1.8}$.

I. INTRODUCTION

Titanium and chromium form two intermetallic Laves phase intermetallic compounds at the composition $TiCr_{1.8\pm0.1}$, a high temperature hexagonal (C-14) phase and a low temperature cubic (C-15) phase. Both allotropes exothermically absorb hydrogen to form very unstable hydrides (1-3). The thermodynamic behavior of the solid solution of hydrogen in $TiCr_{1.8\pm0.1}$ (i.e., the α-phase) exhibits several unusual features (4) when compared to most other metal-hydrogen systems (5). The most striking of these is a pronounced positive deviation from Sieverts' law of ideal solubility, even as $H/TiCr_{1.8}$ approaches zero. This is a consequence of a decline (4) in exothermicity of absorption with increasing hydrogen content; as the H-content increases, the partial molar enthalpy of solution becomes less negative. This trend is opposite to that exhibited by most exothermic hydride forming systems (4-6).

The hydrogen absorption process requires insertion of a H-atom into an appropriate lattice interstitial site where the chemical potential of the hydrogen dissolved in the metal is given (5) by the expression

$$\mu_H = \mu_H^o + RT \ln\frac{n}{1-n} + \Delta\mu_H^+ + \Delta\mu_e^- . \qquad (1)$$

Here, μ_H^o is the standard potential, the second term is the configurational term for ideal statistical distribution of the H-atoms among the available interstitial sites with n being the occupancy factor, $\Delta\mu_H^+$ is the elastic term resulting from lattice dilation with hydrogen insertion into the interstitial sites, and $\Delta\mu_e^-$ is the excess potential contribution that results from the accommodation of the hydrogen electron by the metal conduction band which alters (5) the electronic screening of the proton by shifting the Fermi level. If the last two terms in eqn. (1) are neglected, the metal-hydrogen system behaves as an ideal solution and obeys Sieverts' law. The elastic term $\Delta\mu_H^+$ reflects (5) the attractive interactions between the H-atoms which cause the usual negative deviations from Sieverts' law. Although the electronic term $\Delta\mu_e^-$ is positive,

its contribution has often been found small for low hydrogen concentrations in the Pd alloys (5) and other systems (6) where $N(E_F)$, the density of electron states at the Fermi level E_F, is known (5,7) to decrease with hydrogen content. However, the electronic term $\Delta\mu_e$ has been associated with the positive deviations from Sieverts' law for Ti/Mo alloys (8) and TaV_2 with the C-15 Laves structure (9,10). Although the relationship between changes in $N(E_F)$ and the thermodynamic behavior has not been definitively established, apparent correlations seem to be indicated in several diverse transition metal alloys (5,8-10). The present study was undertaken to investigate the behavior of $N(E_F)$ in the C-14 and C-15 $TiCr_{1.8\pm0.1}H_x$ phases in order to see if the electronic term could be responsible for the unusual thermodynamic behavior of the $TiCr_{1.8}/H_2$ system.

There are several experimental methods that can provide information on the $N(E_F)$ values. Magnetic susceptibility (χ) has been widely used for transition metal hydrides (11,12), but great caution must be exercised when estimating the $N(E_F)$ values from χ data since several other significant contributions (12) are usually present. Nuclear magnetic resonance (NMR) spectroscopy is sensitive (13) to the electronic structure of a metal through Knight shifts (σ_K) of the resonance frequency and conduction electron contributions to the spin-lattice relaxation times (T_{1e}). NMR methods have also been widely used (14) to study the electronic structures in several metal-hydrogen systems and rather detailed analyses of $N(E_F)$ values for several titanium binary and ternary hydride phases were recently reported (15-18). The present measurements of the magnetic susceptibilities, proton Knight shifts, and proton spin-lattice relaxation times indicate a significant increase in $N(E_F)$ for both C-15 and C-14 $TiCr_{1.8}H_x$ with increasing hydrogen content. This trend is the reverse of most metal-hydrogen systems (5,7,10-12) where $N(E_F)$ decreases with hydride formation.

II. EXPERIMENTAL DETAILS

Most of the experimental procedures employed to prepare the samples for the present studies have been described in detail elsewhere (1-3). Thus, details concerning preparation of the starting intermetallics with C-15 and C-14 structures, activation, hydrogen charging, and poisoning techniques (1-3) that inhibit the loss of hydrogen from the unstable hydrides will not be reiterated here, except to note that the poisoning was accomplished by cooling appropriately charged samples to -196°C before exposure to CO and slowly warming to room temperature under a high pressure CO atmosphere. Several CO poisoned $TiCr_{1.8\pm0.1}H_x$ samples were sealed into evacuated glass tubes for the NMR studies.

The Faraday-type susceptibility apparatus at Brookhaven has been previously described (19). The measurements were made at fields from 2500 Oe to 8650 Oe and for temperatures between 78 K and 298 K. The χ_o values were obtained from extrapolations (10) to infinite magnetic fields to remove the small ferromagnetic contributions.

The proton Knight shifts were measured at 56.4 MHz with the multiple-pulse zero-crossing technique devised by Burum, et al (20) while the T_1 values at 56.4 MHz and 34.5 MHz were obtained with the standard inversion-recovery method. Wide-band transient spectrometers (17,20,21) were used for these measurements. The σ_K values are relative to an external reference of tetramethylsilane and have not been corrected for any demagnetization effects (14,17) arising from the bulk susceptibilities. The sample temperatures during the NMR measurements were regulated within ± 2 K down to 80 K with a thermocouple controlled nitrogen gas-flow and heater system. To prevent accidental decomposition the NMR samples were never heated above 300 K. The reported compositions of the $TiCr_{1.8}H_x$ and $TiCr_{1.9}H_x$ samples were determined by vacuum outgassing after completion of the NMR experiments.

III. RESULTS

Typical magnetic susceptibility data exhibited by several hydrogen-free $TiCr_{1.9}$ specimens are summarized in Table I along with their room

temperature lattice parameters. Both nominal $TiCr_2$ allotropes are Pauli paramagnets with nearly identical susceptibilities, regardless of crystal structure or small variations in Cr content. It has not been possible to prepare single phase alloys with the stoichiometric composition $TiCr_{2.0}$. Only a slight increase in susceptibility was observed with increasing temperature as demonstrated by the single 80 K result included in Table I. Very similar temperature behavior was found for the hydrogen-containing samples indicating they are also Pauli paramagnets.

The variation of room temperature magnetic susceptibility with hydrogen content is displayed in Figure 1 for the C-15 and C-14 allotropes of $TiCr_{1.8}$. All of the χ_o data refer to the region of single phase solid solution (i.e., the α-phase) except for the result at H/Ti = 1.59, which is a two-phase ($\alpha+\alpha'$) specimen. The line drawn through the data points in Figure 1 is merely a visual aid and has no analytical significance; thus, the break suggested at H/Ti $\cong$ 0.8 is speculative. The χ_o data clearly indicate that magnetic susceptibility increases with increasing hydrogen content in the α-phase region of solid solution. Extrapolation from H/Ti $\cong$ 0.9 to higher hydrogen contents suggests $\chi_o = 5.6 \times 10^{-6}$ emu/g for the α'-phase hydride $TiCr_{1.8}H_{2.3}$, an increase of more than two-fold over the value exhibited by the hydrogen-free $TiCr_{1.8}$ alloy. There is no difference in the χ_o values for the C-15 and C-14 allotropes of $TiCr_{1.9}H_x$.

The proton σ_K and $(T_{1e}T)^{-½}$ parameters for $TiCr_{1.8}H_x$ with C-15 structure and $TiCr_{1.9}H_x$ with the C-14 structure are summarized in Figure 2. Because of the high hydrogen mobility in the α and α' $TiCr_{1.8}H_x$ phases (22), proton σ_K or T_1 data obtained above 120 K cannot be readily related to the electronic structure parameters without complications (14,20) from diffusion contributions to the proton relaxation times. Hence, only σ_K and T_1 data obtained at temperatures (T) between 80 K and 120 K have been included in Figure 1. The measured T_1 is assumed equal to T_{1e} for $T < 120$ K. Within experimental error the σ_K and $(T_{1e}T)^{-½}$ parameters increase linearly with hydrogen content in the α and α' phases and there is

essentially no difference between the C-15 and C-14 allotropes.

IV. DISCUSSION

The magnetic susceptibility of a metallic solid consists of several contributions

$$\chi = \chi_{ORB} + \chi_{DIA} + \chi_L + \chi_P \qquad (2)$$

where the orbital term χ_{ORB} (also widely known as the Van Vleck term) arises from the orbital angular momentum and is usually very large for most transition metal elements and their alloys. The diamagnetic term χ_{DIA} reflects contributions from the closed-shell ion cores and is usually quite small. The Landau term χ_L represents the diamagnetism of the conduction electrons and is generally considered to be given by $\chi_L \cong -\chi_P/3$ where χ_P is the Pauli paramagnetic susceptibility. χ_P depends directly on the $N(E_F)$ value and is given by

$$\chi_P = 2\mu_B^2 N(E_F)(1 + \lambda_\chi) \qquad (3)$$

where μ_B is the Bohr magneton and λ_χ represents enhancements of $N(E_F)$ from the simple noninteracting electron model due to various excitation processes (13). There have been numerous studies of magnetic susceptibility behavior in transition metal-hydrogen systems (5,10-12) and χ_o nearly always decreases with an increase in the H/M ratio to give χ_o (hydride) $< \chi_o$ (H-free metal). Indeed, the only exceptions to this trend among the transition metals are Ti and Cr which both exhibit (12) χ_o (hydride) $> \chi_o$ (H-free metal). The decline in χ_o with increasing H/M has often been interpreted (5,12) as reflecting a decrease in the density of states at E_F although only the Pauli term of eqn. (3) depends directly upon $N(E_F)$. Switendick (11) has cautioned against placing undue emphasis on χ data <u>alone</u> to deduce the $N(E_F)$ changes with alloying or variations in hydrogen content since the orbital contribution χ_{ORB}, which can be large, is

normally very difficult to reliably estimate without some supplemental data such as NMR measurements (13,14). With this reservation in mind, the variation of χ_o with H/M exhibited by $TiCr_{1.8}H_x$ in Figure 1 suggests a significant increase in $N(E_F)$ with increasing hydrogen content. The results of the proton NMR experiments completely support this view.

The nuclear spin systems in metals are affected by the electronic structure of the metal through hyperfine fields produced at the site of the nucleus. In transition metal systems the hyperfine fields are usually generated (13,14) by three mechanisms: Fermi contact interaction with the unpaired s electrons at E_F; core polarization of the spin-paired s electrons at energies below the Fermi level by the unpaired d electrons at E_F; and the effect of the orbital motion of d-electrons that is also responsible for the Van Vleck term χ_{ORB} in eqn. (2). Recent NMR studies of TiH_x (16), $Ti_{1-y}V_yH_{1.95}$ (17), and $Ti_{1-y}Nb_yH_{1.94}$ (15) have indicated that the orbital hyperfine interaction gives a negligible contribution to the proton σ_K and T_{1e} parameters. Similar behavior is assumed to hold for the $TiCr_2H_x$ system and any orbital contributions to the proton σ_K and $(T_{1e}T)^{-1/2}$ data in Figure 2 are neglected. After making the conventional assumptions (13,14) to ignore electron-electron coupling and interband mixing terms, the proton NMR parameters are given by

$$\sigma_K = 2\mu_B[H_{hf}(s)N_s(E_F) + H_{hf}(d)N_d(E_F)] \qquad (4)$$

$$(T_{1e}T)^{-1} = 4\pi\hbar\gamma_I^2 k_B\{[H_{hf}(s)N_s(E_F)]^2 + [H_{hf}(d)N_d(E_F)]^2 q\}. \qquad (5)$$

Here, $H_{hf}(s)$ and $H_{hf}(d)$ are the hyperfine fields for the Fermi contact and core polarization interactions, respectively; γ_I is the gyromagnetic ratio for nuclei with quantum number I; $\hbar$ is Planck's constant; k_B is the Boltzmann's constant; $N_s(E_F)$ and $N_d(E_F)$ are the densities of s and d electron states at the Fermi level, and q is the reduction factor resulting from d electron orbital degeneracy at E_F as described by Narath (13). $H_{hf}(s)$ is always positive, but $H_{hf}(d)$ is usually negative (13). Thus,

the contact and core polarization terms make additive contributions to $(T_{1e}T)^{-1}$, but their contributions to σ_K tend to cancel.

The proton σ_K and $(T_{1e}T)^{-\frac{1}{2}}$ values for four nominal $TiCr_2H_x$ samples are compared in Table II with recent results for several other Ti-based hydrides. In every case the σ_K values are negative, indicating dominance of the core-polarization term, and imply that $N_d(E_F) >> N_s(E_F)$. However, the $TiCr_{1.8}H_x$ and $TiCr_{1.9}H_x$ samples have significantly larger $(T_{1e}T)^{-\frac{1}{2}}$ values relative to their σ_K values than are observed for the other Ti-based hydrides. The generalized Korringa expression (13,14)

$$q_{exp} = C_K/\sigma_K^2 \; T_{1e}T \qquad (6)$$

can provide some insight where $C_K = \hbar\gamma_e^2/(4\pi k_B\gamma_I^2)$ and γ_e is the electron gyromagnetic ratio. When the Fermi contact terms dominate both σ_K and T_{1e}, $q_{exp} = 1.0$ if the electron-electron interactions (13) are excluded. For the core-polarization terms, $q_{exp} = q$, which is the reduction factor in eqn. (5) and varies between $0.2 \leq q \leq 0.5$ for cubic lattices (13) depending upon the fractional character of the t_{2g} d orbitals at the Fermi level. However, $q_{exp} > 0.5$ becomes possible if both contact and core-polarization interactions contribute to σ_K because of the fortuitous cancellation of positive and negative shift contributions. Table II also includes the q_{exp} values calculated using the σ_K and $(T_{1e}T)^{-\frac{1}{2}}$ data. While $TiH_{1.96}$, $Ti_{0.5}V_{0.5}H_{1.94}$, $Ti_{0.5}Nb_{0.5}H_{1.94}$, and $TiCuH_{0.94}$ yield q_{exp} values in the range expected (13) for pure core-polarization interactions, the q_{exp} for the $TiCr_{1.8}H_x$ and $TiCr_{1.9}H_x$ samples are significantly greater than one. Hence, it is concluded that $N_s(E_F)$ is proportionally larger in both the C-15 and C-14 $TiCr_2H_x$ systems relative to the vanishingly small $N_s(E_F)$ levels in other Ti-based hydrides (15-18). Since the Fermi contact interaction provides the more efficient T_{1e} relaxation process (13), this conclusion is consistent with the larger $(T_{1e}T)^{-\frac{1}{2}}$ values as well as the partial cancellation of the negative σ_K values for the $TiCr_{1.8+0.1}H_x$ samples. Unfortunately, independent values

for the hyperfine fields $H_{hf}(s)$ and $H_{hf}(d)$ are unknown and more quantitative estimates of $N_s(E_F)$ and $N_d(E_F)$ are not currently possible.

The trends in σ_K and $(T_{1e}T)^{-\frac{1}{2}}$ observed in Figure 2 indicate an increase in $N_d(E_F)$ with increasing H/M since any increase in $N_s(E_F)$ would produce smaller σ_K (i.e., tending towards more positive) values. This view is supported by the q_{exp} values in Table II. The q_{exp} values decrease in the sequence α-$TiCr_{1.9}H_{0.63}$ > α-$TiCr_{1.8}H_{0.88}$ > α'-$TiCr_{1.8}H_{2.40}$ > α'-$TiCr_{1.9}H_{2.85}$ while the σ_K values are systematically becoming more negative. This behavior requires that the negative core-polarization term makes a greater contribution at the larger hydrogen contents. Assuming the hyperfine fields do not significantly change, an increase in $N_d(E_F)$ with hydrogen addition is clearly indicated. However, either substantial $N_s(E_F)$ levels or large $H_{hf}(s)$ exist in the α'-phase samples since q_{exp} still greatly exceeds the values predicted (13) for dominant core-polarization contributions. It is possible that the large $N_s(E_F)$ values are responsible (11,23) for the high instability of the $TiCr_2H_x$ phases (1-3). Band theory calculations of the electron structures of the $TiCr_2$ and $TiCr_2H_x$ phases (which are currently unavailable) should be very enlightening to this interpretation of the proton NMR parameters.

Figure 2 indicates $N_d(E_F)$ is increased by about threefold between α-phase $TiCr_{1.8}H_{0.2}$ and the α'-hydride $TiCr_{1.8}H_{2.8}$. This is in reasonable agreement with the susceptibility result $\chi_o(TiCr_{1.8}) = 2.6 \times 10^{-6}$ emu/g and $\chi_o(TiCr_{1.8}H_{2.3}) = 5.6 \times 10^{-6}$ emu/g and supports our view that the χ_o increase with H/M in Figure 1 reflects an increase in $N(E_F)$. It is also interesting to note that the σ_K and $(T_{1e}T)^{-\frac{1}{2}}$ parameters in Figure 2 extrapolates across the mixed (α+α') phase region. This is consistent with hydrogen occupying identical Ti_2Cr_2 interstitial sites in the isostructural α and α' phases (3) as indicated by the neutron diffraction studies of Reidinger, et al (24).

The NMR and magnetic susceptibility data imply that the electronic structures of the C-15 and C-14 allotropes of $TiCr_{1.8}$ are quite similar in both the α-phase solid solution and the α'-phase hydride. Although

both allotropic hydrides are remarkably unstable, there are significant differences in their thermal stability (1,2). For example, the C-15 allotrope exhibits (1) an equilibrium plateau pressure of about 2 atm at 195 K for the $\alpha \rightleftarrows \alpha'$ transition which is a factor of ten greater than the corresponding plateau pressure, (2) of 0.2 atm for the C-14 allotrope at the same temperature. Thus, while an electron density of states effect may be important in determining the overall general instability of the two $TiCr_{1.8}H_x$ systems, other factors are clearly also significant. For example, the volume of the Ti_2Cr_2 interstitial site occupied by hydrogen in C-14 phase is slightly larger than the similar Ti_2Cr_2 site in the C-15 structure. Lundin, et al (25) have correlated increased stability with larger tetrahedral interstitial volume which is qualitatively consistent with the $TiCr_{1.8}H_x$ results. Considerations in addition to electronic factor appear to play a role in determining hydride stability in $TiCr_{1.8}H_x$ and the same is likely true in the region of solid solution.

V. CONCLUSIONS

The density of states at the Fermi level for both cubic (C-15) and hexagonal (C-14) $TiCr_{1.8\pm0.1}H_x$ have been shown to significantly <u>increase</u> with hydrogen content which is opposite of the $N(E_F)$ change exhibited by most other metal-hydrogen systems. Hence, there may be a basis for the previous suggestion (4) that the unusual positive deviation from Sieverts' law for the $TiCr_{1.8}H_x$ system may be associated with some anomalous electronic effect in the chemical potential μ_H for hydrogen absorption. However, other factors such as defect states (3,24) in the nonstoichiometric $TiCr_{1.8}$ alloys could also prove to be important. Further work on both the electronic and thermodynamic properties of the $TiCr_2$-hydrogen system are required to resolve this problem.

REFERENCES

1. J. R. Johnson and J. J. Reilly, Inorg. Chem. 17, 3103 (1978).
2. J. R. Johnson, J. Less-Common Met. 73, 345 (1980).
3. J. R. Johnson, J. J. Reilly, F. Reidinger, L. M. Corliss, and J. M. Hastings, to be published in Proc. Int. Metal Hydride Symp. Toba, Japan, May 30-June 4, 1982.
4. J. F. Lynch, J. R. Johnson, and J. J. Reilly, Zeit. Physk. Chem. N. F. 117, 229 (1979).
5. E. Wicke and H. Brodowsky, in Hydrogen in Metals II, edited by G. Alefeld and J. Völkl (Springer-Verlag, Berlin, 1978) p. 73.
6. J. F. Lynch, J. J. Reilly, and F. Millot, J. Phys. Chem. Solids 39, 883 (1978).
7. H. E. Flotow, Zeit. Physk. Chem. N. F. 116, 95 (1979).
8. J. F. Lynch and J. Tanaka, Acta Met. 29, 537 (1981).
9. J. F. Lynch, J. Phys. Chem. Solids 42, 411 (1981).
10. J. F. Lynch, R. Lindsay, and R. O. Moyer, Jr., Solid State Commun. 41, 9 (1982).
11. A. C. Switendick, in Hydrogen in Metals I, edited by G. Alefeld and J. Völkl (Springer-Verlag, Berlin, 1978) p. 101.
12. W. E. Wallace, in Reference 11, p. 169.
13. A. Narath, in Hyperfine Interactions, edited by A. J. Freeman and R. B. Frankel (Academic, New York, 1967) p. 287.
14. R. M. Cotts, in Reference 11, p. 227.
15. B. Nowak, O. J. Zogal, and M. Minier, J. Phys. C: Solid State Phys. 12, 4591 (1979).
16. R. Göring, R. Lukas, and K. Bohmhammel, J. Phys. C: Solid State Phys. 14, 5675 (1981).
17. R. C. Bowman, Jr. and W.-K. Rhim, Phys. Rev. B 24, 2232 (1981).
18. R. C. Bowman, Jr., A. J. Maeland, W.-K. Rhim, and J. F. Lynch, Proc. Int. Symp. Electronic Structure and Properties of Hydrogen in Metals Richmond, VA, March 4-6, 1982 (to be published).
19. R. O. Moyer and R. Lindsay, J. Less-Common Met. 70, P57 (1980).

20. D. P. Burum, D. D. Elleman, and W.-K. Rhim, J. Chem. Phys. 68, 1164 (1978).

21. R. C. Bowman, Jr., A. Attalla, and A. J. Maeland, Solid State Commun. 27, 501 (1978).

22. R. C. Bowman, Jr. and J. R. Johnson, J. Less-Common Met. 73, 254 (1980); R. C. Bowman, Jr., B. D. Craft, A. Attalla, and J. R. Johnson, in Proceedings of the 4th World Hydrogen Energy Conference, Pasadena, CA, June 1982 (to be published).

23. A. C. Switendick, Zeit. Physk. Chem. N. F. 117, 89 (1979).

24. F. Reidinger, J. R. Johnson, P. Thompson, L. M. Corliss, and J. M. Hastings, to be published.

25. C. E. Lundin, F. E. Lynch, and C. B. Magee, J. Less-Common Met. 56, 19 (1977).

TABLE I. Susceptibility and x-ray diffraction results for several starting $TiCr_{1.8}$ samples that had not been previously exposed to hydrogen.

Sample	Laves Structure Type	Lattice Parameter (Å)	χ_o(298 K) (10^{-6} emu/g)	χ_o(80 K) (10^{-6} emu/g)
$TiCr_{1.8}$	C-15	6.940 ± 0.004	2.568 ± 0.010	---
$TiCr_{1.87}$	C-15	6.934 ± 0.005	2.582 ± 0.015	2.540 ± 0.005
$TiCr_{1.9}$	C-15	6.932 ± 0.004	2.565 ± 0.020	---
$TiCr_{1.9}$	C-14	a = 4.932 c = 7.983	2.636 ± 0.010	---

TABLE II. Proton Knight shifts (σ_K), $(T_{1e}T)^{-\frac{1}{2}}$ values and Korringa parameters (q_{exp}) for several hydrides containing titanium.

Sample	Structure Type	T (K)	$(T_{1e}T)^{-\frac{1}{2}}$ $(sK)^{-\frac{1}{2}}$	σ_K (ppm)	q_{exp}	Data Source
α-$TiCr_{1.9}H_{0.63}$	C-14	80	0.086	-21	4.6	Present
α-$TiCr_{1.8}H_{0.88}$	C-15	80	0.106	-37	2.2	Present
α'-$TiCr_{1.8}H_{2.40}$	C-15	80	0.223	-90	1.62	Present
α'-$TiCr_{1.9}H_{2.85}$	C-14	80	0.239	-98	1.57	Present
$TiH_{1.96}$	fct	107	0.108	-96	0.34	Ref. 17
$Ti_{0.5}V_{0.5}H_{1.94}$	fcc	110	0.163	-161	0.27	Ref. 17
$Ti_{0.5}Nb_{0.5}H_{1.94}$	fcc	296	0.096	-110	0.20	Ref. 15
$TiCuH_{0.94}$	B11	86	0.150	-113	0.46	Ref. 18

FIGURE CAPTIONS

FIG. 1. Variation of room temperature magnetic susceptibility (χ_o) with hydrogen content exhibited by $TiCr_{1.8}H_x$ system with the Laves C-14 and C-15 structures.

FIG. 2. The proton Knight shifts (σ_K) and $(T_{1e}T)^{-\frac{1}{2}}$ values for CO-stabilized $TiCr_{1.8}H_x$ (C-15 Laves phase) and $TiCr_{1.9}H_x$ (C-14 Laves phase) as a function of hydrogen concentration. The open symbols correspond to a proton resonance frequency of 56.4 MHz while closed symbols correspond to a frequency of 34.5 MHz.

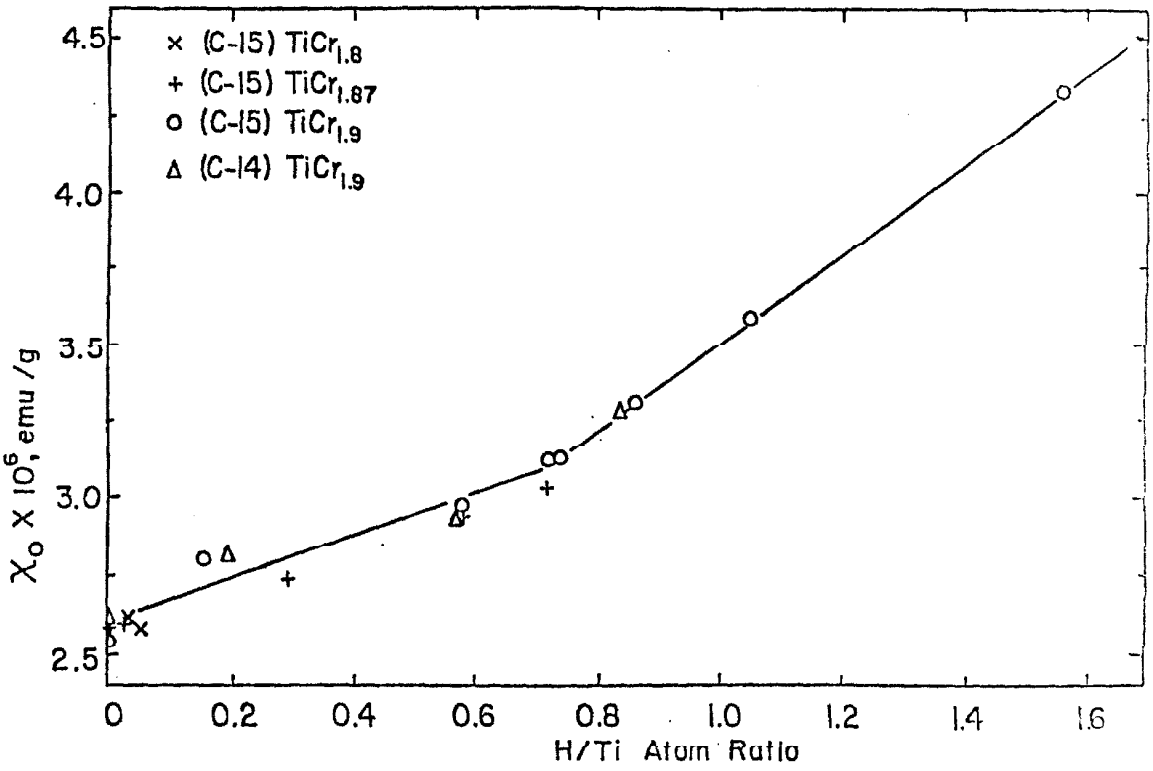
× (C-15) TiCr1.8
+ (C-15) TiCr1.87
o (C-15) TiCr1.9
Δ (C-14) TiCr1.9
4.5
4.0
3.5
3.0
2.5
χo X 10^6, emu /g
0
0.2
0.4
0.6
0.8
1.0
1.2
1.4
1.6
H/Ti Atom Ratio

FIGURE 1

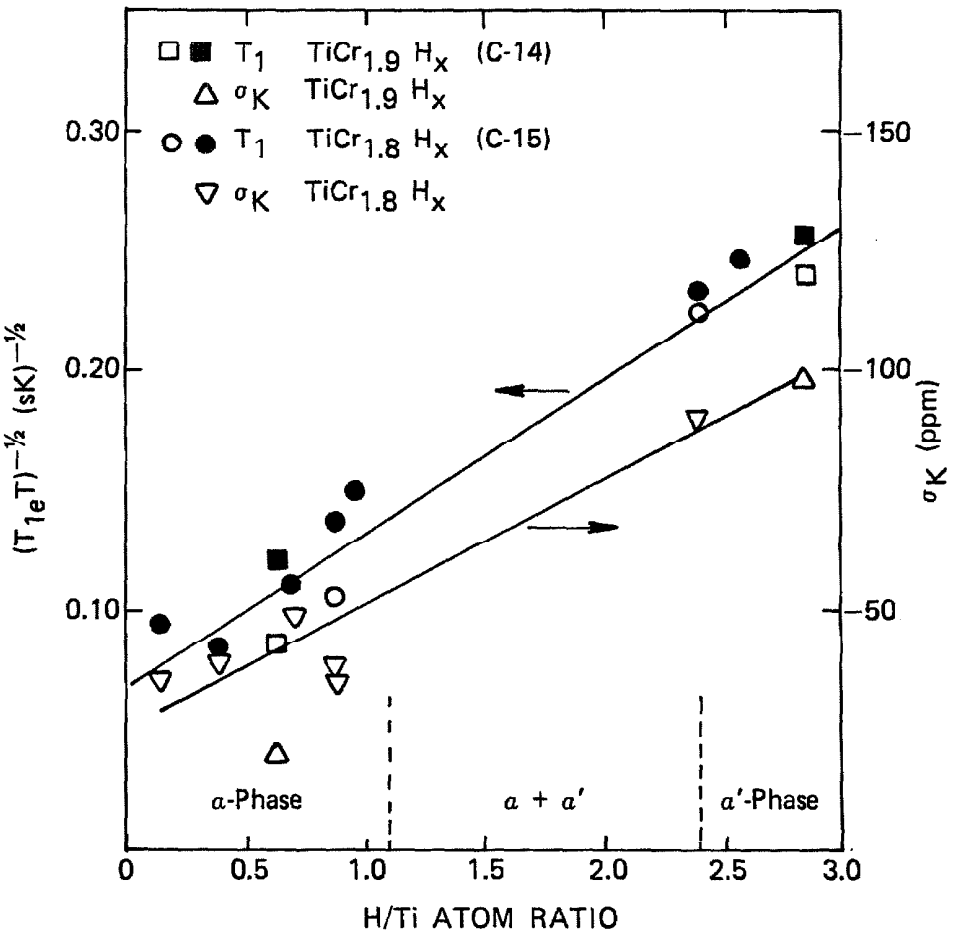
□■ T_1 $TiCr_{1.9}H_x$ (C-14)
△ σ_K $TiCr_{1.9}H_x$
○● T_1 $TiCr_{1.8}H_x$ (C-15)
▽ σ_K $TiCr_{1.8}H_x$
0.30
0.20
0.10
150
100
50
$(T_{1e}T)^{-1/2}$ (sK)$^{-1/2}$
σ_K (ppm)
α-Phase
α + α'
α'-Phase
0
0.5
1.0
1.5
2.0
2.5
3.0
H/Ti ATOM RATIO

FIGURE 2

CHAPTER 8

PROTON NMR STUDIES OF HYDROGEN DIFFUSION AND ELECTRONIC STRUCTURE IN CRYSTALLINE AND AMORPHOUS TITANIUM-COPPER HYDRIDES

[This chapter is essentially an article with the same title by R. C. Bowman, Jr., A. J. Maeland, and W.-K. Rhim, submitted to Physical Review B.]

I. INTRODUCTION

The properties of amorphous alloys (i.e., the metallic glasses) and the behavior of hydrogen in metals are two of the most active research areas for the transition metals. Much of this attention has focused on the electronic structure and diffusion behavior. In the metallic glasses, electronic structure has been related to phase stability (1) as well as the magnetic behavior, superconductivity, and electron transport properties (2) while diffusion phenomena are presumed (3-6) to dominate the structural relaxation processes and crystallization. There have been extensive theoretical (7-9) and experimental (10-13) studies of the electronic structures for numerous transition metal-hydrogen systems in order to better understand the nature of metal-hydrogen bonds and various physical properties of the metal hydride phases. Diffusion behavior of the hydrogen isotopes has also been extensively evaluated (10,14-16) in crystalline metals and alloys. However, the specific roles of crystal structure on the diffusion mechanisms in glassy metals and metal-hydrogen systems remain poorly understood and controversial. Recent studies (17, 18) have indicated very similar electronic structures for amorphous and crystalline transition metal alloys with nominally identical compositions. The structural changes associated with hydrogen absorption can significantly alter (7,8) the electron band structure of the host metal.

Although there is a vast literature on the properties of crystalline metal-hydrogen systems that dates back over several decades, the first report of an amorphous metal-hydrogen system (i.e., a-$Ti_{1-y}Cu_yH_x$) was published by Maeland (19) in 1978. There have been several subsequent papers on amorphous a-$Ti_{1-y}Cu_yH_x$ (20-22) as well as other glassy metal-hydrogen systems (23-28). Furthermore, low concentrations (i.e., $\lesssim 1$ atm %) of hydrogen exert a major influence on the mechanical relaxation properties in many diverse metallic glasses (29-32). Since amorphous alloys and metal hydrides have many potential technological applications as well as inherently interesting fundamental properties, research on the amorphous metal-hydrogen systems has been rapidly escalating with the

expectations for improved understanding of both material classes.

The present study addresses the roles of crystal structure on the interstitial site occupancy by hydrogen atoms, electronic structure properties, and hydrogen diffusion behavior in crystalline $TiCuH_x$ and Ti_2CuH_x and the amorphous hydride a-$TiCuH_{1.4}$. This task has been accomplished by nuclear magnetic resonance (NMR) measurements of the proton lineshapes, relaxation times, and Knight shifts, which are extensions of previous studies (22,33). A preliminary version of the present results, along with some relevant magnetic susceptibility data, was presented at a recent conference (34).

The $Ti_{1-y}Cu_yH_x$ system is a very favorable candidate for comparative studies of crystalline and amorphous metal hydride phases. Metallic glasses form readily in the $Ti_{1-y}Cu_y$ system over the wide composition range of 30-70 atm % Cu which includes the crystalline intermetallic compounds TiCu and Ti_2Cu. Both TiCu and Ti_2Cu have been found (19,21,35) to form ternary hydrides with limiting compositions $TiCuH_{1.0}$ and $Ti_2CuH_{2.80}$. Under suitable conditions the corresponding $Ti_{1-y}Cu_y$ glasses can also absorb hydrogen without crystallization (19,21) to form amorphous hydrides such as a-$TiCuH_x$ where $1.2 \leqslant x \leqslant 1.4$. The present experiments confirm the previous assertion (22,33) that crystal structure has a dominant role in the diffusion behavior for both crystalline and amorphous $Ti_{1-y}Cu_yH_x$ phases. The occupancy of more diverse interstitial sites (i.e., Ti_4Cu_2 sites, for example, in addition to the preferred Ti_4 sites) in Ti_2CuH_x and a-$TiCuH_{1.3\pm0.1}$ greatly enhances the observed hydrogen mobility (with an accompanying decrease in activation energy E_a) in these phases relative to the diffusion rates in $TiCuH_{0.94}$ and γ-phase TiH_x. Analyses of the proton Knight shifts and spin-lattice relaxation times indicate that core-polarization (10) with the metal d-electrons dominates the proton hyperfine interactions in $Ti_{1-y}Cu_yH_x$. The Fermi-level population of d states greatly exceeds the s state population as has been found in other Ti-based hydrides (36-39). Furthermore, the proton NMR parameters suggest that $N(E_F)$, the density of electron states at the Fermi

energy E_F as sampled at the proton sites, is significantly reduced in a-$TiCuH_{1.4}$ compared to crystalline $TiCuH_{0.94}$. A similar $N(E_F)$ difference at the proton sites has been observed (28) between amorphous and crystalline Zr_2PdH_x. Hence, a general tendency for $N(E_F)$ reduction in amorphous metal hydrides may be occurring although there seems to be little difference in the electronic structures of amorphous and crystalline alloys (2, 17,18) when they are hydrogen-free.

II. A BRIEF REVIEW OF THE PROPERTIES OF TITANIUM-COPPER ALLOYS AND THEIR HYDRIDE PHASES

The intermetallic TiCu crystallizes with a tetragonal structure of the B11 type. This structure is illustrated in the upper portion of Figure 1 where the interstitial sites occupied by the H-atoms are also shown. When TiCu is exposed to hydrogen gas and the temperature is maintained below 200°C, a ternary hydride $TiCuH_{1.0}$ forms (19) with a 9% volume increase but no change in the metal host structure. In a neutron diffraction study of $TiCuD_{0.90}$, Santoro, et al (40) determined the crystal structure in Figure 1 where the D-atoms only occupy the interstitial sites with four Ti nearest neighbors. The tetrahedral site occupancy of H-atoms in crystalline $TiCuH_{0.93}$ has also been verified by inelastic neutron scattering measurements (20) while the second moment (M_{2D}) for the proton lineshape (33) in $TiCuH_{0.94}$ agrees with the structure in Figure 1. The absence of H-atoms from the other interstitial sites, which always include several Cu atoms as nearest neighbors, is not surprising since copper is an endothermic absorber of hydrogen with no known stable hydride phases. When the crystal structure of the fcc γ-phase TiD_2 structure (Figure 1a) is compared with the TiCuD structure (Figure 1b), it is clear that the double layer of Ti atoms in TiCuD gives a two-dimensional analog of the TiD_2 structure. Because a double layer of Cu atoms separate each 2-D TiH_x layer, diffusion in crystalline $TiCuH_x$ is restricted to direct jumps between nearest-neighbor tetrahedral sites within the H-atom plane while jumps through vacant octahedral sites are possible (41,42) in fcc γ-TiH_x. In fact, the relatively large E_a value

for the proton relaxation times in crystalline $TiCuH_{0.94}$ has been attributed (16,33) to higher activation energies for the direct jumps between the neighboring sites compared to the lower energy required (41) to jump through the vacant octahedral sites in γ-TiH_x.

If ternary $TiCuH_x$ is heated above 250°C for extended times (19,33), it will disproportionate into a mixture of γ-TiH_x and Cu metal. Similarly, when TiCu alloy is heated above 250°C and exposed to hydrogen gas, it will form (43) the segregated TiH_x + Cu mixture and not the ternary phase $TiCuH_{1.0}$. Maeland (19) has shown by a thermodynamic analysis of the free energies that the ternary $TiCuH_{1.0}$ phase is unstable with respect to TiH_2 + Cu. The formation of metastable $TiCuH_x$ below 200°C occurs because the metal atom mobilities are too slow to permit attainment of the equilibrium products TiH_2 and Cu metal.

The crystal structure of Ti_2Cu is tetragonal of the type $C11_b$ and is illustrated in Figure 2. The Ti_2Cu structure is very similar to the TiCu structure except the double layers of Ti atoms in Ti_2Cu are separated by a single Cu layer instead of the double layer as in the TiCu structure. The presumably preferred Ti_4 interstitial site for hydrogen occupancy is also indicated in Figure 2. At temperatures below 200°C, crystalline Ti_2Cu will absorb hydrogen to form (19,35) a metastable ternary hydride phase Ti_2CuH_x with $x \lesssim 2.8$. However, x-ray and neutron diffraction measurements (19,35,44) indicate a structure change occurs for the Ti_2CuH_x phase. A tentative analysis (44) of the neutron pattern for $Ti_2CuD_{2.5}$ suggests an orthorhombic structure with lattice parameters: a = 0.306 nm, b = 0.333 nm, and c = 1.01 nm. Since hydrogen occupancy of all the Ti_4 sites in the Ti_2Cu structure limits the composition to x = 2.0, other sites must also be occupied to yield $Ti_2CuH_{2.7\pm0.1}$. Inelastic neutron scattering (45) indicates some H-atoms do occupy octahedral sites in Ti_2CuH_x. From Figure 2, the most likely candidates are the Ti_2Cu_4 and Ti_4Cu_2 sites in the Cu-only layers. The poor quality of the x-ray patterns (19,35) and apparent complexity of the Ti_2CuH_x structure has precluded a reliable structure determination at this time. The

ternary Ti_2CuH_x phase is unstable (19,35,43) above about 200°C relative to the TiH_x + Cu mixture as previously described for the TiCu-H_2 system.

The a-$Ti_{1-y}Cu_y$ amorphous alloys are conveniently prepared by standard melt-spinning techniques. The crystallization temperatures of hydrogen-free a-$Ti_{1-y}Cu_y$ metallic glasses are found (19,21,46) to be above 300°C. Although the x-ray patterns of the a-$Ti_{1-y}Cu_y$ metallic glasses gave the broad maxima that are consistent with the absence of crystalline order, recent neutron diffraction (46,47) and EXAFS (48) experiments on amorphous a-$Ti_{1-y}Cu_y$ samples have indicated extensive chemical short range ordering in these glassy metals. These results imply that the local structures for those amorphous a-$Ti_{1-y}Cu_y$ alloys with compositions near the intermetallic phases (i.e., TiCu or Ti_2Cu) should be very similar to the structure in the corresponding crystalline phases. However, there can be a wider distribution (46-48) of local structures in the metallic glass.

The metallic glasses a-$Ti_{1-y}Cu_y$ where $0.35 \leqslant y \leqslant 0.65$ will absorb hydrogen at room temperature to form ternary amorphous a-$Ti_{1-y}Cu_yH_x$ without crystallization (19,21). An interesting aspect of the Ti-Cu system is that the amorphous alloys absorb significantly more hydrogen than the corresponding crystalline intermetallics. This behavior has not been observed in other amorphous-crystalline alloys (23-25,27,28) and may reflect the ability of hydrogen to occupy a wider variety of Ti-Cu interstitial sites than are available in the ordered crystalline structures. A comparison of the neutron vibrational spectra (20) for crystalline $TiCuH_{0.93}$ and amorphous a-$TiCuH_{1.3}$ implies that H-atoms in the amorphous hydride occupy a much broader distribution of local environments (possibly, including some octahedral sites) with nominal tetrahedral symmetry than the single Ti_4 site occupied in $TiCuH_{0.93}$. The proton spin-spin (T_2) and dipolar (T_{1D}) relaxation times have indicated (22) that hydrogen mobility in a-$TiCuH_{1.3}$ is significantly greater than in crystalline $TiCuH_{0.94}$ or γ-TiH_x. Although the proton relaxations for both $TiCuH_{0.94}$ and γ-TiH_x can be represented by single activation energies over wide

temperature ranges (22,33,41,49), four E_a values are required (22) to represent hydrogen diffusion in a-$TiCuH_{1.3}$ between 115K and 420K. The enhanced hydrogen mobility in the amorphous a-$TiCuH_{1.3}$ phase has been attributed (22) to the removal of the structural constraints (33) on the H-atom jump paths in crystalline $TiCuH_{0.94}$. However, a more complete description of the diffusion processes in the amorphous phase was not possible since detailed models of site occupancies and alternative jump paths were not available. The greater mobility in the amorphous phase is consistent with the lower thermal stability of a-$TiCuH_{1.3}$, which segregates (21,22) into the TiH_x + Cu mixture at about 425K whereas crystalline $TiCuH_{0.94}$ does not decompose until the temperature exceeds 550K under similar experimental conditions (33).

There is very little experimental information on the electronic structure of the Ti-Cu alloys or hydrides and apparently no published theoretical results on their band structures. X-ray emission spectra (50) for several crystalline Ti-Cu intermetallics and a photoemission spectrum (51) for an amorphous $Ti_{0.60}Cu_{0.40}$ alloy indicate the valence bands consist of two peaks where the low lying peak (i.e., 3-4 eV below E_F) corresponds to the Cu states and Ti atoms contribute to the peak at the Fermi level. This behavior is apparently typical for crystalline or amorphous alloys (18,51) composed of an early (e.g., Ti) and late (e.g., Cu) transition metal. Although hydride phase formation is presumed to distort the $Ti_{1-y}Cu_y$ valence d bands and form a metal-hydrogen bonding peak (7,8) several electron volts below the Fermi level, there have been no photoelectron spectroscopic experimental studies of $Ti_{1-y}Cu_yH_x$ to collaborate this supposition.

III. EXPERIMENTAL DETAILS

Most of the experimental procedures employed to prepare the crystalline and amorphous samples for the present studies have been described in detail elsewhere (19-22,35) and will not be repeated. The crystalline $TiCuH_{0.94}$, $Ti_2CuH_{1.9}$, and $Ti_2CuH_{2.63}$ samples were prepared by reaction with hydrogen gas at a temperature of about 150°C. The amorphous

a-$TiCuH_{1.4}$ sample was prepared at room temperature to avoid crystallization. Compositions were verified by volumetric analyses during thermal desorption at 1000°C. All the samples were handled and stored in inert atmosphere gloveboxes prior to loading the NMR tubes, which were subsequently evacuated and flame sealed.

The proton lineshapes were measured with a simplified version (52) of the magic-echo sequence and the second moments (M_{2D}) were determined from Gaussian plots of the initial portions of the lineshape decays. The spin-lattice relaxation times (T_1) were measured with the standard inversion recovery method. The proton Knight shifts (σ_K) were measured with the multiple-pulse zero-crossing technique devised by Burum, et al (53) and had an estimated precision of ±2 ppm. The σ_K data are relative to an external reference of tetramethylsilane (TMS) and have been corrected for the demagnetization effects (10,36) with the magnetic susceptibilities measured (34) on the same samples used for the proton NMR experiments. The magic echoes, T_1 values, and Knight shifts were measured at a proton resonance frequency of 56.4 MHz on a wide-band transient spectrometer that was previously described (52). A different spectrometer (33) was used to measure the rotating frame relaxation time ($T_{1\rho}$) at a proton resonance frequency of 34.5 MHz and spin-locking magnetic field of nominally 7.3 G. The total temperature range of the NMR experiments was 80K to 560K; however, the amorphous a-$TiCuH_{1.4}$ was not heated above 420K to prevent the decomposition previously observed (22).

IV. RESULTS

The crystalline $TiCuH_{0.94}$ and Ti_2CuH_x samples yield room temperature proton spectra with the nearly Gaussian lineshapes that are expected (10) for immobile "rigid-lattice" nuclei. However, a motionally narrowed exponential decay is observed (22) at room temperature for the proton spectra in the amorphous a-$TiCuH_x$ samples. When the a-$TiCuH_x$ samples are cooled below 220K, the rigid-lattice lineshapes are obtained. Table I summarizes the proton M_{2D} values determined from the decays generated during the magic echo experiments (52) at temperatures corresponding to

the rigid-lattice conditions. Crystalline $TiCuH_{0.94}$ gives the largest M_{2D} even though the other samples contain greater densities of protons per unit volume. In the next section, this behavior will be related to differences in the distributions of the hydrogen atoms among the available interstitial sites.

The proton T_1 relaxation times below 310K are summarized in Figure 3. The experimental recoveries for the T_1 measurements were always exponential as expected for single phase materials. The $T_{1\rho}$ data are presented in Figure 4 where the minima indicate the dominance (10,16) of the diffusion contributions. Although the $T_{1\rho}$ recoveries for the $Ti_2CuH_{0.94}$ and a-$TiCuH_{1.4}$ samples were usually exponential within experimental uncertainty, the recoveries for the Ti_2CuH_x samples tended to be non-exponential at most temperatures. Hence, the $T_{1\rho}$ values in Figure 4 are defined by the time corresponding to the decay to 1/e of the initial amplitude. This procedure permits consistent comparisons among the samples, but it is apparent that the hydrogen diffusion mechanisms are inherently complex in the Ti_2CuH_x samples.

The temperature dependent behavior of the proton Knight shifts σ_K, referenced to TMS and corrected (36) for the demagnetization effects, are summarized in Figure 5. All of the σ_K values in Figure 5 are negative (i.e., upfield relative to the reference resonance frequency) as has been found previously in γ-phase TiH_x (Refs. 36 and 37), $Ti_{1-y}V_yH_{1.95}$ (Ref. 36), $Ti_{1-y}Nb_yH_{1.94}$ (Ref. 38), and $TiCr_2H_x$ (Ref. 39). Hence, negative σ_K seems to be a common characteristic of Ti-based hydrides. The differences among the σ_K values for the four $Ti_{1-y}Cu_yH_x$ samples will be related to their electronic structures in a later section.

V. ANALYSIS AND DISCUSSIONS

A. Second Moment and Hydrogen Site Occupancies

In the rigid-lattice limit it is often possible (10) to determine the hydrogen locations from the proton M_{2D} values providing the structure of the metal atoms is known from x-ray diffraction or another technique. The general formalism for the dipolar contributions to M_{2D} was originally

developed by Van Vleck (54). A generalized version (55) of the Van Vleck formula for a powder sample that takes account of the contributions from inequivalent lattice sites and nonresonant nuclear spins can be written as

$$M_{2D} = C_I \sum_{i,j}^{N} f_i \alpha_j S_{ij} + C_S \sum_{i=1}^{N} f_i S'_{ij} \qquad (1)$$

where $C_I = (3/5)(\gamma_I \hbar)^2 I(I+1)$ for contributions from other protons with gyromagnetic moment γ_I and spin $I = \frac{1}{2}$, $\hbar$ is Planck's constant, and $C_S = (4/15)(\gamma_S \hbar)^2 S(S+1)$ for the contributions from unlike nuclei with spin S (here ^{47}Ti, ^{49}Ti, ^{63}Cu, ^{65}Cu) and gyromagnetic moments γ_S. Here, f_i is the fraction of all protons located in sites of type i; α_j is the probability of occupation of a j site; and ω_j is the relative number of j sites. Thus, f_i is given by

$$f_i = \omega_i \alpha_i / \sum_{k=1}^{N} \omega_k \alpha_k \qquad (2)$$

where N is the number of inequivalent proton sites. S_{ij} denotes the lattice sum $\sum_{j}^{\infty} r_{ij}^{-6}$ where the origin is taken at an i site and the summation extends over all j sites. Similarly, S'_{ij} denotes the sum over metal nuclei with the origin taken at the ith proton site. The theoretical dipolar M_{2D} is calculated for model arrangements of protons within the host metal structure and is compared with the experimental value to determine which model structure gives the best agreement. The proton M_{2D} method for structure determination in a powder is not nearly as powerful as the neutron diffraction techniques, but M_{2D} can be useful in eliminating many trial structures or choosing between alternative models when the neutron diffraction results are incomplete or not available. In practice, the protons should not occupy more than two inequivalent sites if unambiguous results are to be obtained from eqn. (2).

The structure of crystalline $TiCuD_{0.90}$ has been determined by powder neutron diffraction (40) as shown in Figure 1. Since the H-atoms only occupy the Ti_4 interstitial sites in the presumably isomorphic TiCuH

structure, the M_{2D} expression reduces to a rather simple form, which has been previously evaluated (33) to give a calculated dipolar M_{2D} of 17.8 G^2. The present magic echo experiments on the $TiCuH_{0.94}$ gave $M_{2D} = 18.5 \pm 0.5\ G^2$, which is in good agreement with the theoretical value as well as the previous experimental result $M_{2D} = 17.8 \pm 0.8\ G^2$ obtained from the lineshape of the proton solid echo (33). Hence, the TiCuH structure in Figure 1 seems well established from x-ray and neutron diffraction (19,40), inelastic neutron scattering (20), and the rigid-lattice proton M_{2D} parameters.

Although an orthorhombic structure has been proposed (44) for Ti_2CuH_x, the analyses of the x-ray and neutron diffraction patterns have not been completed and the orthorhombic assignment remains tentative. Since interpretations of the diffusion behavior and the electronic properties require at least cursory knowledge of the interstitial sites that are occupied by the H-atoms, a preliminary assessment of the M_{2D} parameters for the Ti_2CuH_x samples has been performed using the data in Table I and some reasonable estimates (44) for the Ti_2CuH_x lattice parameters for the tetragonal and orthorhombic structures. Because of the poor quality of the x-ray diffraction patterns (19,35) for the Ti_2CuH_x samples, the same lattice parameters were used for both $Ti_2CuH_{1.9}$ and $Ti_2CuH_{2.63}$ during the M_{2D} calculations, which reduces the accuracy to some extent and limits quantitative comparisons between the calculated and experimental M_{2D} parameters.

Based upon the Ti_2Cu structure given in Figure 2 and the inelastic neutron scattering results (45) for $Ti_2CuD_{2.5}$, the three most likely locations for H-atoms are the Ti_4, Ti_4Cu_2, and Ti_2Cu_4 interstitial sites with a preference for the presumably more stable Ti_4 sites. For the tetragonal unit cell of Figure 2, there are four Ti_4 sites, four Ti_4Cu_2 sites, and two Ti_2Cu_4 sites. The limiting compositions for complete occupancy of the Ti_4 sites and either of the octahedral sites are Ti_2CuH_3 (for Ti_2Cu_4 sites) and Ti_2CuH_4 (for Ti_4Cu_2 sites) if the original tetragonal structure is retained. However, an orthorhombic structure can be

generated if H-atoms occupy only half of the Ti_4Cu_2 sites (i.e., those lying along the expanded b-axis) to give the limiting composition Ti_2CuH_3 when the Ti_4 sites are also completely occupied. This particular arrangement of H-atoms in Ti_2CuH_x could provide consistent explanations for the orthorhombic distortion (19,35,44), the presence of vibrational frequencies (45) for hydrogen in both tetrahedral and octahedral sites, and the observed maximum composition $Ti_2CuH_{2.8}$.

The dipolar second moments for $Ti_2CuH_{1.90}$ and $Ti_2CuH_{2.63}$ have been calculated for several distributions of H-atoms in both the tetragonal and orthorhombic structures. Table II summarizes the calculated M_{2D} values where preferential occupancy by the Ti_4 sites has been assumed. During the M_{2D} calculations, the various interstitial sites retain their ideal positions in Figure 2 (i.e., no further distortions to lower symmetry or puckering of alternating hydrogen sites occur) except for the elongation of the b axis for the orthorhombic structure. Comparisons of the calculated dipolar M_{2D} values with the experimental moments from Table I clearly give the best agreement for the orthorhombic structure where the Ti_4Cu_2 sites are occupied when $x > 2.0$. Considering the uncertainty in the Ti_2CuH_x lattice parameters, undue emphasis should not be placed upon the comparisons in Table II since other H-atom distributions with lower occupancies of the Ti_4 sites can also give nearly as good agreement in some cases. However, the proton M_{2D} results in Table II are consistent with the orthorhombic structure and the intuitively satisfying preferential filling of the presumably more stable Ti_4 sites. This structure for Ti_2CuH_x provides a reasonable framework for subsequent analysis of the electronic structure and diffusion behavior.

Since long-range order is absent in amorphous solids, eqn. (1) cannot be directly applied to calculate the dipolar M_{2D} for a-$TiCuH_{1.4}$. Although simulation calculations using Monte Carlo techniques have provided theoretical M_{2D} values in few glassy alloys (56), only qualitative comparison with experiment can be realistically expected. Because local short-range order is present in amorphous $Ti_{1-y}Cu_y$ alloys (46-48), the

random packing calculation procedure (56) will be further compromised in these systems. However, the H-atoms predominantly occupy the same sites in the crystalline and amorphous $TiCuH_x$ phases (20). Table I indicates the experimental M_{2D} for the amorphous a-$TiCuH_{1.4}$ is much closer to the values for the Ti_2CuH_x samples (where Ti_4Cu_2 sites as well as Ti_4 sites are presumably occupied) than for crystalline $TiCuH_{0.94}$. This can be interpreted as suggesting the H-atoms are distributed among similar sites in a-$TiCuH_{1.4}$ and Ti_2CuH_x although greater variation is expected for the amorphous phase. More detailed assessments of the hydrogen distribution in amorphous a-$TiCuH_{1.4}$ are not currently possible.

B. Electronic Structure Properties from Proton T_1 and σ_K Parameters

The nuclear spin systems in metals are affected by the electronic structure of the metal through hyperfine fields (10,57) produced at the site of the nucleus. The two NMR parameters that are determined by the hyperfine interactions are the Knight shift σ_K and the conduction electron contribution (T_{1e}) to the spin-lattice relaxation time. When the paramagnetic relaxation contributions (16) are small (as is assumed for the Ti-Cu hydrides), the total spin-lattice relaxation rate (T_1^{-1}) can be separated into two terms

$$T_1^{-1} = T_{1e}^{-1} + T_{1d}^{-1} \qquad (3)$$

where T_{1d} arises from the atomic diffusion processes (10). T_{1e} is the dominant proton relaxation mechanism at sufficiently low temperatures where the T_{1d} term becomes negligible. According to prior proton NMR experiments (22,33), T_1 should equal T_{1e} below about 450 K in crystalline $TiCuH_{0.94}$ and below 250 K in amorphous a-$TiCuH_{1.3\pm0.1}$. The present study indicates that T_{1d} contributions to T_1 for protons in the Ti_2CuH_x samples are negligible below 350 K. Hence, the proton T_1 data in Figure 3 should represent only the T_{1e} values with the exception of the data points above 240 K for a-$TiCuH_{1.4}$ which contain larger T_{1d} contributions with increasing temperature. In order to facilitate later analyses, the parameters

$(T_{1e}T)^{-\frac{1}{2}}$ have been determined from the proton T_1 data in Figure 3 and are plotted versus temperature in Figure 6.

In transition metal systems the hyperfine fields are usually separated (10,57) into three contributions: Fermi contact interaction with the unpaired s electrons at E_F, core polarization of the spin-paired s electrons at energies below the Fermi level via exchange interactions with the unpaired d electrons at E_F; and the contribution of the orbital motion of d-electrons. Recent NMR studies of several other Ti-based hydrides (36-38) have indicated that the orbital hyperfine interaction does not give significant contributions to the proton σ_K and T_{1e} parameters. Similarly, the orbital contributions are assumed to be unimportant for the proton parameters in the Ti-Cu hydrides. With the conventional assumptions (10,57) to neglect electron-electron coupling and interband mixing effects, the proton NMR proton parameters are given by

$$\sigma_K = 2\,\mu_B[H_{hf}(s)N_s(E_F) + H_{hf}(d)N_d(E_F)] \qquad (4)$$

$$(T_{1e}T)^{-1} = 4\pi\,\hbar\gamma_I^{\,2}\,k_B\{[H_{hf}(s)N_s(E_F)]^2 + [H_{hf}(d)N_d(E_F)]^2 q\} \qquad (5)$$

where $H_{hf}(s)$ and $H_{hf}(d)$ are the hyperfine fields for the Fermi contact and core polarization interactions, respectively; k_B is the Boltzmann's constant; $N_s(E_F)$ and $N_d(E_F)$ are the densities of s and d electron states at E_F, and q is the reduction factor resulting from d electron orbital degeneracy at E_F as described by Narath (57). $H_{hf}(s)$ is always positive, but $H_d(E_F)$ is usually negative (57). The Fermi contact and core polarization terms make additive contributions to $(T_{1e}T)^{-1}$, but their contributions to σ_K tend to cancel.

If eqns. (4) and (5) are assumed to represent the proton hyperfine interactions, the σ_K and $(T_{1e}T)^{-\frac{1}{2}}$ parameters in Figures 5 and 6, respectively, will be directly proportional to the local densities of electron states at the proton sites in the Ti-Cu hydrides. In Table III the upper

and lower temperature limits of the σ_K and $(T_{1e}T)^{-½}$ parameters from Figures 5 and 6 are compared with similar data for several other Ti-based hydrides (36,37,39). Since all the data in Table III were collected at a common-proton resonance frequency (i.e., 56.4 MHz) on the same apparatus (36,52) and all of the σ_K shifts are relative to the same TMS reference sample, extraneous effects should be minimal during these comparisons. The proton parameters for the Ti-Cu hydrides are within the range of values obtained for the other samples, which implies that the basic character of $N(E_F)$ must be similar in all of these Ti-based systems. Since the H-atoms preferentially occupy tetrahedral interstitial sites (with the notable exceptions of $Ti_2CuH_{2.63}$ and, possibly, a-$TiCuH_{1.4}$, which have mixed Ti_4 and Ti_4Cu_2 site occupancies) in these hydrides, this observation is not completely unanticipated. Because negative σ_K values were obtained for every sample included in Table III, the core polarization term dominates the proton hyperfine interactions which further implies that $N_d(E_F) > N_s(E_F)$ in these hydrides. Although this last conclusion is substantiated by the recent band theory calculations (7-9) for TiH_2, no theoretical estimates of $N_d(E_F)$ or $N_s(E_F)$ are currently available for the various ternary Ti-based hydrides. However, the existence of negative σ_K shifts is strong evidence, by itself, for large $N_d(E_F)$ values since a dominant core polarization contribution to σ_K normally requires (36,37,57) a high density of d electron states at the Fermi level.

Additional insights on the character of $N(E_F)$ are provided by the generalized (37) Korringa expression

$$q_{exp} = C_K/\sigma_K^2 \, T_{1e}T \qquad (6)$$

where $C_K = \hbar\gamma_e^2/(4\pi k_B\gamma_I^2)$ and γ_e is the electron gyromagnetic ratio. When the Fermi contact interaction dominates both σ_K and T_{1e}, $q_{exp} = 1.0$ if the electron-electron interactions (57) are excluded. For exclusive core polarization interactions, $q_{exp} = q$, the reduction factor in eqn. (5). Typical values for q vary between 0.2 and 0.5 in cubic lattices (57)

which are assumed to be representative of the range expected for the core polarization terms in other structures. However, larger q_{exp} becomes possible when both contact and core polarization interactions contribute to σ_K to give fortuitous cancellation of positive and negative shift term.

Table III includes the q_{exp} values derived from the σ_K and $(T_{1e}T)^{-\frac{1}{2}}$ data. $TiH_{1.96}$ and $Ti_{0.5}V_{0.5}H_{1.94}$ exhibit q_{exp} values that are consistent with only the core polarization interactions from $N_d(E_F)$. However, a significant contact term from a relatively large $N_s(E_F)$ is indicated for $TiCr_{1.8}H_{2.40}$ since its q_{exp} exceeds one. Although the q_{exp} values for $TiCuH_{0.94}$ and a-$TiCuH_{1.4}$ are within the range expected for pure core polarization terms, some contact contributions are probably also present. Somewhat larger $N_s(E_F)$ values are indicated for Ti_2CuH_x samples since their q_{exp} are between 0.7 and 0.8. However, these assessments must not be taken too seriously but should be merely regarded as qualitative trends. Since the σ_K parameters can only be approximately corrected (36, 37) for chemical shift and bulk susceptibility (10) contributions, the corresponding uncertainties in the q_{exp} values are about ±0.1 - 0.2. Furthermore, substantial changes in q can occur as the fractional populations of d orbitals at the Fermi level are altered (57). Hence, it is usually very difficult to discriminate between small $N_s(E_F)$ contributions and variations in the d orbitals unless some supplemental information (such as partial densities of state from theoretical band structures) is also available. At least two types of interstitial sites are occupied by protons in Ti_2CuH_x and a-$TiCuH_{1.4}$ (i.e., Ti_4 and Ti_4Cu_2) and the hyperfine fields are expected to differ at these inequivalent sites. However, the experimental parameters σ_K and $(T_{1e}T)^{-\frac{1}{2}}$ in Figures 5 and 6 and Table III represent averages over all occupied proton sites and they cannot discern contributions from the inequivalent sites. Hence, the variations in the $N_d(E_F)$ ratio for these samples could be obscured by the changes in proton site occupancies. The combination of these factors restricts any quantitative evaluation of $N_s(E_F)$ and $N_d(E_F)$. Nevertheless, the relative populations of $N_d(E_F)$ and $N_s(E_F)$ that were deduced from the q_{exp} values in

Table III should be qualitatively correct. In particular, the $N_d(E_F)$ to $N_s(E_F)$ ratio for the Ti-Cu hydrides is intermediate to the limiting situations of nearly vanishing $N_s(E_F)$ (i.e., $TiH_{1.96}$ and $Ti_{0.5}V_{0.5}H_{1.94}$) and the substantial $N_s(E_F)$ contribution for $TiCr_{1.8}H_{2.40}$.

A closer examination of the proton σ_K and $(T_{1e}T)^{-\frac{1}{2}}$ data reveals some interesting properties on the behavior of $N(E_F)$ in $TiCuH_x$ and Ti_2CuH_x. Both parameters suggest the largest absolute $N(E_F)$ values occur for crystalline $TiCuH_{0.94}$ where the protons occupy only the Ti_4 sites as in γ-phase TiH_x. However, Table III shows that $TiCuH_{0.94}$ has a larger $(T_{1e}T)^{-\frac{1}{2}}$ and a smaller σ_K that is observed for $TiH_{1.96}$. These differences can be directly correlated with an increased $N_s(E_F)$ population in the $TiCuH_{0.94}$ sample compared to the apparently small (9,36,37) $N_s(E_F)$ in $TiH_{1.96}$. This explanation is also consistent with a larger q_{exp} for $TiCuH_{0.94}$ since the positive shift from the $N_s(E_F)$ will partially cancel the negative shift from $N_d(E_F)$ to produce a less negative total σ_K value. The proton parameters for $TiH_{1.96}$ have a greater temperature dependence because the $N_d(E_F)$ decreases with the Jahn-Teller distortion (7,36,37) of the fcc structure. The σ_K and $(T_{1e}T)^{-\frac{1}{2}}$ data indicate lower total densities of states at the proton sites in the Ti_2CuH_x samples; however, their q_{exp} values imply that $N_s(E_F)$ is proportionally larger in these samples. The pronounced $N(E_F)$ increase between $Ti_2CuH_{1.9}$ and $Ti_2CuH_{2.63}$ can be mainly attributed to an increase in $N_d(E_F)$ since σ_K becomes more negative and q_{exp} decreases. However, the earlier analysis of the M_{2D} parameters for Ti_2CuH_x have indicated that protons occupy Ti_4Cu_2 sites in addition to the preferred Ti_4 sites when the composition exceeds $Ti_2CuH_{2.0}$ since all the Ti_4 sites have been filled. Hence, interpretations of the proton σ_K and $(T_{1e}T)^{-\frac{1}{2}}$ parameters in terms of different $N_d(E_F)$ and $N_s(E_F)$ populations with a change in the position of Fermi level may not be entirely valid. The local density of states can be different for protons in Ti_4 and Ti_4Cu_2 sites, but the present NMR experiments only respond to the "average" hyperfine interactions and cannot resolve these differences. Unfortunately, no other experimental or theoretical results are available

to help identify the relative contributions at these proton sites. However, it is possible that the hyperfine interactions and local $N(E_F)$ are actually similar since both proton sites have four Ti nearest neighbors. The x-ray (50) and photoelectron (51) spectra of Ti-Cu alloys indicate the Cu states lie several electron volts below E_F and they are not expected to contribute significantly to either the hyperfine fields (57) or $N(E_F)$. Thus, the Ti atoms should determine these quantities at Ti_4Cu_2 sites as well as Ti_4 sites and comparison between the $Ti_2CuH_{1.9}$ and $Ti_2CuH_{2.63}$ samples regarding changes in $N(E_F)$ behavior at the protons is probably all right as a first approximation. Under these assumptions, the larger $(T_{1e}T)^{-½}$ and more negative σ_K for $Ti_2CuH_{2.63}$ suggest that $N_d(E_F)$ has become larger at the "average" proton site as more hydrogen is absorbed. This view is supported by similar behavior in magnetic susceptibility (34) where $Ti_2CuH_{2.63}$ has the larger value. One reasonable interpretation is that with increasing hydrogen contents E_F has moved further into the d band regions where $N_d(E_F)$ is now larger. Another possibility is the continuing modification (7,8) of the d bands with additional hydrogen to produce a greater density of d states in the region of the Fermi level. However, detailed band theory calculations of the electron densities in Ti_2CuH_2 and Ti_2CuH_3 are required before these ideas can be more thoroughly considered.

The much smaller proton σ_K and $(T_{1e}T)^{-½}$ values for amorphous a-$TiCuH_{1.4}$, compared to the corresponding data for crystalline $TiCuH_{0.94}$, are particularly interesting since a significant reduction in $N(E_F)$ is indicated. Because the q_{exp} for $TiCuH_{0.94}$ and a-$TiCuH_{1.4}$ are similar, $N_d(E_F)$ and $N_s(E_F)$ would appear to be reduced by comparable amounts unless there have been significant alterations in the proton hyperfine fields, which seem unlikely according to the arguments in the preceding paragraph. The larger hydrogen content in a-$TiCuH_{1.4}$ would presumably favor an increase in the proton NMR parameters and $N_d(E_F)$ if amorphous a-$TiCuH_x$ is analogous to Ti_2CuH_x. In fact, analysis of the M_{2D} data in Table I has already suggested very similar hydrogen site occupancies and distributions

in a-$TiCuH_x$ and Ti_2CuH_x. Although the σ_K and $(T_{1e}T)^{-\frac{1}{2}}$ parameters are in good agreement for a-$TiCuH_{1.4}$ and $Ti_2CuH_{1.9}$, significantly larger proton NMR parameters are found for the $Ti_2CuH_{2.63}$, which has an effective hydrogen concentration much closer to the amorphous sample composition. The smallest proton $(T_{1e}T)^{-\frac{1}{2}}$ parameter, which also implies the lowest local $N(E_F)$, occurs for a-$TiCuH_{1.4}$. The slightly smaller σ_K values (i.e., the least negative) for $Ti_2CuH_{1.9}$ probably results from a larger $N_s(E_F)$ contribution since its q_{exp} values are also nearer to one. Hence, the lowest local $N_d(E_F)$ for protons in Ti-Cu hydrides occurs for the amorphous a-$TiCuH_{1.4}$. Similar behavior has been recently observed (28) for protons in crystalline and amorphous Zr_2PdH_x. Hence, a reduction in $N_d(E_F)$ at proton sites may be a characteristic property of amorphous transition metal hydrides. However, recent evaluations of hydrogen-free amorphous and crystalline transition metal alloys of similar compositions (2,17,18) found little difference in electronic structure behavior. The absence of long range order in amorphous solids should remove some electronic degeneracies which would tend to smear the peaks in $N(E)$ and decrease their amplitudes. Hence, reduced values for $N(E_F)$ would occur whenever E_F falls in regions near these maxima. It is likely that the proton parameters are very sensitive to these $N(E_F)$ reductions. In the Ti-Cu hydrides, E_F is expected to lie in the Ti d electron states (50,51) while protons preferentially occupy the interstitial sites with only Ti neighbors (20,40,45). Since the proton hyperfine field primarily arises from the exchange polarization (36,37) from the Ti states at E_F, the proton σ_K and $(T_{1e}T)^{-\frac{1}{2}}$ would readily respond to any variation in $N_d(E_F)$. Thus, the proton parameters may be monitoring subtle differences in the electronic properties of crystalline and amorphous $TiCuH_x$ and Ti_2CuH_x. These materials warrant further study by other techniques that can probe local and total densities of the electronic states.

C. Hydrogen Diffusion Behavior

The NMR techniques have been very successful in evaluating diffusion behavior in many metal-hydrogen systems (10,14-16). Since protons are

spin ½ nuclei without a quadrupole moment to interact with electric field gradients, atomic motion influences proton relaxation only through time dependent modulations of the nuclear dipolar interactions (10). The diffusion correlation time τ_c is the parameter that relates nuclear relaxation times to microscopic diffusion processes. The formal connection between the diffusion coefficient D and τ_c is given by

$$D = K_d \ell^2/\tau_c \qquad (7)$$

where K_d is a numerical parameter for symmetry and possible correlation effects and ℓ is the mean jump distance. Various models have been developed (10) to provide a theoretical framework for τ_c that can reliably describe the diffusion contributions to the nuclear relaxation times. The simple exponential correlation function model of Bloembergen, et al (58), widely called the BPP model, has provided reasonable activation energies (E_a) and relative τ_c values for numerous solids including many metal-hydrogen systems (10,16). However, the absolute τ_c values from the BPP model may be in error by as much as 50% and more detailed models have been developed (10). Unfortunately, these later models are complicated and require explicit computations of lattice summations that are not available (10) except for the simplest cubic lattices. Unless very accurate estimates of D or ℓ are desired, the BPP model is normally adequate to determine the parameters E_a and τ_c with sufficient precision to characterize the major features of diffusion behavior. Since the Ti-Cu hydrides have low symmetry crystal structures and moderately complex diffusion properties (22,33), analyses based solely upon the BPP model have been used to evaluate the diffusion contributions to the proton relaxation time data. This is not a serious limitation since the major intent of these proton NMR measurements has been to understand relative changes in hydrogen diffusion as the crystal structures and interstitial site occupancies are altered. Accurate absolute diffusion rates are not required for these evaluations.

Although most previous determinations of τ_c behavior in metal hydrides have employed (10,16) the diffusion contribution T_{1d} to the proton spin-lattice relaxation times, the low hydrogen mobilities in the Ti-Cu hydrides (22,33) prevented T_1 measurements in the region of the T_1 minima due to the irreversible decompositions of the ternary $TiCuH_x$ and Ti_2CuH_x phases (19,21,22,33) at much lower temperatures. Without the minimum T_1 values meaningful determination of the τ_c parameters from the T_{1d} data is seriously impaired (10,41). Consequently, the prior studies (22,33) of diffusion behavior in $TiCuH_{0.94}$ and a-$TiCuH_{1.3}$ had relied upon the proton T_2 and T_{1D} parameters to obtain the E_a values. However, these parameters can only provide order-of-magnitude estimates for τ_c since it is usually difficult to define (10,16) a quantitative correlation between τ_c and the absolute T_2 and T_{1D} values. Furthermore, the T_2 parameters represent atomic mobility at temperatures above the onset of motional narrowing (i.e., $\gamma_I M_{2D}^{\frac{1}{2}} \tau_c << 1$) where the weak-collision theory (10,16) of nuclear relaxation is valid. Analysis of the experimental T_{1D} values obtained at temperatures below the motional narrowing region requires the strong collision theory (59) to describe the effects of single atomic jumps on the dipolar order. Thus, comparative analyses of the T_2 and T_{1D} data to deduce the τ_c behavior over the entire temperature ranges were not attempted (22) for the $TiCuH_{0.94}$ and a-$TiCuH_{1.3}$ samples.

The proton $T_{1\rho}$ relaxation times offer several advantages in characterizing diffusion behavior in the $TiCuH_x$ and Ti_2CuH_x samples. First, $T_{1\rho}$ is dominated by the diffusion processes over wide ranges of τ_c to include the slow hopping regime (59) well below motional narrowing (i.e., until τ_c approaches 10^{-3} sec). In the present case the $T_{1\rho}$ data in Figure 4 represented proton diffusion in the Ti-Cu hydrides as τ_c varied over four orders-of-magnitude from well below motional narrowing (i.e., upper limits of the T_{1D} results) until the decomposition reactions (19, 21,22,33) altered the diffusion behavior. The presence of distinct and easily detected minima for the $T_{1\rho}$ data in Figure 4 allows straightforward identification of unique τ_c values, within the framework of the weak-

collision theory (10,49,59), at specific temperatures that are not sensitive to the details of a given model (10) in contrast to analyses based upon the T_2 results. The $T_{1\rho}$ data are not particularly sensitive to the various inhomogeneous contributions at zero frequency that can greatly complicate (10,16) the measurement and interpretation of the T_2 parameters. Finally, proton $T_{1\rho}$ data for diffusion in γ-TiH_x are available (49) for direct comparison.

In order to determine the τ_c parameters for the $TiCuH_x$ and Ti_2CuH_x samples, the $T_{1\rho}$ data of Figure 4 were first corrected for small conduction electron contributions (primarily, at the lowest temperatures) with the relation $T_{1\rho}^{-1} = (T_{1\rho})_d^{-1} + (T_{1e})^{-1}$ where the same hyperfine interaction constants are assumed (60) for the proton T_1 and $T_{1\rho}$ relaxation processes. The average $(T_{1e}T)^{-1/2}$ values from Figure 6 were used to estimate the T_{1e} contributions at each temperature. Since the spin-locking fields H_1 for the $T_{1\rho}$ data in Figure 4 obey $H_1^2 >> M_{2D}/3$, the weak collision theory (10,59) remains applicable even at the temperatures below motional narrowing. Using the BPP model for the dipolar correlation function, τ_c^{-1} is obtained from the formula given by Korn and Goren (49)

$$(T_{1\rho})_d^{-1} = 4/3(T_{1\rho})_{d,min}^{-1}\left[\frac{3y}{y^2+4} + \frac{5y}{y^2+a^2} + \frac{2y}{y^2+4a^2}\right] \qquad (8)$$

where $(T_{1\rho})_{d,min}$ is the minimum value of $(T_{1\rho})_d$, $y = (\omega_1\tau_c)^{-1}$, $\omega_1 = \gamma_H H_1$, $a = \omega_o/\omega_1$, and ω_o is the proton resonance frequency in radians/sec. The temperature dependences of the τ_c^{-1} values, which are proportional to D through eqn. (7), for the $TiCuH_x$ and Ti_2CuH_x samples are plotted in Figures 7 and 8. The E_a values and preexponential factors A, where $\tau_c^{-1}(T) = A\exp(-E_a/k_B T)$, are summarized in Table IV along with the temperature for $(T_{1\rho})_{d,min}$, the τ_c^{-1} value at 300 K, and the limits for Arrhenius behavior of τ_c values.

When the τ_c^{-1} values for crystalline $TiCuH_{0.94}$ and amorphous a-$TiCuH_{1.4}$ are compared with τ_c^{-1} results of Korn and Goren (49) for

γ-$TiH_{1.90}$, all of the major observations from the earlier studies involving the T_2 and T_{1D} measurements (22,33) are completely confirmed. First, a much slower hydrogen diffusion rate below 550 K and a larger E_a value are obtained for $TiCuH_{0.94}$ compared to the results for TiH_x as is clearly evident from Figure 7 and Table IV. The greatly enhanced diffusion rate in amorphous a-$TiCuH_{1.4}$ is also unmistakable where its τ_c^{-1} (300 K) is 8×10^5 times larger than the corresponding value for $TiCuH_{0.94}$ and more than 200 times larger than τ_c^{-1} (300 K) for $TiH_{1.81}$. The E_a values for a-$TiCuH_{1.4}$ are smaller than the diffusion activation energies for TiH_x and crystalline $TiCuH_{0.94}$. While τ_c^{-1} for crystalline $TiCuH_{0.94}$ and γ-TiH_x follow Arrhenius behavior over the entire measured temperature ranges, distinct non-Arrhenius temperature dependence is observed for a-$TiCuH_{1.4}$ with three E_a values representing the τ_c^{-1} results between 150 K and 415 K.

The hydrogen diffusion behavior for the crystalline Ti_2CuH_x samples are compared to $TiCuH_{0.94}$ and γ-$TiH_{1.90}$ in Figure 8. The proton mobilities for the Ti_2CuH_x samples are somewhat greater than observed in $TiCuH_{0.94}$ but not quite as rapid as in γ-$TiH_{1.50}$ when the temperature exceeds about 350 K. However, the smaller E_a values for the Ti_2CuH_x samples produce slightly faster mobilities (i.e., larger τ_c^{-1} values) at temperatures below 350 K. Whereas the τ_c^{-1} values for $Ti_2CuH_{1.9}$ follow Arrhenius behavior over the entire range of the $T_{1\rho}$ measurements, two E_a values are required for the $Ti_2CuH_{2.63}$ sample.

The differences in hydrogen diffusion properties in the $Ti_{1-y}Cu_yH_x$ system are believed to illustrate the importance of metal atom structure and hydrogen site occupancy on the microscopic jump processes. The slowest diffusion rate and largest E_a values occur for $TiCuH_{0.94}$ where the crystal structure (see Figure 1) presumably requires (16,33) the H-atoms to jump the high barriers (61) between the nearest neighbor tetrahedral sites within the plane of the double Ti-atom layer. The lower E_a values for γ-TiH_x and $Ti_2CuH_{1.9}$ reflect smaller barriers (61) for jump paths through octahedral interstitial sites. It is interesting to note that in

the hydrides where H-atoms occupy one type of site (i.e., the Ti_4 sites in γ-TiH_x, $TiCuH_{0.94}$, and $Ti_2CuH_{1.9}$) the Arrhenius relation is obeyed throughout the range of the $T_{1\rho}$ measurements. However, the τ_c^{-1} results for $Ti_2CuH_{2.63}$, where the protons occupy both Ti_4 and Ti_4Cu_2 sites according to the M_{2D} analysis given in section V-A, show distinct non-Arrhenius behavior where two E_a values are obtained. It is speculated that the smaller value (i.e., E_a = 0.29 eV) may correspond to jumps among the octahedral sites while the larger E_a is a composite energy (22,62) which represents complex jump paths that involve both the octahedral intermediate sites as well as direct tetrahedral-tetrahedral jumps. In $Ti_2CuH_{1.9}$, the Ti_4Cu_2 sites are presumably vacant and H-atoms in the Ti_4 sites can diffuse without interference by jumping through the normally empty Ti_4Cu_2 sites to give a tendency towards a channel pathway along the c-axis. However, the occupancy of most Ti_4Cu_2 sites in $Ti_2CuH_{2.63}$ would tend to block this channel and the H-atom would often be required to perform direct tetrahedral-tetrahedral jumps before finding a vacant Ti_4Cu_2 site. Of course, assuming H-atoms in the Ti_4Cu_2 sites are more mobile gives an increased probability that a vacant octahedral site becomes available for occupancy by a H-atom from a neighboring Ti_4 site. Consequently, this rather complex diffusion process should yield an intermediate E_a to the activation energies for $TiCuH_{0.94}$ and $Ti_2CuH_{1.9}$. Figure 8 shows that this appears to be the situation above 400 K where the absolute τ_c^{-1} parameters for $Ti_2CuH_{2.63}$ are only slightly larger than the values in $TiCuH_{0.94}$, which is qualitatively consistent with impedance of the more direct jump paths proposed for $Ti_2CuH_{1.9}$. Unfortunately, more complete information on the relative interstitial site occupancies as well as independent estimates of activation energies for the several elementary jump barriers are required before a detailed analysis can be presented. There are simply too many unspecified parameters to give anything other than the present very qualitative description. However, the experimental results in Figure 8 and Table IV are at least consistent with this tentative explanation.

The three E_a values for a-$TiCuH_{1.4}$ from the proton $T_{1\rho}$ measurements are in good agreement with earlier values (22) from the T_2 and T_{1D} data for the a-$TiCuH_{1.3}$ samples at corresponding temperatures. The $T_{1\rho}$ experiments are not sufficiently sensitive to the very slow diffusion contributions to determine whether a smaller E_a exists below 150 K as was suggested by the T_{1D} experiments. If the arguments of the preceding paragraph are extended to a-$TiCuH_x$, three (or four) types of interstitial sites are being occupied by protons in the amorphous phase. The low E_a values imply that direct tetrahedral to tetrahedral jumps are not important hydrogen diffusion pathways in the amorphous phase. Alternative diffusion pathways are permitted in the disordered structure and are probably responsible for the greatly enhanced diffusion in a-$TiCuH_x$ relative to crystalline $TiCuH_{0.94}$. However, the amorphous phase irreversibly decomposes (19,21,22) at such a low temperature (i.e., about 425 K during the NMR experiments) that the possible contributions of tetrahedral to tetrahedral jumps to the overall hydrogen diffusion process are never observed. If amorphous a-$TiCuH_x$ has retained much of the short range order, which has been indicated in the a-$Ti_{1-y}Cu_y$ alloys (46-48), some neighboring Ti_4 sites should exist in a-$TiCuH_x$ and be occupied by H-atoms. However, the microscopic diffusion processes are probably even more complicated than the proposed mechanism for crystalline $Ti_2CuH_{2.63}$. Nevertheless, the sharp breaks in the temperature dependence of τ_c^{-1} for a-$TiCuH_{1.4}$ in Figure 7 as well as in the previous T_2 and T_{1D} data (22) suggest that only a relative few distinct changes in the diffusion process occur rather than a gradual variation from a quasi-continuous distribution of processes with slightly different activation energies. The latter situation would be expected (6) for a completely random arrangement of proton environments in the amorphous hydride. Since only relatively few processes apparently determine the proton diffusion behavior in a-$TiCuH_x$, the retention of short range order in the amorphous hydride may have limited the number of allowed H-atom jump pathways. A brief, qualitative description of the diffusion processes that is similar to the mechanism

proposed above for $Ti_2CuH_{2.63}$ has been given (22). Unfortunately, additional knowledge of the types and distributions of occupied H-sites as well as E_a values are again required before a detailed interpretation of hydrogen diffusion behavior in a-$TiCuH_x$ is attempted.

Although the proton NMR experiments have provided unequivocal evidence for orders-of-magnitude enhancement of the hydrogen diffusion (with accompanying E_a decreases) in amorphous a-$TiCuH_{1.3\pm0.1}$ relative to crystalline $TiCuH_{0.94}$, recent studies of amorphous alloys with low-hydrogen concentrations (26,29-31) indicated that hydrogen mobilities are comparable or even slower (i.e., with larger E_a values) than obtained in essentially identical crystalline alloys. These apparent discrepancies can be reconciled if some reasonable conditions are imposed. First, it is probably safe to assume that at low concentrations most H-atoms in an amorphous alloy are trapped either at defect sites or small voids although this does not appear to have been experimentally demonstrated. A hydrogen in such a trap is more tightly bound than an H-atom in the normal interstitial site and should also have a higher activation barrier (14,15) for any subsequent diffusive jump. However, at large hydrogen concentrations (i.e., in a-$TiCuH_{1.3\pm0.1}$) most H-atoms will occupy a much wider distribution of interstitial sites which may include many sites where the diffusion E_a values are much smaller than the jump paths allowed for sites occupied in the corresponding crystalline structure. Consequently, an enhanced hydrogen diffusion rate with smaller E_a values than are observed in the crystalline phase becomes possible. This is assumed to be the situation for a-$TiCuH_{1.3\pm0.1}$. However, the constraints that are imposed on hydrogen diffusion by the $TiCuH_{1.0}$ crystal structure, whose τ_c^{-1} (300 K) in Table IV is more than three orders-of-magnitude smaller than the corresponding values for γ-TiH_x and Ti_2CuH_x, probably produce an exceptionally large differential between amorphous and crystalline structures. In very recent studies of internal friction in hydrogen doped amorphous a-$Zr_{0.76}Ni_{0.24}$, Agyeman, et al (32) found the relaxation times, which are inversely proportional to D, to decrease and the activation

energies to decrease with the addition of more hydrogen. Hence, their results are in complete accord with the present description. Proton lineshape measurements (28) in crystalline and amorphous $ZrPdH_x$ with $x \geqslant 1.9$ have also indicated greater hydrogen mobility in the amorphous hydride phases. However, extensive and systematic studies of hydrogen diffusion behavior in several amorphous and corresponding crystalline hydrides are needed to establish the specific contributions of short range order and interstitial site occupancies on the basic diffusion mechanisms.

VI. CONCLUSIONS

The NMR measurements of the proton lineshapes, relaxation times T_1 and $T_{1\rho}$, and Knight shifts have indicated that crystal structure and hydrogen site occupancies play important roles on the electronic properties at proton sites and the diffusion behavior. In particular, there are distinct difference between the crystalline and amorphous phases for the Ti-Cu hydrides even though the Ti_4 sites appear to be preferentially occupied in every case. The $N(E_F)$ populations at the proton sites are substantially reduced in $a\text{-}TiCuH_{1.4}$, which seem to be caused by differences in the local electronic structure rather than H-atoms residing in different interstitial sites. The greatly enhanced proton diffusion with small E_a values (relative to $TiCuH_{0.94}$ and $\gamma\text{-}TiH_x$) and non-Arrhenius temperature dependence has been confirmed for amorphous $a\text{-}TiCuH_{1.3\pm0.1}$. The hydrogen diffusion in crystalline Ti_2CuH_x is intermediate to crystalline $TiCuH_{0.94}$ and amorphous $a\text{-}TiCuH_x$ and supports the earlier assertions (16,33,41,61) that lower activation energies occur for H-atom jumps through octahedral sites when compared to direct tetrahedral to tetrahedral jump paths.

ACKNOWLEDGEMENTS

The assistance of Dr. J. F. Lynch with the magnetic susceptibility measurements and of Dr. M. P. Guse with the analysis of the $T_{1\rho}$ data is greatly appreciated. These studies were partially supported by the Division of Chemical Sciences, Office of Basic Energy Sciences, U. S.

Department of Energy, and the Caltech President's Fund. Mound is operated by Monsanto Research Corporation for the U. S. Department of Energy under Contract No. DE-AC04-76-DP00053. Jet Propulsion Laboratory is operated for NASA under Grant No. NAS7-100.

REFERENCES

1. J. Tauc and S. R. Nagel, Comments Sol. State Phys. 7, 69 (1976).
2. W. L. Johnson and M. Tenhover, in The Magnetic, Chemical, and Structural Properties of Glassy Metallic Alloys, edited by R. Hasegawa (CRC Press, Boca, Florida), Chap. 3 (in press).
3. M. Kijek, M. Ahmadzadeh, B. Cantor, and R. W. Cahn, Scripta Met. 14, 1337 (1980).
4. G. Edelin and C. Tete, Scripta Met. 15, 739 (1981).
5. P. Valenta, K. Maier, H. Kronmüller and K. Freitag, Phys. Stat. Sol. (b) 105, 537 (1981).
6. M. Ahmadzadeh and B. Cantor, J. Non-Cryst. Solids 43, 189 (1981).
7. A. C. Switendick, in Hydrogen in Metals I, edited by G. Alefeld and J. Völkl (Springer-Verlag, Berlin, 1978) p. 101.
8. A. C. Switendick, Zeit. Physk. Chem. N.F. 117, 89 (1979).
9. M. Gupta and J. P. Burger, Phys. Rev. B 24, 7099 (1981).
10. R. M. Cotts, in Reference 7, p. 227.
11. H. E. Flotow, Zeit. Physk. Chem. N.F. 116, 95 (1979).
12. J. H. Weaver and D. T. Peterson, J. Less-Common Met. 74, 207 (1980).
13. L. Schlapbach and H. R. Scherrer, Solid State Commun. 41, 893 (1982).
14. J. Völkl and G. Alefeld in Diffusion in Solids, Recent Developments, edited by A. S. Nowick and J. J. Burton (Academic, New York, 1975) p. 231.
15. J. Völkl and G. Alefeld, in Reference 7, p. 321.
16. R. C. Bowman, Jr., in Metal Hydrides, edited by G. Bambakidis (Plenum, New York, 1981) p. 109.
17. A. Amamou, D. Aliaga-Guerra, P. Panissod, G. Krill, and R. Kuentzler, J. de Physique Colloque C8 41, C8-396 (1980).
18. J. Kübler, et al., Phys. Rev. B 23, 5176 (1981).

19. A. J. Maeland in Hydrides for Energy Storage, edited by A. F. Andressen and A. J. Maeland (Pergamon, Oxford, 1978) p. 447.
20. J. J. Rush, J. M. Rowe, and A. J. Maeland, J. Phys. F: Metal Phys. 10, L283 (1980).
21. A. J. Maeland, L. E. Tanner, and G. G. Libowitz, J. Less-Common Met. 74, 279 (1980).
22. R. C. Bowman, Jr. and A. J. Maeland, Phys. Rev. B 24, 2328 (1981).
23. F. H. M. Spit, J. W. Drijver, and S. Radelaar, Zeit. Physk. Chem. N.F. 116, 225 (1979).
24. F. H. M. Spit, J. W. Drijver, W. C. Turkenburg, and S. Radelaar, J. de Physique Colloque C8 41, C8-890 (1980).
25. F. H. M. Spit, J. W. Drijver, W. C. Turkenburg, and S. Radelaar, in Reference 16, p. 345.
26. Y. Takagi and K. Kawamura, Trans. Japan Inst. Metals 22, 677 (1981).
27. T. Kajitani, H. Kaneko, and M. Hirabayashi, Sci. Rep. RITU 29A, 210 (1981).
28. R. C. Bowman, Jr., M. J. Rosker, and W. L. Johnson, submitted to J. Non-Cryst. Solids.
29. B. S. Berry and W. C. Pritchet, J. Appl. Phys. 52, 1865 (1981).
30. B. S. Berry and W. C. Pritchet, Phys. Rev. B 24, 2299 (1981).
31. B. S. Berry and W. C. Pritchet, Scripta Met. 15, 637 (1981).
32. K. Agyeman, et al., J. de Physique Colloque C5 42, C5-535 (1981).
33. R. C. Bowman, Jr., A. Attalla and A. J. Maeland, Solid State Commun. 27, 501 (1978).
34. R. C. Bowman, Jr., A. J. Maeland, W.-K. Rhim, and J. F. Lynch, to be published in Proc. Int. Symp. Electronic Structure and Properties of Hydrogen in Metals, Richmond, VA, March 4-6, 1982.
35. A. J. Maeland and G. G. Libowitz, J. Less-Common Met. 74, 295 (1980).
36. R. C. Bowman, Jr., and W.-K. Rhim, Phys. Rev. B 24, 2232 (1981).
37. R. Göring, R. Lukas, and K. Bohmhammel, J. Phys. C: Solid State Phys. 14, 5675 (1981).

56. I. Bakonyi, L. Takács, and K. Tompa, phys. stat. sol. (b) 103, 489 (1981).

57. A. Narath, in Hyperfine Interactions, edited by A. J. Freeman and R. B. Frankel (Academic, New York, 1967) p. 287.

58. N. Bloembergen, E. M. Purcell, and R. V. Pound, Phys. Rev. 73, 679 (1948).

59. D. C. Ailion, in Advances in Magnetic Resonance, Vol. 5, edited by J. S. Waugh (Academic, New York, 1971) p. 177.

60. M. Goldman, Spin Temperature and Nuclear Magnetic Resonance in Solids (Clarendon, Oxford, 1970).

61. C. L. Bisson and W. D. Wilson, in Proc. Int. Conf. Effects of Hydrogen Behavior in Materials, edited by A. W. Thompson and Petroleum Engineers, New York, 1976) p. 416; C. F. Melius and T. H. Upton, Bull. Am. Phys. Soc. 23, 234 (1978).

62. P. A. Fedders, Phys. Rev. B 18, 1055 (1978).

TABLE I. Experimental second moments (M_{2D}) of the proton lineshapes for the titanium-copper hydrides.

Sample	Metal Sublattice Structure	T (K)	M_{2D} (G^2)
$TiCuH_{0.94}$	Tetragonal	299	18.5[a]
a-$TiCuH_{1.4}$	Amorphous	80	14.8
$Ti_2CuH_{1.9}$	Orthorhombic(?)	289	13.7
$Ti_2CuH_{2.63}$	Orthorhombic(?)	289	14.3

[a]Experimental error of ±0.5 G^2 for all samples.

TABLE II. Comparisons of some calculated dipolar second moments (M_{2D}) for the proton lineshapes in $Ti_2CuH_{1.9}$ and $Ti_2CuH_{2.63}$ where the experimental values from Table I were obtained with magic echo sequence (Ref. 52).

Sample	Metal Structure	Occupancy Factors in the Interstitial Sites	Calculated M_{2D} (G^2)	Experimental M_{2D} (G^2)	Deviation Between M_{2D} Values (%)
$Ti_2CuH_{1.9}$	Tetragonal[a]	0.95 Ti_4	16.2	13.7(5)	+18
$Ti_2CuH_{1.9}$	Orthorhombic[b]	0.95 Ti_4	12.7	13.7(5)	- 7.3
$Ti_2CuH_{2.63}$	Tetragonal[a]	1.00 Ti_4 & 0.63 Ti_2Cu_4	15.8	14.3(5)	+11
$Ti_2CuH_{2.63}$	Tetragonal[a]	1.00 Ti_4 & 0.315 Ti_4Cu_2	18.5	14.3(5)	+29
$Ti_2CuH_{2.63}$	Orthorhombic[b]	1.00 Ti_4 + 0.63 Ti_4Cu_2*	14.5	14.3(5)	+ 1.4

[a]Lattice Parameters: a = 0.3064 nm and c = 1.0963 nm

[b]Lattice Parameters: a = 0.306 nm; b = 0.333 nm; c = 1.01 nm

*Only the Ti_4Cu_2 sites along b-axis can be occupied.

TABLE III. Proton σ_K, $(T_{1e}T)^{-\frac{1}{2}}$, and Korringa parameters for several hydride phases containing titanium.

Sample	T (K)	$(T_{1e}T)^{-\frac{1}{2}}$ $(sK)^{-\frac{1}{2}}$	σ_K (ppm)	q_{exp}	Data Source
$TiCuH_{0.94}$	306	0.163	-121	0.48	Present
	86	0.150	-113	0.46	
$a\text{-}TiCuH_{1.4}$	209	0.111	- 76	0.55	Present
	89	0.108	- 83	0.44	
$Ti_2CuH_{1.9}$	306	0.118	- 68	0.81	Present
	110	0.115	- 69	0.74	
$Ti_2CuH_{2.63}$	297	0.137	- 85	0.69	Present
	88	0.145	- 92	0.68	
$TiH_{1.96}$	296	0.138	-131	0.29	Ref. 36
	107	0.108	- 96	0.34	
$Ti_{0.5}V_{0.5}H_{1.94}$	303	0.170	-159	0.30	Ref. 36
	110	0.163	-161	0.27	
$TiCr_{1.8}H_{2.40}$	80	0.223	- 98	1.62	Ref. 39

TABLE IV. Summary of hydrogen diffusion parameters for Ti_yCuH_x and TiH_x that have been derived from proton $T_{1\rho}$ relaxation times with the exponential correlation time model where $\tau_c^{-1}(T) = A \exp(-E_a/k_BT)$.

Hydride	Structure	Temperature for $T_{1\rho}$ Minimum	τ_c^{-1}(300K) (s^{-1})	A (s^{-1})	E_a (eV)	Temperature Range	Reference
$TiCuH_{0.94}$	Tetragonal	483K	1.1	4.4×10^{14}	0.87 ± 0.03	360 - 560K	Present work
a-$TiCuH_{1.4}$	Amorphous	275K	-	2.8×10^{12}	0.42 ± 0.03	355 - 415K	Present work
			8.0×10^{5}	-	0.22 ± 0.02	210 - 355K	
			-	-	0.089 ± 0.01	150 - 210K	
$Ti_2CuH_{1.9}$	Orthorhombic	424K	5.5×10^{3}	2.5×10^{10}	0.40 ± 0.03	280 - 520K	Present work
$Ti_2CuH_{2.63}$	Orthorhombic	470K	-	2.7×10^{12}	0.64 ± 0.04	425 - 540K	Present work
			5.2×10^{3}	-	0.29 ± 0.02	280 - 405K	
$TiH_{1.81}$	fcc	~410K	3.9×10^{3}	1.29×10^{12}	0.51 ± 0.01	270 - 660K	Korn & Goren
$TiH_{1.90}$	fcc	~430K	2.4×10^{3}	0.793×10^{12}	0.51 ± 0.01	270 - 660K	Korn & Goren

FIGURE CAPTIONS

FIG. 1. Comparison between structures of (a) TiD_2 and (b) TiCuD where for clarity the unit cell (upper figure) of TiCuD is doubled.

FIG. 2. Crystal structure of Ti_2Cu where one of Ti_4 interstitial sites that is a preferred site for hydrogen occupancy has been identified.

FIG. 3. Temperature dependence of proton spin-lattice relaxation times T_1 at a resonance frequency of 56.4 MHz.

FIG. 4. Proton rotating-frame relaxation times $T_{1\rho}$ at a resonance frequency of 34.5 MHz.

FIG. 5. Temperature dependences of proton Knight shifts σ_K relative to external standard of TMS.

FIG. 6. Temperature dependent behavior of $(T_{1e}T)^{-\frac{1}{2}}$ parameters derived from proton T_1 data in Fig. 3.

FIG. 7. Temperature dependences of diffusion jump rates τ_c^{-1} for crystalline and amorphous $TiCuH_x$ that were obtained from $T_{1\rho}$ data. Also shown are the results from $T_{1\rho}$ measurements for $TiH_{1.90}$ by Korn and Goren (Ref. 49).

FIG. 8. Temperature dependences of diffusion jump rates τ_c^{-1} for crystalline $TiCuH_{0.94}$, $Ti_2CuH_{1.9}$, and $Ti_2CuH_{2.63}$ that were obtained from $T_{1\rho}$ data. Also shown are the results from $T_{1\rho}$ measurements for $TiH_{1.90}$ by Korn and Goren (Ref. 49).

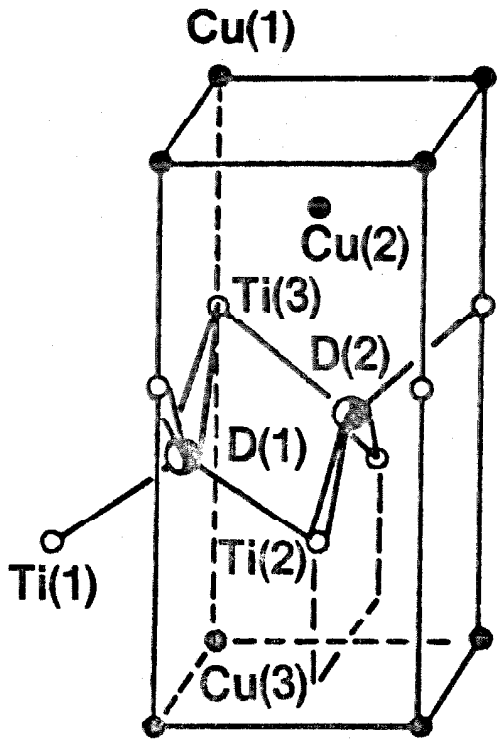

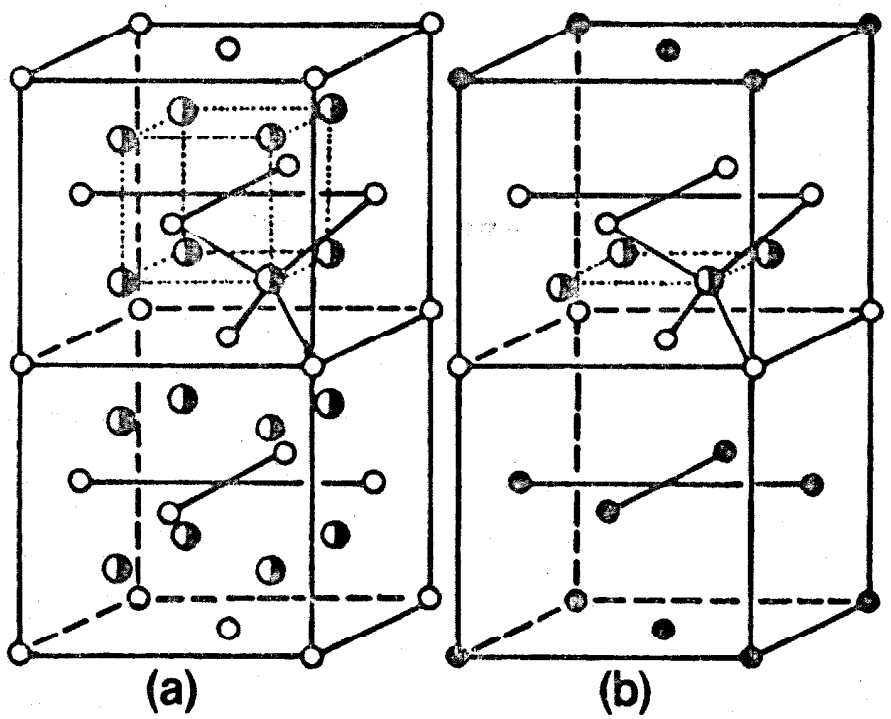

FIGURE 1

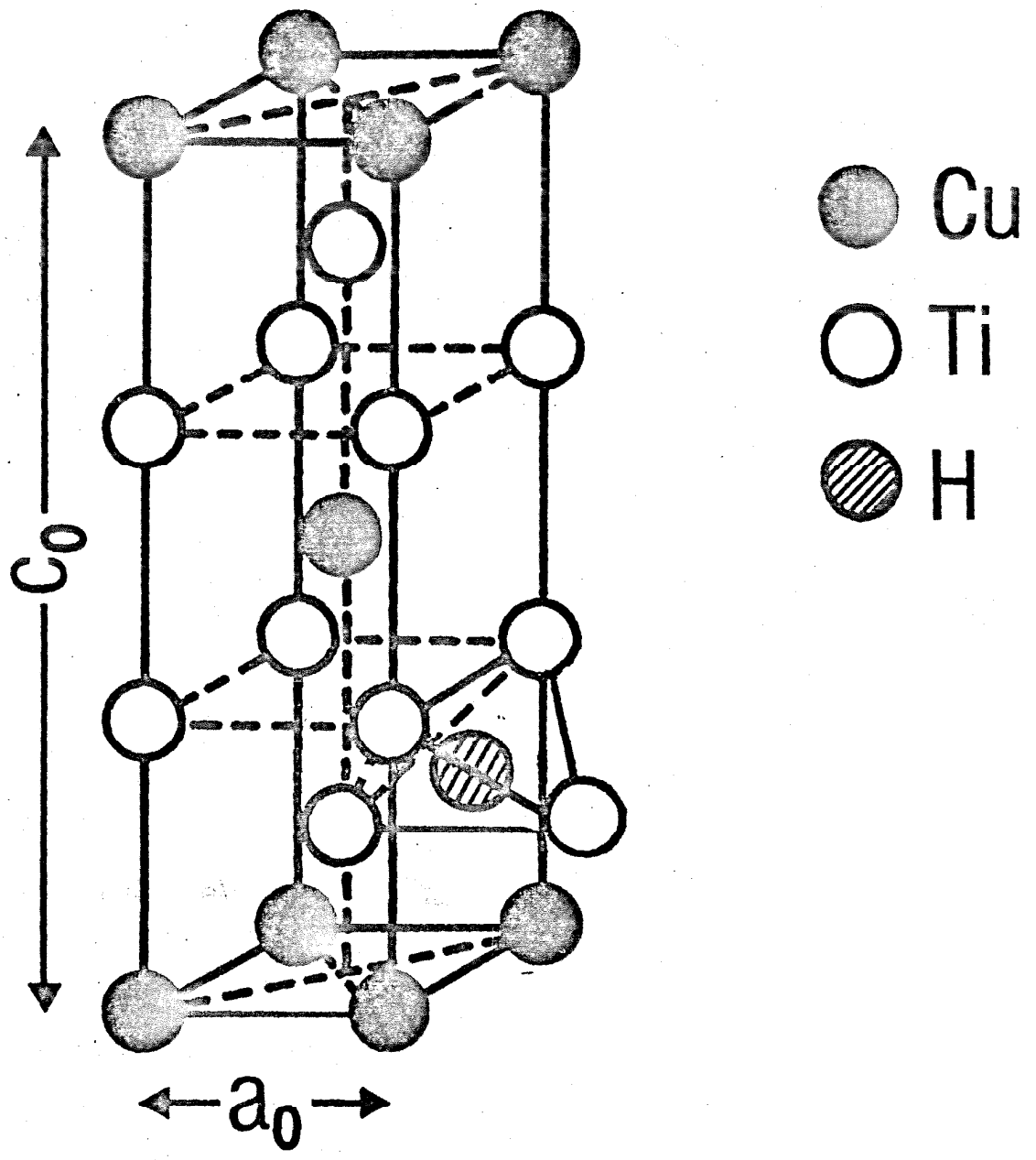

FIGURE 2

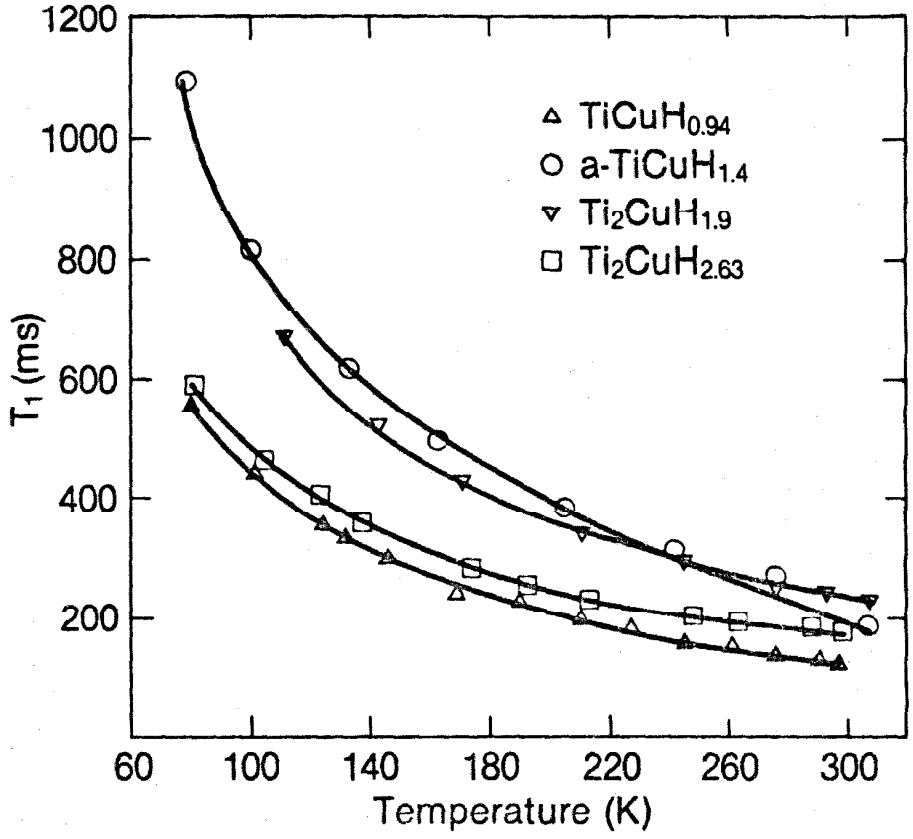
1200
1000
800
600
400
200
T_1 (ms)
60
100
140
180
220
260
300
Temperature (K)
$TiCuH_{0.94}$
a-$TiCuH_{1.4}$
$Ti_2CuH_{1.9}$
$Ti_2CuH_{2.63}$

FIGURE 3

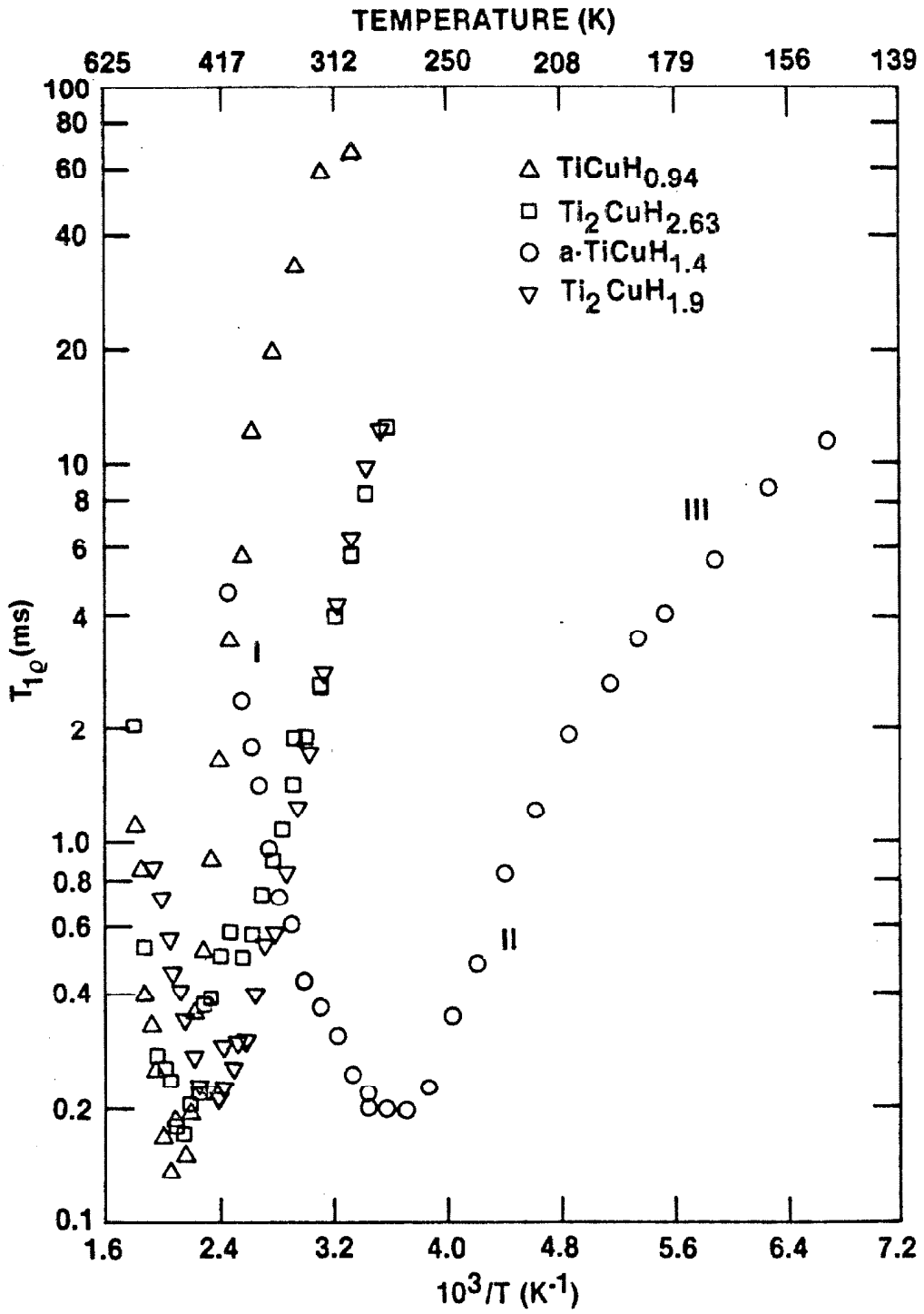
TEMPERATURE (K)
625
417
312
250
208
179
156
139
100
80
60
40
20
10
8
6
4
2
1.0
0.8
0.6
0.4
0.2
0.1
$T_{1\varrho}$(ms)
△ $TiCuH_{0.94}$
□ $Ti_2CuH_{2.63}$
○ a-$TiCuH_{1.4}$
▽ $Ti_2CuH_{1.9}$
I
II
III
1.6
2.4
3.2
4.0
4.8
5.6
6.4
7.2
$10^3/T$ (K^{-1})

FIGURE 4

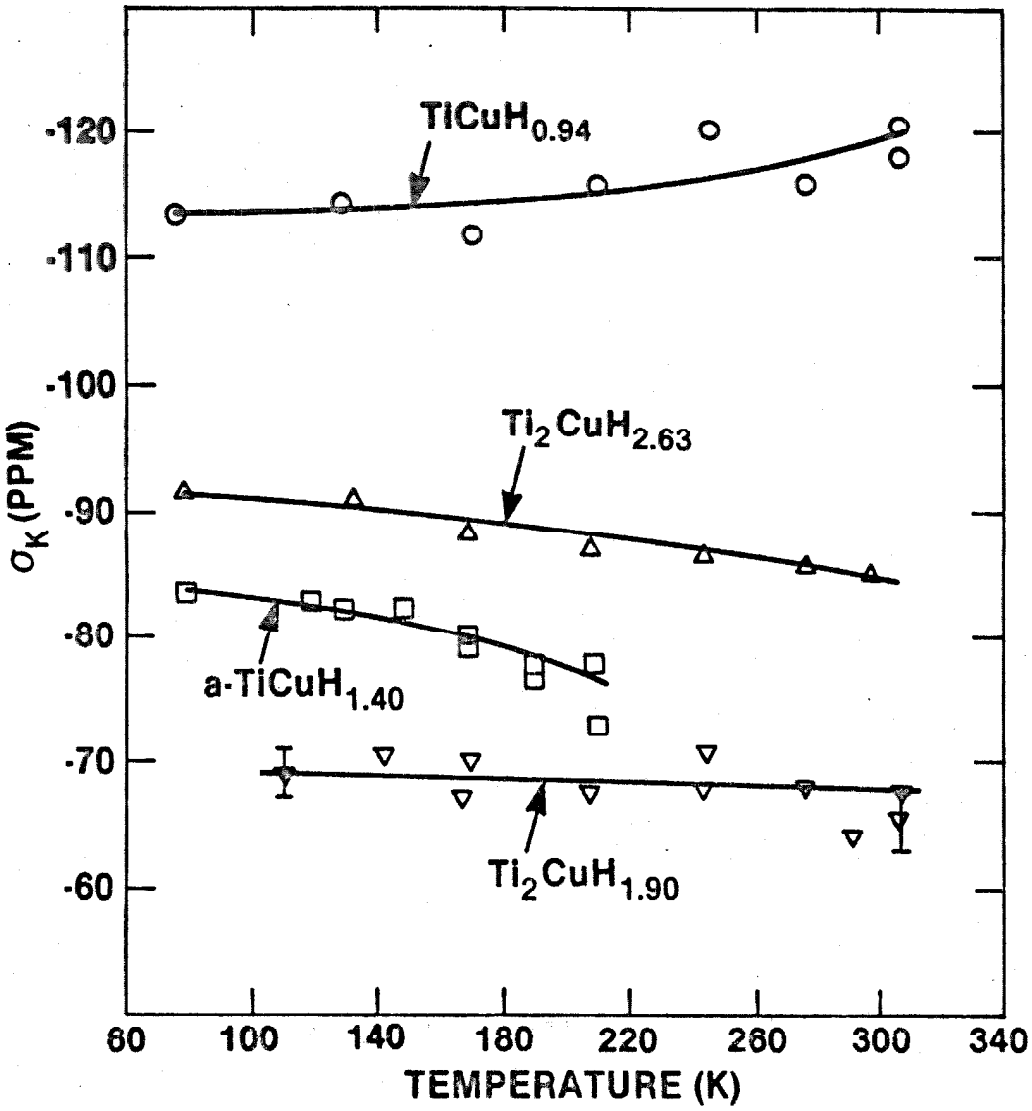
TiCuH0.94
Ti2CuH2.63
a-TiCuH1.40
Ti2CuH1.90
σK (PPM)
-120
-110
-100
-90
-80
-70
-60
60
100
140
180
220
260
300
340
TEMPERATURE (K)

FIGURE 5

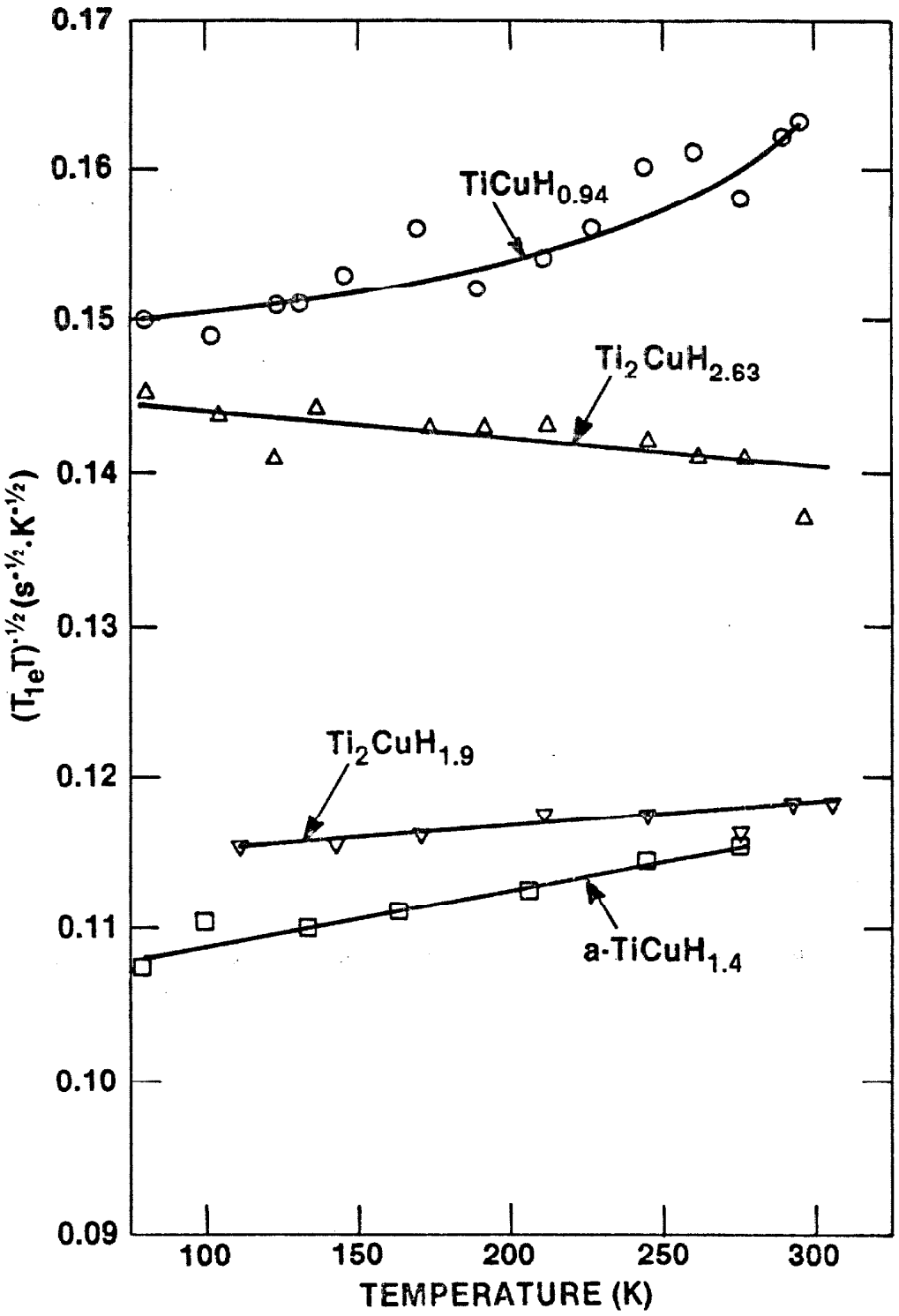
0.17
0.16
0.15
0.14
0.13
0.12
0.11
0.10
0.09
$(T_{1e}T)^{-1/2}(s^{-1/2}.K^{-1/2})$
$TiCuH_{0.94}$
$Ti_2CuH_{2.63}$
$Ti_2CuH_{1.9}$
a-$TiCuH_{1.4}$
100
150
200
250
300
TEMPERATURE (K)

FIGURE 6

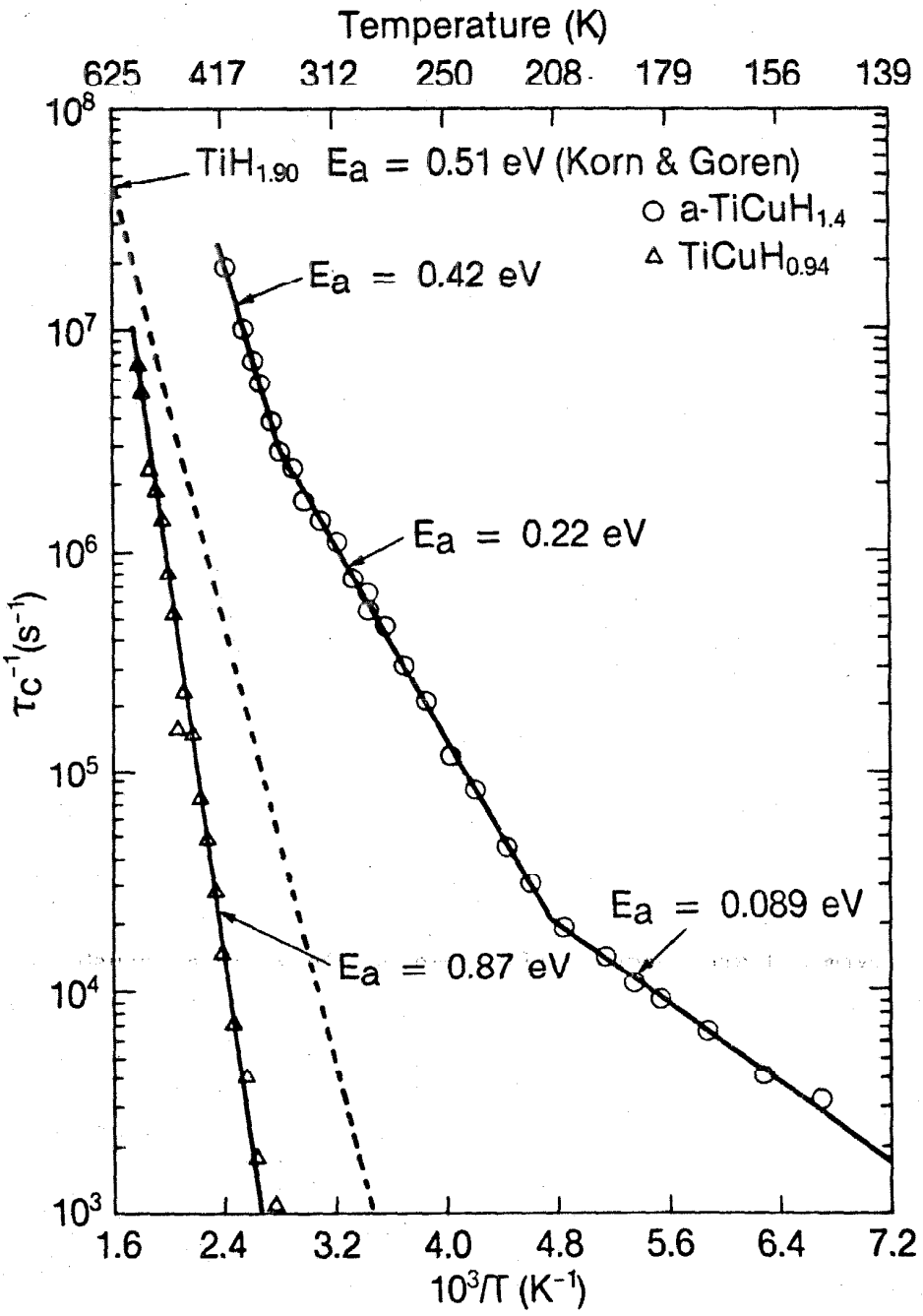
Temperature (K)
625 417 312 250 208 179 156 139
10^8
10^7
10^6
10^5
10^4
10^3
$\tau_c^{-1}(s^{-1})$
$TiH_{1.90}$ E_a = 0.51 eV (Korn & Goren)
○ a-$TiCuH_{1.4}$
△ $TiCuH_{0.94}$
E_a = 0.42 eV
E_a = 0.22 eV
E_a = 0.089 eV
E_a = 0.87 eV
1.6 2.4 3.2 4.0 4.8 5.6 6.4 7.2
$10^3/T$ (K^{-1})

FIGURE 7

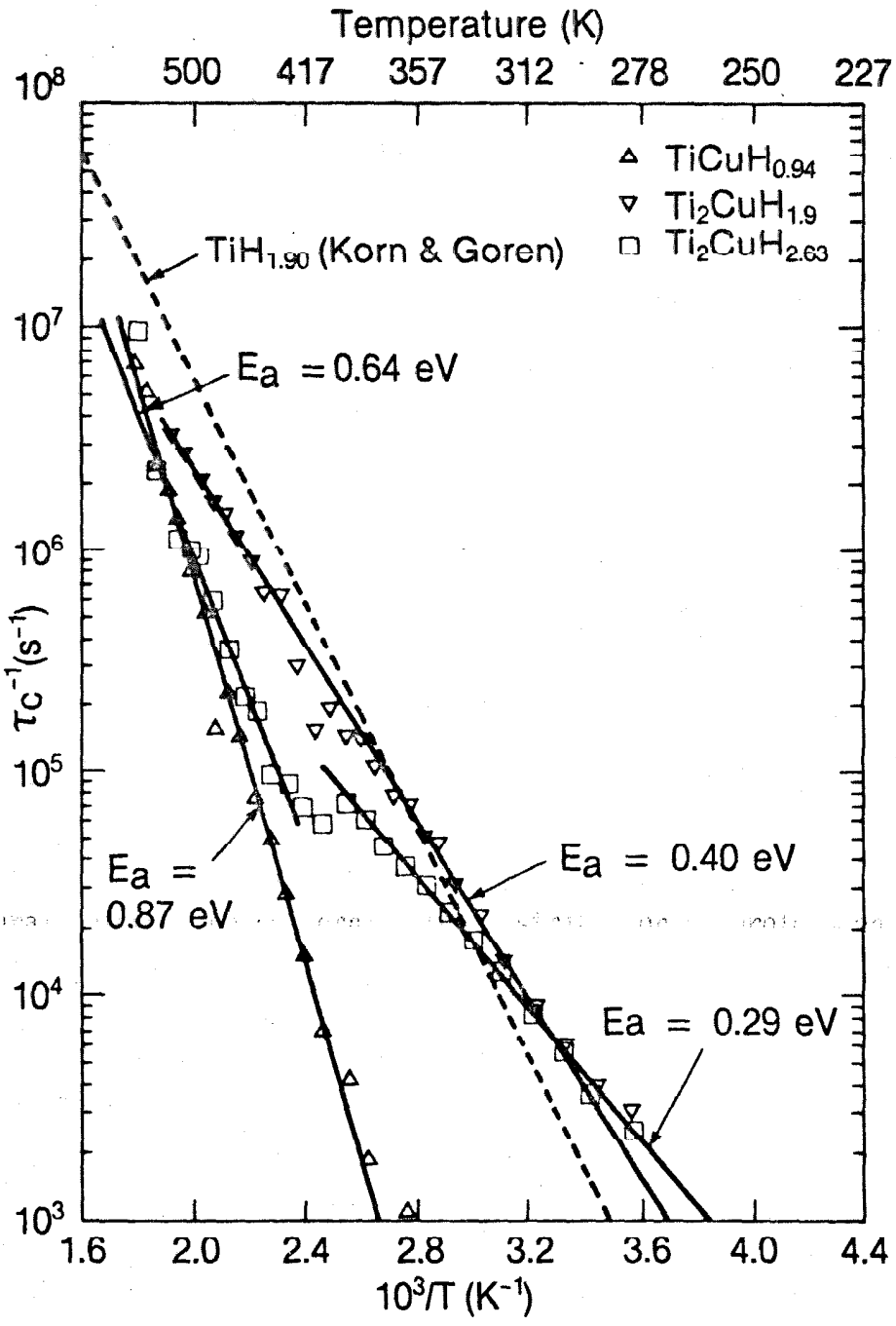
Temperature (K)
500
417
357
312
278
250
227
10^8
10^7
10^6
10^5
10^4
10^3
$\tau_c^{-1}(s^{-1})$
$TiCuH_{0.94}$
$Ti_2CuH_{1.9}$
$Ti_2CuH_{2.63}$
$TiH_{1.90}$ (Korn & Goren)
E_a = 0.64 eV
E_a = 0.87 eV
E_a = 0.40 eV
E_a = 0.29 eV
1.6
2.0
2.4
2.8
3.2
3.6
4.0
4.4
$10^3/T$ (K^{-1})

FIGURE 8

CHAPTER 9

PROTON SITE OCCUPANCIES AND ELECTRONIC PROPERTIES IN CRYSTALLINE AND AMORPHOUS Zr_2PdH_x

ABSTRACT

The proton lineshapes, Knight shifts, and spin-lattice relaxation times have been measured in crystalline and amorphous Zr_2PdH_x. The rigid-lattice proton second moments have been used to identify the interstitial sites occupied by the hydrogen atoms. A preference for tetrahedral sites with as many Zr neighbors as possible was found although octahedral site occupancies were indicated in some samples. Although core-polarization from the Zr d-band appears to dominate the proton hyperfine interactions in Zr_2PdH_x, significant contributions of s-electron through the Fermi contact interactions are also present. The density of d-electron states at Fermi level is apparently reduced in the amorphous phase relative to the density in crystalline Zr_2PdH_x.

I. INTRODUCTION

The reactions between hydrogen and zirconium-palladium alloys to form ternary hydrides have been studied recently by several groups (1-4). Much of this work has been associated with the ability of amorphous $Zr_{1-y}Pd_y$ alloys to form corresponding amorphous hydride phases. Since the crystalline intermetallic Zr_2Pd forms relatively stable ternary hydrides (1), the Zr_2PdH_x system is a very favorable candidate for detailed comparisons between the crystalline and amorphous hydride phases. Some of the topics of greatest interest include the nature of the hydrogen atom occupancies in the interstitial sites (2,4), relative diffusion behavior (3,4), and the electronic structure parameters (4). Although these properties have been studied in some other alloys such as $Ti_{1-y}Cu_yH_x$ (4-7) and $Zr_{1-y}Ni_yH_x$ (8,9), the Zr_2PdH_x system is especially interesting since Zr and Pd form stable binary hydrides which have very different characteristics. For example, hydrogen atoms only occupy tetrahedral sites in the ZrH_x phases (10,11) while hydrogen atoms reside in the octahedral sites in PdH_x. Furthermore, hydrogen diffusion is quite rapid (12) in PdH_x while the ZrH_x phases exhibit much slower hydrogen diffusion rates with relatively high activation energies (12,13). Thus, direct comparisons between the crystalline and amorphous Zr_2PdH_x phases are quite intriguing.

The intermetallic Zr_2Pd crystallizes with a tetragonal structure of the type $C11_b$. Table I summarizes the interstitial sites that are most likely to be occupied in this structure. The quantity n_H represents the number of hydrogen atoms per Zr_2Pd formula unit that can be contained in each site. Since ZrH_x is much more stable than PdH_x, the Zr_4 sites should be preferentially occupied if the ternary Zr_2PdH_x phase retains its original tetragonal structure. However, Maeland and Libowitz (1) obtained the stoichiometry $Zr_2PdH_{2.70}$ with a hydrogen pressure below 1 atm while Spada (14) has obtained compositions near $Zr_2PdH_{4.9}$ for a hydrogen pressure of about 30 atm and the reaction proceeding at room temperature. Hence, interstitial sites in addition to the Zr_4 sites must

also be occupied when $x > 2.0$. Although it was originally thought (1) that all crystalline Zr_2PdH_x phases had tetragonal structures, subsequent x-ray diffraction measurements as well as the present NMR studies have shown the situation to be somewhat more complicated - particularly when $x \approx 3.0$. Although the tetragonal structure appears appropriate for any Zr_2PdH_x samples with $1.6 \lesssim x \lesssim 2.0$ as well as samples with x up to about 3.2 when prepared at temperatures below 520 K (afterwards denoted L.T. for low temperature), the Zr_2PdH_x samples with $x > 2.5$ that were prepared or heated above 700 K have a different structure. This later structure has been tentatively identified as a bcc lattice with a presumably random arrangement of the Zr and Pd atoms. The high temperature structure (denoted by H.T.) seems to be indefinitely stable at room temperature after it had been produced. Because the Zr_2PdH_x reaction and phase transformation rates are sluggish, systematic studies of the composition dependence of these phase transactions remain to be done. Although powder neutron diffraction measurements have been performed (15) on several crystalline Zr_2PdD_x compositions, the crystal structure analyses have been severely hampered by the presence of impurity phases or incomplete transformations between the L.T. and H.T. phases. Consequently, detailed structures are not currently available for the several Zr_2PdD_x phases. Inelastic neutron scattering experiments (16) have indicated hydrogen appears to only occupy tetrahedral sites in $Zr_2PdH_{1.84}$ and H.T.-Zr_2PdH_3 while at least some hydrogen atoms probably occupy octahedral sites in L.T.-$Zr_2PdH_{2.9}$.

Below 488 K, amorphous Zr_2Pd will react with hydrogen gas to produce an amorphous hydride where crystallization has been observed (4) at higher reaction temperatures. The reported preparations (2,3) of amorphous $Zr_{0.65}Pd_{0.35}H_x$ above 495 K are suspicious in light of these results (1). However, amorphous Zr_2PdH_x is certainly more stable than amorphous $TiCuH_x$, which undergoes crystallization as well as phase segregation (5,7) near 420 K.

The present NMR studies concern the roles of crystal structure on

hydrogen site occupancies and electronic properties in crystalline and amorphous Zr_2PdH_x. Analyses of the proton second moments suggest some significant differences exist in hydrogen occupancies in the various Zr_2PdH_x phases. However, tetrahedral site occupancy appears to be preferred when $x < 2.0$ and in the crystalline H.T. phase. The proton Knight shifts and spin-lattice relaxation times imply differences also exist in the density of electronic states at the Fermi energy (E_F) as well as in the relative distribution of d and s state populations at E_F. Although variations in site occupancies probably contribute to these differences, the crystal structure is believed to be an important factor.

II. EXPERIMENTAL DETAILS

The crystalline and amorphous Zr_2PdH_x samples used in the NMR experiments had been prepared by the direct reactions between the metal alloys and hydrogen gas. Further details on the preparative procedures are available elsewhere (1,4). Table II lists the various samples and also includes the reaction temperatures as well as the crystal structures and lattice parameters obtained from powder x-ray diffraction measurements. The NMR samples were sealed in evacuated glass tubes.

The proton lineshapes were measured with a simplified version (17) of the magic echo sequence and the second moments (M_{2D}) were determined from Gaussian plots of the proton lineshapes near the maxima of the magic echoes. The spin-lattice relaxation times (T_1) were measured with the standard inversion recovery method. The proton Knight shifts (σ_K) were measured with the multiple-pulse zero-crossing technique devised by Burum, et al (18). The σ_K data are relative to an external reference of tetramethylsilane and have not been corrected for possible demagnetization effects from the unknown Zr_2PdH_x bulk magnetic susceptibilities. The NMR experiments were performed at a resonance frequency of 56.4 MHz on a wide-band transient spectrometer (17) where the magnetic field was locked by an external probe system.

III. RESULTS AND DISCUSSIONS

A. Proton Lineshapes and Hydrogen Site Occupancies

The room temperature proton lineshapes for the two amorphous a-Zr_2PdH_x samples and the L.T. tetragonal crystalline samples $Zr_2PdH_{2.9}$ and $Zr_2Pd_{3.2}$ were motionally narrowed (19) with decay times $T_2^* \gtrsim 20$ μsec. However, the nearly Gaussian "rigid-lattice" lineshapes were observed at room temperature for the H.T.-Zr_2PdH_x samples and the tetragonal Zr_2PdH_x compositions with $x < 2.0$. Motional narrowing of NMR spectra begins (19) when the mean residence time τ_D for the resonant nucleus on a lattice site becomes smaller than $(\gamma_H^2 M_{2D})^{-\frac{1}{2}}$ where γ_H is the nuclear gyromagnetic ratio. Since the diffusion constant is proportional (19) to τ_D^{-1}, the protons are more mobile in a-Zr_2PdH_x and L.T. crystalline Zr_2PdH_x ($x \geq 2.9$) compared to either H.T.-Zr_2PdH_x or Zr_2PdH_x with $x < 2.0$. Preliminary analyses (4) of the room temperature proton relaxation times T_2^* and $T_{1\rho}$ indicate that hydrogen diffusion is most rapid in the a-Zr_2PdH_x samples. This observation is completely consistent with the proton diffusion behavior found (7,20) for crystalline and amorphous $TiCuH_x$.

The experimental proton M_{2D} parameters for the Zr_2PdH_x samples that were obtained from magic-echo lineshapes at temperatures low enough to satisfy the "rigid-lattice" conditions are presented in Table II. Structural information concerning the distribution of protons on lattice sites can be deduced by comparing the experimental M_{2D} parameters with model calculations (19) involving the nuclear dipolar interactions. Since the ^{91}Zr and ^{105}Pd nuclei have small magnetic moments as well as low isotopic abundance, only the proton-proton dipolar interactions are required for Zr_2PdH_x. To take account of the contributions from protons occupying inequivalent lattice sites, the generalized Van Vleck expression (20)

$$M_{2D} = C_I \sum_{i,j} f_i \alpha_j S_{ij} \qquad (1)$$

is required where $C_I = (9/20)(\gamma_H \hbar)^2$, f_i is the fraction of all protons in sites of type i, α_j is the probability of occupation of a j site, N is

the number of inequivalent proton sites, and $S_{ij} = \sum_j r_{ij}^{-6}$ for the separation r_{ij} between the protons i and j with the origin at i and a summation over all the j sites. Because protons should occupy easily identifiable sites in crystalline Zr_2PdH_x, the M_{2D} calculations with eqn. (1) are, in principle, straightforward. However, unambiguous results are usually difficult if more than two inequivalent lattice sites are occupied unless some supplemental information is available. Because ZrH_x is much more stable than PdH_x, the $Zr_4(T_A)$ interstitial sites are assumed to be the preferred sites for proton occupancy. Unfortunately, there does not appear to be any clear-cut way to rank the relative preference among the $Zr_3Pd(T_B)$, $Zr_2Pd_4(O_A)$, and $Zr_4Pd_2(O_B)$ interstitial sites. Consequently, the M_{2D} calculations have been performed on a number of model structures with protons on various combinations of two inequivalent sites from Table I.

Some calculated dipolar M_{2D} values for protons in the Zr_2PdH_x samples with tetragonal metal lattice are presented in Table III. A preference for proton occupancy in the T_A sites has been assumed. Furthermore, no structure with any H-H separation closer than 0.20 nm has been considered since Switendick (21) has observed the such short H-H separations seem to be absent for a variety of metal hydrides. Although the dipolar M_{2D} values calculated with only T_A occupancy gives reasonable agreement with the experimental results for $Zr_2PdH_{1.68}$ and $Zr_2PdH_{1.84}$, the experimental M_{2D} is significantly smaller than the calculated value for $Zr_2PdH_{1.94}$. The experimental M_{2D} for $Zr_2PdH_{1.94}$ can be obtained by placing 6.0% of the protons on either the O_A or O_B sites. The exclusive occupancy of T_A sites in $Zr_2PdH_{1.84}$ is completely consistent with the inelastic neutron scattering spectrum (16) on a portion of the same sample. However, the presence of a small percentage of protons on octahedral sites is usually difficult to detect by the inelastic scattering technique. Table III shows the calculated M_{2D} values for three model proton arrangements in L.T.-$Zr_2PdH_{2.90}$. Clearly, the best agreement with the experimental M_{2D} is obtained for 100% occupancy of the $Zr_4(T_A)$ sites plus

a random 45% occupancy of the $Zr_4Pd_2(O_B)$ sites. This hydrogen distribution also gives reasonable agreement between calculated and experimental M_{2D} for the L.T.-$Zr_2PdH_{3.2}$ sample. The inelastic neutron scattering vibrational spectra (16) for L.T.-$Zr_2PdH_{2.5}$ and L.T.-Zr_2PdD_3 show the presence of a low energy peak below the dominant peak from hydrogen (or deuterium) in tetrahedral sites that probably corresponds to the significant occupancy of some type of octahedral site. The proton M_{2D} results for L.T.-$Zr_2PdH_{2.9}$ and L.T.-$Zr_2PdH_{3.2}$ imply that Zr_4Pd_2 is this octahedral site. It is interesting to note that the proposed hydrogen arrangement (20) in nearly isomorphic $Ti_2CuH_{2.63}$ consists of hydrogen atoms completely occupying the Ti_4 sites and partially occupying the Ti_4Cu_2 sites. Furthermore, neutron diffraction studies (22) have indicated that Ti_4Fe_2 sites are preferentially occupied by deuterium atoms in β-phase TiFeD and γ-phase $TiFeD_2$. Hence, it now appears that Ti_4B_2 sites are amenable to hydrogen occupancy even though the corresponding BH_x hydride is relatively unstable (i.e., Pd) or nonexistent (i.e., Cu and Fe). However, hydrogen may favor other types of interstitial sites (i.e., Zr_3B or Zr_2B_2) under certain conditions or when specific structural constraints are removed.

The hydrogen distribution in crystalline H.T.-$Zr_2PdH_{\sim 3}$ is apparently very different from the arrangements proposed for L.T.-$Zr_2PdH_{\sim 3}$. No model with protons occupying octahedral sites in addition to the T_A sites would give a calculated dipolar M_{2D} that agreed with the experimental values for H.T.-$Zr_2PdH_{2.90}$ or H.T.-$Zr_2PdH_{2.60}$. If the tetragonal structure is used, the only proton distributions capable of any marginally acceptable agreement placed the protons in two types of tetrahedral sites (i.e., T_A and T_B). However, the x-ray diffraction powder patterns have indicated the metal atoms in H.T.-$Zr_2PdH_{2.9}$ are probably randomly distributed on a bcc lattice. Although there are numerous possible arrangements for hydrogen interstitials in a bcc structure (23), many are excluded by the requirement (21) that hydrogen atoms be separated by at least 0.20 nm. The vibrational spectrum (16) for H.T.-Zr_2PdH_3 consists

of a fairly broad peak at the energy corresponding to tetrahedral site occupancies (10,11) and gives no indication for hydrogen in octahedral sites. Consequently, dipolar M_{2D} parameters for protons in H.T.-Zr_2PdH_x have been calculated for tetrahedral site occupancies on a bcc metal lattice. Table IV shows that protons on either a bcc hydrogen lattice (24) or an ordered sublattice analogous to the NbH structure (23) are much smaller than the experimental M_{2D} values for H.T.-$Zr_2PdH_{2.9}$ and H.T.-$Zr_2PdH_{2.6}$. Hence, these structures must be discarded. However, it is possible to randomly locate the protons on various types of tetrahedral sites (i.e., $Zr_{4-y}Pd_y$) in a bcc metal lattice. In order to simulate the dipolar M_{2D} values for this random proton arrangement, Guse (25) has performed lattice summations using Monte Carlo techniques to calculate average dipolar M_{2D} for bcc Zr_2PdH_x. Table V summarizes the calculated stoichiometries and average dipolar M_{2d} for hydrogen occupancies in tetrahedral sites with increasing numbers of Pd nearest neighbors. The bcc lattice parameter corresponds to H.T.-Zr_2PdH_3 and no proton-proton separations shorter than 0.21 nm have been allowed in the lattice sums. It is immediately clear that proton occupancy in only Zr_4 and Zr_3Pd sites will limit the stoichiometry to a value well below the observed composition of $Zr_2PdH_{\sim 3}$. However, if Zr_2Pd_2 sites can also be occupied, this restriction vanishes. Table IV shows that random proton occupancies in mixed $Zr_{4-y}Pd_y$ sites (including $y \geqslant 2$) gives theoretical M_{2D} parameters in excellent agreement with the experimental values. Although these M_{2D} results cannot distinguish between occupancies in only $Zr_{4-y}Pd_y$ sites with $y \leqslant 2$ or in all $Zr_{4-y}Pd_y$ sites, the absence of hydrogen occupancy in Pd_4 sites in PdH_x suggests that the $ZrPd_3$ and Pd_4 sites are probably unfavorable for protons in H.T.-$Zr_2PdH_{\sim 3}$. However, some other technique (i.e., detailed analysis of suitable neutron diffraction patterns, perhaps) will be necessary to establish the complete structure for H.T.-Zr_2PdH_3. Nevertheless, the proton M_{2D} data in Table IV imply protons occupy several inequivalent $Zr_{4-y}Pd_y$ sites (without significant occupancy in octahedral sites) in the H.T.-Zr_2PdH_x samples.

Since long-range order is absent in amorphous solids, eqn. (1) cannot be directly applied to calculate the dipolar M_{2D} for protons in a-Zr_2PdH_x. If the disorder of the metal lattice in the amorphous phase is neglected, the results in Table V for random proton occupancy of tetrahedral sites in a bcc lattice can provide some qualitative insights on the proton distribution in a-Zr_2PdH_x. From Table II, the proton M_{2D} values for a-$Zr_2PdH_{1.91}$ and a-$Zr_2PdH_{2.85}$ are 9.9 ± 0.3 G^2 and 12.2 ± 0.3 G^2, respectively, where the corresponding dipolar M_{2D} values calculated with random occupancy of only $Zr_{4-y}Pd_y$ sites are 9.2 and 13.7 G^2. This is considered satisfactory agreement since a disordered bcc lattice is a very crude representation of the amorphous structure. Although the calculated M_{2D} is smaller than experimental value for a-$Zr_2PdH_{1.91}$, the theoretical value is too large for a-$Zr_2PdH_{2.85}$. The partial occupancy of octahedral sites in the tetragonal $Zr_2PdH_{\sim 3}$ sample gives a reduced dipolar M_{2D} as indicated in Table III. Hence, it is possible that the octahedral sites in a-Zr_2PdH_x have a greater probability for proton occupancy when $x > 2$. This behavior would be similar to the mixed $Zr_4(T_A)$ and $Zr_4Pd_2(O_B)$ site occupancies in crystalline L.T.-$Zr_2PdH_{\sim 3}$. In fact, the neutron scattering experiments on a-$Zr_{0.65}Pd_{0.35}D_x$ by Kai, et al (2) indicate that the average deuterium sites appear to be tetrahedral when $x = 0.17$ but to be octahedral when $x > 0.5$. Hence, a preferential filling of different interstitial sites could be occurring in the amorphous Zr-Pd hydrides.

Substantial proton occupancy of octahedral sites in crystalline L.T.-$Zr_2PdH_{\sim 3}$ and amorphous a-Zr_2PdH_x may be the major contributor to the motional narrowing of the proton lineshapes at room temperature for these samples, whereas rigid-lattice proton lineshapes are obtained for tetragonal Zr_2PdH_x ($x < 2$) and the presumably bcc H.T.-Zr_2PdH_x where nearly exclusive proton occupancy in tetrahedral sites are estimated from the proton M_{2D} results. NMR studies (17,20) of crystalline and amorphous $Ti_{1-y}Cu_yH_x$ have indicated hydrogen mobilities can be significantly enhanced by the presence and occupancy of octahedral sites in the diffusion

jump paths. Similar effects may exist in the Zr_2PdH_x system. Systematic measurements of hydrogen diffusion behavior as well as more complete structural characterizations for crystalline and amorphous Zr_2PdH_x are highly desirable to clarify this particular relationship between structure and hydrogen diffusion mechanism.

B. Electronic Structure Properties from Proton T_1 and σ_K Parameters

The proton parameters σ_K and T_1 have been related to the electronic properties of several Ti-based hydrides (20,26-28) and ZrH_x (29). The dominant terms for the proton hyperfine interactions in transition metal hydrides (26-29) are the Fermi contact interaction with unpaired s electrons and a "core-polarization" of the spin-paired hydrogen s electrons lying several electron volts below the Fermi level by the unpaired metal d electrons at E_F. Following conventional assumptions (20,28,29), the proton parameters σ_K and T_{1e}, the conduction electron contribution to the spin-lattice relaxation time, are given by the expressions

$$\sigma_K = 2\,\mu_B[H_{hf}(s)N_s(E_F) + H_{hf}(d)N_s(E_F)] \qquad (2)$$

$$(T_{1e}T)^{-1/2} = 4\pi\,\hbar\gamma_H^2 k_B\,\{[H_{hf}(s)N_s(E_F)]^2 + [H_{hf}(d)N_d(E_F)]^2 q\}. \qquad (3)$$

Here, $H_{hf}(s)$ and $H_{hf}(d)$ are the hyperfine fields for the Fermi contact and core polarization interactions, respectively; $\hbar$ is Planck's constant; k_B is Boltzmann's constant, μ_B is the Bohr magnetron; $N_s(E_F)$ and $N_d(E_F)$ are the densities of s and d electron states at the Fermi level, and q is the electron orbital degeneracy reduction factor (28,29). Although $H_{hf}(s)$ is always positive, $H_{hf}(d)$ is usually negative (30) to produce partial cancellations in σ_K when both hyperfine interactions are present.

The temperature dependent behavior of the proton $(T_{1e}T)^{-1/2}$ and σ_K parameters for several Zr_2PdH_x samples are presented in Figures 1 and 2, respectively. Averages of these parameters as well as the values for

protons in crystalline ZrH_x, which had been obtained (29) at a common resonance frequency on the same apparatus, are summarized in Table VI. The negative σ_K values in Figure 2 and Table VI demonstrate the dominance of core-polarization hyperfine interactions for protons in Zr_2PdH_x and ZrH_x. Since $H_{hf}(s)$ is usually much larger (30) than $H_{hd}(d)$, the negative σ_K indicate $N_d(E_F) >> N_s(E_F)$ in these hydrides. Negative σ_K and corresponding large $N_d(E_F)$ to $N_s(E_F)$ ratios have also been observed (20,26-28) in TiH_x and several ternary titanium hydrides. The large $N_d(E_F)$ values imply that E_F lie well within the metal d bands, which is consistent with recent band theory calculations (21,31) for TiH_2 and ZrH_2. Although no experimental or theoretical band structures are available for Zr_2PdH_x, photoemission spectra (32-35) for several crystalline and amorphous $Zr_{1-y}Pd_y$ alloys indicate E_F does lie within a broad peak composed almost entirely of Zr 4d states. Since the proton M_{2d} data imply that hydrogen atoms preferentially occupy the Zr_4 and Zr_4Pd_2 interstitial sites in Zr_2PdH_x, the proton hyperfine interactions should be dominated by the Zr d states at E_F. Hence, the negative proton σ_K values are quite reasonable. The absolute magnitudes of $(T_{1e}T)^{-½}$ and σ_K for Zr_2PdH_x and ZrH_x are substantially smaller than the same parameters for TiH_x (28) and the ternary titanium hydrides (20,26,27). This suggests an overall reduction in $N(E_F)$ for ZrH_x and Zr_2PdH_x relative to the densities of states in the titanium-based hydrides.

The generalized Korringa expression (19,30)

$$q_{exp} = C_K/\sigma_K^2 \, T_{1e}T \qquad (4)$$

provides some additional insights on the character of $N(E_F)$. Here, $C_K = \hbar \gamma_e^2/(4\pi k_B \gamma_H^2)$ where γ_e is the electron gyromagnetic ratio. When electron-electron interactions are neglected (30), $q_{exp} = 1.0$ for the Fermi contact hyperfine term and q_{exp} equals the reduction factor q from eqn. (3), which varies between 0.2 and 0.5 in cubic lattices (30), for the core-polarization hyperfine term. If the core-polarization and

contact interactions make comparable contributions, q_{exp} greater than one becomes possible due to the fortuitous cancellation of positive and negative σ_K terms. The proton q_{exp} values for Zr_2PdH_x and ZrH_x are included in Table VI. Although nearly exclusive core-polarization hyperfine interactions are indicated for fct - ZrH_x and H.T.-$Zr_2PdH_{2.90}$, the contact term appears to make significant contributions in fcc - $ZrH_{1.6}$ and the other Zr_2PdH_x samples since their q_{exp} values greatly exceed one. The Fermi levels for fct - ZrH_x are believed (29) to lie within a local peak of $N_d(E_F)$ and a similar situation may occur for H.T.-$Zr_2PdH_{2.90}$. The larger $N_s(E_F)$ contribution in fcc - $ZrH_{1.60}$ has been attributed (29) to E_F lying below the sharp peak in $N_d(E)$.

Since the details of the Zr_2PdH_x band structures are unknown, specific identifications of the factors responsible for the relatively large $N_s(E_F)$ levels at the proton sites in Zr_2PdH_x are difficult. Changing occupancies of the different interstitial sites (i.e., Zr_4, Zr_4Pd_2, Zr_3Pd, etc.) could play a major role. However, different electronic band structures between the ordered tetragonal lattice and the disordered bcc or amorphous structure could also be very important. Although recent evaluations (33-35) of hydrogen-free amorphous and crystalline $Zr_{1-y}Pd_y$ alloys showed little difference in N(E) and the d-electron configurations, the proton parameters in Zr_2PdH_x may be particularly sensitive to subtle changes in $N_d(E_F)$. The Fermi levels in Zr_2PdH_x will fall within the Zr d-states that should have been extensively modified (21) by the formation of the metal-hydrogen bonds. Since the Pd d-band lies several electron volts below E_F in the $Zr_{1-y}Pd_y$ alloys (32-35), the proton parameters σ_K and $(T_{1e}T)^{-\frac{1}{2}}$ should be dominated by core-polarization interaction with the unpaired d-electrons from Zr while the local Pd d-electron states make only minor contributions. However, the Pd atoms may provide a source of s-electron states at E_F to give a larger $N_s(E_F)$ contributions to the proton parameters in Zr_2PdH_x compared to those in ZrH_x. Only slightly larger $N_s(E_F)$ levels are required to rationalize the larger $(T_{1e})^{-\frac{1}{2}}$ and q_{exp} values for the Zr_2PdH_x samples. Detailed band theory

calculations of the electron densities in tetragonal Zr_2PdH_2 and Zr_2PdH_3 would be extremely useful to more thoroughly pursue these suppositions.

Significant differences between crystalline and amorphous Zr_2PdH_x regarding the electronic structures near the hydrogen atoms can be inferred from the results in Table VI. For both $x \cong 1.9$ and $x \cong 2.9$, the amorphous hydrides a-Zr_2PdH_x have smaller $(T_{1e}T)^{-1/2}$, less negative σ_K, and larger q_{exp} than the corresponding crystalline samples with similar compositions. This behavior can be explained by a reduction of $N_d(E_F)$ in the amorphous hydrides through a smearing of the electronic energy levels in the crystalline Zr_2PdH_x. Since the $N_s(E_F)$ levels probably will not vary between the amorphous and ordered structures, the proton contact hyperfine contributions in a-Zr_2PdH_x and the corresponding crystalline phases should be similar. Thus, the total $N(E_F)$ in Zr_2PdH_x is decreased but the $N_s(E_F)$ proton hyperfine contribution is proportionally larger to greatly increase q_{exp}. Very similar $N_d(E_F)$ reductions in the amorphous phase have been observed (20) in $TiCuH_x$. The possibility that the $N_d(E_F)$ reduction may be a characteristic feature of amorphous transition metal hydrides should be explored in other suitable systems. Photoemission spectroscopy studies of the metal valence bands in crystalline and amorphous $Ti_{1-y}Cu_yH_x$ and $Zr_{1-y}Pd_yH_x$ could help to confirm this suggestion as well as provide a more complete understanding of the electronic properties of transition metal hydrides.

IV. CONCLUSIONS

Although hydrogen atoms in Zr_2PdH_x prefer to occupy tetrahedral sites with as many Zr neighbors as possible, some types of octahedral sites (e.g., Zr_4Pd_2) will be significantly occupied in low-temperature crystalline and the amorphous phases. These conclusions agree with inelastic neutron scattering data. The phase relationships in Zr_2PdH_x are much more complicated than originally suggested (1).

The electronic structure at the proton sites are similar in the ZrH_x and Zr_2PdH_x systems where the transferred core-polarization hyperfine

interactions with the Zr d-bands are dominant. However, large contact contributions arise in Zr_2PdH_x, which imply somewhat greater densities of s-electron states at E_F. As in the $TiCuH_x$ system (20), the amorphous Zr_2PdH_x has smaller $N_d(E_F)$ than the crystalline Zr_2PdH_x hydrides with similar compositions.

REFERENCES

1. A. J. Maeland and G. G. Libowitz, J. Less-Common Met. 74, 295 (1980).
2. K. Kai, T. Fukunaga, T. Nomoto, N. Watanabe, and K. Suzuki, Proc. 4th Int. Conf. on Rapidly Quenched Metals, Sendai, 1981, p. 1609.
3. P. Panissod and T. Mizoguchi, Proc. 4th Int. Conf. on Rapidly Quenched Metals, Sendai, 1981, p. 1621.
4. R. C. Bowman, Jr., M. J. Rosker, and W. L. Johnson, submitted to J. Noncryst. Solids.
5. A. J. Maeland, L. E. Tanner, and G. G. Libowitz, J. Less-Common Met. 74, 279 (1980).
6. J. J. Rush, J. M. Rowe, and A. J. Maeland, J. Phys. F: Met. Phys. 10, L283 (1980).
7. R. C. Bowman, Jr. and A. J. Maeland, Phys. Rev. B24, 2328 (1981).
8. F. H. M. Spit, J. W. Drijver, W. C. Turkenburg, and S. Radelaar, J. de Physique Colloque C8 41, C8-890 (1980).
9. T. Kajitani, H. Kaneko, and M. Hirabayashi, Sci. Rep. RITU 29A, 210 (1981).
10. J. G. Couch, O. K. Harling, and L. C. Clune, Phys. Rev. B4, 2675 (1971).
11. R. Khoda-Bakhsh and D. K. Ross, J. Phys. F: Met. Phys. 12, 15 (1982).
12. J. Völkl and G. Alefeld in Diffusion in Solids-Recent Developments, edited by A. S. Nowick and J. J. Burton (Academic, New York, 1975) p. 231.
13. K. R. Doolan, P. P. Narang, and J. M. Pope, J. Phys. F: Met. Phys. 10, 2073 (1980).
14. F. Spada, private communication of unpublished data.

15. A. Santoro and A. J. Maeland, unpublished results.

16. J. J. Rush and A. J. Maeland, unpublished results.

17. R. C. Bowman, Jr. and W.-K. Rhim, J. Magn. Res. (in press).

18. D. P. Burum, D. D. Elleman, and W.-K. Rhim, J. Chem. Phys. 68, 1164 (1978).

19. R. M. Cotts in Hydrogen in Metals I. Basic Properties, edited by G. Alefeld and J. Völkl (Springer-Verlag, Berlin, 1978) p. 227.

20. R. C. Bowman, Jr., A. J. Maeland, and W.-K. Rhim, submitted to Phys. Rev. B.

21. A. C. Switendick, Zeit. Physk. Chem. N.F. 117, 89 (1979).

22. P. Thompson, M. A. Pick, F. Reidinger, L. M. Corliss, J. M. Hastings, and J. J. Reilly, J. Phys. F: Met. Phys. 8, L75 (1978); J. Phys. F: Met. Phys. 9, L61 (1979).

23. B. Stalinski, Ber. Bunsenges. Physk. Chem. 76, 724 (1972).

24. H. S. Gutowsky and B. R. McGarvey, J. Chem. Phys. 20, 1472 (1952).

25. M. P. Guse, unpublished results.

26. B. Nowak, O. J. Zogal, and M. Minier, J. Phys. C: Solid State Phys. 12, 4591 (1979).

27. R. C. Bowman, Jr. and W.-K. Rhim, Phys. Rev. B24, 2232 (1981).

28. R. Göring, R. Lukas, and K. Bohmhammel, J. Phys. C: Solid State Phys. 14, 5675 (1981).

29. R. C. Bowman, Jr., E. L. Venturini, B. D. Craft, A. Attalla, and D. B. Sullenger, submitted to Phys. Rev. B.

30. A. Narath, in Hyperfine Interactions, edited by A. J. Freeman and R. B. Frankel (Academic, New York, 1967) p. 287.

31. M. Gupta and J. P. Burger, Phys. Rev. B24, 7099 (1981).

32. P. Oelhafen, E. Hauser, H.-J. Güntherodt, and K. H. Bennemann, Phys. Rev. Lett. 43, 1134 (1979).

33. P. Steiner, M. Schmidt, and S. Hüffner, Solid State Commun. 35, 493 (1980).

34. C. F. Hague, et al., J. Phys. F: Met. Phys. 11, L95 (1981).

35. J. Kübler, et al., Phys. Rev. B23, 5176 (1981).

Table I. Characteristics of the interstitial sites that can be occupied by hydrogen atoms in Zr_2Pd with a tetragonal crystal structure of type $C11_b$.

Site Label	Metal Atom Neighbors	Maximum n_H	Comments
T_A	Zr_4	2	Preferred Sites
T_B	Zr_3Pd	2	Nearest neighbors, T_A, T_B, and T_C sites are blocked
T_C	Zr_2Pd_2	2	Nearest neighbor T_A, T_B, and T_C sites are blocked
O_A	Zr_2Pd_4	1	
O_B	Zr_4Pd_2	2	H-atoms are very close to Pd neighbors

Table II. Some properties of the crystalline and amorphous Zr_2PdH_x samples including the second moments (M_{2D}) from the proton NMR lineshapes.

x	Preparation Temperature (K)	Metal Lattice	Lattice Parameters a(nm)	Lattice Parameters c(nm)	Second Moments M_{2D} (G^2)	Second Moments T (K)
1.68	671	tetragonal	0.3317(5)	1.1642(1)	8.4(4)	207
1.84	623	tetragonal	0.3348(5)	1.1571(1)	8.5(3)	207
1.94	755	tetragonal	0.3337(1)	1.1582(1)	8.8(4)	207
2.60	696	bcc[a]	--	--	12.6(3)	288
2.9	440	tetragonal	0.3335(1)	1.1596(2)	10.2(3)	207
2.90	746	bcc[b]	0.3465	--	14.2(5)	288
3.2	510	tetragonal	0.3400(5)	1.1360(5)	12.3(2)	207
1.91	478	Amorphous	--	--	9.9(3)	120
2.85	478	Amorphous	--	--	12.2(3)	80

[a] Some tetragonal phase present.

[b] Small ($\lesssim$10%) amount of tetragonal phase.

Table III. Comparison of calculated dipolar and experimental proton second moments for Zr_2PdH_x samples with the tetragonal $C11_b$ structure where L.T. denotes preparation temperature below 520 K.

Zr_2PdH_x Sample Composition	H-site Occupancy	Calculated M_{2D} (G^2)	Experimental[a] M_{2D} (G^2)
1.68	$T_A(0.84)$	8.55	8.4 ± 0.4
1.84	$T_A(0.92)$	8.86	8.5 ± 0.3
1.94	$T_A(0.97)$	9.54	8.8 ± 0.4
1.94	$T_A(0.915)$ & $O_A(0.11)$	8.80[b]	--
1.94	$T_A(0.915)$ & $O_B(0.055)$	8.80[b]	--
2.90(L.T.)	$T_A(1.00)$ & $O_A(0.90)$	8.92	10.2 ± 0.3
2.90(L.T.)	$T_A(1.00)$ & $O_B(0.45)$	10.03	10.2 ± 0.3
2.90(L.T.)	$T_A(0.5)$[c] & $T_B(0.95)$	15.33	10.2 ± 0.3
3.20(L.T.)	$T_A(1.00)$ & $O_B(0.60)$	10.62	12.3 ± 0.2

[a] Data from Table II.

[b] Solved for H-site occupancies that reproduced experimental value.

[c] An ordered structure where only T_A sites that are not nearest neighbors to T_B sites are occupied by protons.

Table IV. Comparison of the calculated dipolar and experimental proton second moments for Zr_2PdH_x samples with a bcc crystal structure. Random occupancy among all allowed sites is assumed when x is less than maximum.

Sample	H-atom Distribution	Calculated M_{2D} (G^2)	Experimental M_{2D} (G^2)	Lattice Sum Source
H.T.-$Zr_2PdH_{2.90}$	ordered on bcc lattice	6.1	14.2±0.5	Gutowsky & McGarvey (24)
"	NbH superlattice	7.4	"	Stalinski (23)
"	Random on Zr_4, Zr_3Pd, & Zr_2Pd_2 sites	14.0	"	Guse (25)
"	Random on all $Zr_{4-y}Pd_y$ sites	14.0	"	Guse (25)
H.T.-$Zr_2PdH_{2.60}$	ordered on bcc lattice	5.5	12.6±0.3	Gutowsky & McGarvey (24)
"	NbH superlattice	6.7	"	Stalinski (23)
"	Random on Zr_4, Zr_3Pd, & Zr_2Pd_2 sites	12.5	"	Guse (25)
"	Random on all $Zr_{4-y}Pd_y$ sites	12.6	"	Guse (25)

Table V. Theoretical dipolar proton second moments (M_{2D}) for Zr_2PdH_x where the metal atoms are randomly distributed on a bcc lattice (a = 0.3435 nm) and protons only occupy the tetrahedral sites $Zr_{4-y}Pd_y$. These values are the averages of 100 trial calculations performed by Monte Carlo techniques and the occupancy of any two H-sites that are separated by less than 0.21 nm is excluded. The results were obtained by M. P. Guse (Ref. 25).

y	x	M_{2D} (G^2)
0	0.93	9.19
1	2.52	13.81
2	3.35	16.09
3	3.57	16.63
4	3.60	17.42

Table VI. Average values of proton Knight shifts (σ_K), $(T_{1e}T)^{-\frac{1}{2}}$ parameters, and Korringa parameters (q_{exp}) for ZrH_x and crystalline and amorphous zirconium-palladium hydrides.

Sample	Structure	$(T_{1e}T)^{-\frac{1}{2}}$ $(s\ K)^{-\frac{1}{2}}$	σ_K (ppm)	q_{exp}
$Zr_2PdH_{1.94}$	Tetragonal	0.088(4)	-27(2)	2.7(5)
H.T.-$Zr_2PdH_{2.90}$	bcc	0.077(5)	-55(4)	0.50(2)
L.T.-$Zr_2PdH_{3.2}$	Tetragonal	0.075(3)	-22(1)	3.3(3)
a-$Zr_2PdH_{1.89}$	Amorphous	0.072(2)	-17(2)	4.8(8)
a-$Zr_2PdH_{2.88}$	Amorphous	0.070(3)	-12(3)	9(4)
$ZrH_{1.60}$	fcc	0.042(2)	-17(1)	1.6(2)
$ZrH_{1.80}$	fct	0.064(2)	-51(3)	0.42(4)
$ZrH_{1.90}$	fct	0.055(1)	-46(2)	0.39(4)
$ZrH_{2.00}$	fct	0.047(1)	-40(1)	0.37(1)

FIGURE CAPTIONS

FIG. 1. Temperature dependence of proton $(T_1T)^{-\frac{1}{2}}$ for Zr_2PdH_x samples.

FIG. 2. Temperature dependence of proton Knight shifts relative to tetramethylsilane for the Zr_2PdH_x samples.

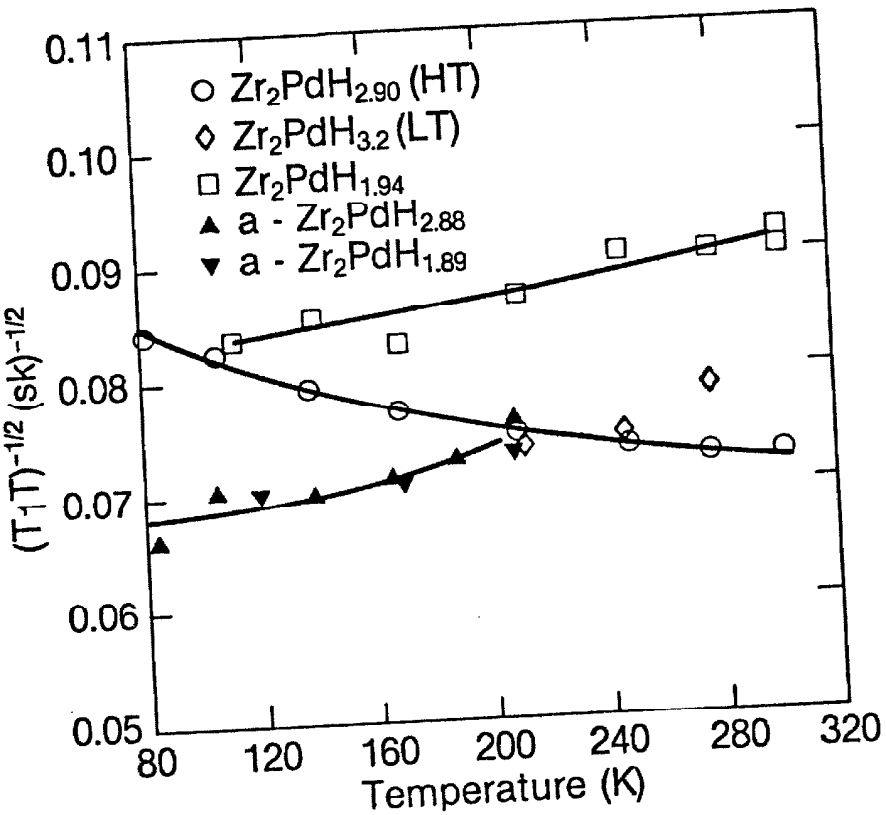
0.11
0.10
0.09
0.08
0.07
0.06
0.05
80
120
160
200
240
280
320
Temperature (K)
$(T_1T)^{-1/2}$ (sK)$^{-1/2}$
○ $Zr_2PdH_{2.90}$ (HT)
◇ $Zr_2PdH_{3.2}$ (LT)
□ $Zr_2PdH_{1.94}$
▲ a - $Zr_2PdH_{2.88}$
▼ a - $Zr_2PdH_{1.89}$

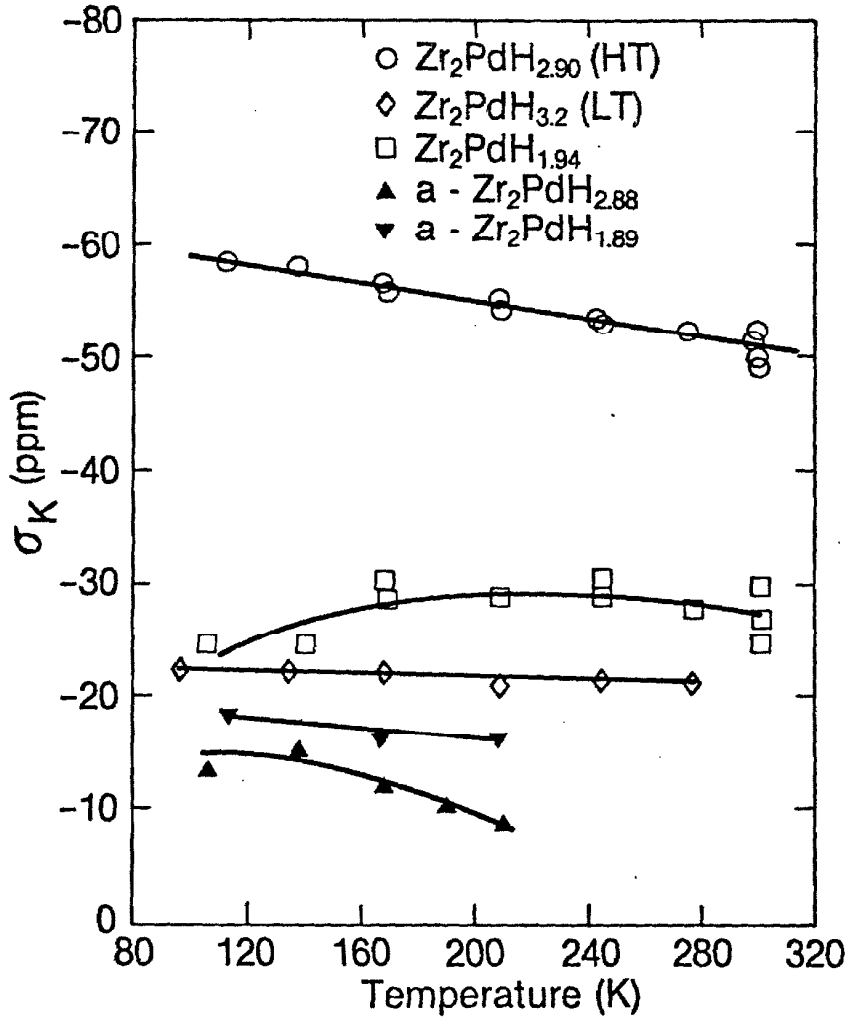
-80
-70
-60
-50
-40
-30
-20
-10
0
80
120
160
200
240
280
320
σ_K (ppm)
Temperature (K)
$Zr_2PdH_{2.90}$ (HT)
$Zr_2PdH_{3.2}$ (LT)
$Zr_2PdH_{1.94}$
a - $Zr_2PdH_{2.88}$
a - $Zr_2PdH_{1.89}$

CHAPTER 10

SUMMARY AND CONCLUSIONS

The proton lineshapes, relaxation times, and Knight shifts have been measured in several transition metal hydrides with the primary objective of evaluating the hydrogen site occupancies and electronic structure properties. Although the previous chapters might suggest some arbitrariness in the systems chosen for study, there are actually many common or closely related characteristics in these hydrides. For example, Ti and Zr are isoelectronic and form very similar hydrides based upon the same fcc structure, which is the same structure as found for VH_2. Furthermore, the crystal structure of TiCuH is essentially a two-dimensional analog of TiH_2 and the structures of Ti_2Cu and Zr_2Pd are similar to TiCuH while the Laves $TiCr_2H_x$ systems have been reported to transform to a disordered structure analogous to TiH_2. The hydrogen atoms prefer tetrahedral sites in all these systems. The available experimental and theoretical evidence places the Fermi level in the metal d-bands that are primarily associated with Ti or Zr atomic states. The $Ti_{1-y}Cu_y$ and $Zr_{1-y}Pd_y$ alloys form amorphous alloys in composition regions of ordered intermetallic phases.

The intent of the present work has been to extend proton NMR from its traditional application of characterizing the diffusion behavior in metal hydrides to include more detailed evaluations of hydrogen site locations and electronic structures. To accomplish this task, some recently developed solid-state techniques were utilized for the first time on metal hydrides. The simplified magic-echo sequence and the multiple-pulse zero-crossing methods were found to be extremely successful when used to measure the proton lineshapes and Knight shifts, respectively. In order to explore the metal hydrides, the same types of experiments were performed on different (but related) systems rather than concentrating in greater detail upon one or two of the more involved hydrides. This choice was influenced by several factors. The need exists to try the new techniques on simple hydrides, where more supplemental data are available, before examining the complex materials. The second moments correspond to powder averages and have limited interpretive power if more

than two inequivalent sites are simultaneously occupied by the protons. Although the zero-crossing technique yields frequency shifts with a precision of ±1-2 ppm, the absolute values of the proton Knight shifts cannot be determined with an accuracy better than ±5-10 ppm because of the chemical shift and bulk susceptibility corrections. Furthermore, the proton hyperfine fields $H_{hf}(s)$ and $H_{hf}(d)$ cannot be reliably estimated from the NMR data alone, which prevent quantitative assessments of the partial densities of states at E_F. Important supplemental experimental results (i.e., lattice parameters, magnetic susceptibilities, photoemission spectra, etc.) are either incomplete or unavailable for the ternary hydrides while only limited theoretical electronic band structure results are currently available. Consequently, comparative evaluations that can identify trends among related systems have been emphasized during the present studies. This approach is within the current capabilities of the utilized NMR techniques.

The highlights of the NMR experiments presented in this thesis can be summarized as follows:

1) The simplified version of the magic echo sequence generates rigid-lattice proton spectra that can be readily analyzed for the second moment M_{2D}. The experimental M_{2D} values for polycrystalline TiH_x and ZrH_x are in excellent agreement with the theoretical dipolar values. In contrast to previous reports of anomalously broad proton lineshapes and large M_{2D} in ZrH_x, the present M_{2D} values for high-purity ZrH_x can be accurately described by dipolar interactions for protons that occupy tetrahedral sites.

2) The proton site occupancies are very similar for the structurally related orthorhombic Ti_2CuH_x and tetragonal Zr_2PdH_x systems with a nearly exclusive occupancy of the A_4 (i.e., Ti_4 or Zr_4) sites when $x < 2$ and the additional occupancy of the A_4B_2 sites when $x > 2$. Mixed tetrahedral and octahedral site occupancies were indicated for the amorphous a-$TiCuH_{1.4}$ and a-Zr_2PdH_x samples while only tetrahedral sites are occupied in crystalline $TiCuH_{0.94}$ and bcc $Zr_2PdH_{2.9}$.

3) The multiple-pulse zero-crossing technique provides accurate measurements of the "average" proton shifts over wide temperature ranges for all the samples investigated, which includes several with large heteronuclear dipolar interactions.

4) Analyses of the proton Knight shifts and conduction electron contribution to proton spin-lattice relaxation times suggest a universal dominance of a core-polarization hyperfine interaction which places the Fermi levels for the Ti and Zr-based hydrides in the metal d-bands. This conclusion is consistent with the available band theory calculations of the electronic structure for these hydrides.

5) A generalized version of the Korringa relation has provided qualitative estimates of the relative populations of s and d electron states at the Fermi levels, which has verified the dominance of d-electron hyperfine interactions at the proton sites.

6) The proton parameters σ_K and T_{1e} for $Ti_{1-y}V_yH_{1.95}$ and ZrH_x ($1.5 \leqslant x \leqslant 2.0$) are entirely consistent with the predictions of the Jahn-Teller model, which related the tetragonal distortions of these cubic hydrides to a splitting of initially degenerate electron states at the Fermi level. Qualitative differences in Jahn-Teller modification of the density of states are proposed for isoelectronic TiH_x and ZrH_x.

7) The proton parameters indicate $N(E_F)$ increases with hydrogen content in $TiCr_{1.8}H_x$, $TiCr_{1.9}H_x$, and Ti_2CuH_x. Although this finding is consistent with the magnetic susceptibilities measured for these particular hydrides, it is opposite to the $N(E_F)$ behavior observed in most other metal-hydrogen systems. It appears that E_F falls on a rising portion or peak in the density of states as a rather special characteristic of Ti-based hydrides. This possibility merits further experimental as well as theoretical study.

8) Significant differences in $N(E_F)$ at the proton sites are observed with the crystalline and amorphous phases of $TiCuH_x$ and Zr_2PdH_x. A tentative interpretation for the reduced $N(E_F)$ levels in the

amorphous hydrides assumes a general smearing of the energy levels that exist in the corresponding crystalline structures. However, some differences in hydrogen site occupancies could also contribute although the proton M_{2D} data imply this may be unlikely.

9) The proton relaxation time measurements in the $Ti_{1-y}Cu_yH_x$ systems indicate the importance of crystalline structure and hydrogen site occupancies on the hydrogen diffusion processes. In particular, the activation energies become much smaller when octahedral sites are introduced in the diffusion path between two tetrahedral sites. A significant enhancement in the apparent hydrogen mobility in the amorphous a-$TiCuH_{1.3}$ phase has been confirmed.

It is hoped that the present research has demonstrated the usefulness of solid-state proton NMR to characterize transition metal hydrides and will stimulate further work in this area. In particular, detailed band structure calculations of tetragonally distorted and non-stoichiometric TiH_x and ZrH_x as well as the various ternary hydrides would be very desirable to provide more quantitative tests of the proposed electronic structures at hydrogen sites. More photoemission spectroscopy studies that also include the amorphous and crystalline ternary hydrides would be very helpful. However, the solid-state proton NMR studies will provide unique information on the structural and electronic properties at the hydrogen site that supplement any of the conventional experimental techniques normally used to evaluate metallic solids. Hence, proton NMR should play greater and more important roles in future studies of the metal hydrides.

PROPOSITIONS

PROPOSITION 1.

NMR RELAXATION AND SELF-DIFFUSION IN CADMIUM FLUORIDE

ABSTRACT

Pulsed NMR measurements of the ^{19}F relaxation times are proposed to determine the ionic transport behavior in pure and doped CdF_2 single crystals. The objectives are to obtain more reliable defect formation and mobility energies and establish if this material becomes a Type II superionic conductor below its melting point.

Within the past few years the transport properties of superionic conductors (i.e., solids whose ionic conductivities are typical of molten salts) have been receiving increasing attention (1). This interest is due to the development of high-performance batteries using superionic conductors as well as the opportunity to gain insights into the dynamics of systems with properties common to both solids and liquids. The connection between ionic conductivity $\sigma(T)$ and ionic transport processes can be made through the Nernst-Einstein expression

$$\sigma(T) = n(T)(Ze)^2 D(T)/k_B T \qquad (1)$$

where $n(T)$ is the concentration of ionic charge carriers at a given temperature T, (Ze) is the electric charge, $D(T)$ is the diffusion coefficient of these ions, and k_B is the Boltzmann's constant. The unique feature of superionic conductors is that ions in one sublattice appear to form a charged ionic liquid which diffuses among the excess empty lattice sites created by the crystalline matrix of essentially immobile ions of the other sublattice. Boyce and Huberman(2) have classified superionic conductors into three general types:

a. Type I exhibits a well-defined first order phase transition where the conductivity jumps by several orders of magnitude at the superionic phase transition temperature. An example is AgI.
b. Type II has a gradual transition from the insulating to conducting state with saturation of $\sigma(T)$ accompanied by a peak in the specific heat. This type is represented by PbF_2.
c. Type III shows a low activation energy exponential increase in an anomalously high conductivity over large temperature regions. An example is sodium-beta-alumina.

Although Type II superionic conductors have not been studied as extensively as Types I and III, these former materials possess several properties that make them slightly more amenable to the comprehensive analyses required to establish the complex dynamical processes involved in the formation of the molten sublattice. Most Type II conductors have the

relatively simple fluorite crystal structure which consists of a face-centered cubic arrangement of cations and the anions occupying all the tetrahedral sites to form a simple cubic sublattice. The anions are mobile while the cations form the immobile FCC cage sublattice. Diffraction studies(3) have shown that the immobile sublattice in Type II conductors is the same in both the low temperature insulating and high temperature conducting phases and the mobile anions disorder gradually from the simple cubic sublattice to previously unoccupied interstitial sites as the temperature increases. Since this disordering occurs over a rather wide temperature range about the transition temperature (T_c) which is usually taken(2) to be the temperature for the peak in the specific heat, it should be possible to experimentally characterize the transformation to the superionic state by techniques sensitive to either lattice site occupancy (i.e., diffraction) or dynamical properties (i.e., vibrational frequencies or diffusion parameters). In fact, the recent reviews by Boyce and Huberman(2) and Shapiro and Reidinger(3) indicate a number of such studies have been performed on Type II conductors-primarily on the halides with fluorite structures-as well as supplemental theoretical model calculations of various dynamical behavior. However, there exists such a diversity of observations and alternative interpretations that a comprehensive mechanism to describe ionic transport behavior in the Type II superionic region remains undeveloped. Table 1 compares the superionic transition temperature for several halides with fluorite structure. For the purposes of the present proposition, CdF_2 with its unknown T_c is also included. PdF_2 has the lowest known T_c for a Type II fluorite conductor and has been extensively studied (1-3).

The absence of a measured T_c for CdF_2 is particularly noteworthy since its estimated value may be ~1100 K using the average T_c/T_{melt} ratio for all the other halides in Table 1 or possibly as low as ~870 K considering only the PdF_2 ratio. On the other hand, Shapiro and Reidinger (3) have observed that T_c for the fluorites appears to be approximately linearly correlated with the frequency (ω_{TO}) of the transverse optic mode.

Table 1. Transition and melting temperatures for Type II ionic conductors with fluorite structure (after Boyce and Huberman[2]).

halide	Mobile Ion	T_c (K)	T_{melt} (K)
PbF_2	F	703	1095
CaF_2	F	1423	1691
SrF_2	F	1453	1673
BaF_2	F	1233	1593
CdF_2	F	?	1351
$SrCl_2$	Cl	993	1148

Gobeau, et al(4) obtained $\omega_{TO} = 217\ cm^{-1}$ for CdF_2 from infrared and Raman measurements. When this frequency is used in the Shapiro-Reidinger correlation, the estimated T_c is ~1400 K. Since this temperature is above the CdF_2 melting point, CdF_2 would not exhibit any superionic conductivity region. Although several conductivity studies of CdF_2 have been published (5-7), they provide little information on the high temperature ionic behavior since above about 600 K, CdF_2 becomes a semiconductor and electron transport processes completely mask the ionic contributions to conductivity. Furthermore, unless great precautions to avoid impurity contamination are taken, irreproducible and unrealistic results(6,7) can be obtained from the conductivity data below 600 K. Consequently, there are still incomplete evaluations of the formation and transport parameters of the defects responsible for ionic transport in CdF_2.

Nuclear magnetic resonance (NMR) is a powerful and versatile technique that provides microscopic information of the motions of ions. Consequently, NMR has been extensively applied to the three types of superionic conducting materials as described in the recent reviews of Boyce and Huberman(2) and Richards(8). Because NMR works equally well for both electronic conducting and insulating materials, it can be used to determine the ionic contribution to conductivity under conditions where

electron transport is a major contributor. The various nuclear relaxation times yield the most complete information on the diffusion process. For nuclei with spin quantum number I = ½, only the magnetic dipolar interactions contribute to nuclear relaxation processes as long as paramagnetic impurity concentrations are low. The theory of nuclear spin relaxation caused by self-diffusion of the nuclei, which modulates the nuclear dipole-dipole interactions has been well established.

NMR relaxation times have generated D values in excellent agreement with conductivity results that used equ. (1) to determine D over ten orders of magnitude in pure and doped BaF_2 crystals(9), which covers a temperature range between 300 and 1200 K. Furthermore, NMR has been used to monitor fluorine mobility in PbF_2(10,11) through temperatures well above T_c and yielded results entirely consistent with independent ionic conductivity measurements.

It is proposed to characterize the ionic transport behavior of CdF_2 between 300 K and about 1300 K with NMR measurements of the ^{19}F relaxation times T_1, $T_{1\rho}$, and T_2. Since NMR should work as well for CdF_2 as BaF_2 or PdF_2, the absence of any previous NMR study of ionic motion in CdF_2 was a rather surprising result of a literature search. Besides the previously mentioned ionic conductivity studies(5-7), the only other measurements of ionic transport in CdF_2 was the use of radioactive ^{18}F tracers by Süptitz, et al(12). These workers found CdF_2 to behave like a typical fluorite where the fluorine diffusion is much larger than cation diffusion and is consistent with anion Frenkel disorder. However, Süptitz, et al(12) presented only a relatively limited amount of data covering the temperature range 540-1010 K and give no indication of the very large diffusion constants expected (2) for a Type II conductor in the region of T_c. Since the ^{19}F relaxation times should not be seriously affected if the CdF_2 samples become semiconductors (in contrast, to conductivity measurements), it should be possible to follow ionic transport with NMR up to near its melting point. Consequently, more complete determination of the CdF_2 defect formation and mobility parameters will be available to compare

with the ^{18}F tracer results.

Before continuing a description of the proposed NMR study of CdF_2, a brief review of the point defects in halides with the fluorite structure will be helpful. The predominant intrinsic defects are the anion-Frenkel pair-consisting of X^- vacancies and X^- interstitials. The two most probable diffusion mechanisms are vacancy jumps or non-collinear interstitialcy displacements. Doping with substitutional M^{+3} cations will create X^- interstitials while doping with substitutional M^+ cations will create X^- vacancies. The added impurities can be associated with oppositely charge defects on neighboring sites to form electrically neutral pairs. However, at sufficiently elevated temperatures (i.e., usually above 400 K-500 K for most fluorites) association becomes negligible and the free defect concentration will equal the concentration of the aliovalent impurity. In this temperature region (usually called extrinsic) the diffusion activation energy corresponds exactly to the free energy (g_m) of the mobile defect. Since X^- vacancies have been found more mobile in fluorites, M^+ cations will increase D while M^{+3} will decrease D in the extrinsic range. When the thermally induced Frenkel defects greatly exceed the number of impurity induced defects, the diffusion constant will have a temperature dependence proportional to $g_m + g_F/2$ where g_F is the Gibbs free energy for the formation of the anion Frenkel pair. This temperature range is known as the intrinsic region. Superionic conductivity begins in the upper temperature range of the intrinsic region when the concentration of interstitials and vacancies becomes so large that sublattice melting occurs. Large correlations in X^- motions are now predicted(2) and the apparent diffusion activation energy decreases(2,10,11).

In order to obtain the maximum information on ionic transport behavior in CdF_2, NMR relaxation time measurements are required on three distinct samples: 1) highest purity CdF_2 available; 2) CdF_2 doped with about 200 ppm La^{+3}; 3) CdF_2 doped with 200 ppm Na^+. These samples should be single crystals to minimize possible contamination from surface reactions (i.e., attack from traces of moisture or oxygen). A conventional pulse

NMR spectrometer, which is capable of applications to solids, should be suitable for measurements of the ^{19}F relaxation times T_1, $T_{1\rho}$, and T_2. The only specialized instrumental component would be a high temperature probe (9) capable of temperatures approaching 1300 K. The volume in the sample region should be minimized to inhibit CdF_2 vaporization and not contain materials such as silica, which apparently reacts with CdF_2 above 600 K (7,12). Collection of the ^{19}F relaxation time data should be straightforward. Subsequent data analysis to extract the correlation time and diffusion parameters has been facilitated by the published(9) numerical parameters for fluorite structure materials.

The anticipated results of this proposed NMR study of CdF_2 will now be briefly summarized. From the earlier conductivity(5-7) and ^{18}F tracer studies(12), CdF_2 should exhibit ionic transport behavior below about 1000K that is typical of fluorite materials. Since F^- vacancies should dominate the diffusion mechanism, the $T_{1\rho}$ minima in Na-CdF_2 and La-CdF_2 will occur at lower and higher temperatures, respectively, relative to pure CdF_2. The temperature dependences of the F^- correlation times in the three samples will permit determination(2,8-11) of the defect enthalpies for Frenkel-pair formation, free vacancy motion, and free interstitial motion. Comparisons of these results for CdF_2 with published parameters on the other fluorite structure fluorides should provide interesting insights on the role of cation mass and ionic size on F^- mobility and defect formation. If CdF_2 exhibits superionic behavior below its melting point (possibly as low as ~900 K), the ^{19}F relaxation times should establish its occurrence in a manner analogous to the previous observations(10,11) on PbF_2. Namely, in the region where fluorine sublattice melting begins, the temperature dependence of correlation times from the ^{19}F T_1 data should first give an anomalously large increase followed by a saturation (i.e., significant decrease in slope) above T_c. Consequently, these NMR measurements should indicate whether fluoride ions will give mobility behavior consistent with superionic processes with an estimate of its transition temperature or retain normal ionic transport near its melting point as predicted by the

Shapiro-Reidinger correlation (3). As a final point, conductivity measurements of CdF_2 cannot provide an answer since electron transport dominates (6,7) above 600 K; however, NMR should accurately monitor F^- mobility behavior in semiconducting CdF_2.

REFERENCES

1. P. Vashishta, J. N. Mundy, and G. K. Shenoy (Eds), Fast Ion Transport in Solids-Electrodes and Electrolytes (North-Holland, New York, 1979).
2. J. B. Boyce and B. A. Huberman, Phys. Repts. 51, 189 (1979).
3. S. M. Shapiro and F. Reidinger in Physics of Superionic Conductors, M. B. Salamon (Eds.) (Springer-Verlag, Berlin, 1979), p. 45.
4. J. Gobeau, M. Heuret, J. P. Mon, and K. Recker, phys. stat. sol. (a) 20, 687 (1973).
5. Y. T. Tan and D. Kramp, J. Chem. Phys. 53, 3691 (1970) and 55, 5146 (1971).
6. M. Cyris, P. Müller, and J. Teltow, J. Physique Coll. C9 34, C63 (1973).
7. J. Oberschmidt and D. Lazarus, Phys. Rev. B21, 5813 (1980).
8. P. M. Richards, in Physics of Superionic Conductors, M. B. Salamon (Ed), (Springer-Verlag, Berlin, 1979) p. 141.
9. D. R. Figueroa, A. V. Chadwick, and J. H. Strange, J. Phys. C: Solid State Phys. 11 55 (1978); D. R. Figueroa, J. H. Strange, and D. Wolf, Phys. Rev. B19, 148 (1979).
10. J. B. Boyce, J. C. Mikkelsen, Jr., and M. O'Keefe, Sol St. Comm. 21, 955 (1977).
11. R. E. Gordon and J. H. Strange, J. Phys. C: Solid State Phys. 11, 3213 (1978).
12. P. Süptitz, E. Brink, and D. Becker, phys. stat. sol.(b) 54, 713 (1972).

PROPOSITION 2.

CHARACTERIZATION OF RADIOLUMINESCENCE IN TRITIATED ICE

ABSTRACT

A spectroscopic study involving simultaneous measurements of optical emission and EPR spectra of tritiated samples of H_2O, D_2O, and T_2O cooled to 78 K is proposed. The purpose of this study is to identify the transient species, created by the tritium beta particles, that are responsible for the frequently observed, but poorly understood, radioluminescence.

The radiolysis behavior in the three states of water is a vast field and has been extensively studied (1,2) over the years. However, the radiolysis processes are so varied and complex that while the main features appear to be well established, many details remain unresolved. Considering only the neutral (i.e., pH $\approx$7) solid phase, radiolysis of ice produces (1,2) the molecular species H_2, O_2, and H_2O_2; various metastable paramagnetic free radicals OH, H, e^-_s (solvated electron), HO_2, O^-, and, possibly, H_3O; and, possibly, transient excited molecule states of the various species H_2O^*, OH^-*, H_3O^+*, and H^-*. The formation and reactions of the transient excited species remain the most poorly understood aspect of radiolytic behavior.

A literature search revealed several previous observations of luminescence from irradiated ice samples. X-rays have produced luminescence (3-5) in crystalline H_2O and D_2O ices below 200 K while stimulated luminescence has been reported (6,7) for γ-irradiated H_2O and D_2O ices. Finally, there are two early and brief descriptions of self-induced radioluminescence in H_2O containing 3% tritium (3) and T_2O ice containing ~99% tritium (8). The radioluminescence spectra of the isotopic ice samples consist of two bands peaked at about 375 nm and 535 nm. Steen and Holteng (5) have concluded these two bands arise from different species created by different mechanisms. Furthermore, large isotope differences have been found. The 535 nm band is absent (or very weak) in H_2O ice (5), about equal intensity with 375 nm band in D_2O ice (5), and is dominant in the T_2O ice spectra (8). Steen and Holteng (5) also reported that the 375 nm consisted of both fluorescent (lifetime $\lesssim 10^{-4}$ sec) and phosphorescence (lifetime $\geqslant$1 msec) components whereas the 535 nm had no phosphorescent component since it decays completely within 10^{-4} sec. The species corresponding to the 375 nm band increases (5) with continuing irradiation, but the species producing the 535 nm band remained constant during irradiation. Although the early work of Grossweiner and Matheson (3,4) suggested neutralization of cation impurities as being responsible for the 375 nm band, the later work (5-7)

clearly indicated radioluminescence in ice is predominantly intrinsic and cannot be associated with cation impurities. However, interpretation of the optical spectra during radioluminescence remains very controversial. Bernas and T. B. Truong (6) have postulated that triplet state H_2O^* from the reaction

$$(H_3O^+)_{hyd} + e^- \rightarrow H + H_2O^* \qquad (1)$$

responsible for the 375 nm band and later rejected (7) contributions from excited neutral radiolysis products (i.e., H*, OH*, etc.) as well as excited OH^-* and H^-* species. However, using the observation that electron and OH scavengers do not affect radioluminescence behavior, Steel and Holteng (5) do not accept eqn. (1) as the likely mechanism for the production of H_2O^*. Steen and Holteng (5) also presented contradictory evidence on the role of H-atoms as a luminescence species. In spite of extensive optical studies involving temperature variations, isotopic mixtures, various electron and hole scavengers, and kinetics measurements, Steen and Holteng (5) were unable to give the probable identities of either the luminescent species or their precursors. Apparently, optical techniques by themselves are insufficient to establish the radioluminescence mechanisms in ice.

In order to provide new insights of the radioluminescence mechanisms in ice with emphasis on identifying the responsible radiation produced species, a combined optical-electron paramagnetic resonance (EPR) study of tritiated ice samples is proposed. The tritiated samples are to be prepared by reacting (8) accurately known mixtures of the gaseous hydrogen isotopes with CuO and trapping the resulting pure water vapor in a cooled quartz tube. The sample tube will be contained in a variable temperature liquid nitrogen dewar of a commercial EPR x-band microwave cavity which has an optical window on one wall to permit essentially unobstructive detection of the luminescence. The optical system would consist of a calibrated monochromator and photomultiplier-detector

similar to the one described by Steen and Holteng (5). This arrangement should yield simultaneous measurements of the optical emission spectra and EPR spectra of the paramagnetic species produced by the constant irradiation of the tritium beta decay. Although initial measurements will be at 78 K, the temperature dependence could be easily monitored with this system. Table 1 lists the five tritiated ice samples that are required for an initial characterization of radioluminescence behavior in tritiated ices.

Table 1. Tritiated ice samples with calculated radiation does rate (average energy of tritium beta particle is 5.9 KeV).

Sample	Composition	Dose Rate (eV/g-min)
A	T_2O	3.5×10^{19}
B	HTO	1.9×10^{19}
C	DTO	1.8×10^{19}
D	H_2O(3.6% T)	1.3×10^{18}
E	D_2O(3.6% T)	1.3×10^{18}

Sample D and E will experience a dose rate nearly equal to the x-ray irradiated H_2O and D_2O ice samples, respectively, of Steen and Holteng (5). This should permit more reliable comparisons on the luminescence behavior for x-ray and beta particles. The simultaneous recording of the time dependence of the optical emissions and EPR spectra for each sample should greatly facilitate determining whether any of the paramagnetic species can be correlated with either luminescent species or their products.

The advantages in using tritium for EPR studies of self-radiolysis was first mentioned by Kroh, et al (9). Since the tritium beta particles have very low energies (<18 KeV) and short ranges (<1 μm in most solids), they give little, if any, radiation damage in the quartz sample tube to doses of about 10^{21} eV/g (9,10). Using relative low tritium

concentrations ($\leq$0.04% T) to produce paramagnetic defects in frozen H_2O and D_2O at 77 K, Kroh, et al (9,10) obtained identical EPR spectra as observed (11) in γ-irradiated H_2O and D_2O ices under similar conditions. Table 2 summarizes the EPR parameters for the paramagnetic species found (9-13) in H_2O ice irradiated at low temperatures.

Table 2. EPR parameters in tritium (dose rate $\leq 1.3 \times 10^{16}$ eV/g-min) and γ-irradiated ice.

Species	g-factor	Spectra	Hyperfine splitting(G)	Comments
H	2.002	doublet	510	Stable below 50 K in in pure ice, below ~100 K in acidic glasses
OH	g_x=2.06	broad	--	
	$g_y=g_z$=2.01	doublet	40	Stable below 140 K
HO_2	2.00	distorted doublet	~20	Stable above 140 K
e^-_s	2.002	singlet	--	Intense blue color, usually seen only in basic ices
$^{16}O^-$	$g_\perp$=2.083	singlet	--	
	g_{11}=2.002	singlet	--	Stable below 30 K

It is important to note that for the low dose rate of $\sim 10^{16}$ eV/g-min (relative to samples A to E in Table 1), Kroh, et al (10) did not obtain EPR spectra for H-atoms or e_s^- from pure ice at 78 K. Furthermore, the concentration of OH species appeared (10) to saturate near 10^{18} spins/g with a much smaller HO_2 content. Since H and T are both I = ½ nuclei with tritium having a 6.7% larger magnetic moment, EPR spectra from free radical species containing T-nuclei will be easy to identify for samples A, B, and C. Deuterium with I = 1 and a much smaller magnetic moment is also easy to distinguish for the free radicals in Table 2.

Although paramagnetic species are not required for radioluminescence, there are at least five distinct paramagnetic species which

may be associated with one or both luminescent bands in irradiated ice. These free radicals are O^-, triplet state H_2O^*, H^-*, H-atoms, and H_3O. Although the earlier EPR studies (9-11) did not detect H-atoms in pure ice at 77 K, the 10^3-10^4 greater dose rate for samples A, B, and C may produce a much higher steady state concentration of H-atoms. Assuming the lifetime of an individual H-atom gives the lower limit of the spin-lattice relaxation time, average H-atom lifetimes $\geq 10^{-8}$ sec will yield EPR linewidths sufficiently narrow (i.e., <50 G) to permit ready detection. If the species H_3O is present during irradiation of ice, it should be easy to identify by its 1: 3: 3:1 quartet hyperfine splittings. Since isolated triplet states give distinctive EPR spectra (14) as well as possible double quantum transition spectra, it should be possible to determine whether the excited triplet states H_2O^* or H^-* are present during the radioluminescence of ice and can be associated with either or both bands in the emission spectra. If the radioluminescent process involves O^-* decay to produce paramagnetic O^- species, the expected O^- EPR spectra (13) will not show any hyperfine effect with the H, D, or T isotopes. Isotope effects will play a crucial role in both the analysis and interpretation of the radioluminescence of tritiated ice. Differences in hyperfine spectra will assist in correctly identifying which free radicals are present. Furthermore, the isotopic differences in the emission spectra (i.e., the relative contribution of the 535 nm band) may be directly correlated with the concentration of the paramagnetic species and allow assignment of specific transient species to each band. Enhancements of a particular isotopic free radical may reflect dynamic differences in the luminescence mechanisms as discussed by Steen and Holteng (5). In conclusion, the proposed EPR-optical spectroscopic study of the tritiated ice samples listed in Table 1 should provide a more comprehensive assessment of the radioluminescence. These measurements should help resolve the controversies concerning which transient species are responsible for a very interesting aspect of the radiation damage behavior in ice.

REFERENCES

1. J. K. Thomas, in Advances in Radiation Chemistry, Vol. 1, M. Burton and J. Magee (Eds.) (Wiley-Interscience, New York, 1969) p. 103.
2. J. H. O'Donnell and D. F. Sangster, Principles of Radiation Chemistry (Elsevier, New York, 1970), Chap. 6.
3. L. I. Grossweiner and M. S. Matheson, J. Chem. Phys. 20, 1654 (1952).
4. L. I. Grossweiner and M. S. Matheson, J. Chem. Phys. 22, 1514 (1954).
5. H. B. Steen and J. Aa. Holteng, J. Chem. Phys. Phys. 63, 2690 (1975).
6. A. Bernas and T. B. Truong, Chem. Phys. Lett. 29, 585 (1974).
7. A. Bernas and T. B. Truong, Chem. Phys. Lett. 39, 379 (1976).
8. W. M. Jones, J. Chem. Phys. 20, 1974 (1952).
9. J. Kroh, B. C. Green, and J. W. T. Spinks, Nature 189, 655 (1961).
10. J. Kroh, B. C. Green, and J. W. T. Spinks, Can. J. Chem. 40, 413 (1962).
11. S. Siegel, J. M. Flournoy, and L. H. Baum, J. Chem. Phys. 34, 1782 (1961); H. S. Judeikis, J. M. Flournoy, and S. Siegel, J. Chem. Phys. 37, 2272 (1962); J. M. Flournoy, L. H. Baum, and S. Siegel, J. Chem. Phys. 36, 2229 (1962).
12. H. C. Box, Radiation Effects: ESR and ENDOR Analysis (Academic, New York, 1977).
13. M. C. R. Symons, J. Chem. Soc. Faraday Trans. I 78, 1953 (1982).
14. J. E. Wertz and J. R. Bolton, Electron Spin Resonance (McGraw-Hill, New York, 1972), Chap. 10.

PROPOSITION 3.

DEGRADATION OF $CaNi_5H_x$ DURING THERMAL CYCLING

ABSTRACT

The potential self-decomposition of the $CaNi_5H_x$ phase during thermally induced absorption-desorption cycles will be evaluated by combined volumetric-NMR study. The proton lineshapes and spin echo decays should be able to establish whether the expected degradation occurs via the irreversible formation of the stable CaH_2 phase.

Within the past few years, metal hydrides have received increasing attention as potential energy storage systems (1,2). The prime consideration in these applications is a sufficiently rapid and reversible reaction between the 'metal' and gaseous hydrogen. The development of the moderately unstable hydride phases of intermetallic compounds has provided the major impetus for these applications (1,2). The desired reaction between an intermetallic and hydrogen can be written

$$AB_n + xH_2 \rightleftarrows ABH_{x/2} \qquad (1)$$

where metal A forms a stable binary hydride AH_x, but metal B either forms no hydride or else a very unstable one. If B were to form a stable BH_x phase, the ternary $ABH_{x/2}$ is almost certain to be sufficiently stable to preclude energy storage applications. However, AB_n could also disproportionate according to the alternate reactions

$$AB_n + xH_2 \rightleftarrows AH_{x/2} + nB \qquad (2)$$

or

$$AB_n + \frac{xy}{(n+y)} H_2 \rightleftarrows \frac{y}{(n+y)} AH_{x/2} + \frac{n}{(n+y)} AB_{n+y} \qquad (3)$$

where, for simplicity, the enriched intermetallic AB_{n+y} is also assumed not to form a hydride. In nearly all intermetallics currently being considered (1,2) for energy storage applications, thermodynamics predict AH_x formation through the reactions of eqns. (2) or (3) should be favored. However, numerous relatively low temperature (i.e., below 200 - 300°C) reactions have yielded distinct ternary AB_nH_x phases. It is currently believed (1) that the limited diffusion of the A and B atoms at these reaction temperatures inhibits phase segregation to produce the metastable AB_nH_x in preference to the predicted AH_x.

For any application the intermetallic must undergo literally thousands of the hydriding-dehydriding cycles corresponding to eqn. (1) without significant degradation which would reduce hydrogen storage capacity

or otherwise interfere. The recent photoelectron spectroscopy and magnetization studies of Schlapbach, et al (3) have clearly shown that many intermetallics (i.e., TiFe, $LaNi_5$, Mg_2Ni, and $ErFe_2$) experience a decomposition on the surface to form oxide AO_y and, generally, free metal B. When the hydrogen gas is very pure, this decomposition is too small to limit total AB_nH_x composition and, actually, promotes (3) the hydride reaction. However, oxygen, water, or other impurities can induce more extensive surface segregation until the AB_nH_x composition is seriously reduced as has been observed by many researchers. In addition, the thermal cycling in very pure hydrogen could give bulk decompositions from reactions analogous to eqns. (2) and (3). When Reilly (4) subjected $TiFeH_x$ to ~13,000 hydriding-dehydriding cycles in the temperature range: -7°C to +110°C, he saw no deterioration in storage capacity and did not detect the presence of any TiH_2 or Fe by x-ray diffraction. However, Cohen, et al (5) recently found the storage capacity of $La_{0.9}Eu_{0.1}Ni_{4.6}Mn_{0.4}H_x$ reduced to only 29% of its initial value after ~1500 cycles between 25 and 307°C. Using ^{151}Eu Mössbauer spectroscopy, Cohen, et al (5) found a dehydrided sample after 1500 cycles to consist of both hydrided and "pure" metal phases. They proposed this hydride was $La(Eu)H_{\sim 3}$. Subsequent ^{61}Ni Mössbauer measurements (6) indicated ferromagnetic Ni metal in thermally cycled $LaNi_5H_x$, but the x-ray diffraction patterns of degraded $LaNi_5H_x$ did not yield (5,6) the lines expected for LaH_x ($x \cong 2$-3) or free nickel. Sheft, et al (7) has reported the plateau (i.e., effective storage) capacity of $CaNi_5$ to be substantially reduced when contained with hydrogen over long time periods. Although x-ray diffraction and magnetic susceptibility measurements indicated some free nickel and Ca_2Ni_7, Sheft, et al (7) did not detect the expected CaH_2 and were not willing to interpret their observations in terms of reactions (2) and (3).

With excellent physical properties including very rapid hydriding-dehydriding kinetics and wide ranges of plateau pressures using alloy substitution, the AB_5 intermetallics are leading candidates (1,2,7) for

many storage applications. However, the recent observations of Cohen, et al (5,6) and Sheft, et al (7) raise the disturbing possibility that many AB_5 materials may follow eqns. (2) and (3) during thermal cycling. Hence, there is a need to verify whether AH_x formation and segregation can occur under moderate conditions and assess the extent of decomposition. From the results of Sheft, et al (7), $CaNi_5H_x$ may be particularly susceptible to degradation during thermal cycling and a good initial system to evaluate.

It is proposed to characterize the behavior of $CaNi_5H_x$ during thermal cycling using proton nuclear magnetic resonance (NMR) techniques. There are several factors which should make this study experimentally convenient and reasonably straightforward to interpret. First, previous pressure-composition-temperature measurements (8,9) of $CaNi_5H_x$ desorption properties reveal that 1.0 atm H_2 pressure at 25°C yields $CaNi_5H_{\sim 5}$ while 2.0 atm H_2 pressure at 85°C yields $CaNi_5H_{\sim 1}$. Hence only a modest temperature change at relatively low gas pressures will give an 80% composition change for thermal cycles between ~25°C and ~90°C. The low pressures will permit use of a glass sample tube for the NMR measurements. The hysteresis factor for the absorption-desorption cycle of $CaNi_5H_x$ is found (8) to be small. This permits large composition changes to actually be obtained for this temperature range. Proton NMR studies have been conducted on CaH_2 (10) and $CaNi_5H_x$ (11) and very large differences are noted at room temperature. The H-atoms are immobile in CaH_2 to give broad spectra with second moment M_2 of 9.0 ± 0.5 G^2; whereas, hydrogen diffuses rapidly at 25°C in $CaNi_5H_{\sim 5}$ and spin echo signals give $T_2 \approx 1$ msec. If both CaH_2 and $CaNi_5H_{\sim 5}$ are present, proton lineshapes and echoes can readily identify their presence as well as permit quantitative determinations of the relative concentrations. The formation of the CaH_2 phase during low-temperature thermal cycling is expected to result in small crystalline broadening mechanisms. However, the dipolar lineshape arises from short range proton-proton interactions according to

$$M_2 = C_H \sum_i r_i^{-6} \qquad (4)$$

where C_H is the nuclear coupling constant. Since the dipolar terms decreases as r^{-6}, the particle dimensions only need to be of order ~10Å - 20Å to yield the "infinite" lattice dipolar sum for eqn. (4). Hence, if CaH_2 particles with these dimensions, or larger, remain in dehydrided multi-cycled $CaNi_5H_x$, analysis of the measured dipolar lineshapes should provide identification from comparison with the published (10) CaH_2 second moment.

The proposed experiment requires a sample container and gas measurement system to permit simultaneous NMR and volumetric measurements. A 0.5 g $CaNi_5$ sample would be placed in a 7 ml glass tube connected via a glass-to-metal seal to a non-magnetic stainless steel manifold with a 75 ml gas collector volume. A valve just above the glass-to-metal seal could isolate the sample chamber and the gas pressure would be continuously monitored by a pressure transducer (PT). This system gives an approximately 80% composition variation when the $CaNi_5H_x$ sample is cycled between 25°C and 90°C. The glass tube fits into the rf-coil of a variable temperature probe for a transient NMR spectrometer.

After loading the $CaNi_5$ sample, the volumes will be calibrated using an inert gas (i.e., argon) and subsequently evacuated using a high-vacuum pump. Upon closing the valve, 2.0 atm of very high purity (i.e., 99.999+%) H_2 gas will be placed in the remainder of the apparatus. The high purity hydrogen is needed to minimize the impurity induced surface reactions (3). When the valve is opened, reaction between $CaNi_5$ and H_2 should begin almost immediately at ambient temperature (8,9) to yield $CaNi_5H_{\sim 5}$ under a final H_2 of about 1.0 atm. The PT output will monitor the course of the reaction. NMR measurements of the proton lineshape, spin echo decay, and T_1 relaxation times will provide initial characterization of the singly hydrided $CaNi_5H_{\sim 5}$. Thermal cycling would commence

with periodic NMR measurements on the cooled and reformed $CaNi_5H_{\sim 5}$ product. The PT output would indicate the onset of degradation. From the results of Sheft, et al (7) approximately 20-40% of the initial hydrogen content may form segregated CaH_2. The proton lineshapes and spin echo decay should permit good discrimination since the properties of the CaH_2 and $CaNi_5H_5$ phases are very different (10,11). Assuming a broadline (i.e., $T_2 \approx 20$ μsec) component corresponding to CaH_2 is formed, the connection of this spectral species with the stable hydride phase can be verified by closing the valve at the maximum temperature of the heating cycle and permitting the dehydrided $CaNi_5H_x$ to cool with minimal H_2 gas. If CaH_2 is now the dominate phase, only the short T_2 component should be present for the proton lineshape and spin echo. A comparison of these parameters with the known (10) CaH_2 lineshape should establish whether the segregated phase is actually the expected CaH_2. When the valve is reopened at room temperature, the NMR spectra should give the two component behavior as the $CaNi_5H_{\sim 5}$ phase forms. The free nickel produced by decomposition can also be qualitatively monitored by the NMR experiments. With the continued formation of magnetic free Ni, the susceptibility of the $CaNi_5H_{\sim 5}$ sample will increase - resulting in a narrowing of the proton spin echo linewidths.

In conclusion, the present NMR experiments would provide a detailed in situ evaluation of possible intrinsic self-decomposition of $CaNi_5H_x$ during thermal cycling. Analyses of the proton lineshapes and echoes should identify the expected formation of the CaH_2 phase (which is probably not possible by x-ray diffraction techniques) as well as quantitative estimates of the relative concentrations of CaH_2 and $CaNi_5H_x$ phases to correlate with the volumetric gas measurements.

REFERENCES

1. J. J. Reilly, Zeits. Physk. Chem. N.F. 117, 155 (1979).
2. R. L. Cohen and J. H. Wernick, Science 214, 1081 (1981).
3. L. Schlapbach, A. Seiler, F. Stucki, P. Zürcher, P. Fischer, and J. Schefer, Zeits. Physk. Chem. N.F. 117, 205 (1979); L. Schlapbach, A. Seiler, F. Stucki, and H. C. Siegmann, J. Less-Common Met. 73, 145 (1980).
4. J. J. Reilly, in Proc. Int. Symp. on Hydrides for Energy Storage, Geilo, August, 1977 (Pergamon, New York, 1978) p. 301.
5. R. L. Cohen, K. W. West, J. H. Wernick, J. Less-Common Met. 70, 229 (1980); and J. Less-Common Met. 73, 273 (1980).
6. H. Rummel, R. L. Cohen, P. Gütlich, and K. W. West, Appl. Phys. Lett. 40, 477 (1982).
7. I. Sheft, D. M. Gruen, and G. J. Lamich, J. Less-Common Met. 74, 401 (1980).
8. G. D. Sandrock, in Proc. 12th IECEC Conf., Vol. I, ANS, p. 951: G. D. Sandrock, in Proc. Int. Symp. on Hydrides for Energy Storage, Geilo, August, 1977 (Pergamon, New York, 1978) p. 353.
9. J. Shinar, D. Shaltiel, D. Davidov, and A. Grayevsky, J. Less-Commo Met. 60, 209 (1978).
10. A. F. Andresen, A. J. Maeland, and D. Slotfeldt-Ellingsen, J. Solid State Chem. 20, 209 93 (1977).
11. A. Attalla, B. D. Craft, and R. C. Bowman, Jr., Bull. Am. Phys. Soc 26, 377 (1981).

PROPOSITION 4

CHARACTERIZATION OF DEFECT STRUCTURE IN SILICON CRYSTALS

ABSTRACT

It is proposed to assess the lattice defects in single crystal Si by exposing well-characterized samples to tritium gas. The concentration and distribution of tritium trapped by this treatment at elevated temperatures will be determined by liquid scintillation counting analyses and autoradiographic techniques. The objective is to establish whether the void concentrations are sufficiently great to verify a recent model that "interstitial" dislocations in ultrapure tetrahedral semiconductors are actually composed of clusters of small (i.e., $\lesssim 6$ nm) voids formed by vacancy precipitation and surface reconstruction.

A long standing problem in the study of semiconductors is the nature of lattice defects which are found in all semiconductor materials. Aside from impurity derived defects, vacancies and self-interstitials have long been known as sources of defects. In spite of intensive study of defects for many years, it has not been conclusively established (1) which point defects are responsible for the majority of dislocations and stacking faults found in high purity silicon. Although self-interstitials are apparently extremely unstable (1) in Si, transmission electron microscopy (TEM) reveals that most dislocations (2) in Si appear to have "interstitial" character (i.e., the lattice planes distort away from the dislocation as if there were interstitials to push the atoms apart). However, it has been argued (1) that vacancies must be the source of many of these defects since rather stable vacancy and vacancy complexes exist in Si. Van Vechten (1) has described a mechanism whereby vacancies can cluster in such a way as to create a dislocation that has "interstitial" characteristics in TEM studies. If the vacancies were to cluster into flat holes, the attraction between opposite faces could cause them to bow inward until they eventually touch. This would create a "vacancy" type dislocation to be easily identified by TEM. Since the atoms on the inner faces of a void have dangling bonds, the free energy of these atoms can also be reduced by a reconstruction of the crystal structure on the void surface to tie up these dangling bonds. Van Vechten (1) suggests that this latter process releases some surface atoms to form bridges between the faces of the flat void. Because Si expands upon solidication, the bridges push the void faces apart to create the appearance of an interstitial dislocation in TEM studies. Van Vechten predicts that perhaps $\sim 10^{15}$-10^{16} voids/cm^3 with dimensions $\lesssim 6$ nm would exist in high-purity Si crystals if this model is valid whereas an "interstitial" mechanism for dislocation formation would imply orders of magnitudes fewer vacancies or voids. Although such small voids would be extremely difficult to identify by conventional TEM methods, their presence might be detected (1) by the diffusion of a radioactive gas through the solid where voids could trap

this gas to retain excess quantities well above the normal solid solubility limits. Since the permeation of hydrogen isotopes in single crystal silicon is known (3,4) to be very rapid at elevated temperatures, the radioactive tritium isotope should be an excellent choice for these experiments.

In order to establish whether the void concentrations in single crystal Si are sufficiently large to be consistent with Van Vechten's description (1) of the formation and character of "interstitial-type" dislocations, measurements of total tritium solubility in Si crystals are proposed. The approach is to expose well-characterized ultrahigh purity Si crystals to tritium gas while heating the samples to between 900 and 1100°C where the permeability and solubility behavior are known from previous studies (3,4). After the tritium exposure, representative samples would be dissolved in acidic media and the total trapped tritium contents measured by conventional scintillation counting methods. Concurrently, autoradiographic techniques (5) would be employed on several identical samples to deduce any inhomogeneous tritium distributions with the bulk crystals (e.g., possible diffusion profiles, enrichments near surfaces, grain boundaries, or dislocations, etc.).

To carefully test the relationship between tritium trapping in voids and Van Vechten's mechanism (1) for the formation of dislocations, the Si single crystals need to be grown under different conditions that will vary the dislocation densities (i.e., variable crystal growth rates, annealing, etc.). TEM would be used to characterize the types and distributions of lattice defects in crystal pieces that are adjacent to those crystals exposed to the tritium gas. From the hydrogen solubility and permeation data (3,4) in crystalline Si, it is estimated that 10^{15}-10^{16} 6 nm voids/cm^3 should trap at least 10-100 times more tritium than is retained at the equilibrium levels. This enhanced concentration should be readily and quantitatively detected by the very sensitive radiocounting analysis. Dissolution of the Si samples should occur in a closed reactor that captures any evolved gases to convert molecular tritium into water for a

complete analysis of total tritium contained in the crystals. The results from the TEM and radiocounting measurements should permit direct comparisons between the concentrations of dislocations and the amounts of trapped tritium in identical samples. Hence, extraneous factors should be minimal. The autoradiographic measurements should verify that any excess tritium is actually concentrated in the regions of greatest dislocation density.

If small voids are responsible for the presumably "interstitial" dislocations in ultrapure tetrahedral semiconductors like single-crystal Si, there should be a positive correlation between the quantity of trapped tritium over the expected (3,4) solubility limits and the dislocation density. If this agreement is observed, it would provide strong experimental support to the "interstitial-type" dislocation mechanism developed by Van Vechten (1). Since direct identifications of these voids by TEM are probably unlikely (1), the present experiments may provide the most amenable method to give independent evidence for the voids. A previous study (4) of tritium solubility in single-crystal Si cannot be related to Van Vechten's vacancy-void models since only the quantity of tritium released from Si had been measured and no information on the total tritium retention (which would include amounts possibly trapped in voids) is available.

REFERENCES

1. J. A. Van Vechten, Phys. Rev. B 17, 3197 (1978).
2. A. Staudinger, J. Appl. Phys. 49, 3870 (1978).
3. A. van Wieringen and N. Warmoltz, Physica 22, 849 (1956).
4. T. Ichimiya and A. Furuichi, Int. J. Appl. Rad. Isotopes 9, 573 (1968).
5. J. D. Braun, G. L. Downs, and G. W. Powell, Metallography 4, 231 (1971).

PROPOSITION 5

RESONANCE RAMAN STUDIES OF THE GROUND AND EXCITED STATES IN $[\eta^5\text{-}C_5H_5Fe(CO)]_2$ - $\mu\text{-}Ph_2P(CH_2)PPh_2$

ABSTRACT

Time-resolved resonance Raman spectroscopy would be used to determine changes in the Fe-Fe and CO stretching frequencies in the lowest photolytically excited states relative to these vibrations in the ground electronic state. The intent is to establish whether the Fe-Fe σ-bond or a theoretically predicted non-bonding orbital is the highest occupied molecular orbital in the named compound.

Among the many interesting aspects of photochemistry in the transition-metal organometallic compounds, the behavior of the polynuclear species with direct metal-to-metal bonds is currently very active because these complexes may have applications for solar energy conversion and storage (1). Since the irradiation of the single M-M bond may be viewed as

$$\sigma^2 \xrightarrow{h\nu} \sigma^1 \sigma^{*1} \qquad (1)$$

where σ and σ^* are the bonding and antibonding molecular orbitals of the metal-metal bond, photolysis of a dimeric complex with a single metal-metal bond usually ruptures that bond (2) to produce reactive monomeric complexes. However, Tyler, et al (3) have suggested that irradiation of $Cp_2Fe_2(CO)_4$, a dimer with a single Fe-Fe bond and two carbonyl bridges where Cp denotes cyclopentadienyl, generates an excited state dimer without the Fe-Fe bond but held together by the dual carbonyl bridges. This interpretation presumes (4) that σ(Fe-Fe) is the highest occupied molecular orbital (HOMO) in $Cp_2Fe_2(CO)_4$. It is anticipated that irradiation of the related system $Cp_2Fe_2(CO)_2(P_2Ph_4CH_2)$ should also produce a photochemically stable intermediate as

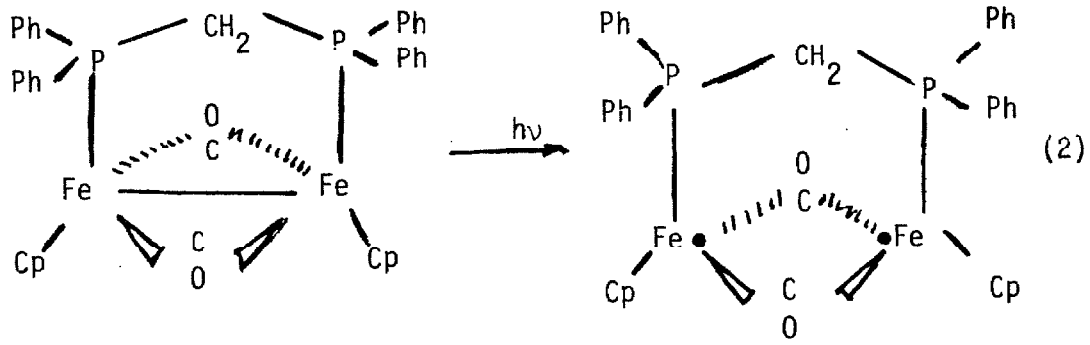

(2)

which is held together by the bridging carbonyls and phosphine ligands. However, the molecular orbital (MO) calculations of Sherwood and Hall (5) predict that the HOMO in this complex is largely Fe-Fe non-bonding in character with substantial contributions to the CO π-bonds while σ(Fe-Fe) lies at a lower energy. Thus, this MO calculation (5) suggests that the

Fe-Fe bond should be similar in the ground and photolytically excited states of $Cp_2Fe_2(CO)_2(P_2Ph_4CH_2)$ in contrast to the behavior indicated in eqn. (2). Raman spectroscopy studies of the vibrational properties in the ground and excited states are proposed to determine which interpretation is correct.

Raman spectroscopy has been extensively used (6-8) to study the characteristics of metal-metal bonds in the ground states of transition metal complexes. The recent development of the time resolved resonance Raman (TR^3) technique has permitted evaluation of the vibrational properties in the excited electronic states for several transition metal complexes (9-12). Whenever the M-M bond order is altered by photolytic excitation, changes in the M-M stretching vibrational frequency are also expected. In fact, in a TR^3 experiment on tetrakis (1,3-diisocyanopropane) dirhodium(I), Dallinger, et al (10) observed a significantly higher ν_{Rh-Rh} in the excited-state relative to the Raman frequency for the Rh-Rh bond in the ground state. This observation is consistent with simple theoretical predictions (10) that the Rh-Rh bond order is zero in the ground state but the promotion of an electron out of the σ^*_{RhRh} orbital greatly enhances the Rh-Rh bonding in the excited states. If eqn. (2) is valid, a reverse situation is expected for ν_{Fe-Fe} behavior in the ground and excited states of $Cp_2Fe_2(CO)_2(P_2Ph_4CH_2)$ since the removal of an electron from the bonding σ_{FeFe} HOMO will give a much lower ν_{Fe-Fe} in the excited state. However, if a non-bonding state is the HOMO as predicted by the MO calculations (5), ν_{Fe-Fe} should be essentially unchanged between the ground and excited states.

The instrumentation necessary to perform the resonance Raman and TR^3 experiments in a study of $Cp_2Fe_2(CO)_2(P_2Ph_4\ CH_2)$ would be similar to the systems previously described in the literature (9-12). Namely, two lasers and a rapid scan detector system with timing circuits to control and synchronize light pulse generation and detection are required. The probe laser could be an XeCl excimer pumped dye laser to produce narrow band tunable radiation over the range 400 to 900 nm. This feature is desirable

to give great flexibility in observing the resonance Raman effect (13) for various electronic transitions from the ground and excited states. The second (532 nm) or third (355 nm) harmonics of a pulsed Nd:YAG laser would probably serve as the excitation sources for the TR^3 measurements. The resonance Raman scattered light is diffracted by a monochromator for detection by a photodiode system where an optical multichannel analyzer processes the signal for recording. The sample would consist of a benzene solution of $Cp_2Fe_2(CO)_2(P_2Ph_4CH_2)$ prepared by the method of Haines and duPreez (14).

The proposed study of $Cp_2Fe_2(CO)_2(P_2Ph_4CH_2)$ would consist of two parts. First, the ground state vibrational bonds would be determined from the resonance Raman spectra obtained without the use of the excitation laser. The ν_{FeFe} stretching frequency is reported to be ~220 cm^{-1} for the single Fe-Fe bond (8) and ~284 cm^{-1} for the double Fe=Fe bond (7). Hence, a relatively strong Raman scattering peak near 220 cm^{-1} is expected for ν_{FeFe} in the ground state along with a ν_{CO} stretching frequency around 1700 cm^{-1} for the bridging carbonyl (5). Very different behavior in the ν_{FeFe} and ν_{CO} for the excited states are expected for the alternative HOMO descriptions of (a) σ_{FeFe} as implied from eqn. (2) and ref. 3 or (b) the Fe-Fe non-bonding orbital with CO π-character (5). In case (a), the ν_{FeFe} will be substantially decreased in the excited state since the electronic configuration is $\sigma^1\sigma^{*1}$ with zero bond order while only minor variations in ν_{CO} should be seen. Although ν_{FeFe} in the excited state will probably also decrease somewhat for case (b) since the MO calculation (5) predicts that σ^*_{FeFe} is the lowest unoccupied molecular orbital, two electrons would remain in σ_{FeFe} to retain moderate Fe-Fe bond strength. However, the removal of the electron from the non-bonding MO for case (b) should strengthen the CO bond and significantly increase ν_{CO} in the excited state in contrast to the behavior for case (a). Hence, the TR^3 measurements should provide relatively straightforward identification of the HOMO as well as the vibrational properties in the ground and excited electronic states of this interesting dimeric complex.

REFERENCES

1. H. B. Gray and A. W. Maverick, Science 214, 1201 (1981).
2. G. L. Geoffroy and M. S. Wrighton, Organometallic Photochemistry (Academic, New York, 1979).
3. D. R. Tyler, M. A. Schmidt, and H. B. Gray, J. Am. Chem. Soc. 101, 2753 (1979).
4. D. C. Harris and H. B. Gray, Inorg. Chem. 14, 1215 (1975).
5. D. E. Sherwood, Jr. and M. B. Hall, Inorg. Chem. 17, 3397 (1978).
6. T. G. Spiro, Progr. Inorg. Chem. 11, 1 (1970).
7. G. J. Kubas and T. G. Spiro, Inorg. Chem. 12, 1797 (1973).
8. J. SanFilippo, Jr. and H. J. Sniadoch, Inorg. Chem. 12, 2326 (1973).
9. R. F. Dallinger and W. H. Woodruff, J. Am. Chem. Soc. 101, 4392 (1979).
10. R. F. Dallinger, V. M. Miskowski, H. B. Gray, and W. H. Woodruff, J. Am. Chem. Soc, 103, 1595 (1981).
11. J. W. Schindler and J. I, Zink, J. Am. Chem. Soc. 103, 5968 (1981).
12. P. G. Bradley, N. Kress, B. A. Hornberger, R. F. Dallinger, and W. H. Woodruff, J. Am. Chem. Soc, 103, 7441 (1981).
13. M. D. Morris and D. J. Wallan, Anal. Chem. 51, 182A (1979).
14. R. J. Haines and A. L. duPreez, J. Organomet. Chem. 21, 181 (1970).